Analysis of the sources of the systematic errors in GNSS precise positioning : contribution of the constellation Galileo

Hanane Ait-Lakbir

Université Fédérale
Toulouse Midi-Pyrénées

THÈSE

En vue de l'obtention du
DOCTORAT DE L'UNIVERSITÉ DE TOULOUSE

Délivré par l'Université Toulouse 3 - Paul Sabatier

Présentée et soutenue par

Hanane AIT-LAKBIR

Le 16 novembre 2023

Analyse des sources d'erreurs systématiques dans le positionnement précis par GNSS: apport de la constellation Galileo

Ecole doctorale : **SDU2E - Sciences de l'Univers, de l'Environnement et de l'Espace**

Spécialité : **Sciences de la Terre et des Planètes Solides**

Unité de recherche :
GET - Geosciences Environnement Toulouse

Thèse dirigée par
Felix PEROSANZ et Alvaro SANTAMARIA

Jury

M. Gilles METRIS, Rapporteur
M. Jean-Paul BOY, Rapporteur
Mme Joelle NICOLAS, Examinatrice
Mme Marianne MéTOIS, Examinatrice
Mme Florence BIROL, Examinatrice
M. Felix PEROSANZ, Directeur de thèse
M. Alvaro SANTAMARíA-GóMEZ, Co-directeur de thèse

Remerciements

Ces quelques lignes de remerciements ne sauraient véritablement refléter toute la gratitude que je ressens envers ceux et celles qui ont contribué, de près ou de loin, à la réussite de cette expérience.

En tout premier lieu, je remercie chaleureusement mes directeurs de thèse, Félix Perosanz et Alvaro Santamaría-Gómez. Leur disponibilité malgré leurs agendas chargés, leurs conseils avisés, et nos nombreuses discussions – parfois sans fin – ont grandement contribué à ma formation de géodésienne et à l'avancée de ma thèse. Je leur suis profondément reconnaissante pour leur confiance, leur précieuse aide et leur soutien.

Je tiens également à remercier Pierre Exertier et Paul Rebischung pour avoir fait partie de mon comité de suivi de thèse, ainsi qu'aux membres de mon jury - Florence Birol, Jean-Paul Boy, Joelle Nicolas, Marianne Métois et Gilles Métris - pour leur évaluation et leurs suggestions pour améliorer ce manuscrit ainsi que ma thèse actuelle ainsi que de futurs travaux. Also, many thanks to Jim for taking from his time from his retirement to carefully review my work and give me his sincere and helpful feedback.

Je souhaite exprimer ma gratitude envers mes collègues de bureaux au GET, Shambo, Edgar, Daniel, Hugo, Quentin et Florent, pour avoir grandement contribué à une atmosphère de travail des plus agréables, marquée par de nombreuses discussions tantôt scientifiques tantôt plus informelles, et de fous rires mémorables. Je suis également reconnaissante envers Vincent, Christine et Emmanuel pour leur précieuse aide lors de mes premiers pas dans l'enseignement à l'UPS.

De manière générale, je souhaite également adresser mes remerciements à toutes les personnes avec lesquelles j'ai eu la chance de travailler ou échanger, que ce soit virtuellement ou en face à face, et qui m'ont apporté leur aide pour cette thèse, que ce soit directement ou indirectement. Qu'elle ou il trouve ici l'assurance de ma reconnaissance.

Last but not least, mes remerciements ne sauraient être complets sans exprimer ma reconnaissance envers tous mes proches et surtout à ma famille. Un merci spécial à ma sœur pour son soutien et ses conseils. Mais, avouons-le, on sait maintenant qu'il faut assurément plus qu'un BAC+8 pour comprendre ta fameuse méthode PERT 😄 Un grand merci à mon frère, à mon père, et à ma mère – alias la Gardienne du Temps – pour leur tendresse et encouragement tout au long de cette aventure. Je vous suis infiniment reconnaissante pour tout ce que vous avez fait pour moi.

Abstract

Beside their use for navigation, many scientific fields such as geophysics and geodesy use precise positioning by Global Navigation Satellite Systems (GNSS) to measure millimeter-to-centimeter deformations of the Earth's surface. However, many sources of error affect the precision of the positioning, introducing spurious signatures into position series. Understanding them is therefore essential to limit the misinterpretation of GNSS station displacements in terms of geophysical processes. One step towards this goal is to characterize the systematic errors specific to each constellation, as well as the mechanisms involved in propagating these errors to positioning.

This thesis contributes to the current understanding of these systematic errors and the strategies to mitigate them. To this end, we compare the constellations currently available - GPS, GLONASS, Galileo and BeiDou - in order to carry out a comprehensive analysis of these errors. First, we investigate the errors in the modeled displacements induced by ocean tide loading (OTL), and their effects on the periodic signatures observed in the GNSS positions. Then, we analyze the contribution of GNSS satellites' orbital dynamics to the correlated positioning noise.

In part 1, we have improved the estimates of errors in the OTL displacement model by using multi-GNSS observations, by developing a new estimation strategy based on the addition of empirical parameters in PPP and the stacking of normal equations. This enables us to overcome the constellation-specific errors that impact the estimation of OTL model errors, in particular for the K1 and K2 tidal frequencies, which is improved by up to 50 % by using Galileo observations. The subdiurnal tidal model errors produce different signals, depending on the constellation. These aliasing signals are specific to the GPS constellation at the fortnightly (13.6 days) and seasonal frequencies. Additional aliased signals at higher frequencies have been identified for Galileo and GLONASS.

Part 2 discusses the contribution of orbital dynamics to the flicker noise observed in the GNSS position series, and examines two aspects of satellite orbits: the long-term stability of orbital parameters and orbit discontinuities at midnight. We show that part of the colored noise is specific to GPS-only products, suggesting the contribution of the satellite orbits product or the constellation design. Indeed, GPS satellites are more prone to secular behavior than other GNSS constellations, particularly due to lunisolar gravitational acceleration resonances. The thesis also identifies three factors that contribute to the emergence of flicker noise in positions: the time-varying observation geometry caused by long-term instability in satellite orbits, the presence of observation errors that do not average to zero over satellite elevations, and the limitations of observation weighting in mitigating these errors. All three factors are present in GPS-derived positioning, but these findings open up perspectives as to the means to reduce the noise correlation in GNSS positions. Finally, we also give preliminary results about another potential source of colored noise coming from orbit discontinuities, using simplified models to examine the effects of the presence of stochastic accelerations or noise in the satellite's dynamic response.

By providing insight into the systematic errors that affect the accuracy of multi-GNSS positioning, our results will allow us to facilitate the detection and interpretation of geophysical deformations from GNSS positioning. In addition to improving our understanding of the geophysical processes, this also opens up avenues for future work to refine the current processing strategies for GNSS observations and modeling strategies of GNSS position time series.

Résumé

Outre leur utilisation pour la navigation, de nombreux domaines scientifiques comme la géophysique et la géodésie utilisent le positionnement précis par GNSS (Global Navigation Satellite Systems) pour mesurer les déformations de la surface de la Terre avec une précision de l'ordre du millimètre au centimètre. Cependant, de nombreuses sources d'erreurs affectent la précision du positionnement, introduisant ainsi des signatures parasites dans les séries de positions. Les comprendre est donc essentiel pour limiter une interprétation erronée des déplacements des stations GNSS en termes de processus géophysiques. Une étape vers ce but est de caractériser les erreurs systématiques propres à chaque constellation ainsi que les mécanismes impliqués dans la propagation de ces erreurs au positionnement.

Cette thèse contribue à la compréhension actuelle de ces erreurs systématiques et des stratégies pour les atténuer. Pour cela, nous comparons les constellations aujourd'hui disponibles, GPS, GLONASS, Galileo et BeiDou, afin de mener une analyse complète de ces erreurs. Nous étudions d'abord l'effet des erreurs de modèles de déplacements dus à la surcharge des marées océaniques (Ocean Tide Loading - OTL) sur les signatures périodiques observées dans les positions GNSS. Puis, nous analysons la contribution de la dynamique orbitale des satellites GNSS à la corrélation du bruit de positionnement.

Dans la première partie, nous avons amélioré les estimations des erreurs dans le modèle de déplacement OTL grâce aux observations multi-GNSS, et en développant une nouvelle stratégie d'estimation basée sur l'ajout de paramètres empiriques dans le traitement PPP et le cumul d'équations normales. Cela nous permet de passer outre les erreurs systématiques, liées aux constellations, qui impactent l'estimation des erreurs dues au modèle OTL. En particulier pour les fréquences de marée K1 et K2, on obtient une estimation améliorée de 50 % en utilisant les observations Galileo. Les erreurs subdiurnes dues au modèle OTL produisent également des signaux périodiques à longues périodes, différents en fonction de la constellation. On a identifié des signaux spécifiques à la constellation GPS aux périodes de 13,6 jours et saisonnières. D'autres signaux se propagent à des périodes plus courtes pour Galileo et GLONASS.

La seconde partie analyse la contribution des orbites des satellites GNSS au bruit de scintillation (bruit flicker) observé dans le positionnement, sous deux aspects : leur stabilité à long terme et les discontinuités des produits d'orbite. Le bruit flicker ne s'observe qu'avec les produits GPS. En effet, les orbites GPS sont plus enclins à une dérive interannuelle, en comparaison avec les autres constellations GNSS ; ce qui implique une géométrie d'observation variable dans le temps. De plus, deux autres facteurs contribue à l'émergence du bruit flicker dans les positions : la présence d'erreurs d'observation introduisant des biais dépendant de l'élévation des satellites, et les limites des fonctions de pondération des observations GNSS. Ces trois facteurs, présent avec GPS, ouvrent des perspectives quant aux moyens de réduire la corrélation du bruit dans les positions GNSS. Enfin, nous présentons des résultats préliminaires sur une autre source potentielle de bruit coloré, en analysant les discontinuités d'orbites et en utilisant des modèles simplifiés pour déterminer l'effet d'accélérations stochastiques ou de bruit dans la réponse dynamique du satellite.

En examinant les erreurs systématiques qui affectent la précision du positionnement multi-GNSS, nous avons obtenu des résultats qui permettent non seulement de mieux observer les processus géophysiques en facilitant leur détection et l'interprétation des déformations géophysiques à partir des positions GNSS, mais aussi d'ouvrir la voie à des travaux futurs afin d'améliorer les traitements des observations GNSS et la modélisation des séries temporelles de positions GNSS.

Table of Contents

Introduction abrégée en Français

La manière d'aborder plusieurs défis sociétaux et scientifiques a été transformée par le développement des systèmes de navigation par satellite (Global Navigation Satellite Systems - GNSS). Les GNSS offrent en effet un moyen de déterminer la position de points situés sur Terre (et dans l'espace) de manière précise, et leur utilisation s'est répandu ces dernières décennies. Au-delà de la navigation, de nombreux domaines scientifiques tels que la géophysique et la géodésie ont bénéficié du GNSS. Un aperçu complet de ces applications actuelles du GNSS peut être retrouvé dans Bock and Melgar (2016). Dans cette thèse, nous nous concentrerons en particulier sur l'analyse des positions de stations GNSS utilisées notamment pour étudier les déformations de l'écorce terrestre. La variété des domaines scientifiques dans lesquels les résultats de cette thèse trouvent un intérêt est brièvement présentée dans la version en anglais de cette introduction (voir Chapter 1). Compte tenu des signaux et erreurs systématiques présents les séries temporelles de positions GNSS, il est essentiel d'en comprendre les sources afin d'une part, d'améliorer la précision du positionnement GNSS, mais également l'interprétation des déplacements observés par GNSS en termes de processus géophysiques.

Avec une précision de l'ordre du centimètre ou du millimètre, les positions GNSS peuvent mesurer le déplacement de points à la surface de la Terre, ce qui permet de mieux comprendre les déformations de l'écorce terrestre causées par divers processus géophysiques tels que les mouvements des plaques tectoniques, l'activité volcanique, les tremblements de terres mais aussi le redistribution des masses de glace ou d'eau due à l'alternance des saisons, au changement climatique ou à l'utilisation des ressources en eaux. Déterminer des déplacements précis est important pour les applications scientifiques, mais est également devenu une exigence pour de plus en plus de services comme le transport ou l'exploitation de données géolocalisées (imagerie, agriculture, ...). La précision de la mesure de ces déplacements dépend non seulement de la technique de positionnement, mais également de la précision et de la stabilité du repère terrestre par rapport auquel ces déplacements sont mesurés. Or, étant donné que la Terre est une planète dynamique qui est continuellement en déformation, ce repère terrestre de référence nécessite de ne pas être biaisé par des déformations pour que les variations de coordonnées reflètent de vrais déplacements.

La disponibilité actuelle de plusieurs constellations de satellites, à savoir GPS, Galileo, GLONASS et BeiDou, a créé un besoin d'analyser et de caractériser les erreurs systématiques propres à chaque constellation et les mécanismes de propagation d'erreurs impliqués dans le positionnement GNSS. Cette thèse vise à contribuer aux connaissances actuelles sur deux aspects particuliers de ces erreurs: l'effet des erreurs de modélisation de déplacement dû aux surcharges des marées océaniques (OTL) sur les signatures périodiques du positionnement GNSS, et la contribution de la dynamique orbitale et de la conception des constellations aux corrélations spatiotemporelles des erreurs de positionnement.

Erreurs systématiques dans les séries temporelles de positions GNSS

L'approche standard pour modéliser les coordonnées des stations GNSS consiste à ajuster un modèle cinématique qui inclut la vitesse de déplacement de la station, des termes harmoniques, en particulier annuels et semi-annuels, et d'autres paramètres permettant de prendre en compte les discontinuités de coordonnées ou les déplacements co-sismiques. Chacun de ces termes est exploité pour inférer des modèles géophysiques (surcharge non-maréale, rebond post-glaciaire (GIA - Glacial Isostatic Adjustment) ou les sources d'erreurs provenant de la technique GNSS.

Les déplacements résiduels observés après avoir retiré ce modèle cinématique permettent d'identifier les déplacements restants non modélisés (mouvements ou non linéaires de la croûte) mais aussi les signatures systématiques communes aux séries temporelles GNSS. Pour améliorer la précision du positionnement et l'interprétation des positions GNSS, il est donc nécessaire d'avoir une compréhension approfondie de l'origine de ces erreurs systématiques et de la manière dont elles se propagent au positionnement. On peut diviser ces erreurs en deux catégories selon leurs caractéristiques: les erreurs périodiques et la corrélation du bruit de positionnement.

Erreurs périodiques

L'analyse des résidus des positions journalières des stations GNSS montre la présence de signaux périodiques qui peuvent provenir de diverses sources dont des processus géophysiques non modélisés, des erreurs dans les orbites des satellites et des erreurs spécifiques au site. Les signaux périodiques qui prédominent sont les signaux annuels et semi-annuels. Ceux-ci peuvent être attribués à des déplacements saisonniers (Dong et al., 2002; Yan et al., 2009) ou à des changements environnementaux qui influencent la propagation des signaux GNSS, tels que les fluctuations de l'atmosphère (température, humidité) [REF], le multitrajet ou d'autres causes de variations saisonnières de la visibilité des satellites comme la couverture neigeuse (Koulali and Clarke, 2020).

D'autres signaux périodiques spécifiques à la constellation sont également présents dans les positions GNSS aux fréquences draconiques GPS (Ray et al., 2008), aux fréquences de répétition des constellations GLONASS à 8 jours (Rebischung et al., 2021) et Galileo à 10 jours (Zajdel et al., 2022). Ces signatures sont considérées comme étant causées directement par des signatures dans la modèlisation dynamique des orbites (Rodriguez-Solano et al., 2014) ou par l'observation répétée d'erreurs spécifiques au site aux périodes propres de la constellation ou à la période orbitale (King and Watson, 2010; Sidorov and Teferle, 2015).

De plus, des signaux de repliement à 14 jours se produisent en raison du battement des erreurs de modèle de marée subdiurne et de la répétition de la constellation ou de l'échantillonnage à 24 heures utilisé pour traiter les données GNSS (orbite ou positionnement). Ces signaux ont été identifiés non seulement avec les observations GPS (Penna et al., 2007) mais également avec des données GLONASS (Abraha et al., 2018).

Tous ces signaux périodiques ont un impact significatif sur l'analyse des séries temporelles de position GNSS, conduisant à des biais dans les paramètres estimés du modèle de coordonnées dont des biais dans la tendance. Pour atténuer cette source d'erreur, il est important de distinguer les déplacements géophysiques résiduels des erreurs spécifiques à l'utilisation de données GNSS. Si en appliquant des modèles plus précis, nous pouvons réduire les signatures géophysiques, cependant, seule l'amélioration des infrastructures GNSS (par exemple, multi-trajet, stabilité d'antenne) et des stratégies de traitement permettraient d'atténuer les erreurs spécifiques au GNSS.

Corrélation du bruit de positionnement

Les précédents travaux de recherche ont caractérisé le bruit présent dans les positions GPS comme une combinaison de bruit en loi de puissance, en particulier de bruit de scintillation (ou bruit flicker) à basse fréquence et de bruit blanc à haute fréquence. Alors que le bruit blanc est un bruit non corrélé, le bruit de scintillation se caractérise par la corrélation entre deux réalisations du processus quel que soit le délai entre celles-ci.

La connaissance de la nature du bruit dans les positions GNSS est également essentielle pour garantir l'estimation correcte des paramètres du modèle de coordonnées et pour dériver des incertitudes fiables à partir des données de séries temporelles. L'investigation de la source de ces erreurs corrélées dans les positions GNSS est un domaine de recherche actif. Un certain nombre d'études ont tenté d'identifier les sources de cette corrélation temporelle des positions GNSS. Une explication possible est les déplacements résiduels du sol qui ne sont actuellement pas pris en compte lors du traitement des données GNSS et qui résultent d'une variété de processus géophysiques tels que l'instabilité du sous-sol, des mouvements aléatoire dus à la tectonique, ou encore les variations non-linéaire des déplacements dues aux surcharges hydrologiques. Le bruit blanc ainsi qu'une partie du bruit en loi de puissance peuvent être attribués à de ce type de déplacements (Boy, 2022; Gobron et al., 2021; Memin et al., 2020; Rebischung et al., 2018). On suppose que du bruit lié à la technique GNSS est responsable du reste de la corrélation inexpliquée, bien que les sources exactes et les mécanismes sont inconnus. Les positions GNSS sont non seulement corrélées temporellement, mais également corrélées spatialement. Les causes de ces corrélations sont encore à explorer telles que les sources d'erreurs susceptibles d'affecter de la même manière toutes les stations GNSS situées dans un rayon d'influence comme les conditions atmosphériques ou les erreurs des orbites des satellites.

Objectifs de la thèse

Bien que plusieurs systèmes GNSS soient disponibles pour améliorer la précision du positionnement précis, il est important de comprendre les caractéristiques que chaque système peut introduire dans les séries de positions. La constellation GPS est de loin le système le plus utilisé pour les applications scientifiques en raison de la disponibilité de longues séries et de la couverture fournie par le nombre de récepteurs au sol suivant les signaux GPS. Cependant, les constellations Galileo et BeiDou ont commencé à apporter des contributions importantes à l'amélioration de la précision du positionnement. Par conséquent, dans cette thèse, nous discuterons comment l'utilisation de la constellation Galileo, et dans une moindre mesure des autres constellations: GLONASS et BeiDou, peut contribuer à l'identification et à la compréhension des erreurs systématiques dans les séries temporelles de position.

Dans cette thèse, nous étudierons d'abord l'impact des erreurs de modélisation des déplacements dus aux surcharges de marées océanique (OTL) sur les erreurs de positionnement GNSS, en mettant particulièrement l'accent sur l'évaluation des erreurs de modèle avec des mesures multi-GNSS et sur les signatures périodiques résulant de la propagation des erreurs sous-journalières. Cette thèse abordera les questions suivantes dans une première partie:

1. Quelle est la stratégie la plus efficace pour réduire les erreurs spécifiques à chacune des constellations et les erreurs formelles lors de l'évaluation des erreurs de modèle OTL?
2. Dans un contexte multi-GNSS, quelle est l'approche optimale pour utiliser chaque système pour minimiser les erreurs d'estimation ?
3. Quelles sont les implications pour les signaux de repliement, en particulier aux fréquences bimensuelles et saisonnières?

Dans une seconde partie, nous étudierons la contribution de la dynamique orbitale au bruit coloré dans les positions de station dérivées du GNSS à travers les questions suivantes:

1. Le bruit en scintillation (ou bruit flicker) observé pour GPS est-il également observé lorsque les positions sont déterminées avec la constellation Galileo ? En d'autres termes, y a-t-il une contribution de l'orbite ou de la constellation au bruit coloré observé dans les séries de positions?
2. Quelles sont les natures de ces contributions orbitales, le cas échéant?
3. Quel est le mécanisme sous-jacent à la propagation de l'orbite des satellites aux erreurs corrélées dans le positionnement GNSS ?

CHAPTER

1 Introduction

Several societal and scientific questions have benefited from the development of Global Navigation Satellite Systems (GNSS). GNSS offer a means of determining accurate and precise positions on earth, and its use has increased dramatically in recent decades. Beyond navigation, many fields such as geophysics and geodesy have become dependent on GNSS. A comprehensive overview of the current geoscientific applications of GNSS can be found in Bock and Melgar (2016). In this thesis we will focus especially on analyzing the estimated GNSS station positions used to monitor the Earth's surface deformations. The variety of scientific fields in which our work can be applied is briefly introduced in this chapter. Since GNSS-derived precise positioning is affected by a number of errors, understanding them is essential for achieving high-precision positions that can be properly interpreted in terms of geophysical displacements.

The current availability of several satellite constellations, namely GPS, Galileo, GLONASS and BeiDou, has made possible to investigate and characterize the systematic errors particular to each constellation and the mechanisms involved in GNSS positioning. This thesis aims to contribute to the current knowledge of GNSS positioning errors and how to mitigate them. Two aspects of these errors are investigated: the effect of Ocean Tide Loading (OTL) errors on GNSS positioning periodic signatures, and the contribution of orbital dynamics and constellation designs to the spatiotemporal correlations of the positioning errors.

1.1 Applications of GNSS station position time series in geosciences and geodesy

GNSS is one of the fundamental space techniques used in geodesy, the science that studies the shape of the Earth, its gravitational field, and its rotation, and how they change over time. Accurate to millimeters, GNSS positions can measure the displacement of points on the Earth's surface, enabling a better understanding of crustal deformation caused by various geophysical processes such as tectonic plate movement, volcanic activity, earthquakes, and the redistribution of ice or water masses due to seasonal and climate change. The purpose of this section is to give the reader an overview of the level of precision that GNSS positioning needs to achieve.

Seismology and tectonics

Plate models are important for understanding the dynamics of the Earth's outer layer: the lithosphere. They provide the framework for understanding geophysical processes like mountain formation, volcanoes, and earthquakes, and how the Earth's surface evolves over time (Freymueller, 2011). To build global or regional tectonic plate models, GNSS provide position time series from which linear rates corresponding to the motion of tectonic plates can be derived from a large and well-distributed network of tracking stations (Altamimi et al., 2017; Takahashi and Hashimoto, 2022). While the models agree well with GNSS observations inside the plates, where the crust can be assumed to be rigid, there is clear evidence of deviations from the secular model caused by deformation at the plate boundaries. This can be reconstructed from GNSS observations, e.g. at the Pacific plate boundaries (California) in combination with InSAR imaging (Donnellan et al., 2017), on the western boundary between the African and Eurasian plates (Serpelloni et al., 2007), or on the boundary of the Oceania plate (Takahashi and Hashimoto, 2022). The remaining discrepancy is estimated to be in the order of 0.3 mm/yr (Altamimi et al., 2017) between the plate models and the observed station displacements.

In addition to the analysis of plate deformation, GNSS measurements of coseismic ground displacements are used to investigate the earthquake source and provide constraints on the mechanical properties of faults and their evolution within fault systems (Fialko, 2004). This helps to understand the propagation of the seismic wave, the shape and size of the rupture, and the energy released into the Earth's crust during earthquakes. GNSS measurements can also be used to estimate postseismic deformations, which correspond to the relaxation of the crust after the earthquake (Gonzalez-Ortega et al., 2014). The precision of the estimated GPS velocities needed to discriminate between different fault models is on the order of 1 mm/y (DeVries and Meade, 2013; Tong et al., 2013). Transients, typically slow motions, require measurements of slip rates from millimeters per day (0.1 m/y) to millimeters per year. This is one to three orders of magnitude less than what occurs in regular seism, where rates may reach meters per second. Several algorithms have been applied to detect these transient signals within the daily GPS displacement time series (Crowell et al., 2016; Dong et al., 2006; Ji and Herring, 2013; Walwer et al., 2016). However, today, due to the presence of correlated noise in the time series (Mao et al., 1999), the smallest year-long transients cannot be detected in the GNSS positions.

Climate sciences

Crustal deformation can also occur because of climate change or anthropogenic (e.g. pumping) mass variations on the Earth's surface. The estimated displacements of GNSS stations can also be used to observe these deformations. For example, GNSS receivers are being used to measure the elastic response of the Earth to the ongoing melting of ice masses in Greenland (Bevis et al., 2012, 2019) or in Antarctica (Koulali and Clarke, 2020; Martín-Español et al., 2016). Monitoring this ongoing process is critical to accurately measure the ice mass loss and to predict its contribution to the future sea level rise. In addition, the Glacial Isostatic Adjustment (GIA), which represents the viscoelastic response of the crust to past glacial melt, is assessed using the horizontal and vertical crustal displacement observed by GNSS. These observations help to improve not only the values of the variables in the global GIA models (Argus et al., 2014b; King et al., 2010), but also the model of the current movements of geodetic stations in the affected areas. The differences between current GIA models and the GNSS observations are 0.4 mm/y to 1.5 mm/y (Li et al., 2022; Reusen et al., 2023; Steffen, 2023; Whitehouse et al., 2019).

White et al. (2022) provide an overview of GNSS hydrogeodetic applications that study hydrologic stress using GNSS position time series, among other geodetic techniques. Inversion of crustal deformations provides information on the physical properties of crustal response, which are used to constrain hydrological models (Michel et al., 2021), as well as information on the load responsible for crustal deformation, i.e. mass variation of terrestrial water storage (TWS) over time. (van Dam et al., 2001). These deformations are used to study seasonal variations (Argus

et al., 2014a; Michel et al., 2021), extreme events such as storms, floods and droughts (Argus et al., 2017; Milliner et al., 2018), and long-term trends (Booker et al., 2014) in the volume of continental water. These analyses are becoming more and more important in order to advise water management policies, for example with regard to the extraction of water from aquifers or rivers. The differences of the predicted displacements due to hydrological loading between the current models are of approximately 5 mm to 10 mm for the horizontal and vertical directions (Li et al., 2015).

Calibrating geodetic instruments such as tide gauges and satellite radar altimeters used to monitor the sea level rise is another application of GNSS positioning for climate science. For example, GNSS receivers are co-located with tide gauges to account for vertical land motion, which affects sea-level measurements in the coastal areas (Wöppelmann and Marcos, 2016). GNSS-equipped buoys serve as reference points to calibrate sea level heights with precision requirements at the level of 0.1 mm/y obtained from satellite radar altimeters (Born et al., 1994; Crétaux et al., 2009).

Realization of reference frame

The ability to determine accurate coordinates for points on the surface of the Earth is important for scientific applications, but has also become part of a variety of our everyday activities (UN Commitee of experts on Global Geospatial Information Management (UN-GGIM), 2021). For instance, accurate coordinates are required for navigation (road, rail, sea, and air transport). In addition, more and more services rely on the exploitation of geospatial information (geolocated images, services and activities e.g. surveying engineering, agriculture) also need precise positioning.

The accuracy of the coordinates depends on the precision reached by the positioning technique (e.g. GNSS) but also on the accuracy and stability of the Earth-centered, Earth-fixed reference frame used to determine them. As previously mentioned, the surface of the Earth is being constantly deformed by various phenomena, and that is why the reference frame needs not to be biased by these deformations for the coordinates to correspond to the genuine displacements on the surface. In practice, the realized terrestrial reference frame is based on the coordinates model determined for geodetic points used as references. To ensure the required accuracy and stability for scientific and civilian applications, the current objectives for the uncertainties in these coordinate models are set to 1 mm in position, and 0.1 mm/y in velocity (Plag and Pearlman, 2009).

Global terrestrial reference frames are defined using four spatial geodetic techniques: VLBI, SLR, GNSS and DORIS (Abbondanza et al., 2017; Altamimi et al., 2023; Rebischung, 2021; Seitz et al., 2022). The GNSS stations are of particular importance, since many of the ground sites of the VLBI, SLR, and DORIS ground stations are co-located with GNSS receivers. In doing so, it facilitates the combination of these positioning techniques while determining the global reference system by providing displacement constraints between techniques. The very dense and well-distributed tracking station network available for the GNSS technique allows determination of precise tectonic velocities for the determination of the local reference frame as well as worldwide access to the global reference frame for global navigation or positioning.

This brief overview of GNSS precise positioning applications in geophysics and geodesy illustrates the precision necessary to achieve these goals and obtain reliable results in these fields. The analysis of the position time series has helped identify systematic errors that can significantly impact the accuracy of GNSS-derived ground displacements, especially seasonal signals or ground displacement velocity estimates. Identifying and understanding these errors are therefore essential steps to correct them. This thesis examines two specific systematic errors observed in the GNSS position time series and introduces them in the following section.

1.2 Systematic errors in GNSS positions time series

1.2.1 GNSS coordinates model

The standard approach to modeling the coordinates of GNSS stations is to fit a kinematic model (Equation 1.1 adapted from Equation 1.2 in Montillet and Bos (2020)) that includes linear rate, harmonic terms, and other relevant parameters to account for coordinate discontinuities or co-seismic displacements. The instantaneous coordinate $x(t)$ is computed at time t by

$$x(t) = x_0 + vt + \sum_{i=0}^{n_p} \left\{ c_i \cos(2\pi \frac{t}{T_i}) + s_i \sin(2\pi \frac{t}{T_i}) \right\} + \sum_{j=0}^{n_d} d_j H(t-t_j) + \sum_{k=0}^{n_s} x_k(t) H(t-t_k) + \varepsilon(t) \quad (1.1)$$

, with

- x_0 the station coordinate at the reference epoch t_0
- v the velocity of the station
- $n_p + 1$ the number of periodic terms
- c_i, s_i the amplitudes of sinusoidal displacements with period T_i
- $n_d + 2$ the number of discontinuities
- d_j the magnitude of position discontinuities at the epoch t_j with H representing the Heaviside function.
- $n_s + 1$ the number of co-seismic models
- x_k: post-seismic relaxation displacements starting at the epoch t_k and modeled by exponential and/or logarithmic decay
- $\varepsilon(t)$ position residual noise or errors

Figures 1.1a and 1.1b show examples of the residuals of the daily position time series for stations located in Toulouse, France (TLSE) and in Ōshū, Japan (MIZU) retrieved from the NGL database (Blewitt et al., 2018). Note that we have removed the linear trend as well as the loading displacement models (non-tidal atmospheric loading, non-tidal ocean loading and hydrological loading) provided by ESMGFZ and available in the new format of the NGL time series.

The linear rate, not visible in Figures 1.1a and 1.1b but present in the position time series, is mainly attributed to tectonic plate motion. However, for stations in seismic areas such MIZU or in polar areas, additional processes such as Glacial Isostatic Adjustment (GIA), post-seismic relaxation, or present-day ice melting also contribute to the secular trend. Position discontinuities, which are mainly due to antenna changes, can also be observed in the time series. Seasonal signals, estimated in Figures 1.1a and 1.1b, are attributed to surface loading, mainly hydrology. Even if a model for non-tidal loading displacements is removed, we still observe residual seasonal signals which can come from loading model errors or GNSS-related signals.

The position residuals after removing the kinematic model are represented by $\varepsilon(t)$. These residuals are analyzed in the spectral domain using normalized power spectral density averaged over a network of stations, as shown in Figure 1.2. Averaging spectra over a network of stations reduces the noise present in each time series, thus helping to identify common features across time series. The position residuals include all unmodeled displacements, including transient motion, slow motion, nonlinear surface motion, but also positioning noise specific to the use of GNSS.

To improve positioning accuracy and GNSS position interpretation, it is essential to have a thorough understanding of these systematic errors in GNSS position time series and how they occur. These error sources fall into two categories: periodic errors and stochastic errors, in particular the correlation of the positioning noise.

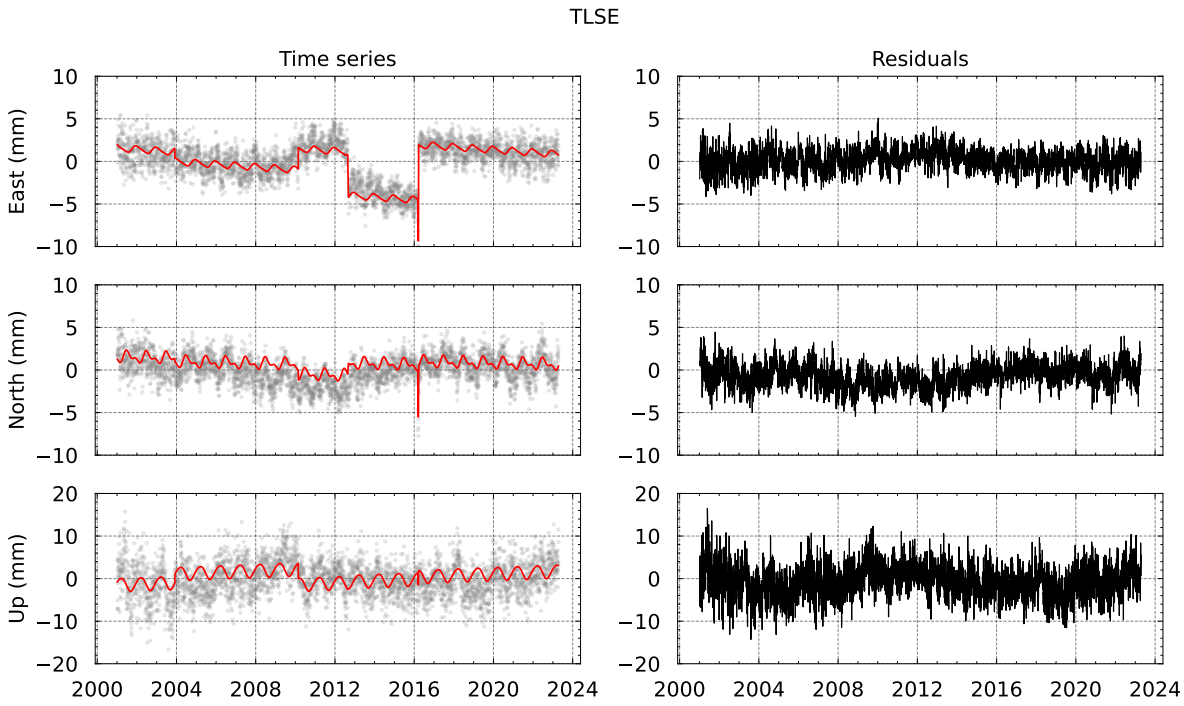

(a) Time series of TLSE station

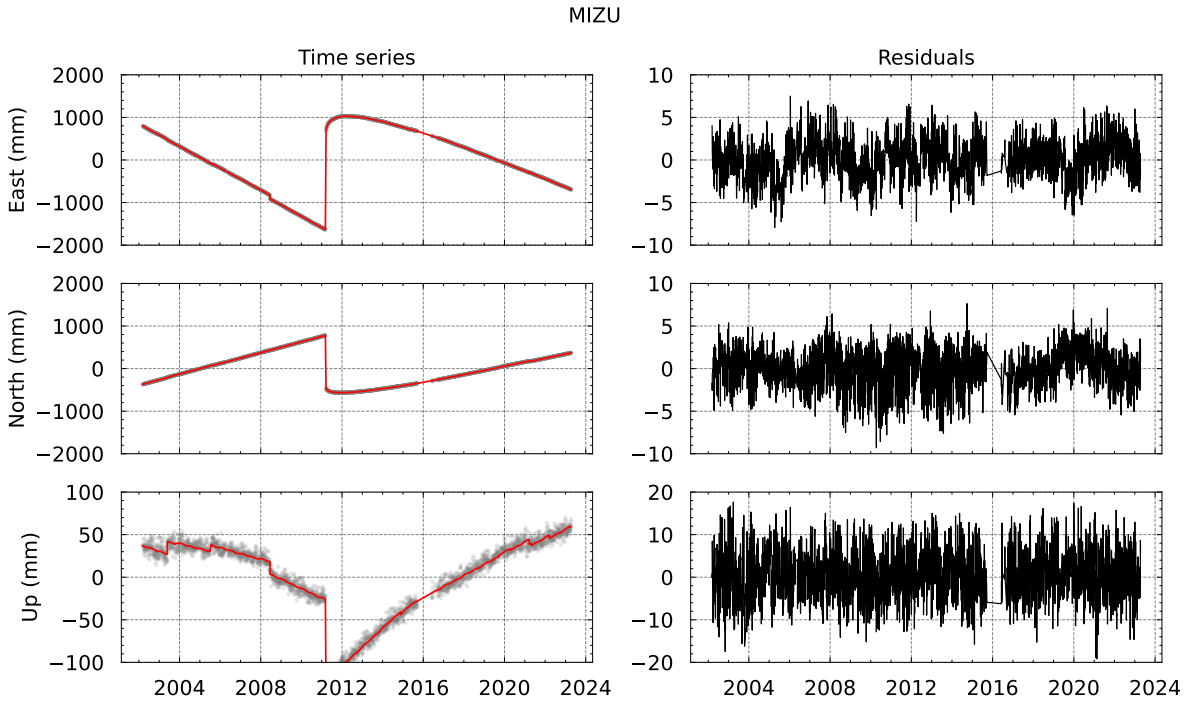

(b) Time series of MIZU station

Figure 1.1: Samples of positions and position residuals time series.

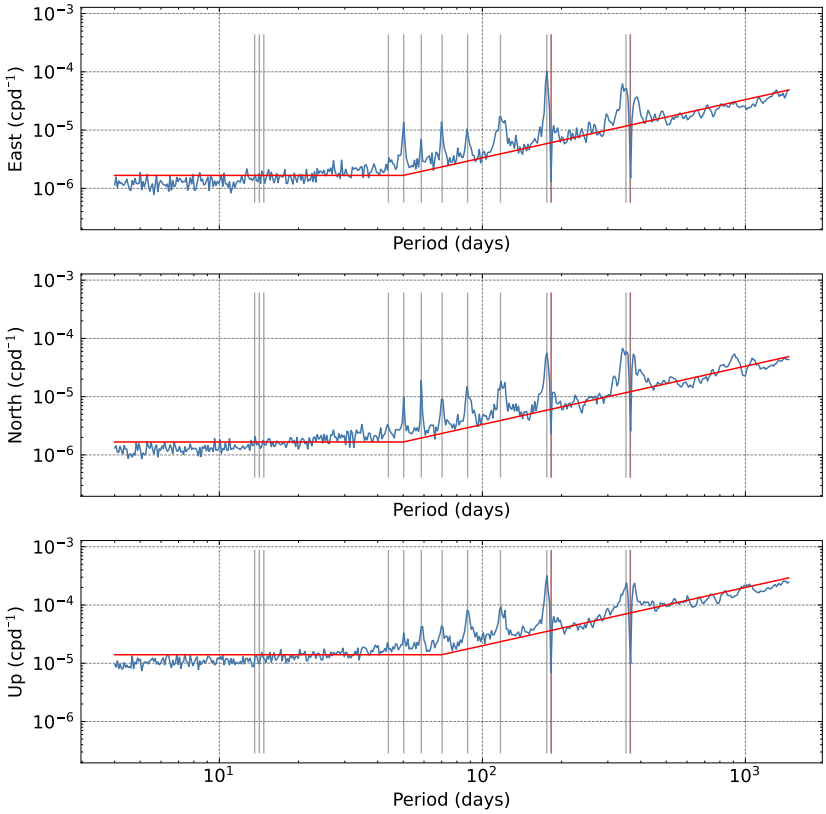

Figure 1.2: Spectral characteristics of GNSS position residuals time series

1.2.2 Periodic errors

The analysis of the residuals of the GNSS daily positions shows the presence of periodic signals that can arise from a variety of sources, including unmodeled geophysical processes, errors in satellite orbits, and site-specific errors.

The most predominant periodic signals are the annual and semi-annual signals. These can be attributed to seasonal displacements (Dong et al., 2002; Yan et al., 2009) or environmental changes that influence the propagation of GNSS signals, such as fluctuations in the atmosphere (temperature, water content), the seasonal deformation of the monumentation caused by the variation of the temperature, multipath or seasonal variations of satellite visibility (snow cover (Koulali and Clarke, 2020)).

Other periodic signals found in GNSS positions are constellation-specific signals: GPS draconitic frequencies (Ray et al., 2008), GLONASS 8-day signals (Rebischung et al., 2021), and Galileo 10-day signals (Zajdel et al., 2022). These periods are thought to be caused directly by signatures in the orbital model (Rodriguez-Solano et al., 2014) or by repeated observations of site-specific errors (King and Watson, 2010; Sidorov and Teferle, 2015).

Additionally, fortnightly alias signals occur due to the beat of subdiurnal tidal model errors and the constellation repetition or 24-hour sampling used to process the position. They were identified with GPS data (Penna et al., 2007) and GLONASS data (Abraha et al., 2018).

These periodic signals can have a significant impact on the analysis of GNSS position time series, leading to biased trend estimates. To mitigate this source of error, it is important to distinguish between residual geophysical displacements and GNSS-specific error signals. The residual geophysical displacements can be reduced by better knowledge of the processes and more accurate displacement models applied during the PPP processing. However, only improvements

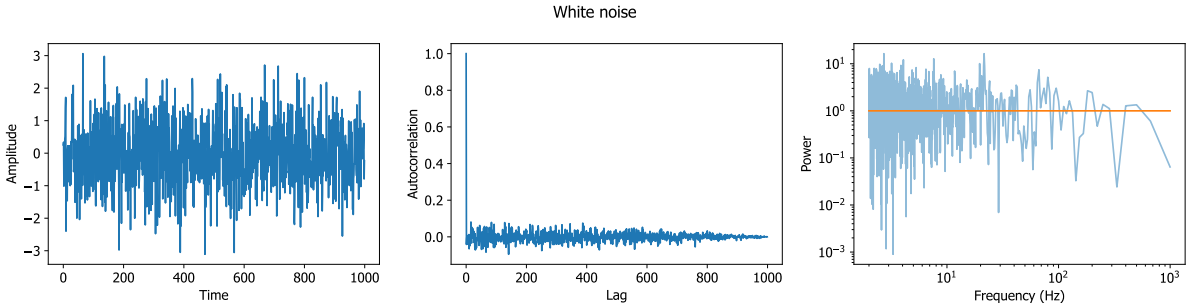

(a) White noise

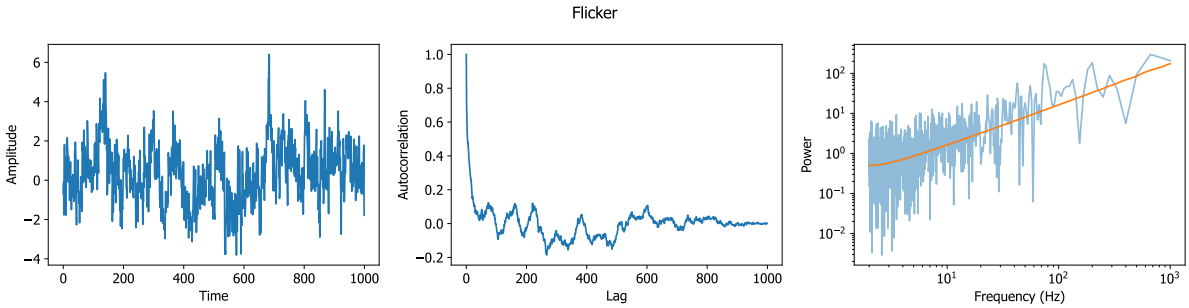

(b) Flicker noise

Figure 1.3: Type of noise identified in the GNSS position time series (left: time series of the errors, middle: autocorrelation functions, right: PSD in a log-log plot)

in GNSS infrastructure (e.g., multipath, antenna) and processing strategies would mitigate GNSS-specific error signals.

1.2.3 Correlation of the positioning noise

In addition to periodic signal, the GNSS position time series are characterized by a background noise that can be observed and measured through the analysis of the power spectral density function (see red curves in Figure 1.2).

Noise models and analysis

The type of the noise observed in GNSS positions is generally represented by one or several power-law (PL) processes, whose power spectral density (PSD) is proportional to f^{κ}, with f the frequency and κ the spectral index of the law. The PSD of a power-law process is represented by a linear function with a slope of κ on a log-log plot.

Two particular types of PL noise are used to model the background noise in GNSS position series: flicker noise (FN) and white noise (WN). While the PSD of the FN model has a spectral index or a linear relationship with a slope of -1 (Figure 1.3b), white noise is characterized by a constant PSD across all frequencies (Figure 1.3a). The two autocorrelation functions (middle panels in Figures 1.3a and 1.3b) show the main difference between these two types of noise. While the white noise shows no correlation at any time lag, the flicker noise shows a non-zero correlation that is not constant and does not reduce over time. Note that 1st-order autoregressive process ($AR(1)$) models can also be used to model the noise correlation in the GNSS positions (Amiri-Simkooei, 2009), but there will not be used in this thesis as we focus on correlation on interannual periods (above 100 days) and $AR(1)$ models are only retrieving short-scale correlation (up to 4 to 10 days).

The PL noise model is described by 2 parameters: the spectral index κ and the variance of the noise σ_0. These parameters can be estimated from the position time series by applying different

methods such as maximum likelihood estimation (MLE, Zhang et al. (1997)), function fitting on the empirical PSD (Mao et al., 1999) or estimation from Allan variance (Le Bail, 2006). The MLE (or its variations) is the most implemented in software used for the noise analysis in geodetic series (Bos et al., 2013; Santamaría-Gómez, 2019; Williams, 2008).

Noise in the GNSS station positions

Previous work has identified a combination of power-law (PL) noise, specifically flicker noise (FN), at low frequencies and white noise (WN) at higher frequencies as the background noise present in most of the GNSS positions (Mao et al., 1999; Williams, 2004).

Knowing the nature of the noise in GNSS positions is essential to ensure proper estimation of coordinate model parameters and to derive reliable uncertainties from time series data. The investigation of the source of these time-correlated errors in GNSS positions remains an active area of research. A number of previous studies have attempted to identify potential sources of these errors. One possible explanation is residual ground displacements that are not accounted for in GNSS data processing and can result from a variety of geophysical processes such as random ground motion or tectonics (Wyatt, 1982, 1989). Other work suggest the contribution of the monument instability (Beavan, 2005; King and Williams, 2009; Williams, 2004). The white noise content and part of the power-law background noise can be also attributed to unmodeled displacements due to non-tidal loading (Boy, 2022; Gobron et al., 2021; Memin et al., 2020; Rebischung et al., 2018; Santamaría-Gómez and Mémin, 2015). It is assumed that GNSS related noise is responsible for the remaining noise correlation. These GNSS positions are not only temporally correlated due to the long-term nature of the underlying geophysical processes, but also spatially correlated. Causes such as atmospheric conditions or satellite orbit errors are assumed to contribute as they may affect the GNSS stations sharing the same portion of the atmosphere or satellite in visibility in a similar manner.

1.3 Research questions and objectives

Although several GNSS systems provide nowadays precise positioning, it is important to understand the characteristics of the systematic errors that each system introduces into the position series. The GPS constellation is by far the most widely used system for scientific applications due to the availability of long time series of data and the global coverage provided by the number of ground receivers tracking GPS signals. However, the Galileo and BeiDou constellations have begun to make important contributions to improving positioning accuracy. Therefore, in this thesis we will discuss how the use of the Galileo constellation, and to a lesser extent the other constellations, GLONASS and BeiDou, can contribute to the identification and understanding of the systematic errors in the position time series. In the scope of this thesis, we will look at two positioning errors: the periodic subdiurnal errors, whose the largest are from ocean tide loading, and the correlated errors over long periods that are generated by the orbital errors.

In this thesis, we will investigate the impact of ocean tide loading (OTL) displacement model errors that appear in the residual GNSS displacements. In particular, we focus on the assessments of the OTL model errors in the subdaily scale, and how they are aliased into long-periodic signals in daily PPP position time series. This thesis will address the following key questions in Part 1:

1. What is the most effective strategy for reducing constellation-specific errors and formal estimation errors when estimating OTL displacement model errors?
2. In a multi-GNSS context, what is the optimal approach for using each system to minimize the GNSS systematic errors while estimating the errors in the OTL displacement model?
3. What are the implications of the subdiurnal OTL displacement model errors for aliased signals, especially at fortnightly and seasonal frequencies, in the scope of multi-GNSS positioning?

In addition, we will investigate the contribution of orbital dynamics to the colored noise in GNSS-derived station positions. The following questions will be addressed in Part 2:

1. Is the combination of a power-law and white noise model observed in the position time series determined by each GNSS constellation? In other words, is there an orbit or constellation-related contribution to the colored noise observed in the positions?
2. What are the characteristics of these orbital contributions, if any?
3. What is the mechanism underlying the propagation of orbital errors to correlated errors in GNSS positioning?

1.4 Overview of the thesis

The thesis is organized as follows: Chapter 2 introduces the principles of the Precise Point Positioning method using GNSS data. The remainder of the thesis is then divided into two parts, which address the two investigation topics: Part 1 focuses on the assessment of OTL errors and their aliased signals, while Part 2 examines the contribution of orbital dynamics and constellation design to the positioning error correlations.

The first part of the thesis, in Chapter 3, will describe an estimation strategy we have developed to reduce constellation-specific errors in the assessment of subdaily OTL displacements and their formal errors of the estimated OTL model errors. It will also investigate the optimal way to take advantage of each GNSS constellation for the estimation of OTL displacement modeling errors. Chapter 4 examines the propagation of the subdiurnal tidal displacement errors and their propagation on the long-periodic signals, especially at fortnightly and seasonal frequencies, in the daily PPP position series.

The second part of the thesis will investigate in Chapter 5 the stability of the GNSS satellite orbit and the underlying dynamic causes between the satellites of each constellation. We also examine the background noise in the positions obtained by different constellations and if the power-law + white noise process, observed in GPS time series, is still observed in the time series from other constellations. Finally, we analyze the mechanism for explaining the propagation from orbital instability to correlated positioning noise. Chapter 6 deals with the correlated noise that is also observed in GNSS satellites' orbit discontinuities between successive daily products. After analyzing the orbits provided for the third IGS reprocessing campaign, we explore a possible cause of the presence of flicker noise in the discontinuities through the effects of stochastic accelerations in the satellites' dynamics.

Finally, Chapter 7 provides a general discussion and the conclusions of this thesis, including ideas for future research.

CHAPTER

2 Principle of Precise Point Positioning

The Precise Point Positioning (PPP) method, as described by Zumberge et al. (1997) is a widely used technique for obtaining precise GNSS receiver coordinates through the use of pseudorange and carrier phase observations. This approach enables the computation of station coordinates without the need for a nearby reference station. This chapter presents an overview of the principles of PPP, including the observation equations, parameter adjustment, and correction models employed to attain positioning accuracy within the range of centimeters to millimeters. Additionally, we introduce the characteristics of the currently available constellations for use, including GPS, Galileo, GLONASS, and BeiDou.

2.1 Constellations

Involved in the International Association of Geodesy (IAG), the International GNSS Service (IGS) is the observation service dedicated to high-precision GNSS data and products for the scientific and civilian communities. It brings together more than 200 international agencies, universities, research institutions and companies. Since this creation in 1992, the uninterrupted series of data and products have been generated and improved over time. These products have evolved in the last decade to include multi-GNSS data. At present, there are four global constellations available, which are routinely processed by the IGS. The latest reprocessing campaign REPRO3, that ended in late 2020, is the first campaign to include several constellations: GPS, Galileo and GLONASS. As for the BeiDou constellation which was not included for REPRO3, products are still available through the Multi-GNSS Experiment (MGEX) working group of the IGS, which promotes the use and processing of multi-GNSS observations.

The Global Positioning System (GPS), operated by the United States government, comprises a nominal constellation of 24 satellites distributed in 4 slots per orbital plane and six planes separated by 60°. Six of these slots have been expanded to accommodate one additional satellite each, resulting in a total of 30 satellites in the expanded constellation (GPS Navigation Center, 2020). Currently, there are 32 satellites (GPS Navigation Center, 2023) in orbit transmitting positioning signals, with two additional satellites positioned near older or malfunctioning satellites to serve as replacements if necessary.

GLONASS, operated by the Russian Aerospace Defense Forces and abbreviated from "Globalnaya Navigatsionnaya Sputnikovaya Sistema" consists of 24 satellites arranged in three orbital planes in a Walker configuration with an inclination of 65°. Although it operates similarly to GPS and Galileo, GLONASS utilizes frequency modulation signals, making data processing more challenging, particularly when it comes to resolving carrier-phase ambiguities. It should be noted that the new generation of GLONASS-K satellites, which began launching in 2020, has adopted code modulation signals, in addition to the legacy frequency-modulated signals, similar to those utilized by other navigation systems (Montenbruck et al., 2017).

Galileo, the European satellite navigation system, is also designed to provide global positioning services. The nominal Galileo constellation consists of 24 satellites arranged in three orbital planes in a Walker configuration. As of May 2023, there are 23 active satellites in orbit capable of providing global positioning service as precise as GPS (European GNSS Service Centre, 2023). As of 2023, there are two generations of flying spacecraft, differing in their design: Galileo-IOV (In-orbit Validation) and Galileo-FOC (Fully Operational Capability). It should be noted that two of these satellites are in eccentric orbits due to a launch issue. These satellites have nevertheless been useful for fundamental physics research such as testing the relativistic effects on in-orbit atomic clocks (Delva et al., 2015) or further validation of Einstein's Equivalence principle (Kouba, 2021; Sośnica et al., 2021).

The BeiDou Navigation Satellite System (BDS) is a Chinese satellite navigation system that encompasses a series of generations of satellites, ranging from BDS-1 to BDS-3. The development of the BDS constellation began in the 1990s, with the first generation of the system, BDS-1, being launched in 2000. BDS-2, launched in 2007, provided limited regional coverage (Montenbruck et al., 2013). Since 2017, the third generation, BDS-3, which is currently in operation, provides in addition global coverage. In the context of this thesis, the term "BeiDou" will refer exclusively to BDS-3. The constellation comprises 35 satellites, including 27 in medium Earth orbit (MEO), five in inclined geosynchronous orbit (IGSO), and three in geostationary orbit (GEO) (China Satellite Navigation Office, 2023). The MEO satellites are situated in three orbital planes at an altitude of approximately 22000 km and have an inclination of 55 degrees. The IGSO satellites have an inclination of 55 degrees and an altitude of around 36000 km, while the GEO satellites are located at an altitude of 36000 km in equatorial orbits. These IGSO and GEO satellites are designed to enhance satellite visibility for users in Asia and Oceania.

Table 2.1 provides detailed information on the nominal characteristics of the four constellations. The ground track repeat period is given in sidereal days (s.d.), i.e. 0.997 solar days. It is important to note that the actual values of orbital parameters can diverge from these nominal values. For example, Choi et al. (2004) showed that the GPS orbital periods have a variability of 12 seconds around the nominal value.

Table 2.1: Nominal characteristics of the four currently flying GNSS constellations

	GPS	GLONASS	Galileo	BeiDou
Numbers of satellites (as of 01/06/2023)	31	24	23	55
Orbital planes	6	3	3	3
Semi-major axis (km)	26560	25508	29601	27910 (MEO) 42160 (IGSO/GEO)
Inclination (°)	55	64.8	56	55 (MEO/IGSO) 0 (GEO)
Orbital period	11h58	11h16	14h05	12h53 (MEO) 23h56 (IGSO/GEO)
Draconitic period (days)	351.2	353.2	355.7	353.6
Ground track repeat period (sidereal days)	1	8	10	7

2.2 Observation equations

By opposition to differential positioning, PPP is based on the processing of direct observations between a single receiver and the satellites in visibility. The observation equations describe the relationship between the measurements and the estimated parameters, including station coordinates, receiver clock bias, and tropospheric zenith path delay. PPP uses pseudorange and carrier phase observations to estimate station coordinates. The pseudorange is the measured distance between a GNSS receiver and a transmitting satellite, estimated from the time it takes for a signal from the satellite to reach the receiver. One advantage of pseudorange observations is that they offer a non-ambiguous measurement, as they directly reflect the distance between the receiver and the satellite. However, the use of pseudorange observations for positioning led to limited accuracy down to a few decimeters due to the high noise present in the measurement. For applications requiring higher accuracy of receiver positioning, GNSS data processing often uses carrier phase observations.

Carrier phase observations also provide measurements of the receiver-satellite distance which have less noise but are subject to phase ambiguities that must be resolved along with the station position, station clock biases, tropospheric zenith path delays (ZTD) and tropospheric gradients.

The pseudorange P and phase L observation equations are summarized in Equations 2.1 and 2.2 with the unknown quantities that are estimated identified by the symbol $\tilde{}$.

$$P = \rho_r^s + c\,(\delta\tilde{t}_r - \delta t^s + \tilde{T}_r^s) + \tilde{T}_r^s + I_r^s + b_r - b^s + (\delta P_r + \delta P^s) + \varepsilon_P \tag{2.1}$$

$$L = \rho_r^s + c\,(\delta\tilde{t}_r - \delta t^s + \delta t_{rel}) + \tilde{T}_r^s - I_r^s + (\tilde{N} + \omega^s)\lambda + \beta_r - \beta^s + (\delta L_r + \delta L^s) + \varepsilon_L \tag{2.2}$$

with:

- P, L: the pseudorange and the corresponding carrier phase observed between the receiver r and the satellite s
- $\rho_r^s = ||\tilde{X}_r - X^s||$: the geometrical range between the receiver and the satellite
  - $\tilde{X}_r$: the estimated position of the receiver
  - X^s: the satellite position retrieved from the IGS orbit products
- $\delta\tilde{t}_r$: the receiver clock bias with respect to the GNSS time
- δt^s: the satellite clock bias with respect to the GNSS time, retrieved from the IGS orbit products
- δt_{rel}: relativistic clock correction
- c: the speed of light
- $\tilde{T}, I$: the signal delay due to the troposphere/ionosphere
- $\tilde{N}$: the carrier-phase ambiguity
- ω^s: the phase wind-up
- λ: the wavelength of the signal
- β_r, β^s: the instrument biases of the receiver's and the transmitter's system
- $\delta P_r, \delta L_r$: antenna phase center correction for the receiving antenna
- $\delta P^s, \delta L^s$: antenna phase center correction for the emitting antenna

- $\varepsilon_P, \varepsilon_L$: the pseudorange and carrier-phase measurement noise (including multipath, thermal noise, receiver/emitter noise)

We have seen that these observation equations for PPP require the positions and clock biases of the satellite, considered as known, and provided by the IGS analysis centers. These parameters are obtained from daily network solutions, that determine simultaneously the positions and clock biases of the satellites and of a selected network of reference stations. To ensure the consistency between the PPP and network solutions, the models involved in the observation equations must be the same as the ones used to calculate the orbits and clock products. This is achieved by following the same international standards provided by the IGS (IGS, 2020) and the International Earth Rotation and Reference Systems Service (IERS) conventions.

There are also uncertainties and errors in the products due to the orbital and observation (e.g. incorrect solution for the ambiguities) modeling errors occurring in the network solutions. This is one of the reasons why the IGS conducts recurrent reprocessing campaigns of the GNSS data using state-of-the-art standards and models over the entire past. The remaining errors present in the orbit/clock products are one of the possible cause of systematic errors in the estimated receiver positions by PPP. This will be examined in the scope of this thesis.

The tropospheric delay T is composed of the hydrostatic (or dry atmosphere) delay and the wet atmosphere delay (Böhm and Schuh, 2013). In PPP, the delay is usually computed using the value of the delay at the zenith direction, which is projected onto the light of sight using a model depending on the elevation e of the satellite: a mapping function. Except in very high latitudes due to larger atmospheric pressure anomalies (Boehm et al., 2009; Böhm and Schuh, 2013)) or in orographic areas because of the resolution of the topographic model (Fund et al., 2011), the current models are more accurate than for the wet delay and their predictions are removed from the total delay. The remaining delay, attributed to the wet part, is more unpredictable and is estimated while determining the position. For that, the value of the wet delay at the zenith is estimated given a specific mapping function. The asymmetry of the atmospheric conditions is taken into account by adding an azimuth-dependent term defined by horizontal gradients. Two gradients for the north-south and east-west directions are additionally estimated while determining the receiver position in PPP.

The ionosphere delay I can be mostly canceled out by using the ionosphere-free combination of dual-frequency signals. This is achieved by applying the following formula: $obs_{IF} = \frac{f_1^2 obs_1 - f_2^2 obs_2}{f_1^2 - f_2^2}$ where obs represents either the pseudorange P or the carrier phase L. By combining measurements from two different GNSS frequencies emitted by the same satellite (for example, L1 and L2 for GPS, E1 and E5 for Galileo), this technique effectively removes the first-order effects of the ionosphere on signal propagation. It is commonly used in PPP software to process GNSS observations.

The carrier phase ambiguities $\tilde{N}$ can be estimated simultaneously with all the other PPP parameters. However, resolving them to integer values improves considerably the positioning accuracy (Ge et al., 2008; Laurichesse et al., 2009). PPP with integer ambiguities resolution (PPP-AR) consist of inferring the more probable integer ambiguities from their float values, and then fixing them while recomputing the PPP parameters. Integer-ambiguities products allowing PPP-AR are currently available for GPS and Galileo (Katsigianni et al., 2019b), but not for GLONASS and BeiDou yet.

The observation equations also include various corrections to reach cm-to-mm level positioning accuracy. On the satellite side, the observation is corrected for the position of the transmitting antenna phase center (phase center offset, PCO) and its variation dependent on the signal direction (phase center variations, PCV) as well as the phase windup effect which is due to the attitude variation of the satellite. The propagation of the signal is also corrected with additional terms due to the relativistic effect on the satellite clock and inter-frequency biases. On the station side, the position of the receiving phase center is also modeled using PCO and PCV maps which

are provided by the IGS, as well as ground displacements that can be modeled and recommended in the IERS conventions Petit and Luzum (2010).

2.3 Site displacement corrections

For the geodetic applications, the IERS Conventions recommended to correct all reference site displacements that introduce large variations of the station coordinates, and that challenge the hypothesis that the reference points are not moving during a certain time span, typically 24 hours. Indeed, the Earth's crust deformation are induced by the gravitational forces acting on all the masses (solid Earth, water and atmosphere) on the surface of the Earth. This include the gravitational forces of the Sun or Moon but also the centrifugal forces due to the Earth's rotation. These deformations are composed of tidal (or periodic) displacements and non-tidal displacements.

As for the tidal displacements, the IERS specify conventional corrections that are included in the computation of the station position X_s while modeling GNSS observations. These corrections take into account various types of deformation caused by tidal forces, including solid Earth tide (up to 0.4 m), ocean tide loading (1-10 cm), pole tide (25 mm), and ocean tide pole loading and atmospheric tide loading (up to 20 mm) (Teunissen and Montenbruck, 2017). The details of the ocean tide loading model will be presented in Chapter 3.

The displacement of GNSS sites is also caused by non-tidal surface loading due to hydrological or atmospheric masses variations. Although these effects are not included in the IGS products and thus in the PPP processing, conventions, they can cause significant deformations, that affect the analyses of the time series of GNSS positions. Non-tidal loading effects include non-tidal ocean loading, which can reach up to 15 mm (Teunissen and Montenbruck, 2017), and non-tidal atmospheric loading, which can reach up to 20 mm (Teunissen and Montenbruck, 2017). Hydrological loading due to variations in mass of groundwater, snow, or ice can also contribute to GNSS site displacement (Michel et al., 2021).

2.4 Parameters adjustment

2.4.1 Linearization of observation equations

The system composed by the previous observation equations is non-linear and cannot be directly inverted to obtain the position of the receiver, the clock bias of a receiver, and other empirical parameters (troposphere biases). This thus requires linearization through a Taylor series expansion to enable the use of linear methods such as the weighted least squares algorithm. We recall the principle of this linearization:

$$y = f(x) \approx f(x_0) + A(x_0)(x - x_0) \tag{2.3}$$

where y is the measurement, x is the vector of unknown parameters, $f(x)$ is the non-linear observation equation, x_0 is the initial estimate of the parameters, and $A(x_0)$ is the Jacobian matrix evaluated at x_0. The Jacobian matrix is the matrix of partial derivatives of the observation equation with respect to each unknown parameter evaluated at the current estimate.

The resulting linear system to be solved reads $Y = AX = [A_{t_0} ... A_{t_M}]^T X$, assuming that the carrier phase ambiguities N_{IF} have been already resolved with

$$X = \begin{bmatrix} \delta X & \delta Y & \delta Z & \delta t_r & \delta T_1 & \dots & \delta T_j & \dots & \delta T_m \end{bmatrix}^T \tag{2.4}$$

$$Y = \begin{bmatrix} P_r^1 - \rho_r^1 - c\delta t^1 - T_0 \\ L_r^1 - \rho_r^1 - c\delta t^1 - T_0 - \lambda_{IF} N_{IF} \\ \vdots \\ P_r^k - \rho_r^k - c\delta t^k - T_0 \\ L_r^k - \rho_r^k - c\delta t^k - T_0 - \lambda_{IF} N_{IF} \\ \vdots \\ P_r^k - \rho_r^k - c\delta t^k - T_0 \\ L_r^k - \rho_r^k - c\delta t^k - T_0 - \lambda_{IF} N_{IF} \end{bmatrix}^T \tag{2.5}$$

and A_t the design matrix at the epoch t for n satellites in visibility

$$A_t = \begin{bmatrix} \frac{X_{r,0}-X^1}{\rho_0^1} & \frac{Y_{r,0}-Y^1}{\rho_0^1} & \frac{Z_{r,0}-Z^1}{\rho_0^1} & \dots & 1_t & \dots & \dots & M_{wet,j}^1 & \dots \\ \frac{X_{r,0}-X^1}{\rho_0^1} & \frac{Y_{r,0}-Y^1}{\rho_0^1} & \frac{Z_{r,0}-Z^1}{\rho_0^1} & \dots & 1_t & \dots & \dots & M_{wet,j}^1 & \dots \\ \vdots & \vdots & \vdots & \vdots & \vdots & \vdots & \vdots & \vdots & \vdots \\ \frac{X_{r,0}-X^k}{\rho_0^k} & \frac{Y_{r,0}-Y^k}{\rho_0^k} & \frac{Z_{r,0}-Z^k}{\rho_0^k} & \dots & 1_t & \dots & \dots & M_{wet,j}^k & \dots \\ \frac{X_{r,0}-X^k}{\rho_0^k} & \frac{Y_{r,0}-Y^k}{\rho_0^k} & \frac{Z_{r,0}-Z^k}{\rho_0^k} & \dots & 1_t & \dots & \dots & M_{wet,j}^k & \dots \\ \vdots & \vdots & \vdots & \vdots & \vdots & \vdots & \vdots & \vdots & \vdots \\ \frac{X_{r,0}-X^n}{\rho_0^n} & \frac{Y_{r,0}-Y^n}{\rho_0^n} & \frac{Z_{r,0}-Z^n}{\rho_0^n} & \dots & 1_t & \dots & \dots & M_{wet,j}^n & \dots \\ \frac{X_{r,0}-X^n}{\rho_0^n} & \frac{Y_{r,0}-Y^n}{\rho_0^n} & \frac{Z_{r,0}-Z^n}{\rho_0^n} & \dots & 1_t & \dots & \dots & M_{wet,j}^n & \dots \end{bmatrix} \tag{2.6}$$

where M_{wet} is the mapping function for the tropospheric correction. Note that this derivative is common to all the rows involved in the observation window j for the tropospheric bias (e.g. 2-hour window). The same hold for the station positions and the receiver clock biases on their respective windows.

2.4.2 Dilution of precision (DOP)

Weighted least squares

Linear regression is a widely used method for estimating parameters, and Ordinary Least Squares (OLS) is one of the most commonly employed approaches to this end. However, OLS has certain limitations, particularly in situations where the assumption of observations of equal variance is not verified (heteroscedasticity). This is the case of GNSS observations which precision can vary depending on the elevation of the satellites above the horizon. In such scenarios, an alternative technique is the implementation of Weighted Least Squares (WLS) that permits the assignment of different weights to different data points (Dodge, 2008).

The model is then

$$Y = AX + \epsilon, \text{ with } \epsilon \sim \mathcal{N}(0, \Sigma)$$

The least squares residuals are assumed to follow a normal distribution $\mathcal{N}(0, \Sigma)$ with zero mean and a covariance matrix Σ. The covariance/variance matrix Σ of the observations errors is modeled in the WLS using a diagonal weighting matrix W by:

$$\Sigma = W^{-1} = \begin{bmatrix} \ddots & & \\ & 1/w_i & \\ & & \ddots \end{bmatrix}$$

where the weights $w_i = 1/\sigma_i^2$ are usually computed from a mathematical model. This model can be based on theory or determined by analyzing the post-fit observation residuals. By attributing higher weights to observations with lower errors and lower weights to observations with larger

errors, WLS produces parameter estimates that are less susceptible to the impact of outliers or less precise data.

Finally, the estimated parameter vector $\tilde{X}$ is iteratively computed by $\tilde{X} = X_0 + \delta X$, with δX, the increments of the parameters based on the previous values of X, and given by $\tilde{X} = (A^T W A)^{-1}(A^T W Y)$

Computation of DOP

DOP is a measure of the quality of the distribution in the sky of the satellites, used for the positioning, for a given position at a given time. It quantifies the effect of the observation geometry on the accuracy of the estimated receiver positions. A low DOP indicates a good satellite geometry and therefore a more accurate position estimate.

The DOP is calculated from the cofactor matrix $Q_X = (A^T A)^{-1}$ of the solution X by

$$DOP = \sqrt{tr(Q_X)} = \sqrt{q_E^2 + q_N^2 + q_U^2 + q_t^2} \tag{2.7}$$

For example, we can compute the design matrix A in Equation 2.6 and the associated cofactor matrix Q_X with the GNSS observations received by a station (e.g. BRST - Brest) retrieved from the RINEX files and the GRGS orbits and clock biases products. The DOP is then computed using Equation 2.7. In Figure 2.1a, we plot the computed DOP for 10 days, between 01/01/2018 and 11/01/2018.

We compare different observation windows: 30 minutes (top panel), 1 hour (middle panel) and 24 hours (bottom panel). The shorter the observation period, the poorer the geometry of the satellite is because they barely move in the sky. Indeed, the passes, windows of continuous visibility of a satellite, last up to 6 hours for GNSS ground stations. The DOP is therefore larger. The DOP also differs between the constellations. We observe larger DOP values for Galileo during these 10 days compared to GPS and GLONASS. This is explained by the poorer geometry of the Galileo satellite during this period (Figure 2.1b) because the constellation was not completed yet in 2018.

2.4.3 Observation weighting functions

Observations at low elevations are important for decorrelating the troposphere zenith delays δT_i, receiver clock δt_r, and station height. However, these observations are of less quality because of increased noise, multipath, and troposphere model deficiencies. Observation weighting functions are used to account for these observations of less quality by assigning lower weights to minimize their effect on the estimated parameters.

Because all the contributing error sources cannot be fully modeled or even observed, empirical models based on prior observation residuals are used to compute the weights as a function of the satellite elevation e. The more usual functions are $\frac{1}{\sin e}$ and $\frac{1}{\sin^2 e}$ (Teunissen and Montenbruck, 2017). These weights are used to model and compute the weighting matrix W used in WLS.

2.5 GINS software

Developed by the Centre National d'Etudes Spatiales (CNES) and the Groupe de Recherche de Géodésie Spatiale (GRGS), the GINS software (Marty et al., 2011) is used to process various types of geodetic observations. In the scope of this thesis, we particularly use this software to compute PPP solutions from real GNSS data, with the possibility to manage zero-difference ambiguity resolution (Katsigianni et al., 2019c; Loyer et al., 2012) for the GPS and Galileo observations.

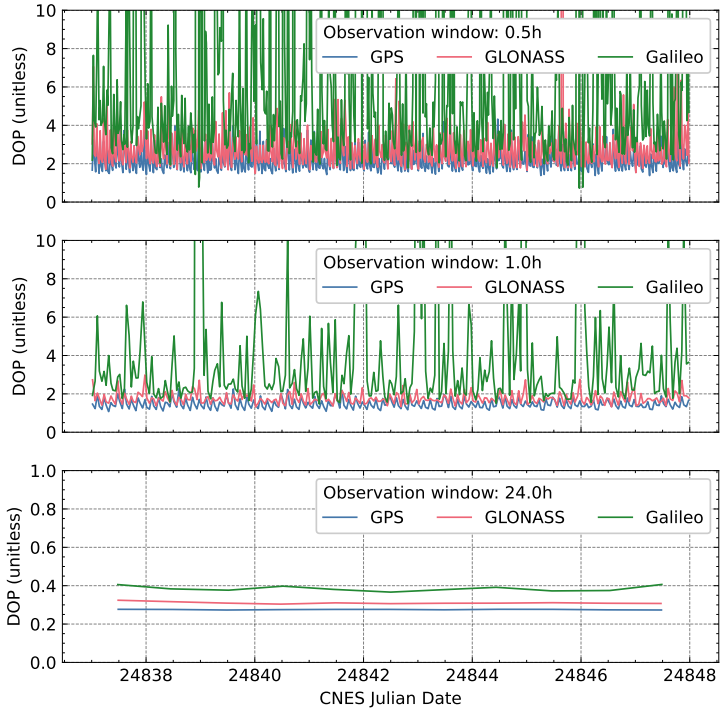

(a) Values of DOP for different observation windows: 30 minutes (top), 1 hour (middle) and 24 hours (bottom)

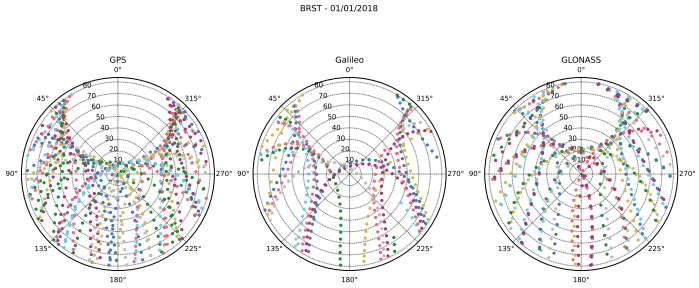

(b) Daily skyplot

Figure 2.1: Observation geometry for the station of Brest (BRST): 01/01/2018 (24837 CNES Julian Day) to 11/01/2018 (24847 CNES Julian Day)

Part I

Ocean tide loading

CHAPTER

3 Subdiurnal OTL correction in GNSS data processing

This chapter presents how multi-GNSS data, especially Galileo, can be used to both quantify errors in the state-of-the-art subdaily ocean tide loading (OTL) displacement corrections. Parts of the methods and results presented in this chapter have been published in Ait-Lakbir et al. (2023a).

GNSS data are processed in 24-hour batches, in which the station positions are assumed to be constant and where subdiurnal ground displacements such as tidal displacements are modeled. However, by computing GNSS positions at a sub-daily rate, we can observe remaining sub-diurnal signals and identify discrepancies between the models used in PPP and the estimated GNSS positions. These errors at the subdiurnal scale can affect the daily GNSS positions, altering our observations of geophysical displacements that occur over longer time scales, from fortnightly up to seasonal frequencies. Therefore, it is important to identify and analyze these errors in the subdiurnal displacement models to ensure accurate observations of geophysical movements.

Several types of residual signatures have been already reported in position time series analyses, resulting from different sources which have been extensively explored: solid earth tides, ocean tides, or atmosphere "tides" (Tregoning and Watson, 2009; Watson et al., 2006), and non-tidal loading (Dach et al., 2011; van Dam et al., 2012; Williams and Penna, 2011). Among all these known and modeled deformations, those caused the ocean tides have potentially the largest impact on the positioning error, for instance in the fortnightly band. Errors in modeling these sub-diurnal deformations can propagate to longer periodic signals in the daily positions due to the orbital characteristic of the GPS constellation. Hence, they can contribute in particular to the annual, semi-annual, and fortnightly spurious signals observed in the daily PPP positions. Simulations have helped to predict the propagated signals for the 8 main ocean tidal constituents (Penna and Stewart, 2003), which have been observed in several analyses with real GPS (Bogusz and Figurski, 2012; Penna et al., 2007) or GLONASS (Abraha et al., 2018) observations. In their work, Stewart et al. (2005) demonstrate the link between the PPP batch length and the sub-diurnal periodic site displacement perturbations through the theoretical derivation of the propagation of sub-diurnal signals. Their model can predict the frequencies and the magnitude of the propagated signals. Therefore, accurate prediction of these displacements at subdiurnal scales should be used when processing GNSS data for precise positioning and assessing the errors of the geophysical models with GNSS positions.

3.1 Modeling OTL displacement corrections in GNSS

Discrepancies in modeling OTL displacements contribute significantly to GNSS systematic errors in the station position time series. Indeed, OTL are responsible of site displacements at the level of up to a few centimeters. To predict these deformations accurately, models of both the earth's crust and the ocean tides themselves must be considered.

3.1.1 Generalities on the computation of displacements due to surface loading

Crustal deformations induced by mass loads can be computed by using Green transfer functions (Farrell, 1972). Assuming an a priori knowledge about the physical properties of the Earth's crustal layers, it is possible to compute the loading deformations at each point on the earth's surface by the convolution of the Green transfer functions and the spatial distribution of mass loading.

In particular, the prediction of the OTL-induced crustal deformation is calculated with a model of Earth, from which we can derive the Green functions, and an ocean tide height atlas. The OTL displacements in the local topocentric frame ENU (East, North, Up) at a point at latitude ϕ and longitude λ can be given by:

$$\Delta u_r = \iint_{\Omega} \rho\ \overline{h}(\phi', \lambda') G_r(\Psi) \cos(\phi') d\phi' d\lambda' \tag{3.1}$$

$$\Delta u_e = \iint_{\Omega} \rho\ \overline{h}(\phi', \lambda') G_h(\Psi) \sin(\alpha') \cos(\phi') d\phi' d\lambda' \tag{3.2}$$

$$\Delta u_n = \iint_{\Omega} \rho\ \overline{h}(\phi', \lambda') G_h(\Psi) \cos(\alpha') \cos(\phi') d\phi' d\lambda' \tag{3.3}$$

with

- Δu_r, Δu_e and Δu_u: the displacements in the radial (up), east and north directions
- Ω: the integration domain corresponding to the surface of a sphere ($\Omega = [-\frac{\pi}{2}, \frac{\pi}{2}] \times [0, 2\pi]$)
- ρ: the mean density of the ocean water
- Ψ the angular distance and α' the azimuth angle between the positions of the point (ϕ, λ) and of the load (ϕ', λ')
- $\overline{h}(\phi', \lambda')$ the height of the ocean tide at a point at latitude ϕ and longitude λ
- G_r, G_h: Green transfer functions for the vertical and horizontal directions

$$G_r(\theta) = \frac{a}{m_e} \sum_{n=0}^{\infty} h'_n P_n(\cos\theta) \tag{3.4}$$

$$G_h(\theta) = \frac{a}{m_e} \sum_{n=0}^{\infty} l'_n \frac{dP_n(\cos\theta)}{d\theta} \tag{3.5}$$

with:

- a: the mean radius of the Earth,
- m_e: the mass of the Earth
- h, l: the radial and horizontal load Love numbers
- P_n: the Legendre polynomials of degree n

The load is computed from the mean density of the water and the water height described by an ocean tide atlas, which provides a map of the ocean tides at a given time and location. We used the FES2014b solutions which was produced by Noveltis, Legos and CLS and distributed by Aviso+ [1], with support from CNES. We also use the pyfes software [2] that is also provided by Aviso+. Figure 3.1 illustrates the subdiurnal OTL displacements determined from the FES2014b model.

3.1.2 OTL corrections in GNSS data processing

In the IERS Conventions (Petit and Luzum, 2010), the OTL displacements are computed by a sum over the 11 main tides (M2, S2, N2, K2, K1, O1, P1, Q1, Mf, Mm, Msa). The harmonic model of the OTL displacement for the direction i (east, north or up) is in the form of:

$$\Delta u_i = \sum_{j=1}^{11} A_{i,j} \cos(\chi_j(t) - \phi_{i,j}) \tag{3.6}$$

Each term expressed for the tide j is associated with its astronomical argument $\chi_j(t)$. The amplitude $A_{i,j}$ and $\phi_{i,j}$ are derived from a model of the structure of the Earth (PREM model) and for ocean tide amplitudes. The periods of these major tides are given in Table 3.1. The values are taken from Lefevre (2000). The 11-tide model is completed by 242 minor subdiurnal tides (Petit and Luzum, 2010). The amplitude and phase of these tides are computed from the nearby major tides by interpolation of the tidal admittance, the relative tide amplitude to the equilibrium tide, which is a function of the frequency (Le Provost et al., 1991). The tide M_{sf} is not included in the conventional model, but is one of the long-periodic tides available in the ocean tides atlases, such as the FES2014 model [3], and appearing in the fortnightly band, with a period around 14 days. This latter tide in included in Table 3.1 only for the purpose of the comparison of the periods of the tides.

Table 3.1: Frequencies of the major ocean tide components included in the OTL models.

	Conventional tides				Other
Subdiurnal					
Tide	M2	S2	N2	K2	
Period (days)	0.5175	0.5	0.5274	0.4986	
Diurnal					
Tide	K1	O1	P1	Q1	
Period (days)	0.9973	1.0758	1.0027	1.1195	
Long-period					
Tide	M_f	M_m	S_{sa}		M_{sf}
Period (days)	13.6608	27.5546	182.6211		14.7653

Several sources of errors are associated with the predicted OTL displacements by the models. One of the main challenges is accurately modeling the earth's structure and computing the associated Green transfer functions. The limitations of the current models rely on how they account for the anelastic response of the crust (Arnoso et al., 2023; Bos et al., 2015; Martens and Simons, 2020; Martens et al., 2016; Wang et al., 2020b), or the spatial variability of the physical properties of the lithosphere (Huang et al., 2022). There are several models available to model the structure of the Earth. In the following, we will use the Preliminary reference Earth model (PREM) described in Dziewonski and Anderson (1981).

[1] The products can be downloaded from https://www.aviso.altimetry.fr/

[2] The software can be retrieved from https://github.com/CNES/aviso-fes

[3] Note that the M_{sf} tide in the FES2014b model is incomplete as the gravitational contribution to the tide has been unfortunately omitted. The complete M_{sf} tide can be retrieved from the FES2014c release of the model (Lyard et al., 2020).

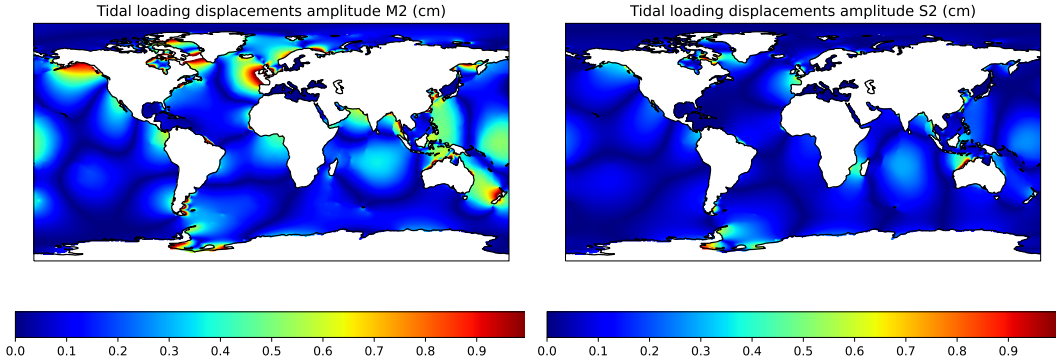

(a) M2

(b) S2

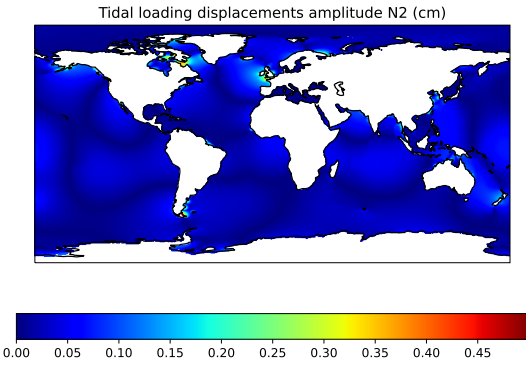

(c) N2

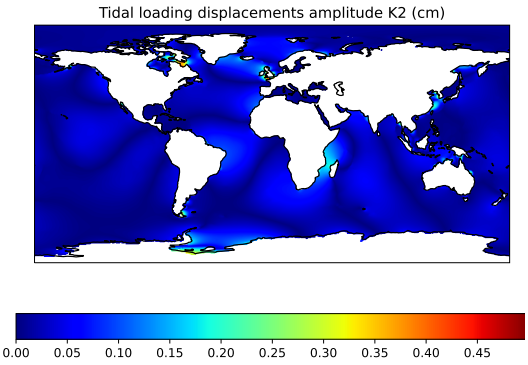

(d) K2

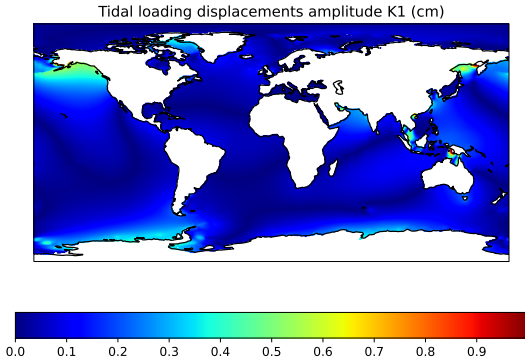

(e) K1

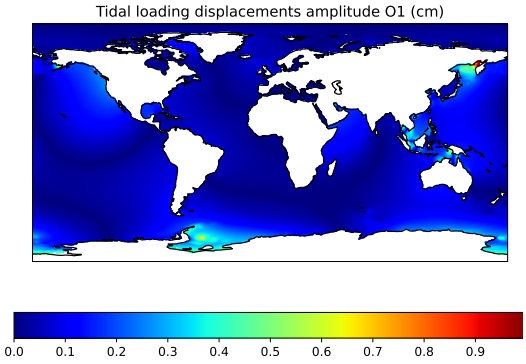

(f) O1

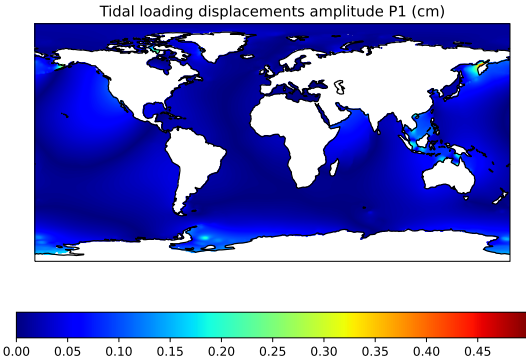

(g) P1

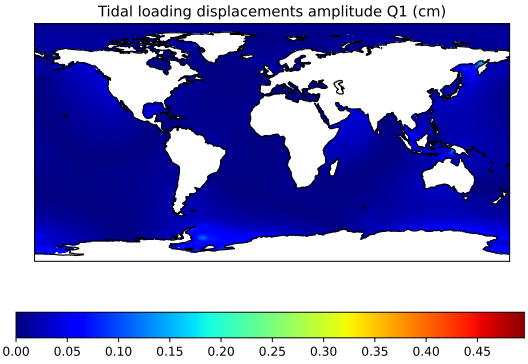

(h) Q1

Figure 3.1: Maps of the ocean tide loading displacements computed from FES2014b and the Preliminary Reference Earth Model (PREM) using pyfes software. Note the different scale for N2, K2, P1 and Q1 tides.

Another challenge is accounting for the complexities of the land-sea interface, which impact the models of ocean tide heights and thus the OTL displacement predictions near the coast. While tide heights in the open ocean can be accurately measured using satellite altimeter, the accuracy of tide measurements in coastal areas varies depending on the location. This is due to the unknown effects of the bathymetry and the limited availability of satellite measurements and tide gauge data in these areas. In addition, another factor is the seasonal variability of the water density due to input of sediments or freshwater due to ice melting (Bij de Vaate et al., 2021; Haigh et al., 2020; Pineau-Guillou et al., 2021; Teke, 2021; Wang et al., 2020b). This induces annual variations of the tide height and thus on the OTL displacements. Up to now, few analysis based on GNSS have oberved them (Zhou et al., 2021).

Despite the ongoing efforts to improve the prediction of OTL-induced deformations, this correction is still introducing systematic errors in the daily estimates of GNSS positions. This is particularly important for stations located at less than 200 km from the coast, which account for 73% of the IGS network stations. A possible approach for evaluating the accuracy of OTL models is to compare the site displacements predicted by the model with the site displacements estimated by GNSS. To illustrate the use of GNSS positions to assess the OTL displacement model, we have computed the sub-daily displacements of the station BRST every 3 hours without applying the OTL correction in the PPP solution (cross symbols in Figure 3.2). From the OTL models, we also computed the predicted displacements of the station (solid line in Figure 3.2).

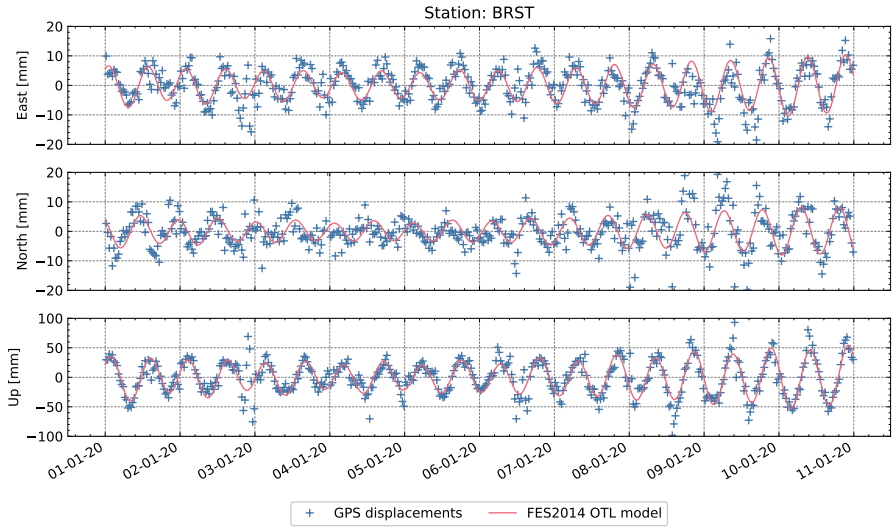

Figure 3.2: Comparison of uncorrected GPS positions and predicted OTL displacements

The estimated displacements agree well to a first approximation with the predicted displacements, but one sees differences up to 10 mm in the horizontal directions, and up to 50 mm in the vertical direction. If the GNSS positions provide valuable information on the precision and errors of the OTL models to help improve their accuracy, using subdaily PPP positions is limited by the precision that can be reached. Indeed, the usual repeatability of PPP solutions that can be used to observe subdaily displacements vary between 5 mm (for static-mode PPP solutions) and a few centimeters (for kinematic PPP solutions). Therefore, with this variability in the PPP positions, it is thus necessary to use very long position series for being able to detect the small tidal displacements that are not well predicted by the models. The currently available models differ by up to 2 mm RMS (Abbaszadeh et al., 2020).

In summary, the availability of GNSS receivers worldwide, mostly GPS receivers, has made it possible to assess the OTL models by comparing them with GNSS positions. It relies only on GPS-based positions, which is limited by technique-specific errors that occur at the same tidal frequencies.

3.2 Current approaches for estimating unmodeled tidal displacement with GNSS measurements

To better assess the OTL displacement modeling errors, the previous works have used subdaily positions computed with GPS data to estimate the amplitudes of residual tidal displacements relative to the a priori model described in the previous section. Melachroinos et al. (2008) and Vergnolle et al. (2008) conducted a study to validate ocean tide models using GPS data from a dedicated campaign on the continental shelf of Brittany in France. The paper examined seven global and regional ocean tide models and found large discrepancies in the semi-diurnal band of M2 between predictions and GPS data. Penna et al. (2015) demonstrated the capability of post-processed kinematic GPS with appropriate noise constraints to recover synthetic model errors in the predicted tidal displacements. They achieve a typical accuracy of 0.2 mm.

3.2.1 Constellation-specific errors

Estimated subdiurnal positions determined with GPS data are subject to systematic errors, related to the orbital period. The K1 and K2 tides coincide with both the GPS orbital period and the repeat period of the GPS constellation. Thus, the errors that repeat themselves with the GPS orbital periods will degrade the estimates of the OTL displacements for these tides. Melachroinos et al. (2008) and Zajdel et al. (2022) observed significant peaks in the harmonics of the orbital periods of GPS satellites, namely the harmonics of the K1 tide. This is the reason why recent studies have explored the use of GLONASS data to mitigate these errors and improve OTL model assessment using multi-GNSS data. With a constellation repeat period of eight sidereal days and an orbital period different from the sub-diurnal period, the GLONASS-related systematic errors occur at different periods than the K1 and K2/S2 constituents. Abbaszadeh et al. (2020), Matviichuk et al. (2020) and Zhao et al. (2021) investigated the potential of using GLONASS constellation for OTL height displacement estimation at different frequencies. They found that GLONASS can estimate OTL height displacement at different frequencies with similar accuracy to GPS, and the accuracy of the K1 and K2 OTL constituents can be improved by a combined GPS+GLONASS solution computed with float-valued ambiguities. The ability for GLONASS to observe the OTL errors increases for stations at higher latitudes due to satellite visibility. Indeed, owing to the higher inclination (66°) of the GLONASS orbits than of the GPS orbits (55°), there are more observation available. Using GLONASS measurements for estimating residual tidal displacements may present some challenges. Currently, the GLONASS orbit/clock products are not as precise as for GPS or Galileo. Indeed, while the GPS and Galileo products benefit of more accurate modeling (e.g. dynamical models for precise orbit determination) and of the ability to solve the carrier-phase ambiguities to integers. This leads to less precise station positioning with GLONASS. Consequently, the positioning noise level may increase and hide the smallest OTL signals.

In 2020, this thesis started with a first objective to rigorously and in depth the contribution of the Galileo constellation to the observation of the OTL modeling errors. It also aims to evaluate the OTL displacements model error from the conventional FES2014b solution on a global scale. Wei et al. (2021) discussed the use of four systems (GPS, GLONASS, Galileo, and BeiDou) to estimate the OTL model errors in Hong Kong Bay between 2016 and 2020. The authors show that combining multi-GNSS observations allows observing submillimeter deviations between the model and the observations. However, for the S2, K2, K1, and P1 tidal constituents, the multi-GNSS combination does not offer the most accurate estimations of the model errors. It is important to mention that the analysis was conducted during a period when the Galileo and BeiDou constellations were still under construction and not fully operational. Consequently, the number of satellites and stations tracking these systems was limited, and this had an adverse effect on the precision of the orbit and clock products. This ultimately resulted in poorer positioning accuracy.

We propose to reassess the discrepancies between the tidal displacements predictions and GNSS and especially Galileo's observations at the sub-diurnal scale. As mentioned earlier, a special focus will be given to the analysis of the poorly observed tidal constituents by GPS data, namely the solar tides K1, K2, S1, and S2. Like GLONASS, Galileo has a different constellation repeat period than GPS. It repeats every 10 sidereal days, causing subdiurnal errors at frequencies different from the K1 and K2 tidal constituents. Furthermore, the release of Galileo satellite metadata, such as surface area and optical properties (European GNSS Service Centre, 2019), helped to improve orbit modeling, and thus the precision of the orbit/clock products. This results in reduced systematic orbit-related errors in the positions than GLONASS. Galileo products improve since the beginning of 2019 as seen by the internal orbit validation and the analysis of the SLR residuals (Sośnica et al., 2020). In addition, the PPP performances are improved while using the combination of GPS and Galileo in AR-PPP solutions, compared to the GPS-only PPP-AR solutions as reported in (Katsigianni et al., 2019a).

3.2.2 Estimation method

In King (2006), the authors present a study on tidal displacement estimation techniques using GPS data from Antarctica. The paper compares kinematic and static methods. The kinematic method relies on the idea that estimated positions at subdiurnal scales, typically every few minutes or hours, are able to retrieve the unmodeled fraction of the station displacement due to tide loading. It consists of analyzing the spectral content of the sub-daily position series to extract the residual tidal displacement, i.e. the OTL model errors. In Penna et al. (2015), the authors make recommendations to recover the residual tidal displacements from real data with the accuracy of 0.2 mm. The process noise constraints in the kinematic PPP processing for the troposphere biases and the coordinates should be carefully tuned, and at least 4 years of data with a minimum availability of 70% must be used. This approach is primarily used to assess the models of ocean tides (Matviichuk et al., 2020; Wang et al., 2020a). These measurements of the residual OTL displacements primarily aim for constraining the structure and physical properties of the lithosphere and upper mantle as ocean tide loading may serve as natural forcing to observe the response of the crust at large scale (Bos et al., 2015; Huang et al., 2022; Martens and Simons, 2020; Matviichuk et al., 2021; Wang et al., 2020b). However, no new OTL displacements model is currently derived from the GNSS observations for positioning.

The direct estimation while processing GNSS observations, also called the static method, consists of adding the simultaneous estimation of an OTL displacement model while processing GNSS measurements in PPP. The station positions, the receiver clock, and the troposphere parameters as well as the parameters of an OTL displacement model are hence simultaneously estimated. King (2006) finds that the static method is more accurate than the kinematic method, with errors generally at the submillimeter level, except for S2, K1, and K2 frequencies because of GPS orbital systematic signals already described earlier (see Section 3.2.1).

In this chapter, several questions are explored about the applications of kinematic and static approaches for estimating the OTL model errors and the consistency between GNSS observations and OTL displacement predictions. We will examine how sensitive the kinematic approach is to PPP processing, in particular if the residual OTL amplitude estimates are affected by the parameter correlations. We also aim to know if the direct estimation of the OTL model error is possible, and if several tidal lines can be separated from each other. We will compare the performance of each approach. The chapter also investigates whether using Galileo observations improves consistency between OTL displacement predictions and GNSS observations. This includes whether the K1 and K2 tide lines, which are not correctly observed with GPS, are better observed and consistent with previous GLONASS analysis, as well as whether other tidal constituents are equally observed and consistent with OTL predictions.

3.3 Impact of the estimation strategy

3.3.1 Kinematic and static estimation of sub-daily OTL errors

3.3.1.1 Kinematic estimation

PPP configuration

The description of the models and the estimation strategies used to generate daily station coordinates is given in Table 3.2. Daily solutions were generated by computing subdaily PPP solutions obtained with the GINS software (Marty et al., 2011). The station coordinates are estimated on 3-hour observation windows, beside estimated tropospheric biases and horizontal gradient coefficients every 2 hours and 24 hours, respectively. For this study, The GPS, Galileo, and GLONASS orbit/clock products were retrieved from the processing performed by the GRGS analysis center for the REPRO3 campaign led by the IGS. The carrier-phase ambiguities are solved for integer values. The a priori OTL displacement model used in our study is the one derived from the FES2014b model, since this is consistent with the model used by the GRGS analysis center to produce the orbits. Because the orbit/clock products have been aligned to a terrestrial reference frame centered on the center of figure (CF), the OTL displacement corrections are computed in a CF frame beforehand being applied in the observation modeling for PPP.

Table 3.2: Description of modeling and parameter estimation strategies in PPP processing

	Common settings	
Satellites products		
Orbits and clocks	GRGS products from IGS REPRO3	
Satellite biases	GRGS wide-lane biases	
Measurement models		
Ambiguity strategy	Zero-difference ambiguity resolution (Loyer et al., 2012)	
Elevation cutoff	8 °	
Antenna phase center correction	igsR3_2077 antex	
Troposphere model	GPT2 meteorological and mapping function	
Loading		
Solid earth pole tidal loading	2010 IERS Conventions with updated linear mean pole model	
Ocean pole tidal loading	2010 IERS Conventions with updated linear mean pole model	
Ocean tidal loading (tide atlas)	FES2014b ocean tides atlas (Lyard et al., 2021)	
Ocean tidal loading (earth response)	Load deformation function from PREM model (Dziewonski and Anderson, 1981)	
Atmospheric loading	2010 IERS S1/S2 model	
Non-tidal surface loading model	None	
	Kinematic approach	**Static approach**
Parameters estimation		
Processing batch length	24 h	24 h for NEQ generation
Station coordinates	1 set per 3 h	1 set per 24 h
Observation sampling	30 s	300 s
Clock corrections	1 per observation	
Troposphere: ZTD	1 piecewise linear model every 2h	
Troposphere: horizontal gradients	1 constant parameter per 24h	

Station selection

The analysis was conducted between 2019.0 and 2021.0, which corresponds to the period when the Galileo constellation had been operational for a sufficient duration to enable worldwide station visibility for Galileo-only PPP solutions. Over the course of the testing period, the availability criterion for GPS, Galileo, and GLONASS measurements has been set at 80%. Based on a 30-day sample selected randomly, the GPS and Galileo integer-ambiguity fixing rates must exceed 80% and the vertical repeatability should be less than 3 cm on average. Included in the study are IGS stations located within a 200 km distance from the coastline, where OTL has a greater impact than other loading effects like atmosphere tide loading. Figure 3.3 illustrates the network of stations selected for this analysis.

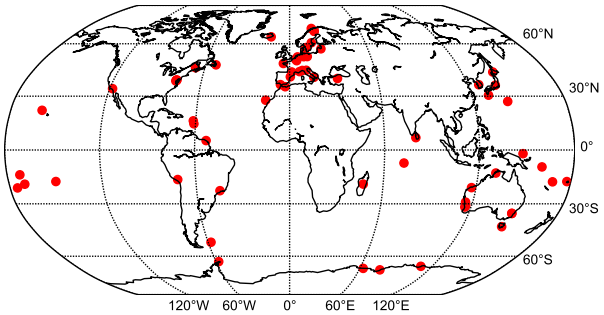

Figure 3.3: Stations network

3.3.1.2 Some limitations for the kinematic estimation

We mention here the limitations that can arise when using kinematic positions to extract the OTL residual displacements. Penna et al. (2015) extensively discusses the importance of tuning the stochastic model parameters to be able to retrieve the small tidal displacements with the accuracy of 0.2 mm. The authors also mention that this accuracy with the kinematic approach is reached for a minimum data length of 4 years. The authors also demonstrate that the estimated troposphere propagation delay partly retrieves the synthetic tidal displacement they introduce. The same question can be asked for subdaily positions estimated on longer windows (e.g. 3 hours) : do the tidal displacements, retrieved from these subdaily positions, and troposphere biases can be properly separated?

To answer this question, a test was carried out by estimating the positions of the station of Brest (BRST) every 3 hours with PPP-AR. We then analyzed the correlation between the positions and the troposphere parameters over a day. To this end, we use the cofactor matrix (see definition in Chapter 2, section 2.4.2) resulting from the second inversion (positioning with fixed ambiguities). The parameter covariances are then converted into correlations, shown in Figure 3.4.

We observe a correlation of 30% to 50% between the X-positions, and the Z-positions which corresponds to the vertical displacements in Brest, and the estimated troposphere biases and gradients. This implies that the residual station displacements estimated with PPP cannot fully be attributed only to OTL displacements. Indeed, due to the correlations between the estimated positions and troposphere biases and gradients, the estimated displacement can recover 30% to 50% of the errors coming from diurnal or sub-diurnal variations in the troposphere.

Hence, the observation of OTL errors below the millimeter level can be more challenging without accounting for the correlation between the positions and the other estimated parameters in PPP.

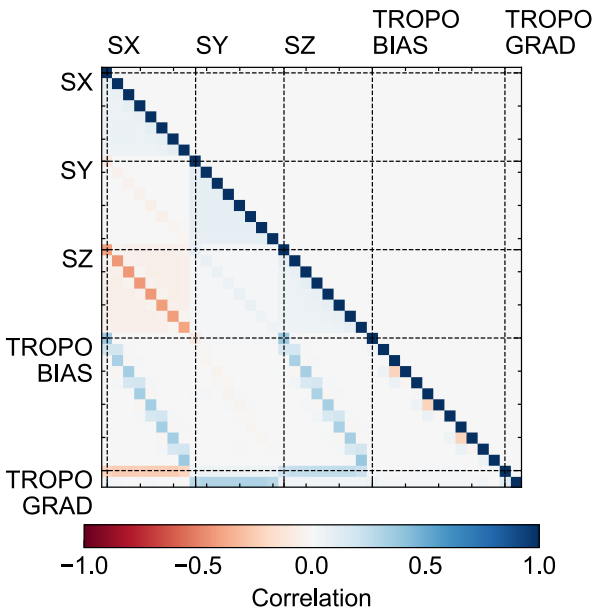

Figure 3.4: PPP parameters correlations - kinematic approach

3.3.1.3 Static estimation

Implementation in GINS

Because this was not available in GINS software nor in any other scientific GNSS software to our knowledge, I implemented in the possibility to directly estimate the parameters of the OTL displacement model while processing GNSS observations required for the implementation of the static estimation strategy. As mentioned earlier, the static method requires to choose a model for the OTL-induced displacement to retrieve the errors in the amplitudes $A_{i,j}$ and phase angles $\phi_{i,j}$ of the OTL corrections (see Equation 3.6). We adopted a simplified model derived from King (2006); King et al. (2005); Yuan et al. (2013). This model is for the eight diurnal and semi-diurnal tides (M2, S2, N2, K2, K1, O1, P1 and Q1, see Table 3.1) is given for the kth coordinate by

$$\Delta OTL_i(t) = \sum_{j=1}^{8} \delta OTL_{i,j} = \sum_{j=1}^{8} C_{i,j} \cos(\omega_j t) + S_{i,j} \sin(\omega_j t) \tag{3.7}$$

with

- $\Delta OTL_i(t)$: the residual OTL displacements resulting in the i^{th} direction
- $C_{i,j}$, $S_{i,j}$: the in-phase and out-of-phase coefficients of the OTL displacement in the ith direction.
- ω_j: the angular frequency of the j^{th} tide

We use only 3 years, when data were available for Galileo, thus the long-term modulation at 18 years cannot be separated from the short-term variation.

This OTL displacement model has been described in the same way as the station coordinates in GINS, that is to say in an Earth-centered, Earth-fixed Cartesian frame. The partial derivatives corresponding to this model have been implemented in GINS, allowing for the estimation of parameters for any tide. However, for this analysis, we only include the 8 major subdaily tides (M2, S2, N2, K2, K1, O1, P1 and Q1). It should be noted that the computation of the minor tides by admittance modulation is not corrected for the estimated amplitudes for the major tides. In other words, if not re-estimated, the minor tides are only computed from the a priori OTL model.

Separation of the tides

A 24-hour observation window, that is usually applied for processing GNSS data, prevents us from reaching the required spectral resolution to separate all 8 tides.

The previous analyses using the static method improved the accuracy of OTL coefficient estimates by stacking the daily estimates and their uncertainties at the parameter level. For that, they used a sequential algorithm like a Kalman filter (King, 2006) or covariance matrix filter (Yuan et al., 2013). The final accuracy of the OTL error estimates depends on the convergence of the filter. This differs between the tides. The convergence requires between 100 days for the lunar tides (M2, S2, N2, O1) and several years (1000 to 3000 days) for the solar tides, in particular the K1 and K2 tides. For the latter tides, the filters have more difficulty converging because of the GPS systematic errors (King, 2006; Yuan et al., 2013).

Instead of a combination at the level of the parameters, we opted for an alternative and original strategy based on the combination of the normal equations, before the resolution of the parameters. Combining geodetic parameters determined by different satellite geodetic techniques at the normal equation level is a frequent practice for example for the Earth rotation parameters or the station coordinates estimation. If the two approaches are theoretically equivalent, in practice, the combination at the level of the parameters is more sensitive to the difference of errors between the parameters (poorly observed parameters, outliers, constellation-specific signals,...). Moreover, if the covariance matrices of the parameters are not combined, this ignores possible correlations between the parameters estimated in PPP processing, in particular between the OTL parameters and the troposphere parameters. Thus, the normal equation (NEQ) level combination becomes conceptually more rigorous. In addition, the static estimation using NEQs stacking is equivalent to construct a long PPP batch (typically over one year), whose all GNSS observations contribute to the estimation of the OTL coefficients. Consequently, this also minimizes the formal errors of the estimates.

To reduce the calculation load, the resolution of the ambiguities is performed beforehand with 24-hour batches, and fixed-ambiguities measurements are merged prior to the NEQ generation step. Note that, at this stage, there can be ambiguities parameters left regarding whether the fixing was successful or not, or for GLONASS measurements. We generated per-station daily NEQs including the daily station coordinates, the OTL parameters, and the tropospheric parameters (biases every 2 hours, and daily horizontal gradients). Other parameters such as the remaining ambiguities or the receiver clocks are reduced. For that, the rows and columns of the matrix are rearranged, and its QR decomposition is recomputed. We extract the sub-matrix associated with the station coordinates, OTL parameters and troposphere parameters. The partial derivatives of the reduced parameters are removed from the normal equations but still influence the combined solutions. Figure 3.5 summarizes the workflow of the estimation of OTL errors with single-constellation solutions (left) and multi-constellation solutions (right). For the latter, the details will be described later in the chapter (see Section 3.3.2.3).

Comparison between kinematic and static methods

The first analyses focus on the agreement between the residual errors in amplitude estimated by both the kinematic and static approaches for the same stations. This test is performed with GPS-only solutions. The amplitudes $A_{i,j}$ and phase angles $\phi_{i,j}$ of the residual OTL-induced displacements were fitting from the series of east, north and up (ENU) 3-hour coordinates estimated by PPP (kinematic estimates). These estimates were compared with the results from the direct (or static) estimation of the OTL coefficients $C_{i,j}$ and $S_{i,j}$ (see Equation 3.7). The latter were converted into ENU coordinates and amplitude/phase parameters, to be comparable with the kinematic estimates. Figure 3.6 summarizes with boxplots the distribution of the estimated residual errors in amplitude with both approaches. The points outside the interval [Q1-1.5*IQR; Q3+1.5*IQR] are represented by crosses, where Q1 and Q3 are the first and third quartiles, and IQR is the interquartile range (Q3-Q1).

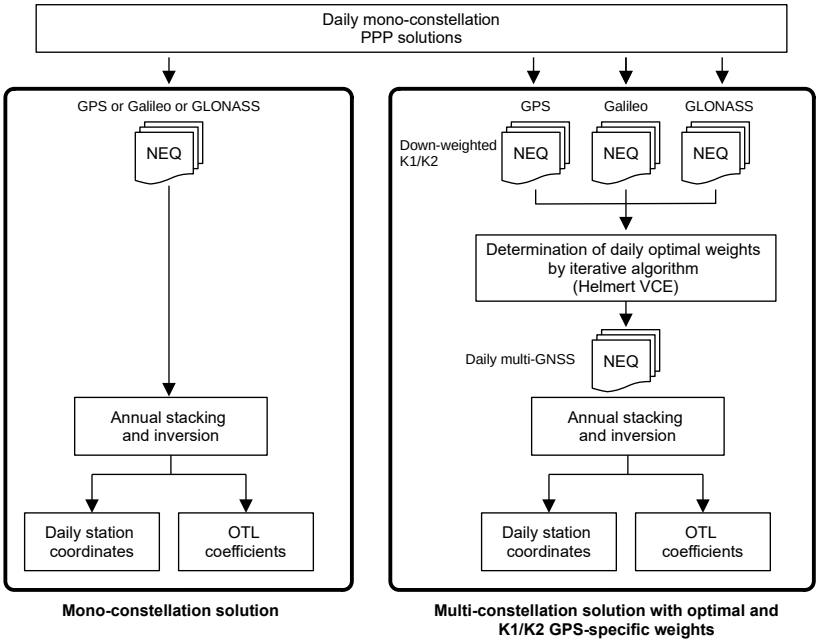

Figure 3.5: Implementation of the static method

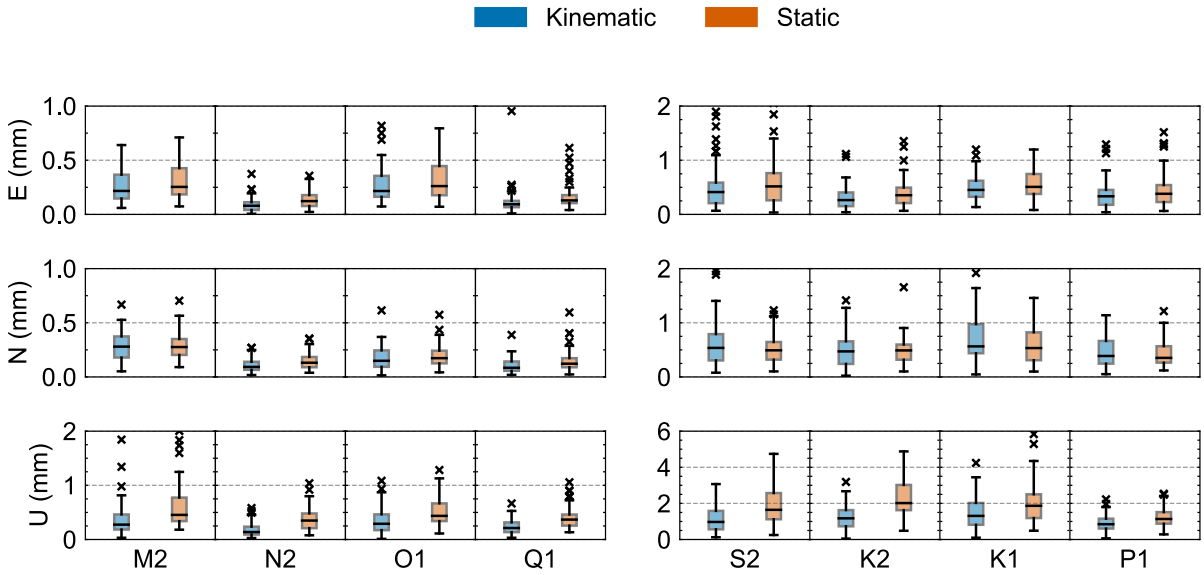

Figure 3.6: GPS-only residual displacements compared to FES2014b-derived OTL displacements. The left plot shows Moon-driven tides, while the right plot shows Sun-driven tides. Note the change in scale between the two plots.

For the solar tides, the differences between the two methods are larger. The mean differences between the kinematic and static estimates are 0.7 mm for S2, 0.9 mm for K2, 0.6 mm for K1 and 0.29 mm for P1. For the height, we observe differences up to 0.5 mm, which represent between 10% and 25% of the predicted OTL displacements with the FES2014b model. The gap is even more important for the K1 and K2 tides, for which the differences between the two estimation methods stand at 65% of the estimated errors (0.8 mm). For the lunar tides (M2, N2, O1 and P1), the values estimated by the static method concur with those estimated with the kinematic methods within 0.2 mm for the tide N2, 0.07 mm for Q1 and 0.28 mm for M2. In the east and north directions, the error estimated by the two methods does not differ by more than 0.06 mm (30% of the total errors estimated).

We used two approaches to estimate with GINS the residual OTL displacements. The results from both methods, the standard kinematic method and the static method we implemented, with a difference of 0.5 mm for most of the tides to 0.8 mm for K1 and K2 tides.

Correlation between parameters with the static estimation

We have seen with the kinematic estimation that the OTL displacement model errors through the subdaily positions may also reflect errors in other models used in PPP. They can retrieve errors in the troposphere propagation model because of the correlation between the estimated positions and the tropospheric parameters (biases, gradients). Therefore, we wanted to compare the correlation between the OTL coefficient parameters for 1 year and the other estimated parameters in the static approach. For the station BRST, we analyze the cofactor matrix retrieved after stacking the daily NEQs of one year and inverting the resulting system. This matrix gives the correlation between the OTL coefficients, the daily station positions and the troposphere biases and gradients. Owing to the number of parameters involved (more than 5000), we opt to plot the distribution of the correlations between each estimated OTL coefficient ($C_{i,j}$, $S_{i,j}$) and the other PPP parameters in Figure 3.7. We analyze the most significant case where the correlations are the largest, that is the correlations for GPS-only solutions and for the K1 and K2 tides. The parameter correlations are extracted from normal equations, and the empirical distribution is computed by Kernel Density Estimation using Gaussian kernels.

When we compare the correlations for station BRST in Figures 3.4 and 3.7, we see that the static approach allows reducing the correlations between the OTL coefficients and the troposphere parameters by two orders of magnitude compared to the kinematic approach. The correlations between the 3-hour station coordinates, used to retrieved the OTL model errors, and the troposphere parameters were as high as 50% for the kinematic approach. On the contrary, the correlations between the estimated OTL coefficients are up to 4% (correlation between the troposphere bias and Z coordinates) with the static estimation. By stacking the NEQs, the OTL coefficients are observed through an observation window of 365 days, while the troposphere parameters are observed only by a window of 2 hours (bias) or 24 hours (gradient).

In summary, the static estimation improves the separation between errors in the OTL displacement model and errors in other models used in PPP, such as troposphere models.

3.3.2 Single- and multi-constellation estimates of sub-daily OTL errors

So far, we have only used GPS observations to estimate the OTL errors. In the next section, we will deal with using other GNSS constellations, like Galileo and GLONASS. We will start by describing the specific signatures of each constellation that can affect OTL error estimates. Then, we will explain our strategy for reducing the effects of these signatures when using multi-GNSS observations in this thesis.

3.3.2.1 Identification of spurious sub-diurnal signals by each constellation

In this thesis, I studied two types of errors specific to each constellation that can cause signals at sub-daily frequencies and affect our ability to correctly estimate OTL errors. The first type of spurious signals occurs around the 24-hour spectral band and is caused by incorrect modeling of Galileo's orbit during the eclipse seasons. The second type is the presence of signals at the harmonics of the repeat period of the constellations, which are observed for all constellations.

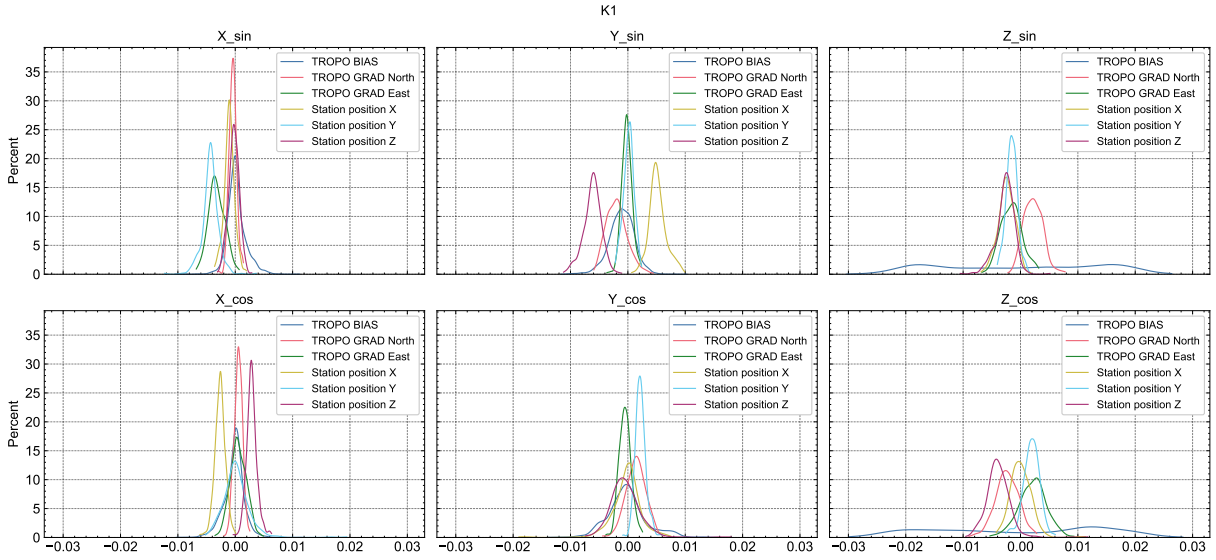

(a) K1

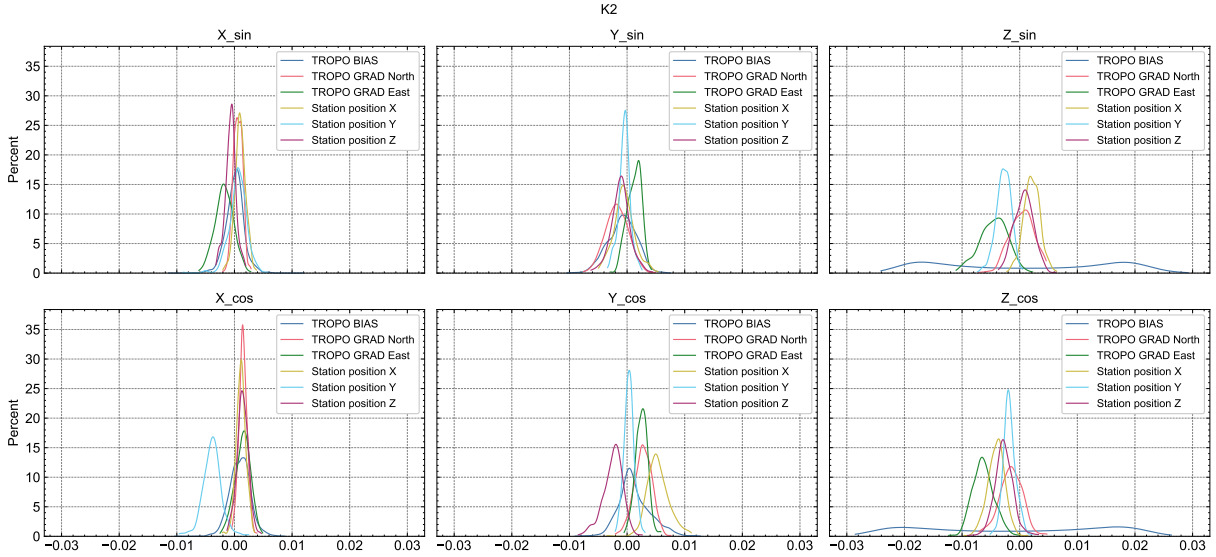

(b) K2

Figure 3.7: Correlation of parameters estimated in the static method.

Beat modulation of orbital errors during the Galileo eclipse seasons

Modeling the dynamics of the GNSS satellites during the eclipses, that is when the satellite passes through the shadow of the Earth, is a challenging task. Indeed, the presence of eclipses influences the computation of the solar radiation pressure and the thermal-induced forces applied to the satellites. Furthermore, the satellite attitude variations during the eclipse season are not accurately known or modeled because the attitude control system cannot rely on the Sun sensors when the satellite passes through the Earth's shadow, and because the required yaw changes at the orbit moon and midnight to keep the nominal attitude cannot be physically performed. In addition, the entry and exit of satellites of the eclipse periods are relatively fast events, which require being smoothed over several integration steps. In particular, for the second generation of Galileo spacecraft, Galileo-FOC (Full Operational Capability), the thermal accelerations during the eclipse, resulting from heat emission through the radiators, are not fully corrected by empirical parameters during the orbit determination (Duan and Hugentobler, 2022; Sidorov et al., 2020). This is one of the possible orbital modeling errors that can introduce signals in the position time series.

And, this is precisely this sort of signals that we can observe in the series of positions estimated every 3 hours. We use the series that we generated for the kinematic estimation from the Galileo data. For each station, we computed the spectra in amplitude using the Lomb-Scargle algorithm, and then computed the averaged spectra over the entire network. This enables to detect the signals commons to all stations. On these stacked spectra of the Galileo-only positions (red curves in Figure 3.8), we observed signals around 1 cpd (period of 24 hours). They are only visible on the horizontal positions, in particular in the north direction (middle panel in Figure 3.8). Moreover, these peaks were not visible on the GPS-only or GLONASS-only positions spectra, and the peak frequencies do not correspond to any tide. Therefore, I assume that the cause is specific to the Galileo data or clock/orbit products, which are used for determining the PPP positions. Because the signatures are predominant in the north direction, I assume that the origin could be signatures occurring during the eclipsing season in the along-track direction of the Galileo orbits.

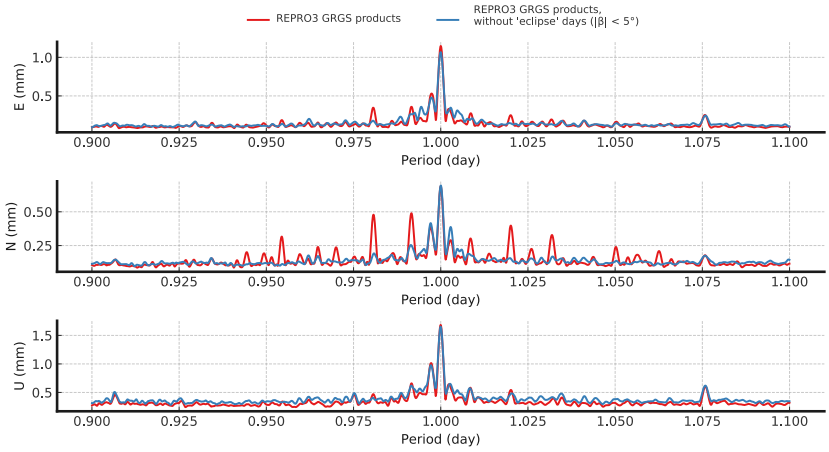

Figure 3.8: Stacked amplitude spectra of the 3-hour station positions series computed with and without the epochs where one Galileo plane is in an eclipse season.

The aforementioned Galileo-FOC spacecraft's specific thermal emission during the eclipses resulting in accelerations mainly in the along-track direction. Thus, not accounting for them introduced errors in the along-track direction. From the point of view of low to mid-latitude stations, a variation of the satellite positions along this direction is observed in the north-south direction which is parallel to the ground track of the satellites.

A first confirmation of this assumption is obtained by analyzing the frequencies of these signals. The eclipse seasons are defined by the beta angles, the angle between a satellite orbital plane and the direction of the Sun. A Galileo satellite is in an eclipse season if this angle is between $\pm$ 12.4°. We plot the evolution of the beta angles for the three Galileo planes in Figure 3.9. The shaded areas represent the eclipse seasons. While considering the three planes, the occurrence frequency of the eclipses is approximately 3.75 cpy.

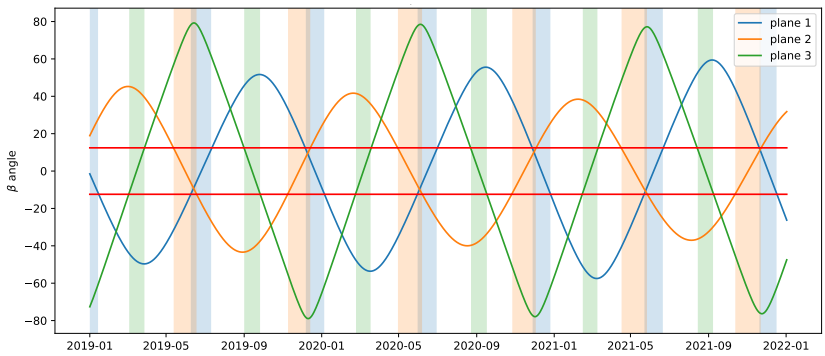

Figure 3.9: Beta angles for the Galileo orbital planes

Indeed, the periods T_{obs} of the peaks visible around 1 cpd in Figure 3.8 are given in Table 3.3. We want to compare the frequencies of the peaks we observed match the frequencies of the signals produced by the beat between the daily frequency and the 3.75 cpy frequency of the Galileo eclipse season. The daily frequency is based on the length of the processing arcs for the generation of the GNSS orbit/clock products. The frequency of the resulting modulated signals reads

$$T_{\pm n} = \frac{1}{f_{24h} \pm n f_0} \tag{3.8}$$

where $T_{\pm n}$ the periods of the nth harmonic, f_{24h} the daily frequency and f_0 the occurrence frequency of the eclipse seasons.

The theoretical periods T_{th} of the modulated signals, computed using Equation 3.8, are given for $n \in |[-5, 5]|$ in Table 3.3. This simple model explains well these signals as the relative error between the observed and theoretical frequencies are below 0.2 %.

Table 3.3: Theoretical and observed periods (in days) for "eclipse" signals modulated by a 24-hour window

Harmonic (n)	T_{th}	T_{obs}	Relative error (%)
5	0.9512	0.9521	0.0976
4	0.9606		
3	0.9701		
2	0.9799	0.9806	0.0736
1	0.9898	0.9909	0.1074
0			
-1	1.0104	1.0097	0.0667
-2	1.0210	1.0220	0.1014
-3	1.0318	1.0323	0.0504
-4	1.0428		
-5	1.0541		

To verify the hypothesis, additional analyses were performed by removing the positions that could be affected by the eclipses in the series. For that we filtered the positions of the days when at least one Galileo orbital plane was in the eclipse season, that is when the absolute value of the β-angle of at least one orbital plane below 5°. The spectra of the edited series is given in blue curves in Figure 3.8. We observe that the removal of these days reduces the spurious signals around the period of 24h (frequency of 1 cpd). Hence, this can be a solution to clean the spectra and improve the detection of the residual tidal displacements.

A finer method is to edit the observations impacted by the orbital mismodeling directly at the measurement level. In a second test, we reprocessed PPP solutions with removing the Galileo observations received from a satellite while it is in an eclipse season. We perform the test for one station (BRST) and on one day (30/05/2019 - CNES Julian Day 25351). During this day, the plane B of the Galileo constellation was in the eclipse season.

In particular, we analyze the post-fit carrier-phase residuals of the second PPP solution with fixed ambiguities. Indeed, the degradation of the residuals can be the evidence that the inversion of the PPP parameters is incorrect, as theoretically the residuals should not be biased (zero mean), neither have a drift. Figure 3.10 shows the phase residuals obtained from this daily PPP solution for the BRST station, with and without the edition of observations from the eclipsing satellites. To improve clarity, we only plot the residuals from the satellites of orbital plane B and

those with an elevation above 20, neglecting the observations that could be impacted by other factors (multipath, atmosphere).

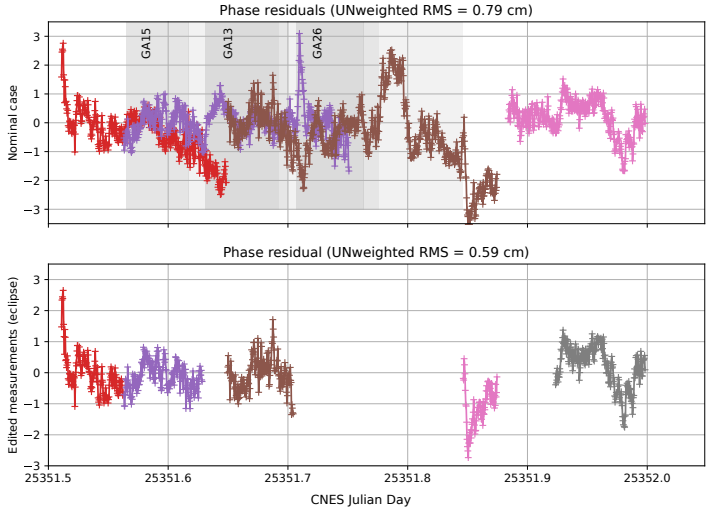

Figure 3.10: Carrier-phase measurements residuals (in cm) with editing the observations of satellites in eclipse (bottom) and without editing (top). The eclipse passes are represented by the shaded figure on the top panel. Note that not all satellites are in eclipse season.

The residuals from the satellites E15, E13, and E26 exhibit significant deviations or drift during the passage of the satellite in the Earth's shadow (shaded areas). However, the residuals from the fourth pass (in pink on the top panel), received from the Galileo-IOV (Initial Operational Capability) spacecraft E12, were not biased, confirming that the potential issue in the orbital modeling only appears for the Galileo-FOC satellites during the eclipse season, and thus the observations received from these spacecraft.

Returning to the spurious subdiurnal signals appearing in the positions series, we analyzed the effects of editing the observations during the eclipses on the 3-hour positions estimated with and without the observations in eclipses. Figure 3.11 gives the estimated positions in the two cases on the same day (30/05/2019 CNES Julian Day 25351) used for the analysis of the phase residuals in Figure 3.10. It is worth noting that station BRST is at latitude 48.380, where the satellite ground tracks are not entirely parallel to the north-south direction. Thus, any orbital errors in along-track direction mostly are projected in the east direction.

We observe that during the second half of the day, when the phase residuals were degraded, there was a significant impact on the estimates of the station coordinates. The differences reached 1 cm in the East coordinate and 2.5 cm for the height. In case the Galileo observations are not edited, the Galileo-derived positions make it difficult to properly detect the subdiurnal OTL displacement model errors.

This analysis highlighted that the observation of the OTL displacement model errors with Galileo observations may be altered by orbital mismodeling during the eclipse season.

Alternative GRGS products were provided in 2021 after the analysis of the REPRO3 product with Galileo-FOC macro-models (GRGS2021) improved to limit the orbits errors during the eclipses. We compared them to the REPRO3 GRGS products, used in the previous analyses, and external REPRO3 products from another analysis center: CODE. Tests were conducted only for January 2019 by computing by PPP 3-hour and 24-hour positions, which are the two configurations that we used for the estimations of the OTL displacement model errors. The first week of the period was the eclipse season for Galileo plane A. The tests were conducted with the same station (BRST), and without editing the observations during the eclipses. Figures

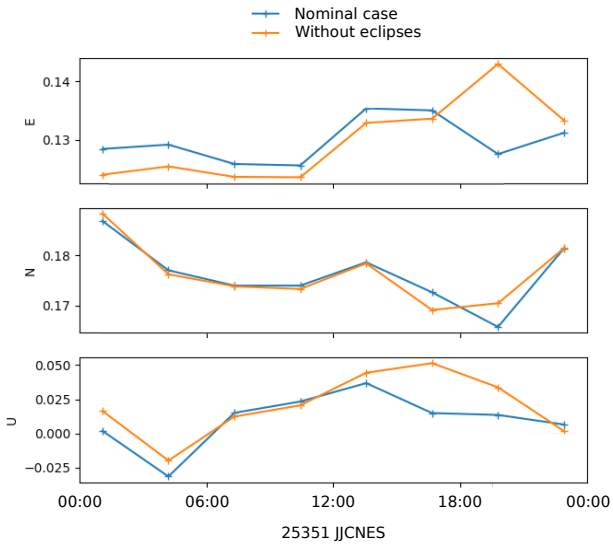

Figure 3.11: Estimated position corrections (in meters) from the reference coordinates, with and without editing the 'eclipse' observations. The orange line represents the estimated position corrections when the eclipse observations are edited, while the blue line represents the estimated position corrections without any observation edition.

3.12a and 3.12b show the comparison of 3-hour ENU positions estimated using two different products: REPRO3 GRGS products and REPRO3 CODE products (COD). The top panels show the estimated coordinates, while the bottom panels show the differences between the coordinates and those estimated using the improved GRGS products (BIS). Likewise, Figures 3.13a and 3.13b show the results for the 24-hour positions.

On both 3-hour and 24-hour positions, the improvement of the orbital modeling during the eclipses has a positive effect on the positions estimated by PPP. Indeed, during the first week, we observe differences up to 2 cm between the REPRO3 and alternative GRGS products. In addition, the alternative GRGS products perform equally as to REPRO3 CODE products. Indeed, the positions computed with these products agree within 0.2 mm for daily positions and 8 mm for sub-daily positions.

As a result, the improved GRGS (GRGS2021) products will be used for the estimation of the OTL displacement modeling errors to reduce the impact of the systematic signals due to orbital mismodeling during the eclipses.

Signatures at the constellation repeat periods

In this section, we analyze another type of constellation-specific signals that are also observed in the spectra of the 3-hour and 24-hour positions series. These signals occur at the harmonics of the repeat period of each constellation. In Figure 3.14, we plot the stacked spectra of the 3-hour ENU position series determined with GPS, Galileo or GLONASS-only observations. We plot a large band covering the periods from 10 hours (approximately 900 cpy) to 100 days (approximately 3.6 cpy).

In Figure 3.14, we observe these constellation-related signals for the three constellations at different frequencies. For GLONASS (top curves, in green), peaks occur at the harmonics of 8 days: 8.0 days (45.6 cpy), 4.0 days (91.2 cpy), 2.7 days (136.9 cpy), 2.0 days (182.5 cpy), 1.6 days (228.1 cpy), 1.3 days (273.8 cpy), 1.1 days (319.4 cpy) and 1.0 days (365.0 cpy). Similar signals are observed for the Galileo-only positions at the harmonics of 10 days: 10.0 days (36.5 cpy), 5.0 days (73.0 cpy), 3.3 days (109.5 cpy), 2.5 days (146.0 cpy), 2.0 days (182.5 cpy), 1.7 days (219.0 cpy), 1.4 days (255.5 cpy), 1.2 days (292.0 cpy). The origin of these peaks related to the

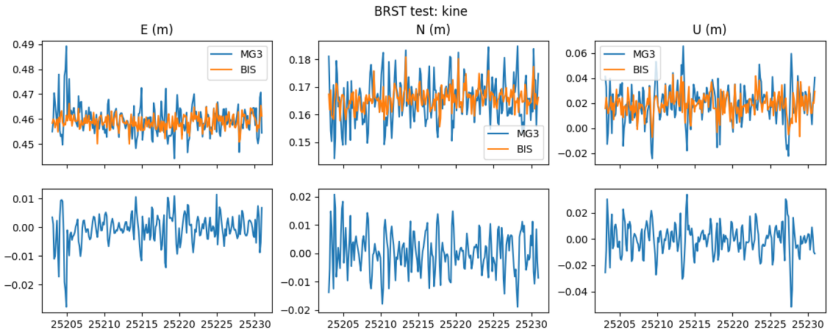

(a) REPRO3 GRGS products

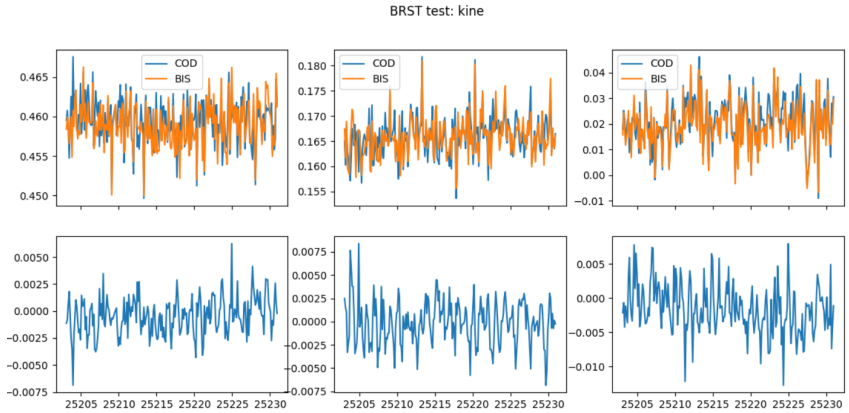

(b) REPRO3 CODE products

Figure 3.12: ENU positions estimated every 3 hours with REPRO3 GRGS (MG3), improved GRGS products (BIS), REPRO3 CODE products (COD). Left: east, middle: north, right: up

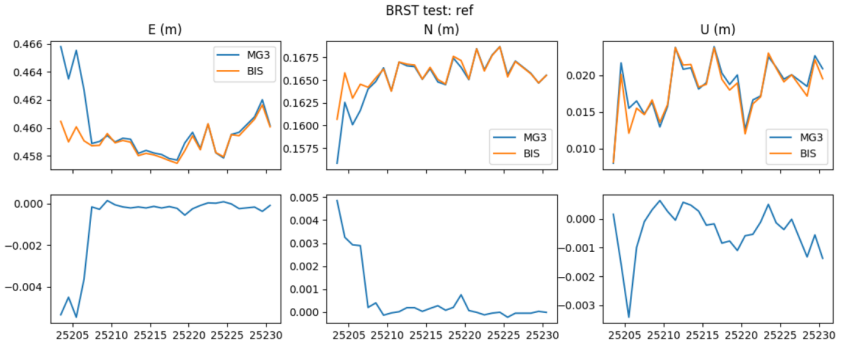

(a) REPRO3 GRGS products

(b) REPRO3 CODE products

Figure 3.13: Daily ENU positions estimated with REPRO3 GRGS (MG3), improved GRGS products (BIS), REPRO3 CODE products (COD). Left: east, middle: north, right: up

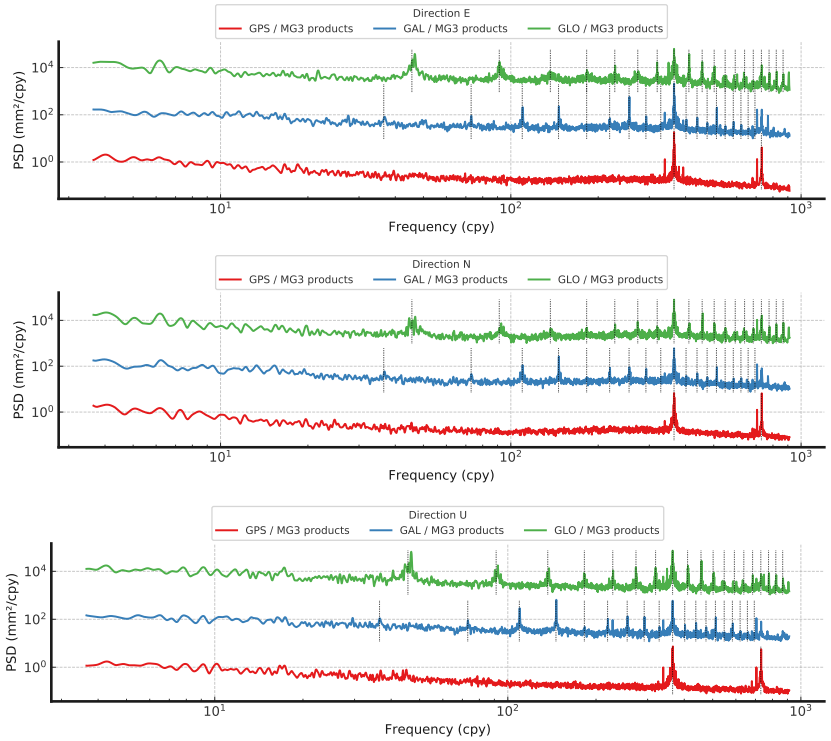

Figure 3.14: Signatures on the single-constellation station coordinate power spectra (top: east, middle: north, bottom: up). For readability purposes, the spectra are shifted. The vertical lines represent the harmonics of the repeat period of the constellation ($\sim$ 10 days for Galileo, $\sim$ 8 days for GLONASS and $\sim$ 1 day for GPS).

repeat period of the constellation is likely to be from orbital mismodeling or observation errors that repeat with the same periodicity (e.g. antenna phase center bias). These long-period signals are not visible in the GPS positions, for which the repeat period of 1 (sideral) day results in signals restricted to the subdiurnal band (Figure 3.15c). These are the already known signals that perturb the observation of the K1, K2, and K3 tide lines. As for Galileo and GLONASS, the higher harmonics of the 10- and 8-day period are also visible in the sub-diurnal band (Figures 3.15a and 3.15b). However, the amplitude of the Galileo's peaks are smaller than the signals for GLONASS or GPS (see zooms in on the sub-daily scale in and 3.15c).

If the Galileo- and GLONASS-specific signals spread on a larger spectral band from intermediate frequencies (10 days for Galileo and 8 days for GLONASS), they also contaminate the higher frequencies. This can perturb the observation of the residual tidal displacements. As already reported for GLONASS (Abbaszadeh et al., 2020), similar Galileo's 10-day harmonic peaks occur close to Q1 (1.1195 d) and N2 (0.5274 d) constituents' frequencies which may impact the tidal displacement estimation (Figures 3.15a and 3.15b). These signals for GPS coincide with the 24h and 12h oscillations and are restricted to the sub-diurnal scale. But they perturbed the observation of the tide lines around the harmonics of K1 (K1, K2, K3) as shown in Figure 3.15c.

While all the constellations have spurious peaks in the sub-diurnal band, they are much stronger for GPS than Galileo. Galileo has also fainter peaks than GLONASS due to its better orbit modeling. Thus, they will will have less impact on the use of Galileo in the rest of the analysis.

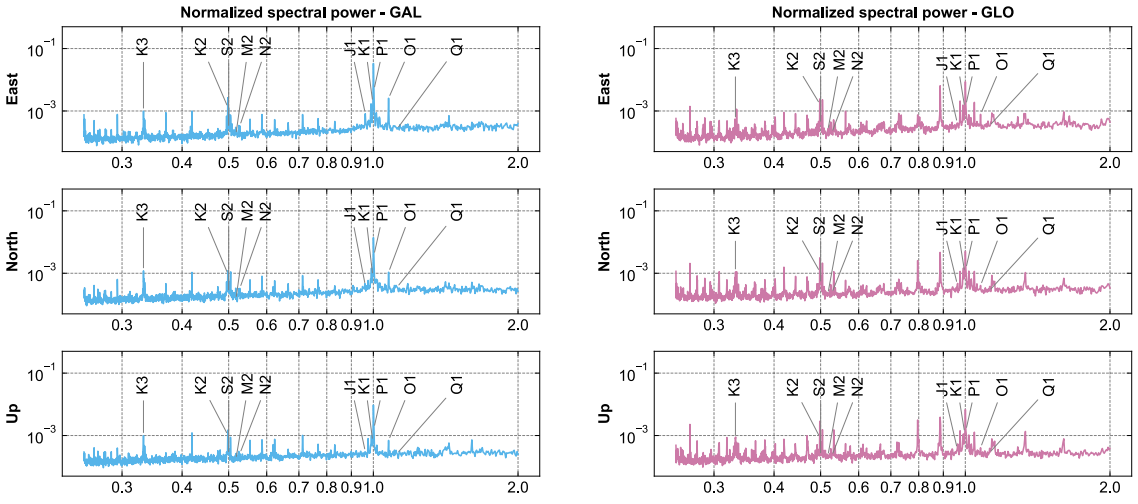

(a) GAL (b) GLO

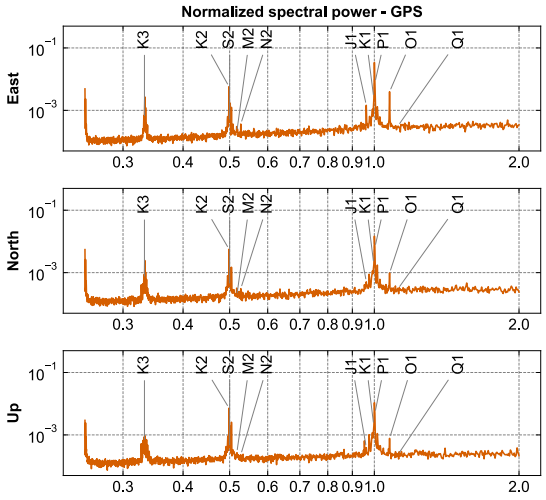

(c) GPS

Figure 3.15: Stacked spectra of 3-hour coordinates - zoom on the sub-diurnal scale. The X-axis is the periods (in days).

3.3.2.2 Single-constellation estimates

After identifying the potential constellation-specific systematic errors that can impact the estimation of the OTL displacement model errors, we compare the residual OTL displacements as estimated with the static estimation approach. We first focus on the single-constellation estimates and the resulting amplitudes ($\sqrt{C_{i,j}^2 + S_{i,j}^2}$). The boxplots in Figure 3.16 describe the statistics of the estimated amplitudes of the residual tidal displacements for the 8 main tides (M2, N2, O1, Q1, S2, K2, K1 and P1). We compare the estimates derived with GPS, Galileo and GLONASS, in the three directions ENU (east, north and up).

In terms of magnitude, the GPS-only and Galileo-only estimates are consistent for the M2, N2, O1, Q1, and P1 tidal frequencies. In comparison, the GLONASS-only estimates stay in the same error bar than the estimates with GPS and Galileo, but show a larger variability. For these tides for which all constellations concur within their specific uncertainties, the residual tidal displacements are likely OTL model deficiencies. However, the GPS estimates for the S2, K2, and K1 tides are biased and have a larger variability compared to the estimates from the other two constellations.

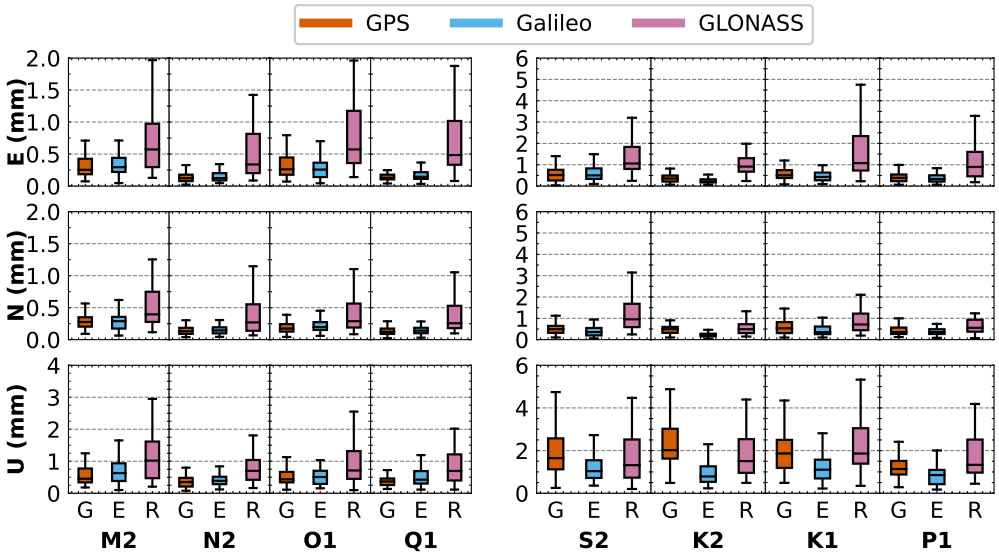

Figure 3.16: Residual tidal displacements for 67 stations determined by each constellation. The left plot shows Moon-driven tides, while the right plot shows Sun-driven tides. Following the IGS naming, G stands for GPS, E for Galileo and R for GLONASS.

In addition, we notice the effects of integer-ambiguity fixing on the east displacements estimates, in particular the degradation of the GLONASS estimates. In Figure 3.16 (top panels), the GLONASS-derived estimates are biased and have a larger variability than GPS-only and Galileo-only estimates. Processing GPS and Galileo observations with integer-fixed ambiguity improves the accuracy of the PPP solution, especially in the east direction. This is due to the additional constrain obtained by the observation geometry. On the contrary, GLONASS observations are processed with floating ambiguities. Consequently, this results in more noise in the estimated east displacements and thus less precise estimation of the OTL displacement model errors.

In summary, GPS, Galileo and GLONASS provide consistent estimated of the OTL displacement model errors for most of the 8 major tides. However, Galileo and GLONASS outperforms GPS when it comes to the modeling errors for the K1, K2 and S2 tides. Even more, only Galileo provides accurate estimates for the east components thanks of the possibility to resolve integer-valued carrier-phase ambiguities.

3.3.2.3 Constellation-based optimal weighting

We investigate if using a combination of constellations can improve the observation of residual OTL displacements. This could help us to better isolate OTL model errors while reducing systematic errors from each constellation. This is the reason why in the multi-constellation workflow (Figure 3.5) we add an additional step to weight the contribution of each constellation in the estimation of the OTL errors. For each station, we determine the optimal weights for each daily and single-constellation NEQ involved in a combined multi-GNSS solution. The optimal weights are computed iteratively using the Helmert Variance Component Estimator (VCE). For that, we use the implementation of the algorithm available in the DYNAMO module of GINS software. The optimal weights are then used to combine the daily NEQs prior to solve for the OTL coefficients, the daily station positions and the troposphere parameters (biases and gradients).

First, we compare the computed optimal weights of each possible combination of constellations: GPS+Galileo, GPS+GLONASS, Galileo+GLONASS and GPS+Galileo+GLONASS. For that purpose, we compute the averages of the daily weights given for each constellation, per station. Figure 3.17 illustrates the average of the weights as a function of the latitude of the station. The

weight is represented through the relative contribution (in percent) of each constellation to the multi-GNSS combination used for estimating the per-station OTL parameters.

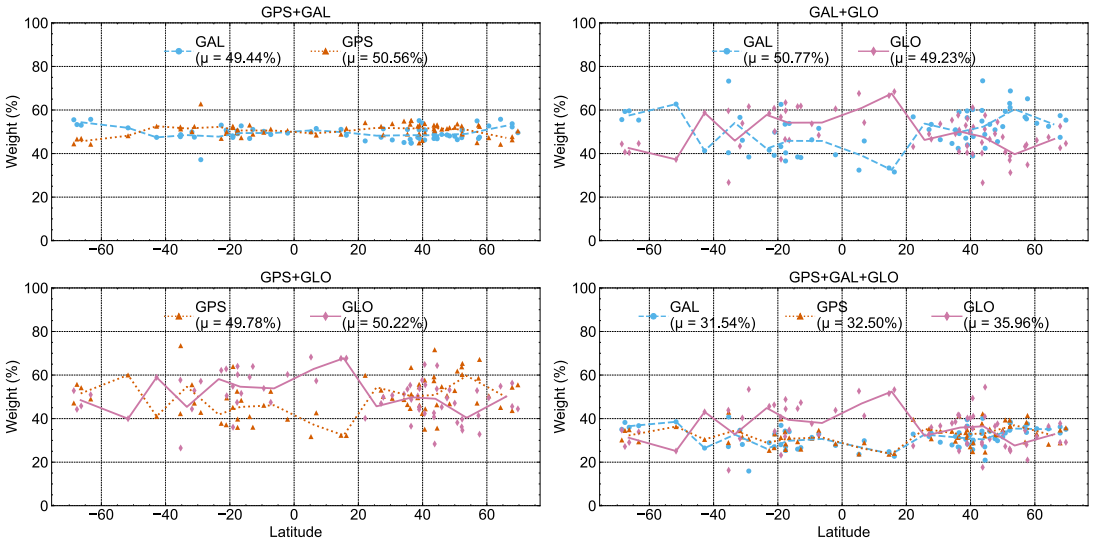

Figure 3.17: Optimal weights applied to each constellation for each multi-GNSS combination. Each marker represents the daily weights averaged for a station, and the μ value is the average over the station network.

Despite being generally close to the case where equal weighting is given to each constellation, we can see small differences between the constellation. The GLONASS observations tend to slightly dominate the GPS+GLONASS (50.22% for GLONASS) and GPS+Galileo+GLONASS (35% for GLONASS) combinations. As for the contribution of Galileo, it appears to be slightly smaller in the GPS+Galileo (49% for Galileo) and GPS+Galileo+GLONASS (31% for Galileo) combinations. The number of observation equations per constellation included in the NEQs is one of the factors that influence the determination of the optimal weights: the more observations, the larger the weight. This can explain the slightly larger weights given to the GLONASS constellation as the PPP processing involves both phase and code observations when the ambiguities are not fixed. This is the case for all GLONASS observations, although the latter is down weighted, whereas the Galileo observations were processed with ambiguity fixed to integers, meaning that only the phase observation equations are kept for the positioning.

More interestingly is the analysis of the geographical distribution of the weights according to the latitude of the station. We observe that there is a neat correlation between the optimal weights and station latitudes. GLONASS weights decrease at high latitudes in the GPS+GLONASS and Galileo+GLONASS combinations. By comparison, the weights of GPS and Galileo are constant with the latitudes in the GPS+Galileo combination. This suggests that GLONASS is less consistent than GPS or Galileo with the a priori OTL model at high latitudes, or that GLONASS observation of the OTL coefficient parameters are more sensitive to deviations of the a priori OTL model coefficients. The observation of the OTL coefficients may be facilitated for the high-latitude stations because of the larger number of GLONASS data. Indeed there are more GLONASS satellites visible from these stations due to the higher inclination of the plane of the constellation (65) compared to GPS (55) and Galileo (56).

We further compare the estimates of the OTL coefficients issued from each possible multi-GNSS combination. In the same way as done for single-constellation estimates, we analyze the distribution of the estimated amplitudes of the residual OTL displacement errors with the boxplots (solid bar) in Figure 3.18.

We analyze the OTL residual displacement model errors from the multi-GNSS combination with the optimal weights issued from the Helmert VCE algorithm. They show that the residual amplitudes of solar tides K1, K2, and S2 still contain systematic errors when GPS is involved in

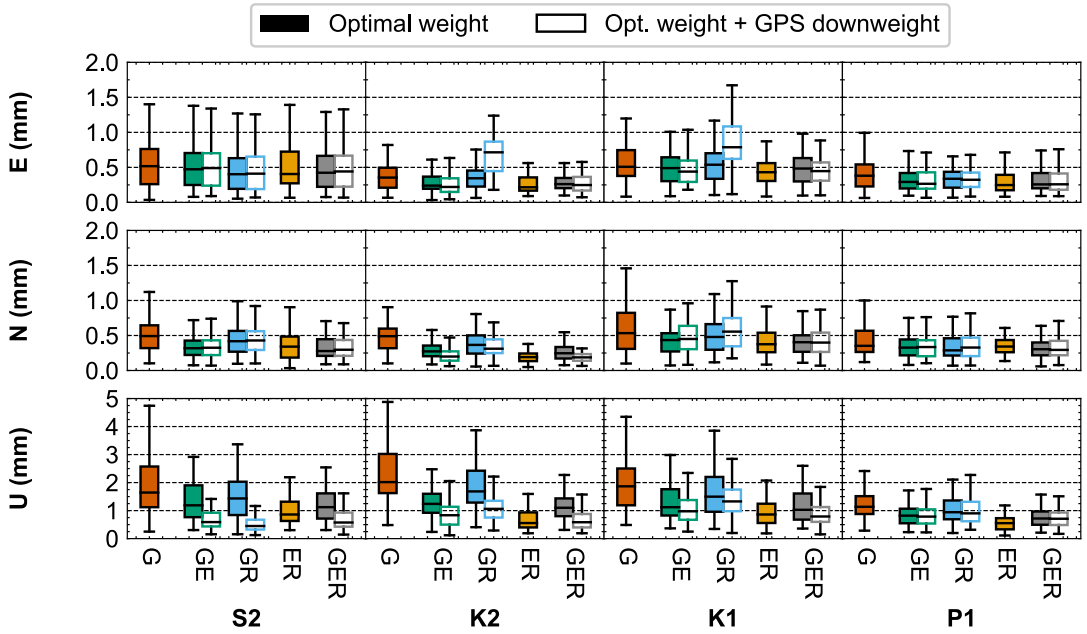

(a) Solar tides

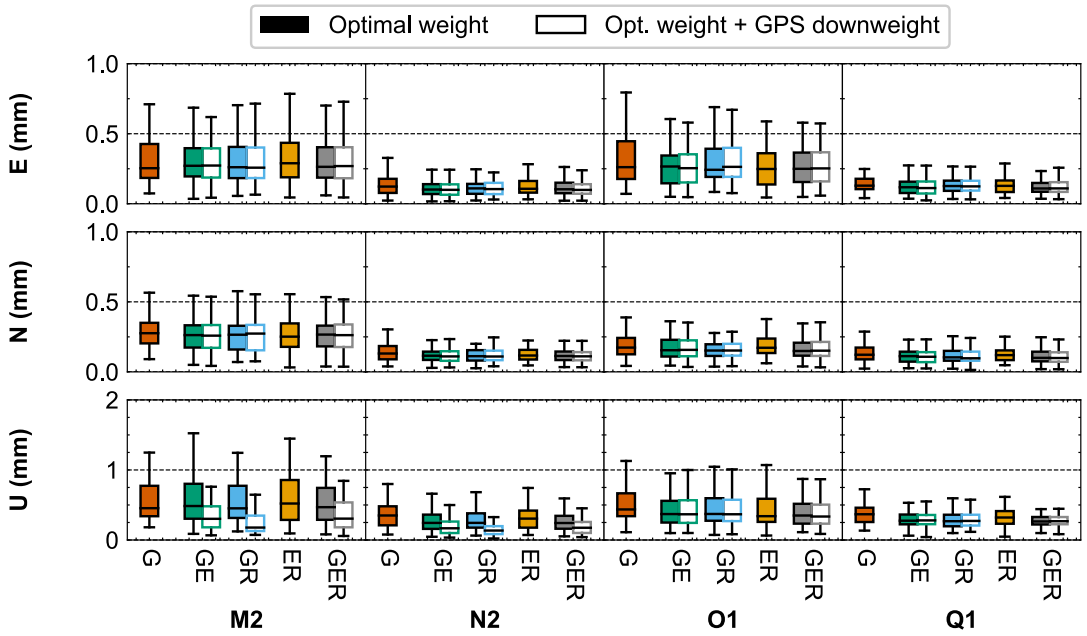

(b) Lunar tides

Figure 3.18: Amplitudes of residual displacements of the 8 major tides estimated by the combination of different GNSS constellations. The combination is performed using the optimal weighting (solid) or with additional down weighting of GPS for the K1 and K2 tides (hatch). Following the IGS naming, G stands for GPS, E for Galileo and R for GLONASS.

the combinations: GPS+Galileo (GE), GPS+GLONASS (GR) and GPS+Galileo+GLONASS (GRE). This is particularly visible in the vertical direction where the differences between the estimates with GPS (GE, GR, or GER) and the estimates with only Galileo and GLONASS (GR) are up to 1.5 mm (for the K2 tide). Using Galileo seems to have a larger impact on reducing the sensitivity of multi-GNSS estimation when comparing GE to GR solutions. The best agreement with the FES2014b OTL model is achieved when only Galileo and GLONASS observations are combined. Indeed, the differences between GNSS data and the model reach up to 0.5 mm horizontal and 1.1 mm vertical.

To reduce the impact of GPS systematic errors at the K1 and K2 frequencies and increase the consistency between the combinations with and without GPS, an alternative solution was explored. The NEQs are combined by either removing or reducing the weight of GPS observations for the tides K1 and K2. These tides are particularly impacted by GPS systematic errors because they exactly correspond to the frequencies of GPS orbital and constellation repeat. The hatched bars in Figure 3.18 show the distribution of the amplitudes of the OTL residuals obtained by combining constellations using this tide-specific weighting approach for GPS. For the height, there is a significant improvement in the consistency with Galileo+GLONASS (GR) estimates not only for the K1 and K2 tides but also for the S2 tide, even is the down-weighting of the NEQ did not account for this tide. This demonstrates the impact of GPS systematic errors on the frequencies adjacent to K1 and K2, for example due to the parameter correlations in the normal equations. Furthermore, we see with the down-weighting of GPS that GLONASS is not able to observe alone the tides K1 and K2 in the east direction. This agrees with the results already obtained with the GLONASS-only estimates (Figure 3.16) and the less precise solutions obtained when using float-valued ambiguities. This demonstrates the advantage of using Galileo in the combination. Indeed, the ambiguity can be solved for integers for Galileo observations and thus provide a more accurate the estimates for OTL errors in the east direction.

These results show that to obtain the most accurate and consistent estimation of residual OTL errors for solar tides, an optimal weighting strategy that depends on both the constellation and the tidal constituents is necessary. In contrast, the lunar tide constituents (M2, N2, O1, and Q1) are not significantly affected by the constellations involved or their relative weights in the multi-GNSS combination.

3.3.3 Discussions and conclusions on the assessed OTL errors of the FES2014b model

We used a "static" estimation strategy based on NEQ stacking to estimate OTL residual errors along with standard PPP parameters, including station positions and tropospheric parameters. We then compared our results to those obtained using the kinematic approach. Our findings show that the estimated errors from both methods are consistent within their formal uncertainties. However, when using the kinematic approach, we found that the sub-daily positions were still significantly correlated with other PPP parameters, particularly the troposphere bias, while in the static approach, the errors from the troposphere and the OTL models can be distinguished. In King (2006), the remaining correlation between the estimated OTL parameters is shown when the estimated OTL model errors were combined at the parameter level. Such correlation is reduced in our implementation of the static approach as we stacked the observations over a period that enables to separate each OTL parameters, rather than combining the estimates, with possibly their systematic errors. In our study, we managed to separate and estimate the modeling error for the 8 major subdiurnal tides. However, we did not consider the effects of the minor tides, which are determined from the major ones by admittance interpolation.

Using the three constellations currently available (GPS, GLONASS and Galileo) provides a more accurate evaluation of OTL displacement model errors. Indeed, the multi-GNSS estimation

allows distinguishing constellation-related systematic errors and OTL mismodeling. Table 3.4 summarizes the errors estimated during this study.

Table 3.4: Comparison of OTL residual errors for major tides using GPS-only and the GER combination using optimal weighting and additional down-weighting of GPS for K1 and K2 tides, presented as median and quartile (first and third) range (in mm). Larger errors in each direction are indicated in bold.

	East		North		Up	
Tide	G	GER	G	GER	G	GER
M2	0.25 [0.18-0.43]	0.27 [0.18-0.40]	0.28 [0.20-0.35]	0.26 [0.18-0.34]	0.45 [0.34-0.77]	0.31 [0.18-0.54]
N2	0.12 [0.08-0.18]	0.10 [0.07-0.14]	0.13 [0.09-0.18]	0.11 [0.08-0.14]	0.35 [0.21-0.48]	0.17 [0.10-0.26]
O1	0.26 [0.18-0.45]	0.25 [0.16-0.37]	0.17 [0.13-0.24]	0.15 [0.11-0.21]	0.44 [0.34-0.67]	0.34 [0.23-0.50]
Q1	0.13 [0.10-0.18]	0.11 [0.08-0.15]	0.12 [0.09-0.17]	0.10 [0.07-0.14]	0.37 [0.26-0.46]	0.27 [0.22-0.33]
S2	0.52 [0.26-0.76]	0.44 [0.22-0.67]	0.49 [0.32-0.65]	0.30 [0.21-0.44]	1.64 [1.12-2.57]	0.58 [0.43-0.93]
K2	0.35 [0.21-0.49]	0.25 [0.17-0.36]	0.49 [0.32-0.60]	0.19 [0.14-0.23]	2.02 [1.62-3.02]	0.59 [0.40-0.88]
K1	0.51 [0.38-0.75]	**0.45 [0.31-0.57]**	0.53 [0.31-0.82]	**0.40 [0.26-0.54]**	1.87 [1.19-2.50]	**0.79 [0.60-1.13]**
P1	0.38 [0.23-0.54]	0.26 [0.18-0.41]	0.35 [0.26-0.57]	0.29 [0.22-0.42]	1.14 [0.88-1.52]	0.71 [0.49-0.93]

Based on the global stations tested in this study, and multi-GNSS observations, the lower consistency (or largest errors) with respect to the FES2014b model is 1.13 mm (for the height direction and the K1 lines). The estimated agreement between the model and the multi-GNSS data increases by 33 to 55% when using Galileo and/or GLONASS, compared to using only GPS, which is the current standard. This is especially true for the solar tides: K1, K2, S2 and P1. Our results are consistent with recent publications showing that using GLONASS (Abbaszadeh et al., 2020; Matviichuk et al., 2020) or a combination of GLONASS, Galileo, and BeiDou (Wei et al., 2021) can lead to similar reductions in residual amplitudes for certain tidal constituents compared to using GPS alone. Additionally, we found that Galileo performs even better than GLONASS in the east direction because it allows for the resolution of integer-valued ambiguities, which is not commonly done with GLONASS observations.

This work opens new perspectives for the assessment of other tidal loading errors that affects GNSS station positions, including those for solid Earth, atmosphere, and ocean pole tides, which have been shown to produce seasonal signals according to previous studies (Li et al., 2018; Niu et al., 2021; Tregoning and Watson, 2009; Watson et al., 2006).

CHAPTER

4 Propagation of tidal displacements modeling errors and impact on the GNSS coordinates time series

We investigate in this chapter the propagation or aliasing to longer periods of the OTL displacement model errors occurring for the subdiurnal tides. A theoretical model for the propagation of subdiurnal station displacement perturbations was developed and validated based on the GPS data. We first analyze the validity of this model for Galileo and GLONASS data. In the second part of the study, we will examine these aliased signals in real GNSS time series, caused by errors in the OTL displacement model. We will use the coordinates issued of the static estimation strategy presented in Chapter 3. These coordinates are thus corrected for the OTL model errors. The results of the second section of this chapter have been published in Ait-Lakbir et al. (2023a).

4.1 Theoretical model of subdiurnal signal propagation

Stewart et al. (2005) developed an analytical model to explain the propagation of subdiurnal periodic positioning errors into longer periodic signals related to the orbital characteristics of the GPS constellations. Equation 4.1 gives the apparent long-periodic site displacements for a sub-diurnal perturbation of angular frequencies ω_P.

$$
\begin{aligned}
\Delta y(t) = k_1^{-1} & \left[1 + k_2 \sin(\omega_S t + \frac{\omega_S \Delta T}{2}) + k_3 \cos(2\omega_S t + \omega_S \Delta T)\right]^{-1} \\
& \cdot \Big[q_1 \sin(\omega_P t + f_1) \\
& + q_2 \sin((\omega_P - 2\omega_S)t + f_2) + q_3 \sin((2\omega_S + \omega_P)t + f_3) \\
& + q_4 \cos((\omega_P - \omega_S)t + f_4) + q_5 \cos((\omega_P + \omega_S)t + f_5) \\
& + q_6 \sin(\omega_S t + f_6) \\
& + q_7 \cos(2\omega_P t + f_7) \\
& + q_8 \sin((2\omega_P + \omega_S)t + f_8) + q_9 \sin((2\omega_P - \omega_S)t + f_9) \\
& + q_{10}\Big]
\end{aligned}
\tag{4.1}
$$

with

- ω_S the orbital frequency of the constellation
- ω_P the frequency of the perturbing site displacement
- ΔT the length of the observation window (typically 24 hours for GNSS processing)
- (q_i, f_i) the amplitude and phase of the propagated signal, and (k_1, k_2, k_3) a triplet of reals. We refer the reader to Stewart et al. (2005) for the expression of these terms which depends

on the amplitude y_P and frequency ω_P of the perturbing site displacement and the orbital frequency of the constellation ω_S.

Figure 4.1 give the theoretical admittance and frequencies for the propagated signals for a selection of tides that are more likely to introduce errors while processing GNSS data:

- M2 and O1 that are two of the larger corrections
- K1 and K2 which coincide with the GPS orbital characteristics
- S1 (not included in the OTL models) and S2 (included in the OTL models) that are affected by ocean and atmosphere tides

The propagation model has been validated with simulated GPS data and positioning (Penna and Stewart, 2003) as well as with real GPS data (Penna et al., 2007). More recently, the prediction for GLONASS has been validated with real datasets in Abraha et al. (2018). Nevertheless, the predictions for Galileo (or BeiDou) have not been performed yet.

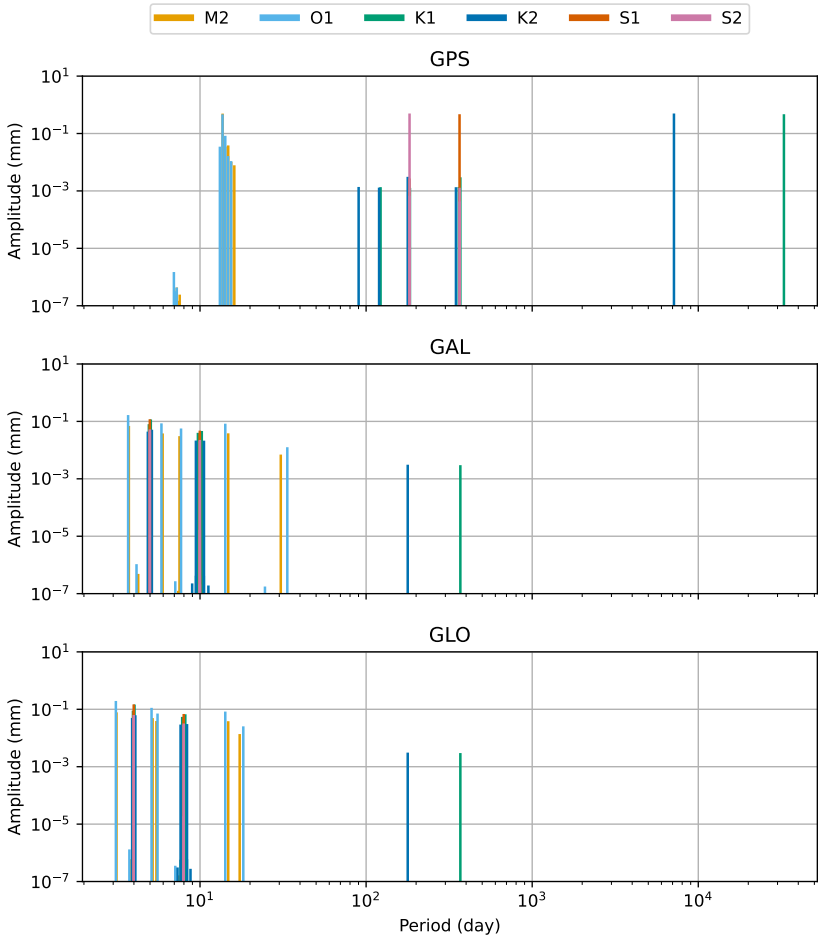

Figure 4.1: Admittance (amplitude for a 1 mm input error) and periods (in days) of propagated subdiurnal signals for the GPS (top), Galileo (middle) and GLONASS (bottom) constellations

4.1.1 Analysis of the propagation model for Galileo and GLONASS

4.1.1.1 Verification of the assumption for the Galileo and GLONASS constellation

One of the assumptions made in the afore described propagation model is that the denominator in Equation 4.1 (term in red) is always equal to one. This holds in the case of the GPS constellation, but was not discussed for GLONASS in Abraha et al. (2018). Indeed, with different orbital and constellation characteristics, this assumption is not necessarily true for GLONASS or Galileo, or if the observation window ΔT is not 24 hours.

We first computed the values of the denominator based on Equation 4.1 with the orbital characteristics of the GPS, Galileo and GLONASS satellites (Figure 4.2) assuming that the perturbing site displacement (amplitude and frequency) is the same for the three constellation. While, for GPS, the terms (k_2, k_3) are sufficiently small for this term to stay close to 1, the model gives different results for Galileo and GLONASS. We observe a modulation, depending on the constellation repeat period of 10 days for Galileo and 8 days for GLONASS, that will lead to an amplitude modulation of the long-period propagated signals. Moreover, we can focus on the average power that the propagated signal will convey via the RMS of the signal, given by the horizontal line in Figure 4.2.

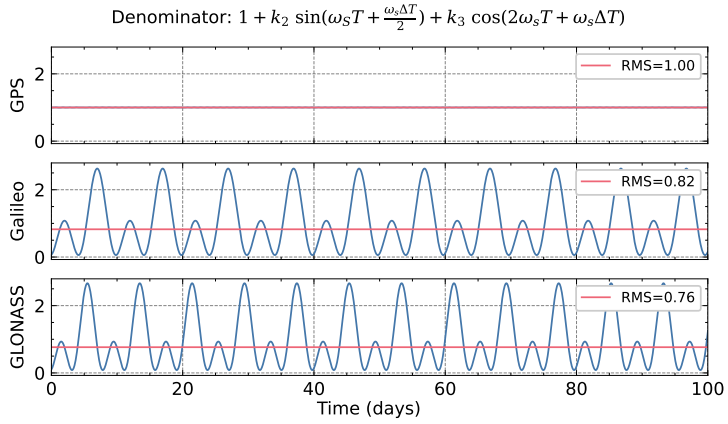

Figure 4.2: Verification of the denominator assumption for GPS, Galileo, and GLONASS

It must be mentioned that this result also shows the model leads to local singularities for Galileo and GLONASS. These happen when the value of the denominator gets closer to 0, meaning that the propagated signal should be amplified to infinity. As this is not physically possible, this shows a limitation in this propagation model. To overcome this difficulty, I decided to analyze the mean variability of the signal in the denominator term with its RMS (red line in Figure 4.2). In the case of GPS, we come to the hypothesis made in (Stewart et al., 2005). In the case of Galileo and GLONASS, there is an overall amplification by a factor of $1/0.82 \approx 1.21$ for Galileo and $1/0.76 \approx 1.31$ for GLONASS of the propagated signal, compared to GPS.

Therefore we conclude that the propagation model by Stewart et al. (2005) only works for GPS data, and not for Galileo nor GLONASS, despite having been used in the literature.

4.1.1.2 Predicted and observed spectra of the subdiurnal error propagation: cases of the 14.19-day and 14.79-day signals

In the daily GNSS position time series, the stronger signals attributed to the propagation of OTL model errors occur at fortnightly periods: 13.6, 14.19 and 14.79 days (Penna and Stewart, 2003). The 14.19- and 14.79-day signals correspond respectively to errors in the O1 and M2 tides and are induced by the aliasing of the subdiurnal errors by the 24-hour observation window. These signals are commonly observed in GPS-only and GLONASS-only positions (Abraha et al., 2018). As for the 13.6-day signal, it is caused by errors in the M2 or O1 tides and results from the combination of the aliasing by the 24-hour window and the orbital characteristics of the GPS constellation. In addition, the 13.6-day signal may also be induced by modeling error of the long-periodic tide Mf, which happens at 13.66 days. Using only GPS data cannot then discriminate the origin of the 13.6-day signal. These are the reasons for focusing on the fortnightly spectral band.

Using the whole form of Equation 4.1, without applying the assumption that the denominator is 1 for Galileo and GLONASS and accounting for the modulation induced by the denominator instead, we computed the theoretical spectra of the propagated signals for errors in the O1 tide (Figure 4.3a) and in the M2 tide (Figure 4.3b). They are given in admittance, the amplitude fraction of the input error transferred to the propagated signal.

We can compare these predictions with the observed error propagation in the spectra of the positions determined with real GPS or Galileo data and orbits. For that, we test to introduce a synthetic error that can be significantly observed above the level of noise in the spectra. Based on the PPP configuration described in Table 3.2, we have introduced an error of 10 cm in the OTL ENU displacement model corrections, separately for each tide (M2 and O1). The daily PPP solutions are then computed with GINS. We do this using GPS-, Galileo- and GLONASS-only data. The normalized spectra of the estimated coordinates are given in Figure 4.4 for the error introduced in the O1 tide and Figure 4.5 for the error introduced in the M2 tide.

As predicted by the propagation model (Equation 4.1) and visible in the theoretical spectra of the propagated signal (Figures 4.3a and 4.3b), additional peaks at higher frequencies appear for Galileo and GLONASS compared to the error propagation with the GPS constellation, although the frequencies do not exactly coincide.

The model for the propagation of errors in O1, shown in Figure 4.3a, does not agree as well as for the propagation of the M2 errors in PPP position (Figure 4.4). For Galileo, only the peaks at $\sim$ 33 days are visible. The peaks near 9 days do not match with the nearest predicted peaks (7.68 days). Besides, the propagation in the 14-day band is a wider band ranging between 12 and 16 days. For GLONASS, the prediction from the model and the spectra resulting from the introduction of synthetic errors in the OTL displacement model agree together for the peaks at $\sim$ 5.04 days and at $\sim$ 18 days. Still, the peak at approximately 11 days is not explained by the propagation model. Similarly to M2, the predicted peaks at higher frequencies are not visible.

The predicted signals in Figure 4.3b and the observed signals in Figure 4.5 coincide for the propagation of the M2 errors near 31 days in the three direction, for Galileo-only positions. But we also observed peaks between 8 and 9 days in the PPP positions that seem not to agree with the predicted frequency of 7.5 days. Moreover, the peaks at higher frequencies (below 6 days) are not visible at all. As for GLONASS, we can see the predicted peaks at $\sim$ 2.23 days (in the up and east directions), at $\sim$ 3.1 days (in up) and at $\sim$ 5.04 days (in east, north and up).

In accordance with the propagation model and the previous observations made for GLONASS in Abraha et al. (2018), we find more complex propagation spectra for Galileo and GLONASS. However, we found differences in the frequencies between the theoretical and observed signals, which could be explained by the length of the time series (3 years). Indeed, it prevents us to reach sufficient spectral resolution to properly observe nearby peaks. Perhaps, more stations would also be beneficial to reduce the background noise and facilitate the detection of the smallest peaks, whose periods are below 5 days.

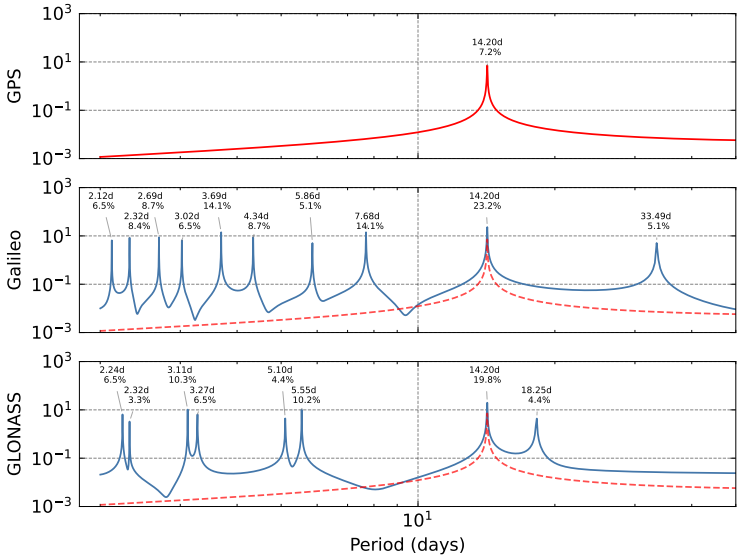

(a) 14.19-day signals (O1 aliasing)

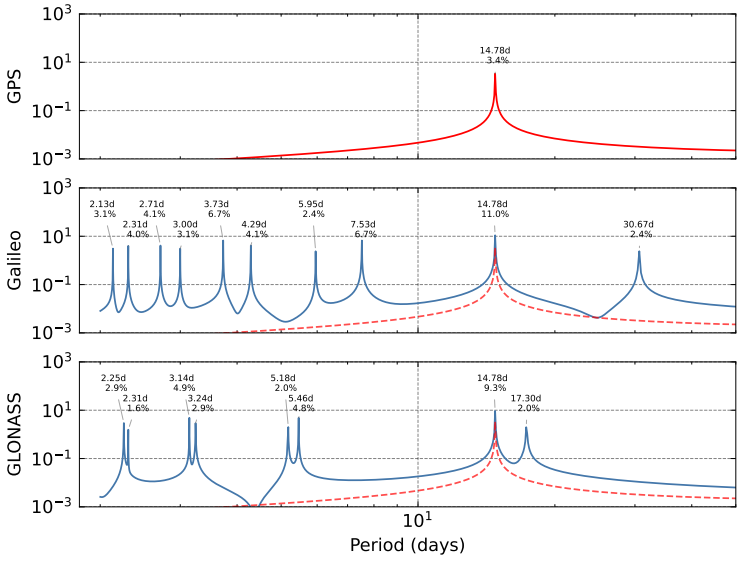

(b) 14.79-day signals (M2 aliasing)

Figure 4.3: Amplitude spectra of the theoretical output daily coordinates time series with a systematic input error of 1 mm. Note that the vertical axis is equivalent to the admittance in the amplitude of the propagated error signal. The red curves are the propagated signal for GPS, while blue curves are for Galileo (middle panel) and GLONASS (bottom panel).

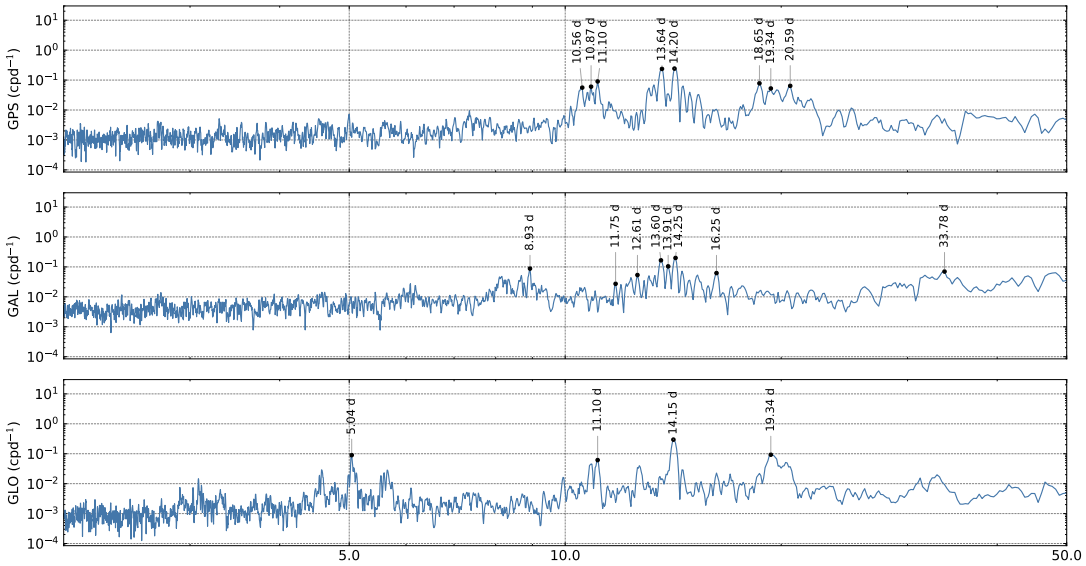

(a) East

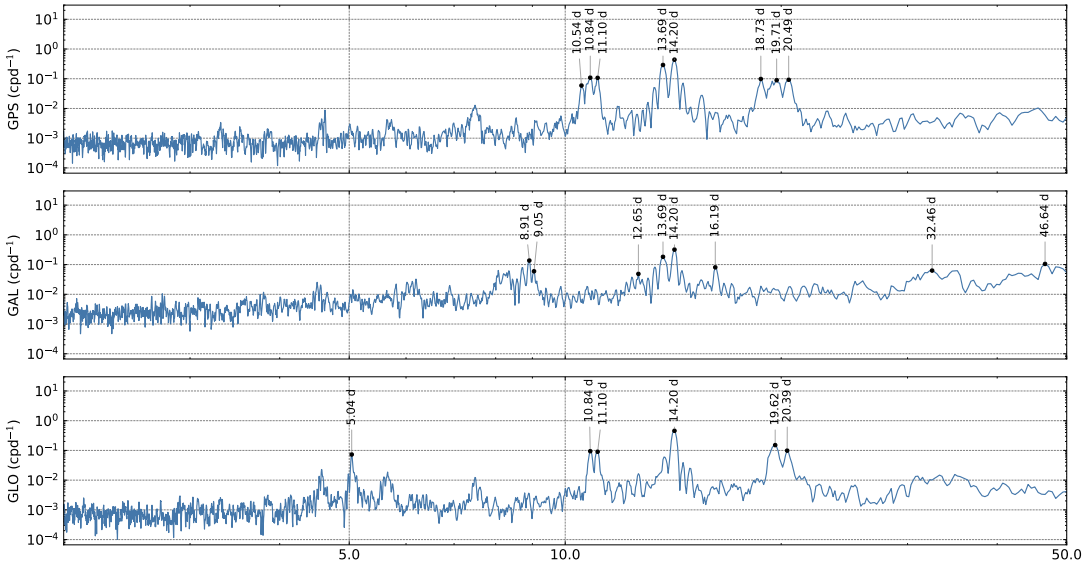

(b) North

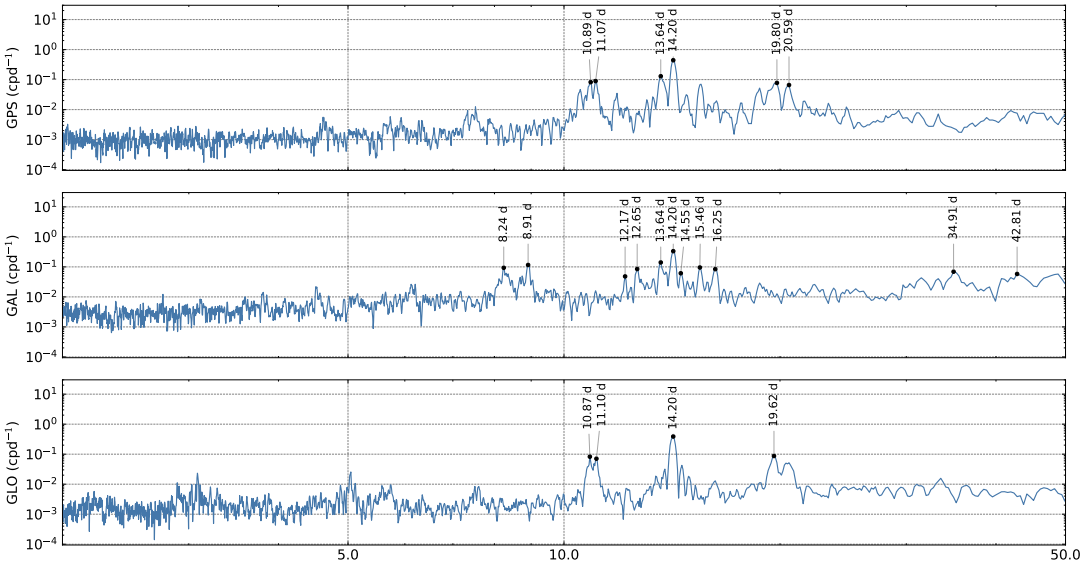

(c) Up

Figure 4.4: Normalized power spectra of the estimated daily east position time series given a 10-cm error in the O1 tides, aliased at 14.19-day frequency. The X-axis represents the periods (in days).

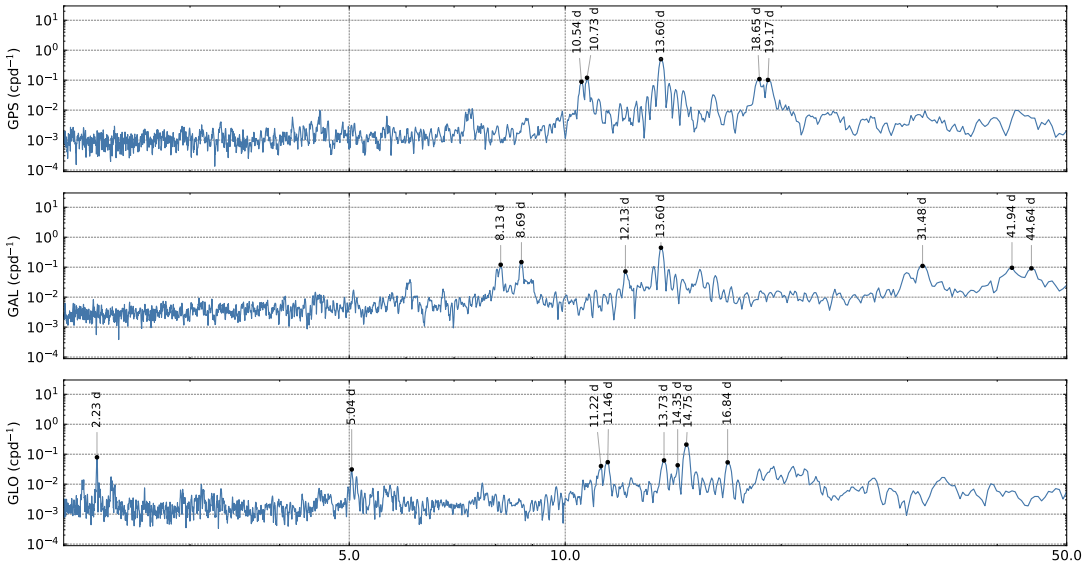

(a) East

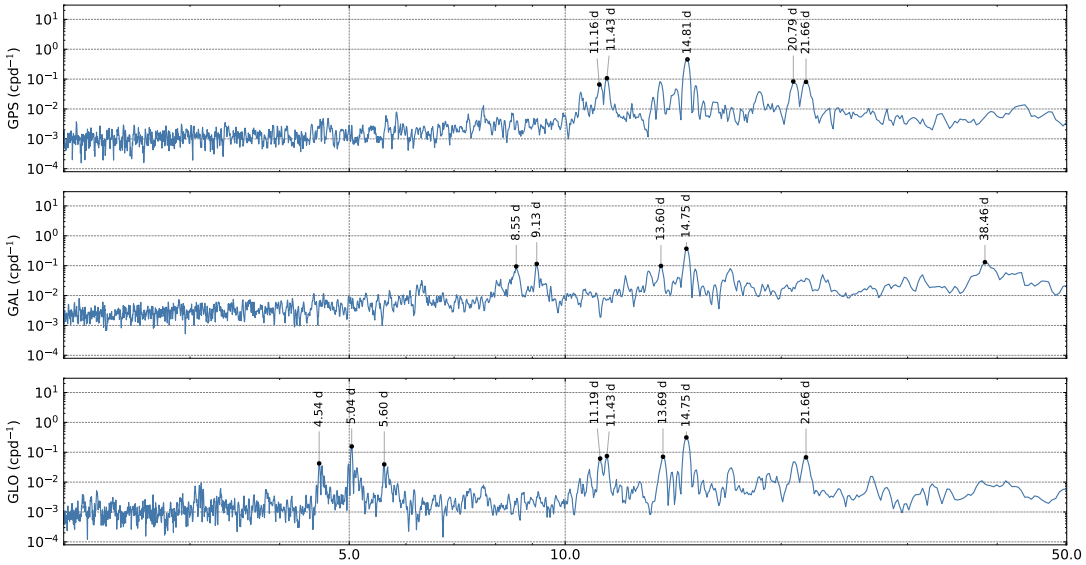

(b) North

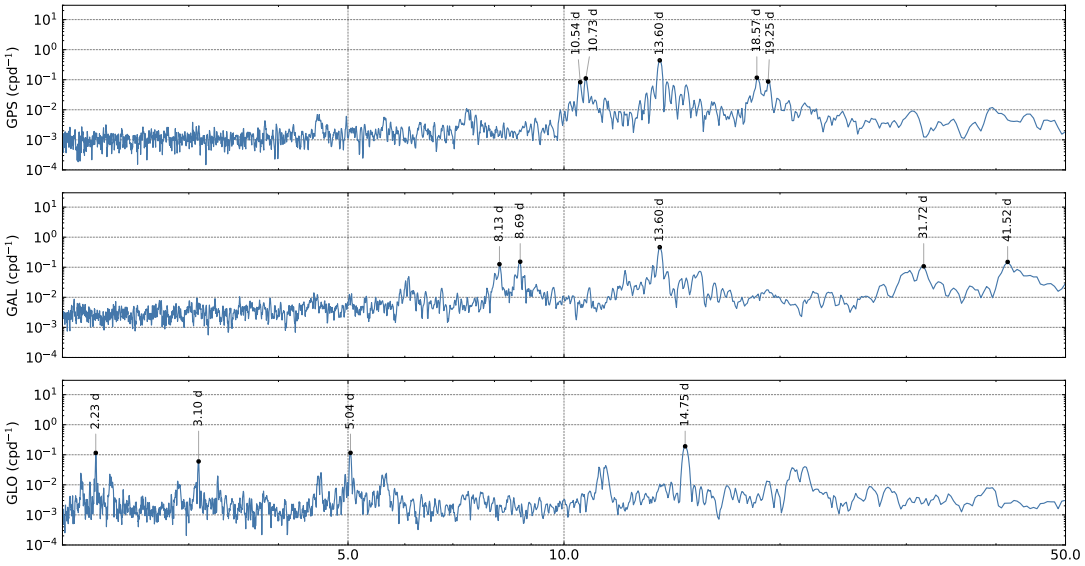

(c) Up

Figure 4.5: Normalized power spectra of the estimated daily east position time series given a 10-cm error in the M2 tides, aliased at 14.79-day frequency. The X-axis represents the periods (in days).

4.1.2 Discussion about the effects of the observation window ΔT

The mechanism of propagation is not only influenced by the orbital characteristics of the constellation but also by the length of the observation window ΔT on which the station positions are assumed constant (Equation 4.1). The processing of GNSS data is commonly performed on a 24-hour basis. However, changing this parameter may be a way to reduce the aliased signals in the position time series.

Based on the same propagation model (Stewart et al., 2005), we computed the frequencies and amplitude of the propagated signal for the three constellations (GPS, GLONASS and Galileo) but making the values of the parameter ΔT varying from 1 hour to 4 days. We only kept the aliased signal when the admittance of the aliased signals, that is the amount of the input error propagated, is above 1%. We summarize the resulting spectra by the range of frequencies of the propagated signal in Figure 4.6a for GPS, Figure 4.6b for Galileo and Figure 4.6c for GLONASS. In these figures, the horizontal axis represents the periods of the propagated signals while the vertical axis represents the length of the observation window ΔT.

We observe that, when the observation window length is larger than the usual 24-hour window, it is possible to deplace the impact of propagated signals on lower frequencies (longer periods than 10 days). However, the errors in the K1 and K2 frequencies are still propagated up to the semi-annual and annual frequencies for GPS regardless of the length of the processing batch. In comparison, there is no propagation at periods above 100 days with the Galileo and GLONASS constellations. As for the fortnightly spectral band, we can see potential propagated signal coming from all the tides tested, in particular for the M2 and O1 tides. Thus, the use of Galileo could help to separate geophysical annual/semi-annual signals, but introduce spurious signal in the higher frequencies. As for the fortnightly band, it remains contaminated by aliased signals regardless of the constellation, and the length of the observation window.

In summary, this analysis of the propagation model suggests two options to mitigate these signatures. First, processing the GNSS data on larger arcs may result in attenuated signatures in high frequencies, and in a limited impact on the annual and semi-annual band. However, the possibility to increase the arc in standard PPP processing is limited in practice because most of the orbit products generated by IGS analysis centers are on a 24-hour basis. Some analysis centers do compute solutions on longer windows (e.g. 30 hours for GRGS or JPL, 3 days for CODE (Dach et al., 2021)). But no significant differences in annual or semi-annual propagated signals have been observed in the position time series yet (Rebischung et al., 2021). Note that the contribution of the tidal error propagation in the error budget of these two signals cannot be as important as the contribution of other factors such as unmodeled non-tidal loading deformations, orbital errors or multipath among others.

Another way to reduce errors in the subdiurnal displacement is to assess and/or decrease the inconsistency between the GNSS observations and predicted OTL displacement model. This can be done by improving the computation of predicted OTL displacements or by adding empirical parameters to correct model errors when calculating daily station coordinates. This is the second solution that will be investigated in Section 4.2

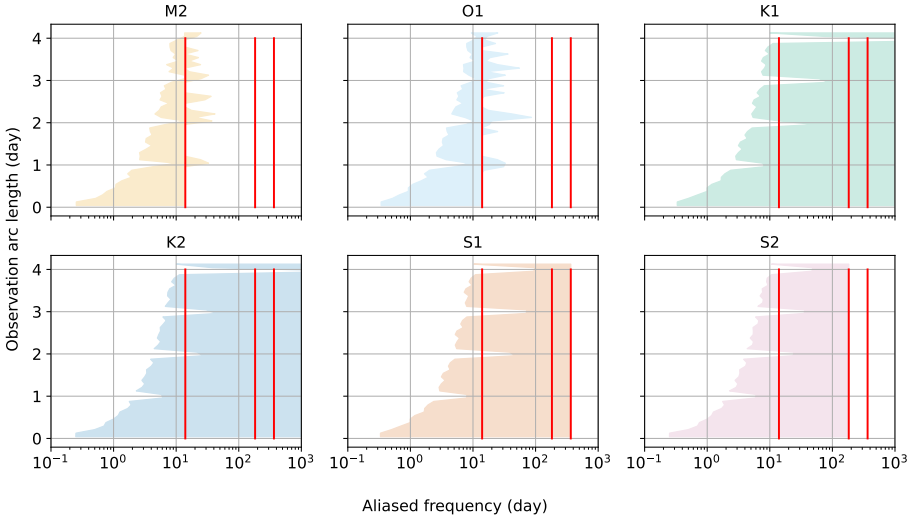

(a) GPS

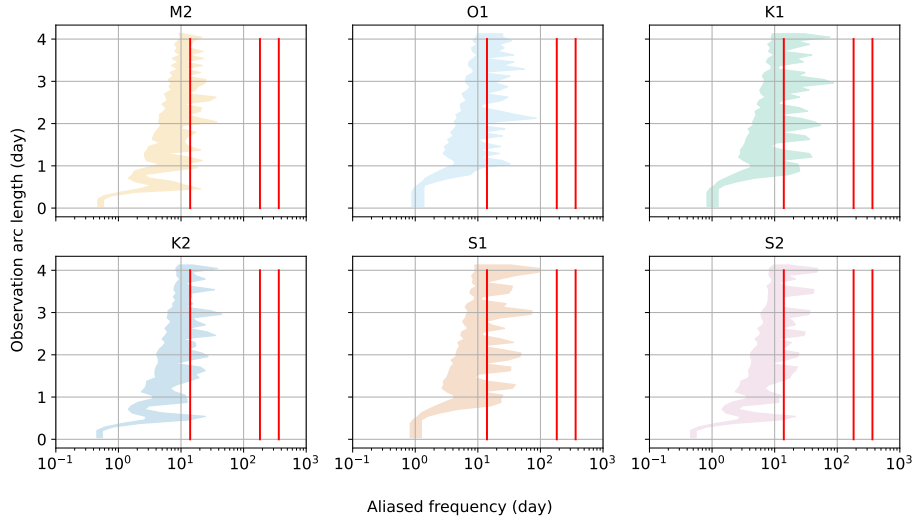

(b) Galileo

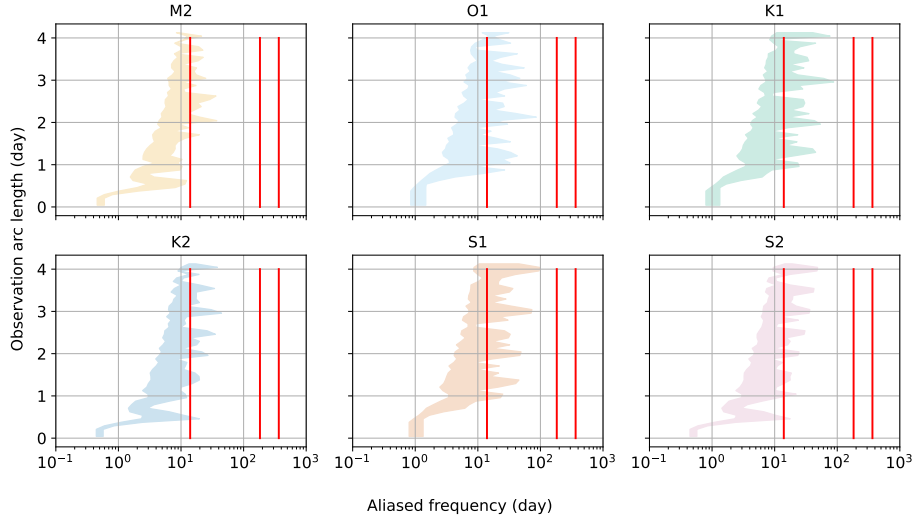

(c) GLONASS

Figure 4.6: Minimal and maximal periods of propagated signals with different lengths of observation windows. Only the propagated signals with admittance above 1% have been represented. The vertical lines are drawn at the 13.6-day, semi-annual (182.5 days) and annual (365 days) frequencies.

4.2 Analysis of the spurious propagated signals in real GNSS positions

The objective now is to confront the OTL-related propagated signals predicted by the model that we analyzed in the previous section, and the spurious signals observed in the daily GNSS position time series determined with real GNSS data. In Chapter 3, we introduced the static estimation strategy that we used to assess the OTL displacement model errors. This simultaneous adjustment of the OTL model coefficients with GNSS data alongside the determination of the station coordinates makes it possible to obtain time series corrected for the residual tidal signals. We want now to compare the propagated signals in the GNSS position time series issued from the static OTL estimation to the positions determined with the nominal OTL model computed with FES2014b.

For the same network of stations used in Chapter 3 (see Figure 3.3), we computed daily PPP positions with GPS, Galileo and GLONASS data between January 2019 and December 2021. We used the same configuration as for the static estimation described in Table 3.2, with and without estimating the OTL coefficients. In addition to compute single-constellation solutions, we also analyzed the positions estimated with multi-constellation observations. In the following, we will show and discuss the results for the height coordinate, but the conclusions are the same for the horizontal coordinates (see Appendix B).

4.2.1 Propagation of OTL model errors

To isolate the effects of the OTL coefficient estimation, we compare the spectra of the coordinate differences with and without the additional parameters. Figure 4.7 shows the averaged spectra of the coordinate differences for each constellation.

All common errors in both series of positions, in particular errors in the Mf tides that are not re-estimated, will cancel out, which leaves only the effects of the propagated subdiurnal tidal errors. We found the aliasing peaks at the fortnightly frequencies predicted by the propagation model (Stewart et al., 2005).

Up to now, the origin of the peaks at 13.6 days in GPS positions was unclear despite previous work (Abraha et al., 2018). Indeed, by using GPS and GLONASS data and the kinematic estimation approach, previous studies attributed them to both OTL model errors in the Mf tide or from the propagation of errors in the M2 and O1 tides. Our results confirm that these signals are caused by the aliasing of errors in the O1 or M2 tides specifically when we use only the GPS constellation. However, with Galileo and GLONASS, we do not find any peak at this 13.6-day frequency.

For the three constellations, we also identify in Figure 4.7 the 14.19-day peaks. These signals correspond to the common propagation of the O1 tide error due to the assumption that the coordinate is constant over 24 hours made during the data processing. As for the power of the propagated signal, we can also see the peak is larger for Galileo than for GPS, as we predicted in the analysis of the model (Section 4.1.1). No significant difference is visible between GLONASS and GPS. As for the signal at 14.79 days, corresponding to the propagation of the M2 tide error, a faint peak at is perceptible only for GLONASS. But with a transferred admittance in the amplitude of 3.5 % common to all constellations (see Table 4.1), these signals for GPS and Galileo could be below the noise level.

Table 4.1: Period (in days) and admittance in amplitude (percent) of the first largest spurious signals for GPS, Galileo and GLONASS computed from the expressions developed in Stewart et al. (2005)).

Each row corresponds to a term in Equation 4.1.

GPS		Galileo		GLONASS	
O1	M2	O1	M2	O1	M2
13.662 / 42.1	13.678 / 44.6	3.690 / 15.0	3.729 / 6.3	3.114 / 17.6	3.142 / 7.1
14.193 / 7.5	14.786 / 3.5	5.857 / 7.7	14.786 / 3.5	5.107 / 10.2	5.182 / 4.5
13.169 / 3.1	14.210 / 3.2	14.193 / 7.5	5.956 / 3.4	14.193 / 7.5	5.463 / 3.5
14.766 / 1.5	15.409 / 0.9	7.687 / 5.1	7.524 / 2.8	5.549 / 6.4	14.786 / 3.5
15.389 / 1.0	16.088 / 0.7	33.541 / 1.1	30.636 / 0.6	18.221 / 2.3	17.328 / 1.2

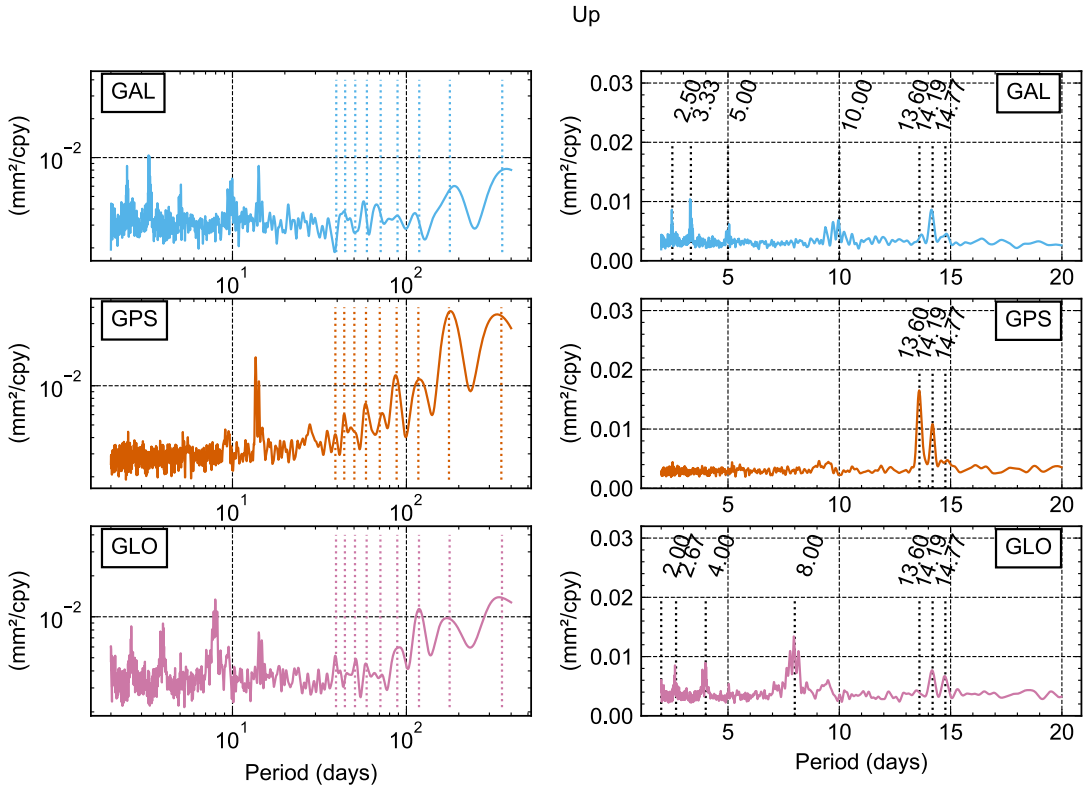

Figure 4.7: Spectral analysis of differences in up coordinates determined with nominal and estimated OTL coefficients. Normalized power spectra have been averaged over the network. The left panel shows the full spectral domain, with the constellation draconitic frequencies and their harmonics indicated by vertical dashed lines. The right panel provides a closer look at the shorter-period band, with vertical dashed lines representing the propagated signal periods (approximately 13.6, 14.19, and 14.77 solar days) and the harmonics of the ground track repeat periods.

4.2.2 Propagation of orbital errors

For Galileo and GLONASS coordinates, we also notice in Figure 4.7 additional errors at the harmonics of the ground track repeat period (10 sidereal days for Galileo and 8 sidereal days for GLONASS). The maximal amplitude is reached for the 8-day harmonic for GLONASS and for the 3.33-day harmonic for Galileo. For the first harmonics near 8 and 10 days, the signals take the shape of wide combs for both constellations. They suggest that the frequency of these peaks may not be constant over the entire time span we considered. Orbital errors can reasonably be the cause of these peaks. Indeed, the annual NEQs stacking used for the static OTL model error estimation (see Chapter 3) does not provide a sufficient spectral resolution to correctly

separate errors at the orbital and tidal frequencies. For example, the Q1 tides at 1.1195 cpd and N2 tides at 0.5274 cpd cannot be separated from the 9th and 19th harmonics of Galileo constellation repeat period, which have values of 1.1111 cpd and 0.5263 cpd, respectively. These peaks decrease distinctively in the spectra of the coordinates computed with the re-estimation of the OTL coefficients (Figure 4.10a).

In addition to reducing peaks at orbital frequencies, the adjustment of the OTL model coefficients also affects the spectra at the harmonics of the draconitic and solar annual frequencies (Figure 4.7). The larger impact occurs for GPS draconitic peaks that can partly be attributed to the propagation of errors at K1, K2 and S2 tide frequencies (Figure 4.8). These errors can originate from the OTL model or from orbital errors. In contrast, the low frequencies in the Galileo or GLONASS spectra are less influenced by the OTL model errors.

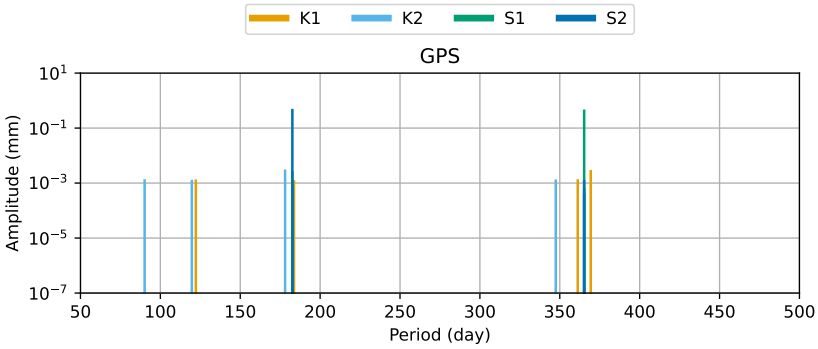

Figure 4.8: Aliasing signals of the K1, K2, S1 and S2 tides with the GPS constellation

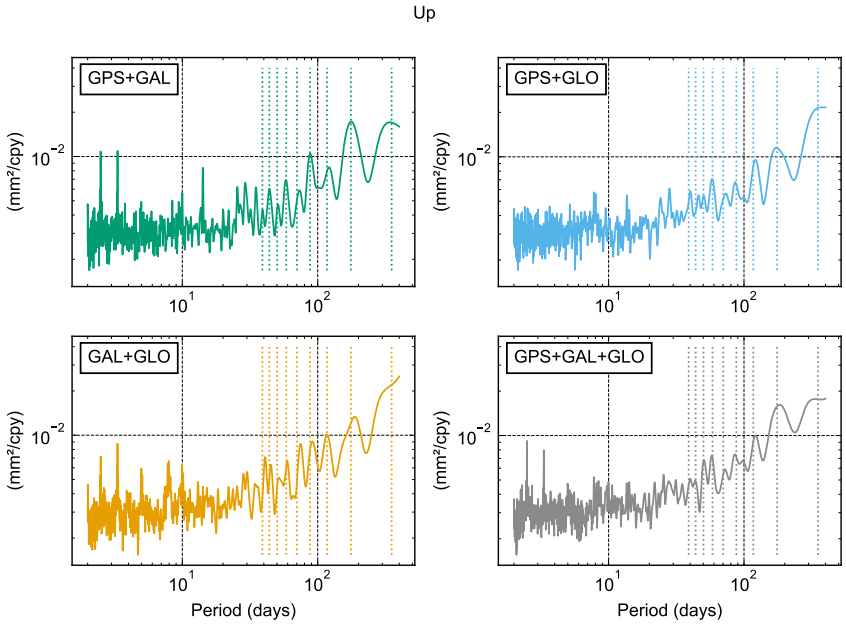

(a) Full spectral range. The vertical dashed lines represent the harmonics of the GPS draconitic year.

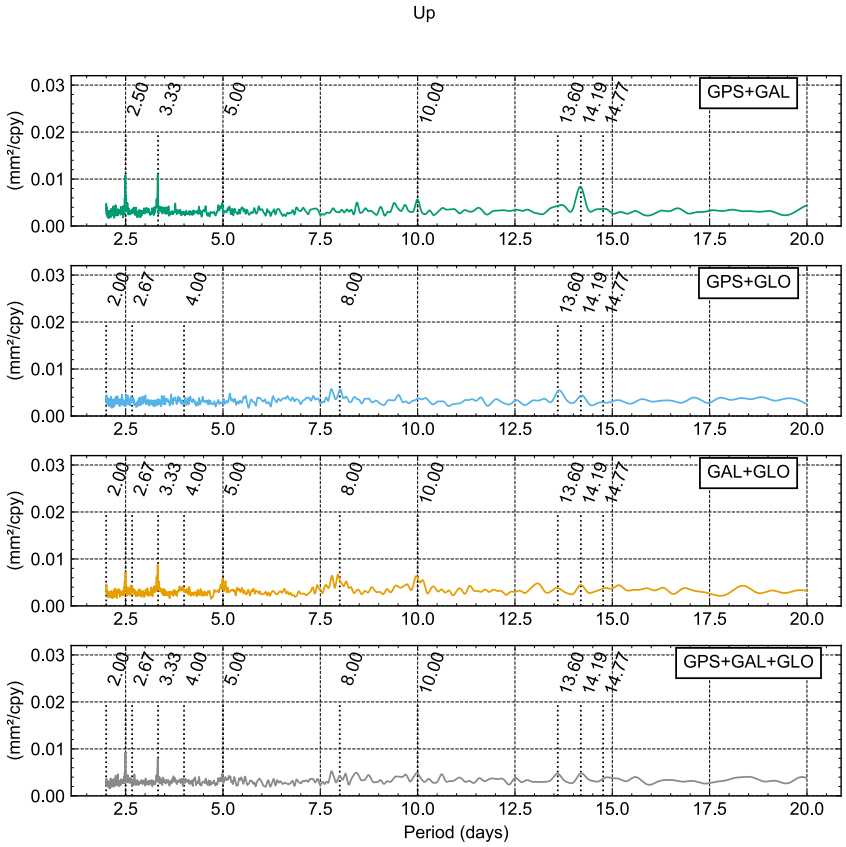

(b) Fortnightly frequencies. The dashed lines represent the frequencies (≈ 13.6, 14.19 and 14.77 days) of the propagated frequencies and the harmonics of the Galileo and GLONASS constellation repeat periods (in sidereal days).

Figure 4.9: Spectral analysis of differences in up coordinates determined with nominal and estimated OTL coefficients, and multi-GNSS solutions.

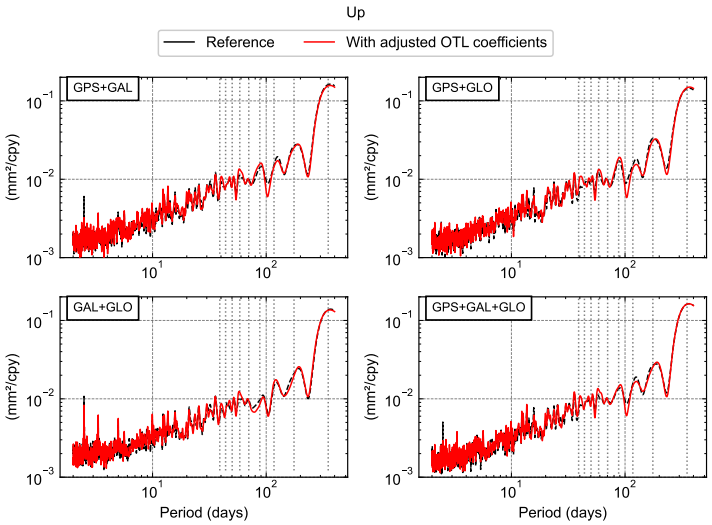

(a) Full spectral range. The vertical dashed lines represent the harmonics of the GPS draconitic year.

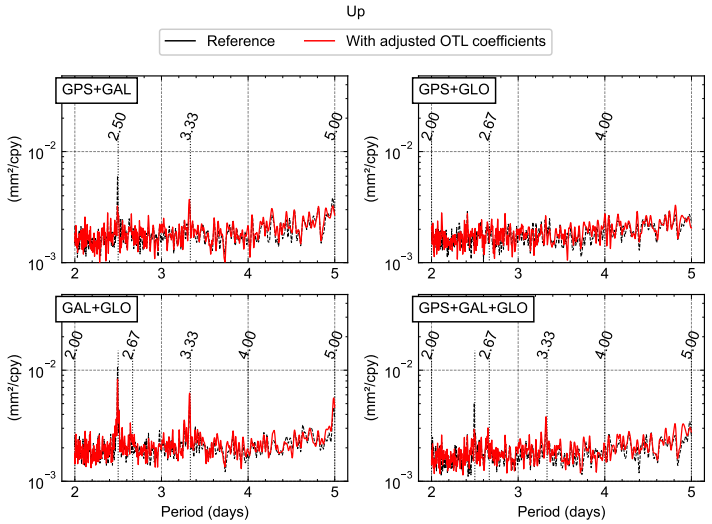

(b) Orbital frequencies. The dashed lines represent the harmonics of the Galileo and GLONASS constellation repeat periods (in sidereal days)

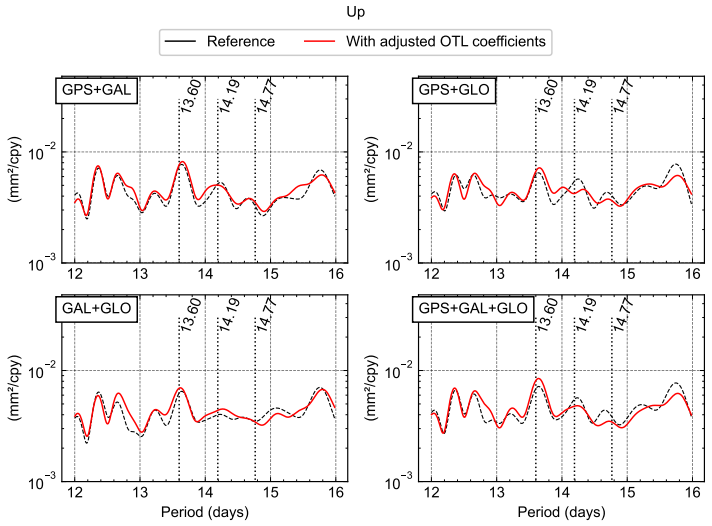

(c) Fortnightly and higher frequencies. The dashed lines represent the frequencies of the propagated tidal signals (≈ 13.6, 14.19 and 14.77 days)

Figure 4.10: Stacked normalized power spectra of the Up coordinates computed with the nominal (black line) and the OTL coefficients adjustment (red line).

4.2.3 Propagation in multi-GNSS position time series

The same analysis was performed with the multi-GNSS coordinates solutions. As shown in Figures 4.9a and 4.9b, the constellation-specific signatures superpose in the spectra of the coordinate differences obtained from multi-GNSS combinations. GPS is useful for reducing the errors specific to Galileo and GLONASS, except for the third (3.33 days) and fourth (2.5 days) harmonics of Galileo, which decrease only when all three constellations are involved in the solution. The signals at 13.6, 14.19, and 14.77 days appear when GPS data are used, and are absent from the Galileo+GLONASS combination. This indicates that the GPS observations' geometry is the primary source of these signals rather than GNSS processing itself. The fortnightly band remains largely unchanged when the Galileo+GLONASS combination is employed, even after adjusting the OTL coefficients. Thus, the O1 and M2 corrections obtained from the FES2014b loading model agree with the observations made by GLONASS and Galileo.

Furthermore, we directly compare the spectra of the coordinates themselves (Figures 4.10a and 4.10c). For each series, the Lomb-Scargle power periodogram of the coordinates is computed and normalized by the variance because the series with the nominal and adjusted OTL models are not expected to have the same variances. This allows evaluating the direct reduction of the aliased signals in the position series. The differences for the 13.6-, 14.19- and 14.79-day signals are significant. The peaks at the harmonics of 8 and 10 days decrease distinctively in the spectra of the coordinates computed with the re-estimation of the OTL coefficients (Figure 4.10b).

4.3 Discussion and conclusions

We aim in this chapter to assess and reduce the aliasing signals at fortnightly, semi-annual and annual periods caused by the subdiurnal errors in the OTL displacement model.

First, we have analyzed the propagation model proposed by Stewart et al. (2005) to predict and understand the mechanism behind the aliasing of subdiurnal positioning errors in the daily GNSS position time series. We test the model in the case of Galileo and GLONASS. In particular, we found that the assumption that the denominator is equal to 1 valid for GPS is not exact for Galileo and GLONASS, due to the different orbital revolution period. As a result, a more complex propagated signal pattern would occur. For example, the propagation of M2 and O1 errors, which is responsible for the larger aliasing signals at the fortnightly band, has additional peaks at longer periods (up to 30 days). The synthetic errors introduced in real PPP solutions validated part of these peaks predicted by the model, but not all of them. Possible explanation could be that the unobserved peaks may be hidden in the noise background, or that some of these peaks occur due to the inadequacy of the model for Galileo and GLONASS constellations.

Furthermore, our work proposes an original way to decrease the aliased signals in the GNSS position time series by simultaneously estimating OTL errors and station positions (static method). We identified for Galileo the frequencies of the aliased signals using the coordinates free of OTL displacement modeling errors by the re-estimation of the model coefficients in the PPP processing. The sub-daily M2 and O1 errors have a fortnightly aliasing at different frequencies, depending on the constellation. The 13.66-day peak is found only for GPS, while the 14.19- and 14.79-day peaks are shared by all three constellations. This was already observed in Abraha et al. (2018), but only with GLONASS measurements and the kinematic approach. The authors also suggest that the 13.6-day signal results from the mismodeling of aliased sub-daily tides or the Mf tide. However, the amplitude of the 13.6-day signal in GPS positions is below the level of noise in GLONASS positions, which could have affected their conclusions. Our analysis shows that GPS data cannot answer this question of the origin of the 13.66-day signal because of GPS-specific aliasing of the modeling errors in the M1 and O1 frequencies. However, Galileo can accurately observe potential errors in the Mf tide because there are no tidal aliasing in this frequency and the position series have as low noise as GPS positions. With multi-GNSS observations and

re-estimated subdiurnal OTL displacement model, we could detect the remaining OTL model errors in the Mf tide.

We also observe a small decrease in the draconitic signals, however, the influence of the OTL errors is not as significant as other sources of errors coming from site-specific or orbital errors. To better assess their effects, more analysis with longer time series or with improved handling of orbital or site-specific errors is needed. Galileo and GLONASS signals also appear at 8- and 10-day harmonics respectively. These signals are not fully explained by the propagation of errors in the major sub-daily tides considered in this study. They are then assumed to be caused by the spectral resolution that is unable to separate the orbital or constellation-specific frequencies from the tide frequencies. Further analysis with longer time series would also be beneficial to determine the exact origin for these signatures.

Beside assessing the signals resulting from the OTL displacement model, the method developed in our study can help to identify and correct the other sources of error in GNSS coordinates. Previous studies have shown the impact of antenna modeling and multipath (King and Watson, 2010; Sidorov and Teferle, 2015), snow intrusion (Koulali and Clarke, 2020), and the dilation of the monument or bedrock due to thermal variations (Wang et al., 2018; Yan et al., 2009). No corrections are currently considered in GNSS processing because of the lack of precise understanding of the underlying mechanism, or of models. However, the ability to estimate empirical models using GNSS to account for these errors like implemented in the present study offer new opportunities to enhance the accuracy of GNSS positions. In addition, our research on ocean tidal displacements can also provide constraints to deduce more complex models including the Earth's anelastic responses and insight into ocean tides themselves, such as the seasonal variations of tides that oceanographers currently predict (Haigh et al., 2020; Zhou et al., 2021).

Part II

Flicker noise

CHAPTER

5 Flicker positioning noise as a result of the chaotic dynamics of the orbits

5.1 Introduction

Importance of understanding the noise contained in the GNSS positions

Knowing the noise in GNSS positions is crucial for accurately deriving the uncertainties of the estimated parameters in the kinematic position model, such as velocity. Several authors have demonstrated that using improper noise models can lead to underestimated velocity uncertainties by a factor of 5 to 11 (Klos et al., 2017b; Langbein, 2012; Mao et al., 1999; Santamaría-Gómez et al., 2011; Williams, 2003a).

In addition to deriving uncertainties, understanding the origin of the colored noise contained in GNSS positions is also important for separating non-linear crustal motion from positioning noise. Correlated noise can decrease the ratio between the magnitude of the systematic signals in GPS positions, and the random variability of the positions, making it more difficult to identify small movements of the earth's crust. It can interfere with the detection of actual crustal motion by causing apparent time-varying motion over a certain range, leading to false detection. Another example is the estimation of variable annual and semi-annual signals from GNSS series that is more difficult in presence of correlated (flicker) noise (Klos et al., 2017a).

Identification of the noise model in GNSS positions

Langbein and Johnson (1997) introduced a method to detect time-correlated noise in geodetic data, indicating that geodetic noise is not always white noise and emphasizing the importance of considering correlated noise in geodetic time series analysis. Zhang et al. (1997), Mao et al. (1999) and Williams (2004) determined that the noise in GPS PPP positions, for a global network of station, is a combination of white noise (WN) at high frequencies and power-law (PL) noise with a spectral index close to flicker noise (-1) at low frequencies. Besides the PL+WN combination, other studies have proposed to model GNSS position noise with other types of noise models. Random walk noise may be detected if the flicker noise is filtered (as in local or regional network solutions) for particular stations located in active tectonic areas (He et al., 2021; Ray et al., 2019) in particular for stations that are tightly anchored to the bedrock through drilled pipes (He et al., 2021; Langbein and Johnson, 1997). Autoregressive processes can also be used to account for short-memory or transient signals, while a generalized Gauss-Markov (GGM) process is used to model the apparent flattening of the spectra at low frequencies. It is worth noting that an observed flattening could also show the limitation of the maximum likelihood algorithm in handling time series with irregular jumps or offsets (Gobron et al., 2022; Griffiths and Ray, 2016; Santamaría-Gómez and Ray, 2021; Williams, 2003b).

Part of the correlated noise in GPS position time series has been linked to real displacements during GNSS data processing. Ground instability causes localized random motion that can be measured through geodetic observations (Wyatt, 1982, 1989). Non-tidal surface loading

displacements due to water and atmospheric mass transport are not conventionally modeled in GNSS processing. The high-frequency white noise in GNSS positions can be attributed partly to non-tidal surface loading (Boy, 2022; Gobron et al., 2021; Memin et al., 2020; Rebischung et al., 2017); nevertheless, limited impact has been found on the correlated noise at the interannual scale. Finally, the comparison of the noise in the positions of stations equipped with different types of monumentation has shown that the correlated noise could be explained, to a lesser extent, by the monument instability (Beavan, 2005; King and Williams, 2009; Langbein and Svarc, 2019; Williams, 2004).

In addition, the GPS position time series also exhibit spatial correlations of the errors, which have also been analyzed. GNSS time series between stations up to 3000 km are correlated in the east, north and up directions, yet no cross-component correlations have been reported (Amiri-Simkooei, 2009; Amiri-Simkooei et al., 2017; Williams, 2004). More precisely, the analysis of GNSS station positions demonstrated that each part of the noise model (PL or WN) has a different spatial correlation (Gobron et al., 2023; Niu et al., 2023). These spatial characteristics provide further insight into the potential sources of each stochastic component. Short-range correlations up to 200 km could be explained by crustal deformation due to atmospheric (Gobron et al., 2021; Petrov and Boy, 2004) or hydrological (Gobron et al., 2021; van Dam et al., 2001) loading. However, the remaining large-range correlation is likely due to errors commonly observed by regional stations, such as correlated errors coming from the GNSS satellite orbits.

Is flicker noise specific to GPS or GNSS positions?

One way to address this question is to compare it with the noise in the station positions derived from other space geodetic techniques. Previous work has shown that a power-law process with a spectral index closer to white noise is a better model for position time series derived from DORIS (Bogusz et al., 2022; Klos et al., 2018; Le Bail, 2006), SLR or VLBI (Feissel-Vernier et al., 2007; Ray et al., 2008). If environmental and geophysical processes were the only sources of correlated noise in GNSS positions, this should be observable regardless of the geodetic technique used, within the limits of each technique's positioning noise level. Hence, part of the correlated noise in the GNSS positions must be dependent on the positioning technique. King and Watson (2010) showed that changes over time in the GPS constellation, along with observation noise such as multipath, could introduce correlated noise. Their study, however, did not examine why satellite geometry might change or how observation errors are transmitted to positions.

Aims of the study

The objective of this study is to examine the role of the orbits and the constellation in the mechanism that could explain spatiotemporal error correlations in GNSS position time series. Previous works have primarily focused on analyzing GPS data, thereby limiting the ability to fully assess the impact of orbit errors or the impact of different constellation designs. With the availability of three additional constellations, GLONASS, Galileo, and BeiDou, this study aims to use a comparative approach to investigate whether the power-law noise observed in GPS position time series is specific to GPS or related to the GNSS technique itself. Additionally, this study seeks to explore the mechanism that explains how gravitational resonance affecting the GNSS orbits contribute to the observed error correlations. The main objectives of this study are:

- Identify whether the stochastic characteristics of the position series are the same regardless of the constellations used for the determination of the positions
- Investigate the contribution of the orbit errors to the spatiotemporal error correlation in the position time series
- Compare and identify the orbital cause, if any, by comparing the different constellation and orbit designs of the currently available systems : GPS, GLONASS, Galileo and BeiDou

The methods and results presented in this chapter have been published in Ait-Lakbir et al. (2023b).

5.2 Long-term behavior of the orbital parameters

5.2.1 Preliminary analysis of the satellites' orbital parameters

Since the 3rd reprocessing campaign, the analysis centers of the International GNSS Service (IGS) provide precise orbits for 3 of the currently available constellations: GPS, Galileo, and GLONASS. The IGS analysis centers provide the satellites' ephemerides (position and velocity) in Cartesian coordinates expressed in a rotating terrestrial reference frame. From these data, the positions and velocities are converted in an inertial reference frame using GINS software and converted into Keplerian parameters using equations detailed in Appendix A. Figure 5.1 shows the evolution over 3 years (January 2018 to December 2020) of the satellites' orbital elements, in particular the eccentricity and inclination. One can see the broader dispersion between the satellites of the GPS constellation with eccentricities going up to 0.025, and inclinations ranging from $\pm$ 2° around the nominal value of 55°. Despite being different from the nominal values, the eccentricities and inclinations of the GPS satellites stay within the operational and tolerance ranges published by the US Navigation Center (GPS Navigation Center, 2020), which is responsible for operating the GPS constellation. For Galileo and GLONASS, the variability among the satellites is smaller, and their orbits are closer to the nominal values published in their respective documentation. No information about the operational ranges for these constellations could be found.

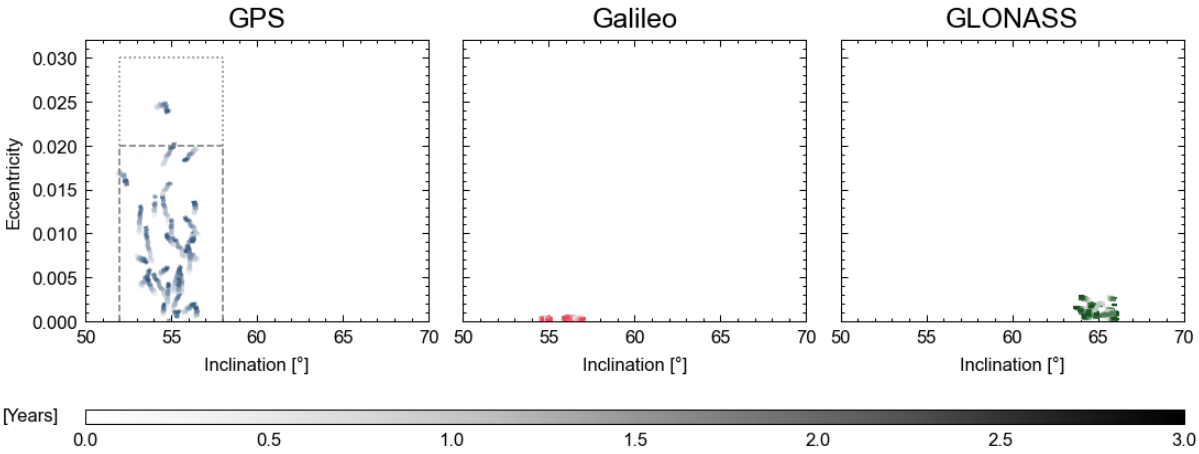

Figure 5.1: Inclination and eccentricities estimated from the IGS precise orbits of GPS, GLONASS, and Galileo satellites. The color gradient represents the time evolution from January 1, 2018 (light shade) to December 31, 2020 (dark shade). For GPS, we have displayed the operational range (dashed lines) and tolerance range (dotted lines).

Figure 5.2 focuses on the eccentricity evolution of the orbits of three satellites (G01, E01 and R01) of each constellation. An eccentricity drift for the GPS satellite that reaches 2 10^{-11} s^{-1} is observed while the eccentricity remains close to zero for the Galileo and GLONASS satellites.

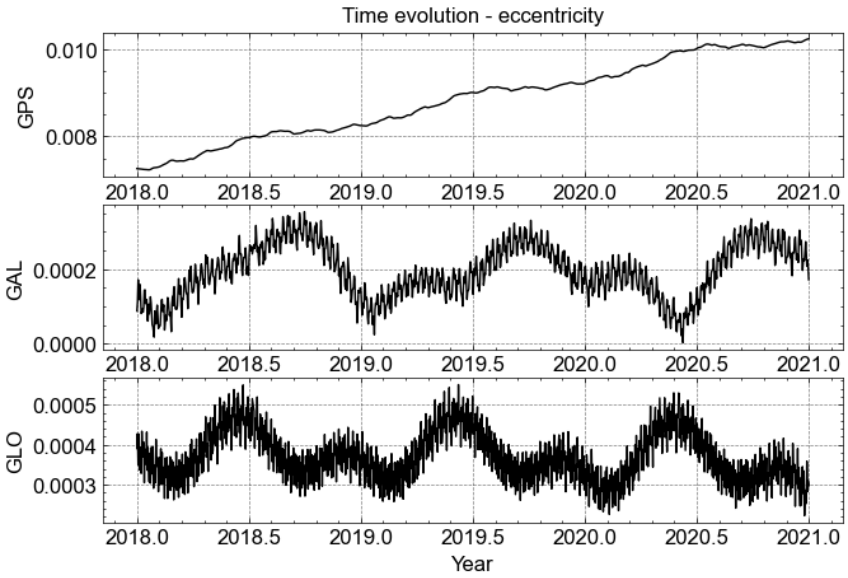

Figure 5.2: Time evolution of eccentricities for a satellite of the GPS (top), Galileo (middle) and GLONASS (bottom) constellations. The slope of the eccentricities for the GPS satellite is approximately 2 $10^{-11} s^{-1}$. Note the different scale of the y-axis for each constellation

5.2.2 Quantification of dynamical stability of the GNSS satellite orbits

Based on this simple comparison of the evolution of the orbital parameters of the GNSS satellites, the GPS constellation seems less stable than Galileo or GLONASS orbits in terms of eccentricity and inclination. In this section, we introduce the theoretical metrics that help us to quantify this difference in the stability of the GNSS orbits.

Theoretical considerations about the Lyapunov exponents

In this section, we aim to quantify the dynamical stability of the orbits through the Lyapunov exponent, which is a quantitative measure of how the dynamics of a system pull apart two nearby trajectories of this system.

We consider a non-linear dynamical system, following deterministic dynamics (i.e. no random forces are involved). This system is Lyapunov-stable if and only if a small perturbation of initial conditions leads to a small perturbation of the trajectory of the system (Wiggins, 2003). It is important to note that the Lyapunov stability does not imply asymptotic stability, which is the tendency of a system to be attracted toward an equilibrium state (such as the stable position of a pendulum). To demonstrate Lyapunov stability, it is necessary to identify a neighborhood of initial conditions that will remain the same. This requires characterizing how the dynamics of the system will tend to separate trajectories that start from initially close positions. The Lyapunov exponent is a quantitative measure of the exponential separation of two nearby trajectories of the system. It is given by the formula $\delta(t) \approx \delta_0 \exp(\lambda t)$ where $\delta(t)$ is the distance between two trajectories at time t, δ_0 is the initial distance, and λ is the Lyapunov exponent.

For multi-dimensional dynamical systems, the separation rate between two nearby trajectories may differ in each direction, which can be described by an n-dimension ellipsoid where the perturbed trajectories will end. To characterize this behavior, a spectrum of Lyapunov exponents λ_1,..., λ_n is used, where λ_i represents the growth rate of perturbations in the i-th direction. In the case of the satellite dynamics, there are 6 dimensions corresponding to the 6 Keplerian parameters describing the state of the satellite. In practice, we often focus on the maximal Lyapunov exponent, denoted by λ_{max}, which represents the fastest divergence rate in the system.

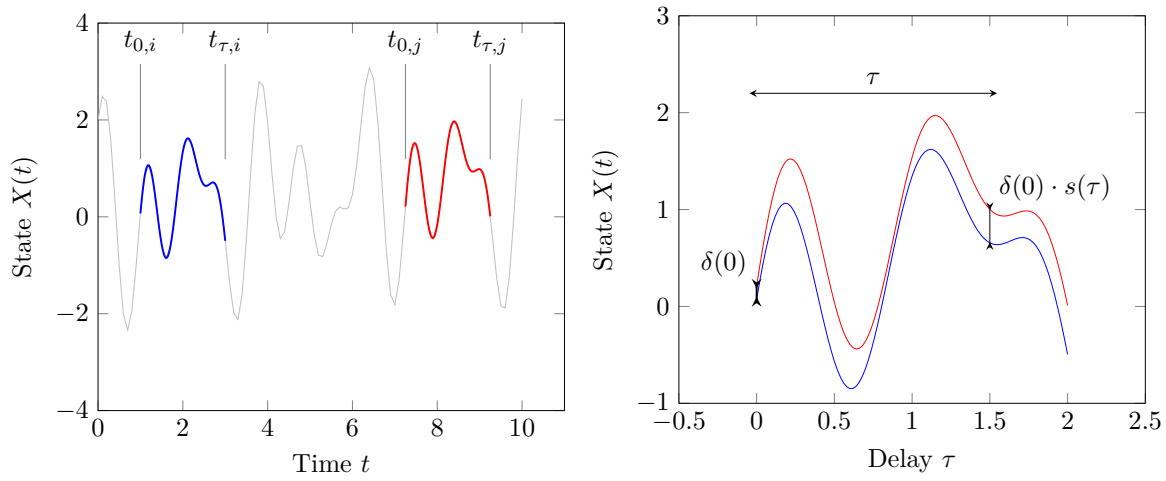

(a) Definition of nearby trajectories

(b) Computation of the stretching factor $s(\tau)$

Figure 5.3: Estimation of the maximal Lyapunov exponent

Definition of deterministic chaos

A deterministic dynamic system is chaotic if it shows long-term aperiodic behavior that is sensitive to initial conditions (Strogatz, 2015). Such a system is therefore predictable on a short-term scale because of its determinism but appears random or irregular over a longer period of time due to the nonlinearity of the dynamics. In other words, this is pseudo-random noise with a long memory that keeps tracks of past states to a certain extent. This chaotic behavior is characterized by the exponential growth of initially small perturbations, which is reflected in the positive values of the maximal Lyapunov exponent λ_{max}. However, it is important to note that a positive λ_{max} does not necessarily imply chaotic behavior, but can also indicate stochastic systems, characterized by unpredictability at every scale (Persson and Wagner, 1996). To illustrate the difference between the two concepts, consider a simple example of a double pendulum. If the pendulum is initially set in motion with a small displacement, its behavior will be regular and periodic. The pendulum's behavior will become chaotic and unpredictable over time due to the sensitivity to initial conditions, showing an apparent random behavior. This is an example of deterministic chaos. In contrast, if the pendulum is subjected to random disturbances, such as vibrations in the supporting structure, or drag due to dust particles, its behavior will also be characterized by random fluctuations regardless of the time scale.

Application to the analysis of satellite orbital parameters

The maximal Lyapunov exponent is a useful metric for quantifying the stability of orbits in GNSS satellite orbits and identifying any chaotic behavior of the satellites' trajectories. In the following, we dismiss the possibility of having a stochastic system with random or noisy forces in the dynamics of the satellite. Under this assumption, the satellites have a deterministic dynamics, and thus the Lyapunov exponent is then an indicator of a chaotic behavior.

Theoretically, the computation of the Lyapunov exponent requires an exact modeling of the system's dynamics and simulating different trajectories with varying initial positions. In practice, this is not possible due to the complexity and variability of the satellite's dynamics. In addition, we need to compute it empirically since we only have access to a single realized trajectory for each satellite, the one that is determined from the observations of the tracking stations. A common approach to compute the maximal Lyapunov exponent is to identify two positions that are initially close to the state space and compute the deviation between the trajectories starting from these positions over time. This allows us to estimate a stretching factor s as a function of

a delay time τ. For that, we search two epochs $t_{0,i}$ and $t_{0,j}$ when the two states $X_{0,i}$ and $X_{0,j}$ of the trajectories are sufficiently close. From the states $X_{\tau,i}$ and $X_{\tau,j}$ at the delayed epochs $t_{\tau,i} = t_{0,i} + \tau$ and $t_{\tau,j} = t_{0,j} + \tau$, the value of $s(\tau)$ is computed by $s = \frac{||X_{\tau,i} - X_{\tau,j}||}{||X_{0,i} - X_{0,j}||}$, with $||.||$ being the Euclidian distance. The stretching factor s can then be related to the maximum Lyapunov exponent by $s = \exp(\tilde{\lambda_{max}}\tau)$.

For the analysis of the IGS precise orbits from January 2018 to December 2020, we implemented the variation of this algorithm described in Rosenstein et al. (1993) and Sprott (2006) and applied it to the 6-dimensional space defined by the Keplerian parameters, that represent the state of a satellite. The analysis is performed for each satellite of the GPS, GLONASS and Galileo constellations. Figure 5.4a shows the stretching factors s computed for the eccentricity parameters, and Figure 5.4b the resulting maximal Lyapunov exponents for each satellite.

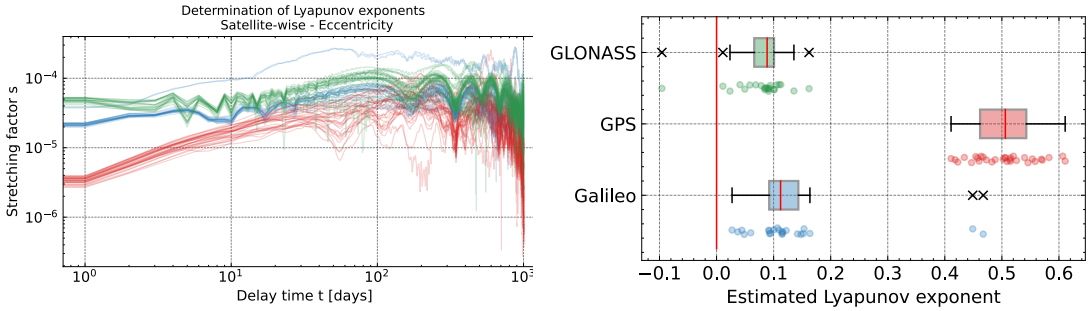

(a) Stretching factor per satellite

(b) Maximum Lyapunov exponents per satellite

Figure 5.4: Dynamical stability of the eccentricities retrieved from the IGS GNSS orbits (Galileo in blue, GPS in red, GLONASS in green). On the left panel, each curve represents one satellite. On the right panel, each dot represents a satellite while the boxplot gives the median exponent and the 1st and 3rd inter-quartile of the exponents. The cross symbols are the outliers detected above 1.5 times the inter-quartile range.

This metric confirms that Galileo, GLONASS, and GPS all differ in terms of eccentricity stability. The stability of the orbit is determined by whether its value is negative or positive. If the value is negative, the orbit is periodic and stable, meaning it follows a predictable pattern. However, if the value becomes positive, the orbit becomes pseudo-periodic, meaning it follows a less predictable pattern. The more positive the value, the more unstable the orbit becomes. For Galileo and GLONASS, the maximum Lyapunov exponents are positive but remain close to zero, indicating stable or quasi-stable satellite orbits. Note that for two Galileo satellites, E14 and E18, the Lyapunov exponent is significantly larger than for the other satellites in the constellation. Due to a launch problem, these satellites were actually launched into an eccentric orbit, which is less stable. For GPS, on the other hand, the values of the maximum exponent are significantly positive and larger (close to 0.5), indicating that the dynamics of the GPS satellites are more unstable.

The analysis of the orbital parameters (eccentricity and inclination) of the GNSS satellites has shown variability in stability between each constellation, with the GPS constellation being less stable than the Galileo and GLONASS constellations. This result raises the question of what may explain the larger instability of the GPS satellites, which will be addressed in the next section, and whether and how it may impact the positioning of ground stations.

5.3 GNSS orbits and gravitational resonances

In the Medium Earth Orbit (MEO) region, gravitational perturbations are primarily responsible for the long-term orbital instability described in the previous section. As an example, the deep resonance resulting from the exact commensurability between earth's rotation and the GPS orbital period has been shown to increase the sensitivity of the orbits to specific terms of the geopotential and to generate long-periodic signals in GPS satellites' semi-major axis (Hugentobler et al., 2003; Ineichen et al., 2003). This is the reason why frequent maneuvers are performed for the GPS satellites to correct for the semi-major axis drift. This deep resonance has effects on various geodetic parameters derived from the GPS technique such as the higher sensitivity of the orbits to geopotential errors (Hugentobler et al., 2003), and signals at K1 and K2 frequencies (both of them being multiples of the GPS orbital period) in the Earth's rotation parameters (Sibois et al., 2017; Zajdel et al., 2020) and station positions (Abbaszadeh et al., 2020; Ait-Lakbir et al., 2023a; Matviichuk et al., 2020; Thomas et al., 2007; Zajdel et al., 2022). Nevertheless, the deep resonance does not affect the eccentricity nor the inclination of the satellites. As a result, the investigation has focused on another cause of gravitational resonance: the gravitational forces from the Sun and the Moon.

5.3.1 Description of the lunisolar resonance

The Moon and Sun also contribute to orbital resonance, causing the eccentricity to drift over time (Chao and Gick, 2004; Deleflie et al., 2011). As a result of the conservation of kinetic energy, perturbations of other orbital elements, such as the inclination, are also induced. As part of the end-of-life management analysis of GNSS satellites, the secular behavior due to the lunisolar resonance of these satellites has been extensively examined (Chao and Gick, 2004; Deleflie et al., 2011; Rosengren et al., 2015). These studies are done to ensure that the regions of the GNSS orbits remain available and free from space debris for decades to centuries.

Analyzing whether this orbital evolution also exists, to a lesser extent, over a satellite's lifetime is beyond the scope of these analyses, and has not been examined yet. In this chapter, we make the working hypothesis that the drift observed in the eccentricity and inclination of the GPS orbits is mostly caused by the lunisolar resonance. We will examine to what extent the resulting long-term dynamic instabilty of the GPS orbits is contributing to the colored noise found in the station positions. To examine this, orbits are simulated for the four current constellations: GPS, Galileo, GLONASS, and BeiDou, with different orbital dynamic models with and without accounting for the lunisolar resonance.

For that, I implemented and propagated the semi-analytical model introduced in Chao (1979) and Chao and Gick (2004) for the orbital parameters of a satellite subject to lunisolar gravitational accelerations. This model, expressed in terms of variational equations of the Keplerian parameters, is derived from the Hamiltonian functions accounting for the potential of the Sun and Moon's gravity. To filter the secular variations, the authors averaged the resulting variational equations of each orbital parameter over the satellite's orbital period and the Sun and Moon's revolutions. That means that all effects occurring with a periodicity below one year are not modeled.

In the simulations, I used the time derivative of the Keplerian parameters of a satellite, subject to the lunisolar accelerations, derived by Chao and Gick (2004). In the following equations, the variables (a, e, i, Ω, ω, M) refer to the Keplerian parameters of the satellites, whilst the same parameters indiced $_{3b}$ refer to the parameters of the third body (Sun or Moon). Note that in this case, in the original equations, the positions of the Sun and the Moon with respect to the Earth (i_{3b}, Ω_{3b}) were modeled through their mean motion over one year (Chao and Gick, 2004), in particular assuming that the orbit is circular and that the obliquity of the elliptic equals to the constant value of 23.45°.

, with

$$\frac{de}{dt} = -\frac{15}{8} e\gamma s \Big[C_1 \sin\left[2(\omega - \Omega + \Omega_{3b})\right] + C_2 \sin(2\omega - \Omega + \Omega_{3b}) + C_3 \sin(2\omega) + C_4 \sin(2\omega + \Omega - \Omega_{3b}) \; C_5 \sin\left[2(\omega + \Omega - \Omega_{3b})\right] \Big]$$

$$C_1 = \frac{1}{2} \sin^2 i_{3b} \; (\cos i + \frac{1}{2} \sin^2 i - 1)$$

$$C_2 = \frac{1}{2} \sin i \;\; \sin i_{3b} \; (\cos i - 1)$$

$$C_3 = \sin^2 i \; (1.5 \sin(2 i_{3b}) - 1)$$

$$C_4 = \frac{1}{2} \sin i \;\; \sin i_{3b} \; (\cos i + 1)$$

$$C_5 = \frac{1}{2} \sin^2 i_{3b} \; (0.5. \sin^2 i - \cos i - 1) \tag{5.1}$$

$$\frac{di}{dt} = \frac{3 n_{3b}^2}{8n} R_m \Big[\cos(i) \sin(2 i_{3b}) \sin(\Omega - \Omega_{3b}) + \sin(i) \sin^2(i_{3b}) \sin(2\Omega - 2\Omega_{3b}) \Big] \tag{5.2}$$

$$\frac{d\Omega}{dt} = \frac{3 n_{3b}^2}{16 n} R_m \frac{1}{\sin(i)} \Big[\sin(2i)(1 - 3\cos^2(i_{3b})) + 2\cos(2i) \sin(2 i_{3b}) \cos(\Omega - \Omega_{3b}) + \sin(2i) \sin^2(i_{3b}) \cos(2\Omega - 2\Omega_{3b}) \Big] + \left(\frac{3}{2} J_2 \frac{R_\oplus}{a} n \cos(i) \right) \tag{5.3}$$

$$\frac{d\omega}{dt} = \frac{3}{16} \frac{\gamma}{\sin i} \Big[\sin(2i)(1 - \cos^2(i_{3b})) + 2\cos(2i) \sin(2 i_{3b}) \cos(\Omega - \Omega_{3b}) \Big] - \frac{d\Omega}{dt} \cos(i) \tag{5.4}$$

$$\frac{dM}{dt} = n \tag{5.5}$$

5.3.2 Analysis of the simulated orbital parameters

Before using these simulated orbits for station positioning, we verify that they can replicate the long-term dynamics observed in the IGS orbits. We propagated the aforementioned model from initial positions of the GPS, Galileo and GLONASS satellites taken on January 1, 2018. In Figure 5.5, we plot the simulated eccentricity and inclination of the satellites for 10 years, whereas Figure 5.1 which shows the observed eccentricities and inclinations of the satellite. While the simulated and actual values differ by satellite, the general dispersion of the eccentricity and inclination drifts of each constellation is reproduced by the model, which supports our working hypothesis. In particular, the GPS satellites seem more sensitive to the lunisolar resonance than the Galileo, and GLONASS satellites for which these parameters stay close to their initial value.

In Figure 5.6, we plot the time-derivative of the eccentricity for all GPS satellite of the plane A over the first three years of the simulation (2018.0 - 2021.0). We first observe that the satellites of the same plane are not equally impacted by the resonance, but depends on the actual eccentricity of each satellite at the moment the lunisolar resonance is propagated. Second, even if the order of magnitude of the eccentricity seems similar to the values observed from the IGS orbits (see

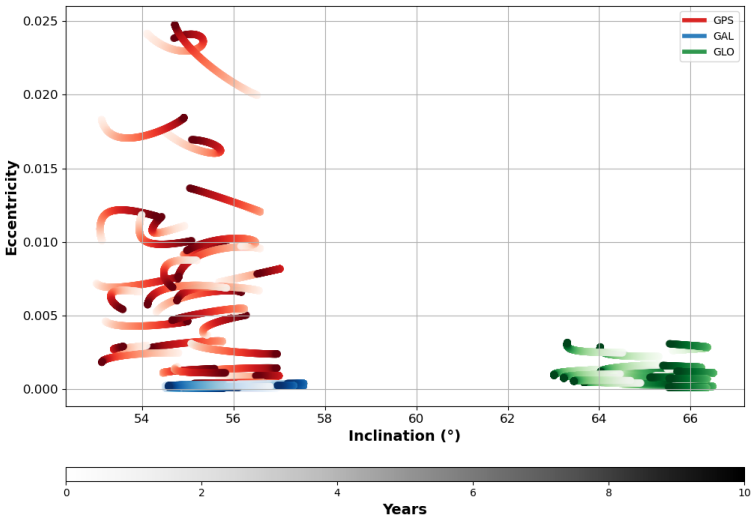

Figure 5.5: Simulated eccentricity (vertical axis) and inclination (horizontal axis)

Figure 5.2), part of the drift of the eccentricity and the draconitic signals cannot be explained by the lunisolar resonance only. For instance, we observe in Figure 5.5 that the eccentricity drift caused by the lunisolar resonance increases for those satellites that are already more eccentric. Since all the GPS satellites are initially launched into orbit at the same nominal eccentricity of 0, the satellites that are more eccentric at a given time correspond to those that were launched earlier. The lunisolar resonance will exacerbate the drift of eccentricity of those satellites, but the driver that initiates the eccentricity drift for each GPS satellite is missing in the model of the lunisolar resonance.

The factors that initiate the eccentricity drift for the GPS satellites only are not clear yet. Hence, other sources need to be explored. For instance, a constant mispointing of the solar panels which has been observed for GPS satellites (Fliegel et al., 1992; Kuang et al., 1996). Even if this is accounting for in the current empirical SRP model used in orbit determination (Rodriguez-Solano et al., 2012), this constant mispointing also induces a constant acceleration that will be projected successively along the track and in the opposite direction, and thus a (potential) increase in the orbit's eccentricity. Whatever the origin of the eccentricity drift, it only exists in the GPS constellation, and in much lesser extent in the GLONASS constellation, but not in Galileo. Based on the official operational and tolerance ranges of the GPS constellation, the eccentriciy drift must be an expected outcome of its design.

The same analysis based on the Lyapunov exponents has been performed to compare the stability of the simulated orbits (Figure 5.7). The results are to be compared to Figure 5.4b previously discussed for the IGS orbits. Our simulations indeed reflect the larger instability of the GPS satellites compared to the Galileo and GLONASS satellites. In addition, the simulations enable to predict the stability of the BeiDou satellites, which is similar to Galileo and GLONASS satellites.

In summary, both the comparison of the evolution of the orbital parameters and the analysis of their dynamical stability indicate that GPS satellites are less stable than Galileo or GLONASS satellites. This instability is partly due to their increased sensitivity to resonance caused by the gravitational forces of the Sun and Moon. Over long periods, typically one year, this results in the drifting of the eccentricity and inclination of GPS orbits, which deform the initial geometry of the constellation over time.

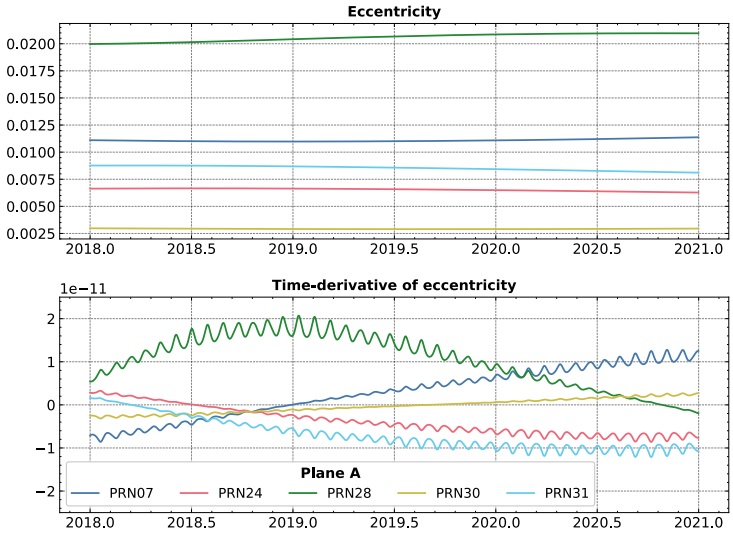

Figure 5.6: Time variations (top) and time-derivative in s^{-1} (bottom) of the eccentricity due to the lunisolar resonance.

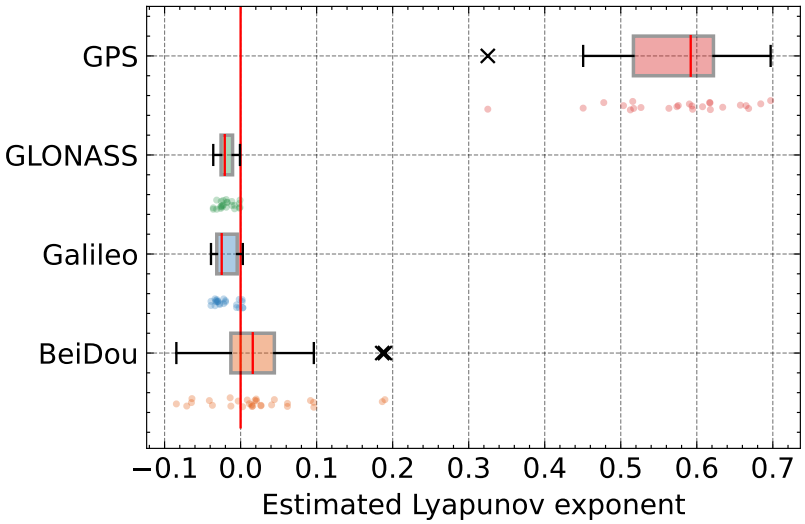

Figure 5.7: Maximum Lyapunov exponents per satellite - simulated orbits with resonant dynamics.

5.4 Linking orbital dynamics to time-correlated noise in positions

In this section, we will investigate whether the long-term evolution of the GPS orbits, specifically their eccentricity and inclination drifts, can affect the noise present in the PPP station positions, through the induced time variation of the geometry between the ground stations and the satellites. For that, we compute PPP positions using both the observed IGS orbits or orbits that we simulate with different dynamic models. For these two simulations, we simulate observations to these orbits and use them to compute PPP solutions. We will also explore the factors, in addition to the variability of the station-satellite observation geometry, which can contribute to the correlated noise, namely the presence of systematic observation noise and the deficiency of the observation weighting function used to estimate the station positions.

5.4.1 Simulation configurations

To examine the impact of variations in GNSS constellation geometry and contributing factors to correlated noise in PPP processing, we compared three test configurations, as outlined in Table 5.1. The first two tests used simulated observations either with IGS orbit products or with simulated orbits. We compared different types of noise in the observations and strategies to handle it in the PPP processing, as well as the effects of the choice of estimated parameters. The last test is the real-case PPP configuration, as already presented in Chapter 3 (static case in Table 3.2, without any OTL parameters estimated).

Table 5.1: Test configurations

Tests	Simulated orbits	Precise IGS orbits	Real PPP solutions
PPP configurations	Simulated		Real
GNSS orbits	Simulated	GRGS orbits (REPRO3)	
Observations	Geometric distance with zero-mean or with non-zero mean noise		RINEX

Simulated orbits

For the first two tests, I generated three subsets of simulated orbits to distinguish the influence of the deviation of the constellation geometry from the nominal one, and the effects of the resonance. Table 5.2 gives a description of each simulation case.

Three simulation configurations are compared to distinguish the influence of the constellation geometry or the sensitivity to the resonant dynamics on the orbits and the positioning. The test is done for the GPS, Galileo, GLONASS, and BeiDou constellations. The nominal ("nom") simulation propagates the Kepler dynamical equations of motion initialized by the nominal satellites' orbital elements provided by the constellations' operating agencies (GPS Navigation Center, 2020). Also using the Kepler's equations of motion, the geometry ("geom") simulation uses the precise IGS orbit products as initial positions to simulate the actual constellation geometry, which differs from the nominal geometry especially for GPS. The resonant ("res") simulation results in propagated orbits accounting for the lunisolar resonant dynamics (Chao, 2005; Chao and Gick, 2004), initialized with the precise orbits as in the "geom" simulation. We propagate the orbits for a time span of 10 years to obtain time series long enough for the proper estimation of the noise model.

Table 5.2: Description of the orbit simulations

Orbit simulation cases	**Nominal ("nom")**	**Geometry ("geom")**	**Resonance ("res")**
Initialization	Theoretical constellation	GR: ESA REPRO3 orbits at epoch 01/01/2018 E: ESA REPRO3 orbits at epoch 01/01/2019 C: Broadcast orbits at epoch 01/01/2021	
Dynamics	Central body + J2		Central body + J2 + secular resonant dynamics
Constellation	GPS	GPS, Galileo, GLONASS and BeiDou	
Time span	10 years		

Simulated observations

For the simulation of the observations, we use the observation equation for the carrier phase measurement already mentioned in Chapter 2 (Equation 2.2) for the iono-free combination. In our simulations, we made additional hypotheses that are not verified in real GNSS observations, for the observations to be sensitive only to the observation geometry. We suppose that the iono-free combination removes all the effects of the ionospheric propagation delay and that the instrument bias β_r, β^s and satellite clocks δt^s are perfectly known. Likewise, we assume that all the carrier-phase ambiguities N_{IF} have been perfectly resolved to integer values. These parameters are then omitted in the observation equations 5.6.

$$L = \rho_r^s + c\,(\delta\tilde{t}_r - \delta t^s) + \tilde{T}_r^s + N_{IF}\lambda_{IF} + \beta_r - \beta^s + \varepsilon_L \tag{5.6}$$

As for the troposphere, we do not add any propagation bias as they are assumed to be common to all observations regardless of the constellations. We have nevertheless tested the validity of neglecting their estimation in the PPP solutions (see Chapter 2, Section 5.4.1). The effects of PCO (Phase Center Offset) and PCV (Phase Center Variation) corrections for satellites and receivers, as well as other site-related displacements are not considered. The simulated GNSS observations are calculated every 900 seconds applying an elevation cutoff angle of 10°. Different sets of observations are generated for each set of simulated orbits, and for the IGS orbits products. A network of 118 stations distributed globally given in Figure 5.8 is used.

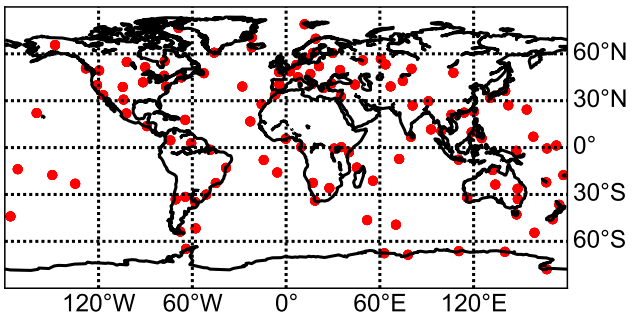

Figure 5.8: Stations used in the simulations

Simulated observation noise ε_L

The most common type of noise visible in the GNSS observations is random noise with zero mean and whose variance depends on the satellite elevation as illustrated in Figure 5.9a. In the rest of the chapter, this noise will be referred to by "zero-mean observation noise". This noise is added to the simulated geometric range for all three tests. In addition to this first noise component, we also test the addition of a systematic error that has non-zero mean dependent on the satellite elevation as illustrated in 5.9b. In the rest of the chapter, it will be named "non-zero mean observation noise". The main difference between these two noise types is that in the latter there is a systematic bias introduced in the observation that may reflect antenna phase center, atmospheric delay, or multipath errors. This systematic error is simulated using the model for multipath errors described in King and Watson (2010), assuming the same antenna characteristics (height and antenna gain) and environment ((ground roughness, refractive indices) for all stations.

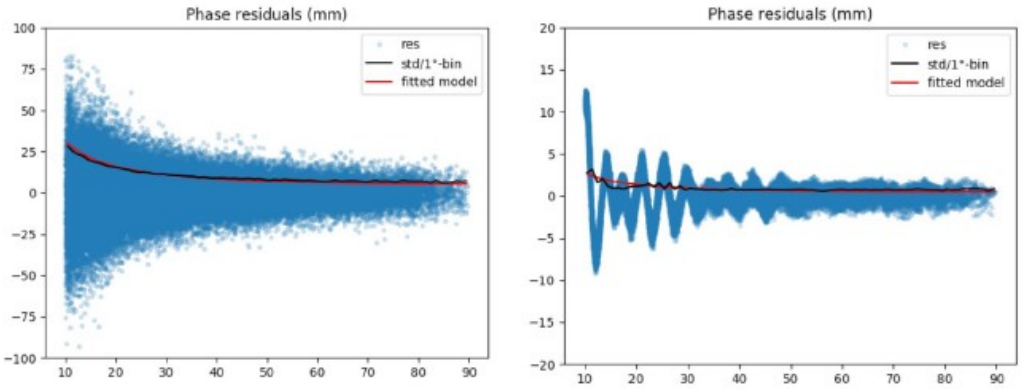

(a) Zero-mean noise

(b) Non-zero mean noise

Figure 5.9: Phase residuals in PPP simulation without any observation weighting. Hence, the residuals directly reflect the noise in the observations.

Observation weighting function in PPP processing with simulated observations

While processing real GNSS data, observations at low elevations are usually down-weighted because they contain larger errors induced by multiple factors e.g. multipath or troposphere model discrepancies. In our PPP solutions simulation, we tested three weighting strategies that are applied while constructing the a priori covariance matrix during the parameters inversion (see Chapter 2, Section 2.4).

The first strategy tagged "equal weight" is not common for the processing of real GNSS data but serves as a reference in the comparison of our tests, as all observations are given the same weight. The post-fit residuals are then fully impacted by the errors in the observations as we can observe in Figures 5.9a. The second weighting strategy uses a more realistic inverse sine function ($\frac{\sigma_0}{\sin \varepsilon}$) that depends on the satellite elevation ε. The constant variance σ_0 is estimated from the post-fit residuals issued from the test "equal weight", which is not very different to what is done today in the state-of-the-art GNSS processing, thus reflecting the standard weighting. In Figures 5.9a and 5.9b, the red curves give samples of such weight function. The position series computed based on this second strategy is tagged "inverse sine" in the following. Finally, we construct a third weighting strategy, tagged "optimal", based on optimal weights determined from the a priori knowledge of the variance of the introduced errors in the simulated observations. In other words, this is equivalent to turning the observation errors previously introduced into an elevation-independent unbiased white noise.

Estimation of PPP solutions from simulated observations

I implemented a simplified version of the PPP processing based on the inversion of the observations equations as already described in Chapter 2, (Section 2.4). Daily station coordinates and epoch-wise receiver clock biases are estimated. In addition, because we assume that the phase ambiguities have been perfectly resolved, there is no corresponding partial derivative in the normal equations.

We have also omitted the estimation of troposphere biases and gradients to reduce the computational burden owing to the absence of spatial variability in the troposphere propagation in our simulated observations. Indeed, the observation of the troposphere parameters is assumed to be the same for all observations at a given elevation, regardless of the satellite. As a result, we do not expect any change in the nature of the positioning noise if we estimate troposphere biases or not. Nevertheless, it remains the issue of a potential error propagation during the parameters inversion caused by the correlation between the estimated parameters. This is what we checked with a subset of 10 stations over a time span of 3 years. For this test, we use the

GPT3 tropospheric mapping function (Landskron and Böhm, 2018) which is a simplified model accounting for annual and semi-annual variations of the atmosphere's properties. Tropospheric biases are then estimated every 2 hours in this solution. Figures 5.10a give the time series of the estimated height of a station, and Figure 5.10b the averaged power spectra of the heights over the entire station network. The primary difference is visible on the height direction (bottom panels in the figures). With the estimation of the tropospheric biases, the height estimates are biased and show a larger noise level. This is due to the high correlation of this parameter and the troposphere bias. However, we cannot notice any change in the power-law nature of the noise in the spectra.

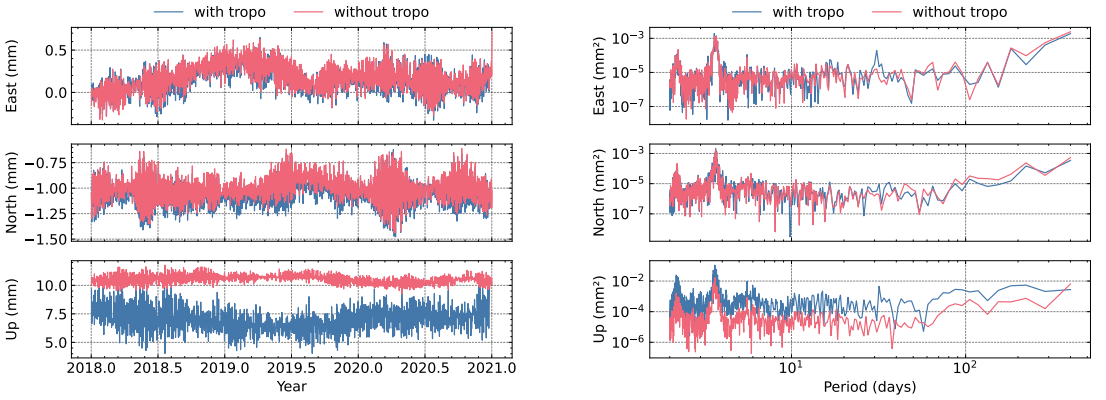

(a) Time series for a station

(b) Unnormalized power spectra averages over the

Figure 5.10: Coordinates solutions with and without the estimation of troposphere biases.

In other words, the estimation of the troposphere biases does not change the noise type at long periods, and for that reason all PPP solutions with simulated observations will omit the estimation of the troposphere parameters in the rest of the analysis.

5.4.2 Noise analysis of PPP positions computed from simulated observations

5.4.2.1 Impact of the observations noise and weighting functions

To observe the impact of the two types of observation noise considered in the tests, we computed two sets of PPP positions from the simulated observations: with zero-mean observation noise only, and with zero mean **and** elevation-dependent non-zero mean noise. For both sets, the observed GPS orbits (REPRO3) provided by the IGS are used. The positions are computed for the entire station network. Figure 5.11a gives samples of the ENU position time series for a station while Figure 5.11b compare the spectra of the estimated up coordinates in both cases. The spectra are averaged over the network to reduce the noise level and to facilitate the identification of the common noise type. The colored noise only occurs when a non-zero mean noise is included in the observations. On the position time series, we indeed observe that the mean is not constant in this case, whilst we can see a slope of approximately 2 of the spectra in the low frequency, characteristic of correlated or colored noise. This may be explained because the presence of non-zero mean systematic errors makes it possible a cumulative and repeated effect of the observation noise as they are observed through the same observation geometry.

There are also additional signals in the spectra of Figure 5.11b at approximately 10, 5, 3.5 and 2.3 days. These peaks only appear when the non-zero mean noise is applied. Already observed in King and Watson (2010), these peaks do not directly relate to the GPS orbital repeat characteristics. The amplitude of these peaks depends on the different IGS analysis centers, whose products are used for the simulation of the GPS observations. These peaks could be explained by the differences in the strategy of each constellation for performing the alignment of the network

solutions to the rotating terrestrial frame or for handling the deficiencies of the orbital dynamics models. Indeed, any errors would be differently absorbed by the orbits, the satellite clock biases and the EOPs that are simultaneously estimated.

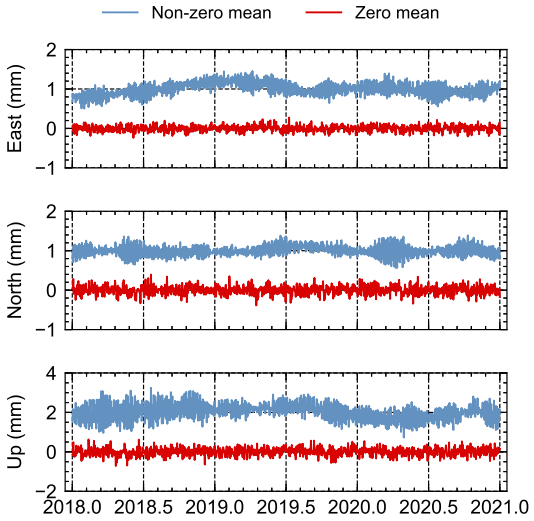

(a) Time series of estimated ENU positions. Note that the blue plots have been shifted by 1 mm for the horizontal components, and 2 mm for the up component.

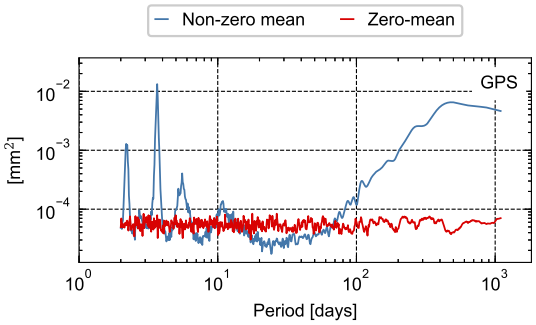

(b) Unnormalized power spectra of the vertical coordinates averaged over the station network.

Figure 5.11: Effect of the type of observation noise.

The second contributing factor we investigate is the contribution of the choice of the weighting function. Indeed, when processing GNSS data, weighting functions that depend on the satellite elevation are often used to reduce the impact of unmodeled observation errors. The same test is done to compute three sets of PPP positions from simulated observations including non-zero-mean errors but differing by the weighting functions applied in the processing:

- an elevation-independent function ("equal weight")
- an inverse sine function calculated from unweighted post-fit observation residuals ("Inverse sine")
- an optimal elevation-dependent function based on prior knowledge of systematic errors ("Optimal")

Similarly as for the previous test, in Figure 5.12a, we plot examples of time series of the estimated positions for each weighting strategy. Figure 5.12b gives the averaged spectra of the estimated heights over the station network. Note that the spectra are unnormalized so that the spectral power of each set of positions can be directly compared.

As shown in Figure 5.12b, using a post-fit estimated weighting function reduces the noise variance in positions by a factor of 10 compared to using a deficient weighting ("equal weight") strategy. However, the power-law noise type is not significantly affected by the post-fit weighting function. Only optimal weights that match the actual statistical characteristics of systematic errors can reduce even more the impact of the observation noise and mitigate long-period colored noise in the positions. Thus, to reduce colored noise in GPS positions, either site-specific systematic errors such as multipath, antenna phase centers, or tropospheric propagation must be limited or an optimized empirical weighting function not solely based on post-fit residuals, as it is the standard practice nowadays, must be used.

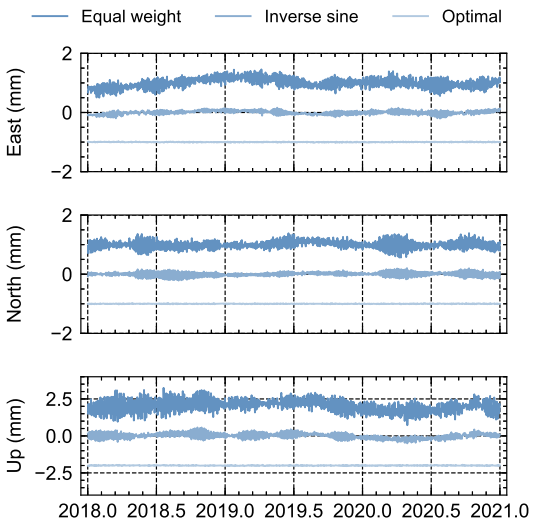

(a) Time series of the estimated ENU positions. Note that the plots have been shifted by ± 1 mm for the horizontal components, and ± 2 mm for the vertical component.

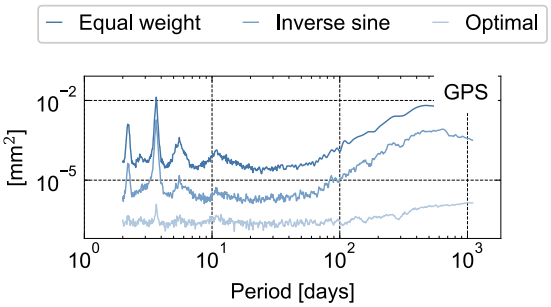

(b) Unnormalized power spectra of the up coordinates averages over the station network.

Figure 5.12: Effect of weighting functions.

These two tests based on the IGS orbits of the GPS constellation only demonstrate that two factors are necessary, but not sufficient, for obtaining colored noise in the estimated station positions. These two factors are the presence of a systematic observation noise that have a non-zero mean bias depending on the satellite elevation, and the deficiency of the observation weighting strategy to mitigate this effect. In the next section, I will examine whether similar results are obtained with the other available GNSS constellations (Galileo, GLONASS and BeiDou).

5.4.2.2 Impact of the evolution of the constellation geometry

Estimated coordinates from simulated observations using IGS REPRO3 orbits

Up to this point, only the GPS constellation has been used in the analysis. To compare the positioning noise occurring with the other constellations, we simulate observations using the other constellations present in the REPRO3 products namely Galileo and GLONASS. The non-zero-mean observation noise is included and we compute the PPP solutions with the three weighting functions previously mentioned. Figure 5.13a shows an example of the ENU position time series for a station, determined by each of the constellations, while Figure 5.13b gives the power spectra averaged over the station network. These results are obtained using the orbits calculated by the ESA analysis center, but the same tests have been performed using orbit products from other analysis centers participating in the IGS REPRO3 campaign (CODE and GRGS).

What is visible on the time series and the spectra at long periods (above 100 days) is the difference in the background noise in the positions. In GPS-derived positions, we observe the correlated noise discussed in the previous sections. However, in positions determined with Galileo and GLONASS, the means of the position series (Figure 5.13a) is nearly constant over the three-year span. In the spectra (Figure 5.13b), this is characterized by a flatter spectrum for periods longer than 100 days, indicating that whiter noise is predominant in the series.

A second observation that can be made from the spectra (Figure 5.13b) of the Galileo and GLONASS positions is the presence of systematic periodic signals occurring at periods up to 47 days. Similar signals previously observed are also visible in the GPS positions at approximately

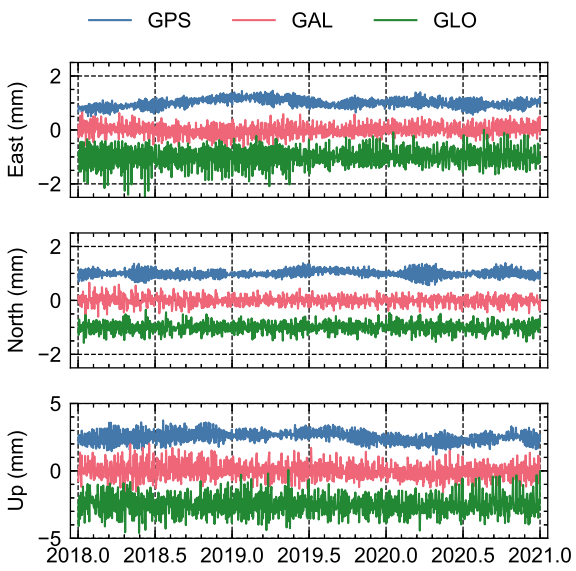

(a) Time series of the ENU coordinates. Note that the plots have been shifted by ± 1 mm for the horizontal components, and ± 2 mm for the vertical component.

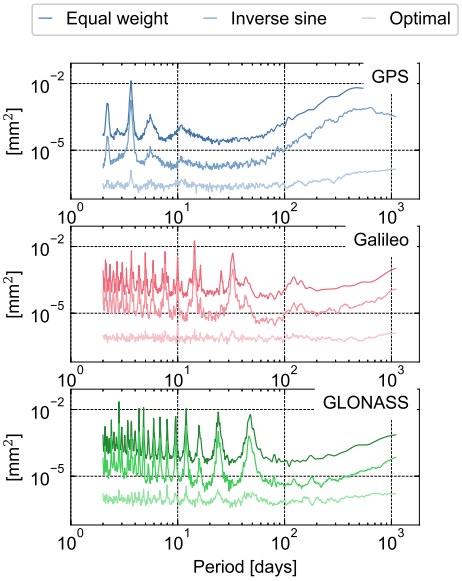

(b) Unnormalized power spectra averaged over the station network.

Figure 5.13: Coordinates solutions with GPS-only, Galileo-only and GLONASS-only simulated observations.

10, 5, 3.5, and 2.3 days. The magnitudes of these signals remain unchanged when using a post-fit weighting function, but can be reduced with optimal weighting. As a result, they only become visible when the systematic observation noise has an effective impact. In the similar tests performed by changing the REPRO3 orbit products used for the simulations of the observations, the amplitudes of these signals differ between the different analysis centers tested (ESA, CODE and GRGS). In addition, the frequencies of these signals do not directly relate to the characteristic orbital periods of the three constellations. No satisfying explanation for these signals has been found, but one common point between these products is that they have been generated in multi-GNSS processing, including GPS, Galileo and GLONASS satellites. While processing real GNSS observations with the IGS products (satellites orbits and clock corrections), these signals do not appear suggesting that these signals may come from global errors that are absorbed by the parameters estimated in the network solutions. Several factors could explain these signals, such as the misalignment of the network solutions to the terrestrial frame or any constellation-specific orbital error transferring to the whole parameters estimated in the network solutions. While further investigation would be necessary, these signals do not affect the main conclusions of this analysis, which focuses on the correlation of positioning noise occurring at periods above 50 to 100 days.

Taken together, these results suggest that there is an actual contribution of the constellation or the satellite orbits to the mechanism responsible for the presence of colored noise in the positions. of the ground stations determined from GPS data.

Estimated coordinates from simulated observations using simulated orbits

To investigate the contribution of the satellite orbits and their stability over time, I conducted the same tests using simulated orbits for the GPS, Galileo and GLONASS satellites, as well as the BeiDou satellites. The latter ones are indeed not available in the REPRO3 products but we can use broadcast orbits to initialize the orbit propagation. I computed the PPP positions from observations simulated, including the non-zero mean observation errors, with three sets of simulated orbits, differing from the initial geometry of the constellation, and the presence of resonant dynamics. The correlation of the positioning noise is then quantified by estimating a power law noise model on the position series by Maximum Likehood Estimation (MLE) (see Chapter 1, Section 1.2.3). For this test, we use the implementation of the algorithm available pytrf [1] software. The spectral index of the model indicates an uncorrelated noise (or white noise) if close to 0, and correlated noise (flicker noise) if close to -1. Figure 5.14 shows the distribution of spectral indices of the power law (PL) noise model estimated from the positions obtained with the nominal, reference, and resonant simulated orbit. We will discuss only the vertical direction, but the conclusions apply to the East and North coordinates.

The effect of the deviation of the constellation's geometry from the nominal GPS constellation geometry (first column) is observed by comparing the spectral indices obtained with the nominal GPS orbits ("nom" test) and with the observed satellite geometry from the IGS products ("geom" test) in Figure 5.14. Indeed, these two tests only differ in the initial geometry of the constellation, but are both obtained with the same propagated dynamics without resonance. With the "nom" test, the spectral indices are centered at zero, implying white noise which is uncorrelated. With more realistic satellite positions ("geom") which have been affected by other gravitational and non-gravitational accelerations, we observe the mean of the spectral indices are negatively biased by -0.3, which indicates a more correlated noise. In addition, the GPS-derived positions seem more susceptible to time-correlated noise than the other three constellations (Galileo, GLONASS and BeiDou) as the spectral indices of noise model estimated from these position series remains centered at zero.

As already mentioned in Section 5.3, the GPS constellation is more sensitive to the resonance due to the lunisolar gravitation than the other constellations. We thus examine the effects of the introduction of this resonance in the orbital dynamics with positions obtained in the test "res" (third rows in Figure 5.14). The GPS-derived positions are even more prone to correlated noise as the spectral indices are even more shifted towards -1 (mean of -0.4). The noise in the position series determined with the other 3 constellations remains uncorrelated (spectral indices close to 0).

We can also examine the normalized power spectra of the position time series obtained from the station-satellite observations to the simulated orbits with the resonant dynamics. In Figure 5.15, we plot the average of the spectra over the station network. The power in the GPS position series increases with longer periods, with a slope of approximately -0.5 (close to the the mean of -0.4 observed in the spectral indices). It is also interesting to observe that the power increases across the entire spectrum, even for periods up to 1000 days. This result is important because it helps us to better understand the part of the spectrum that we currently do not observe well with real GNSS data because of the discontinuities in the position series (Santamaría-Gómez and Ray, 2021). In contrast, the spectra of positions derived from Galileo, GLONASS, or BeiDou are flat and close to the spectrum of white noise, agreeing with the estimated noise model of the series.

Finally, we also consider the positions obtained from the combination of the current GNSS constellations. Even if it is not a widespread standard for precise positioning yet, it has been shown that the precision of the PPP positions improves with using multi-GNSS data. As more and more data will be available, multi-GNSS position time series will be also provided. We compare the GPS-only solutions with two multi-constellation solutions: a combination of the four constellations: GPS, Galileo, GLONASS and BeiDou (GERC combination) and the same

[1]The pytrf sofware is a courtesy of Dr Paul Rebischung from IGN.

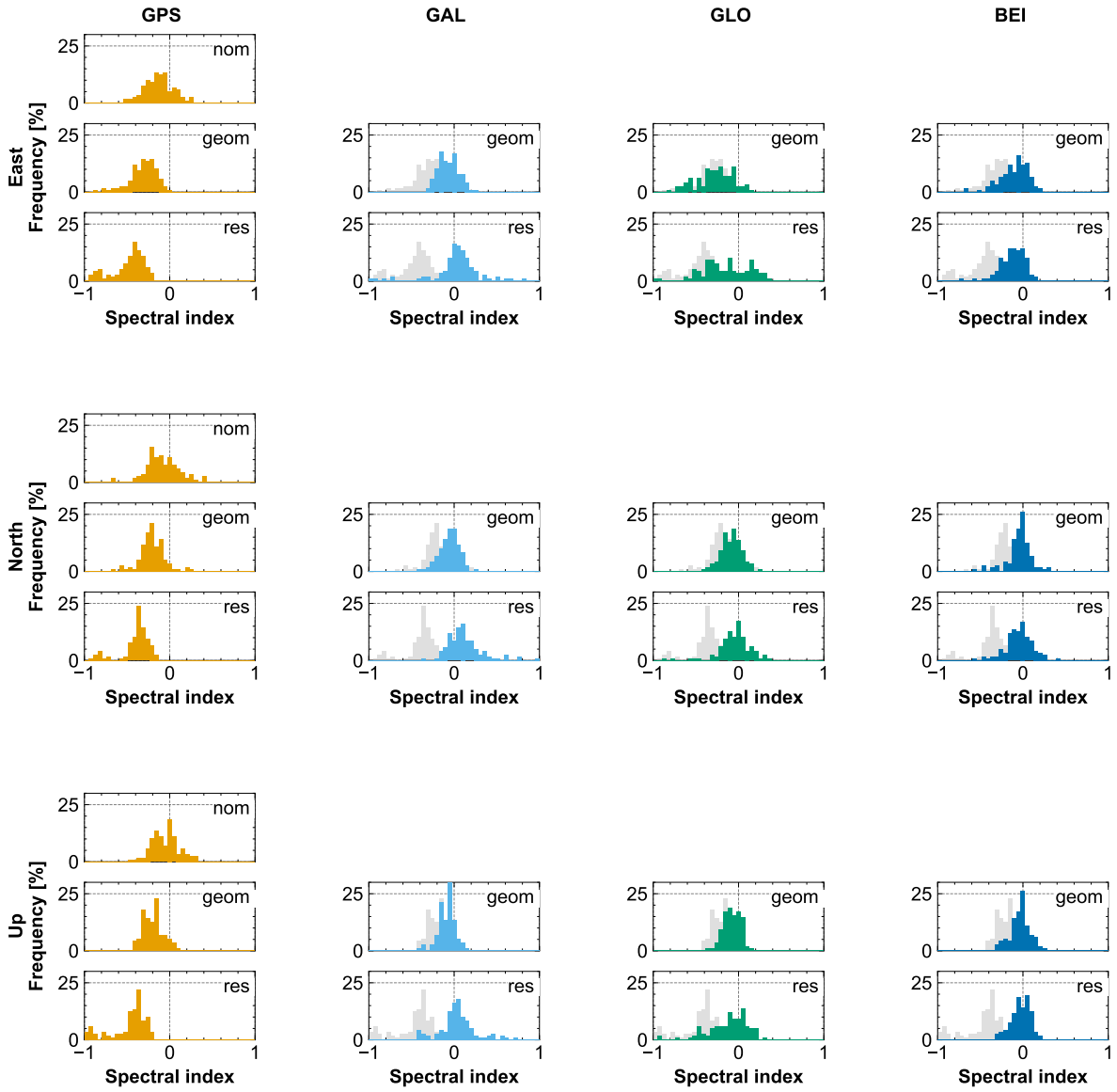

Figure 5.14: Distribution of the spectral indices estimated from the east (top panel), north (middle panel) and up (bottom panel) PPP coordinates obtained with simulated observations and simulated orbits. The nominal ("nom") case is ignored for Galileo, GLONASS, and BeiDou since their orbits are close to nominal, and the GPS histograms are displayed in light gray in the background for comparison.

combination excluding GPS (ERC combination). Figure 5.16 gives the distribution of the spectral indices of the PL noise model estimated from GPS-only position and the two sets of multi-GNSS positions. The positions are still determined from simulated observations and the three sets of simulated orbits ("nom", "geom" and "res"). Note that in this test, the same weights are given to the four constellations, which could not be necessary applied in real GNSS data processing. In presence of GPS in the combination, we still observe correlated noise in the position series, even if slightly less correlated. For instance, the GERC position series obtained in the "res" case, the mean spectral index is approximately -0.25. Omitting the GPS constellation in the combination confirm these findings, as the position series do not show any correlated noise (mean spectral indices of 0).

Further analysis has been performed to investigate the geographical distribution of the noise types present in the station position series. Figure 5.17 gives the spatial distribution of the

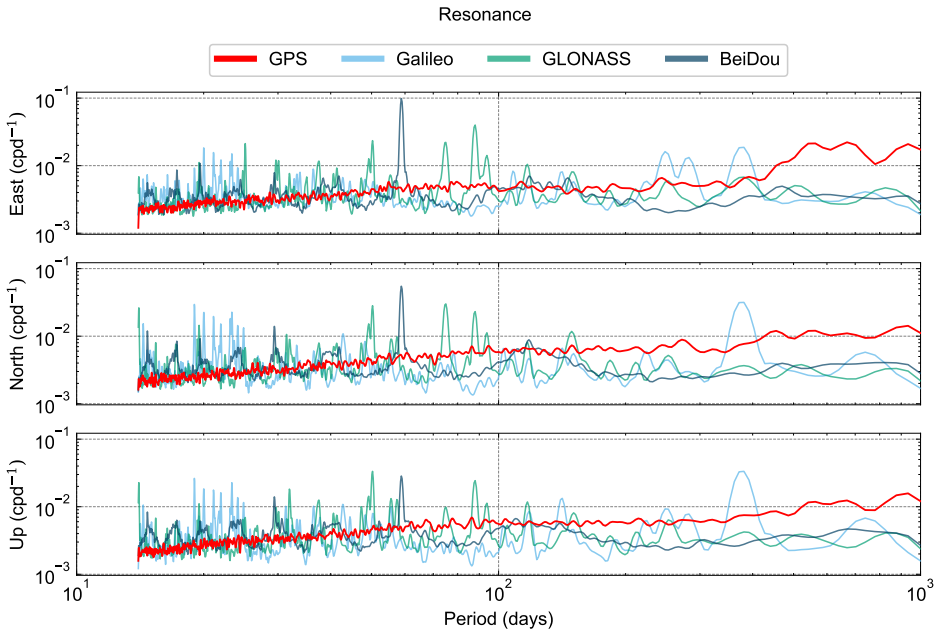

Figure 5.15: Averaged normalized spectra of the positions estimated from simulated measurements and simulated orbits "res".

spectral indices of the estimated PL noise model from the position series. We plot the results for each of the four constellations but only for the "geom" (first column) and "res" (second column) tests. When the geometry of the satellites orbits does not evolve over time ("geom" case), the noise type exhibited by the positions of each station is homogeneously spatially distributed for the four constellations. As previously mentioned, the averaged spectral index for GPS is equal to -0.3, whereas it is equal to zero for the other three constellations. However, when the constellation geometry evolves over time, as it is the case for GPS, we observe that the equatorial stations show a more correlated noise, which comes closer to flicker noise (spectral index of -1). A possible explanation for this might be that the satellite displacement induced by the resonant dynamics affects more the geometry of the station-to-satellite observations at the equatorial stations.

These findings imply that part of the spatial pattern observed in the type of noise with real GPS position series can be explained by the orbital contribution we have identified in this analysis. Indeed, Gobron et al. (2021) explains only part of these spatial patterns by non-tidal loading displacements and shows that loading has less significant impact on the nature of the noise in the position series of equatorial stations than for stations at higher latitudes. Our findings provide a possible explanation of the remaining spatial pattern with the orbital effects we have identified in this analysis.

All together, these results demonstrate that the deviation of the constellation geometry from the nominal configuration also contributes to the emergence of the temporal correlation in the station positioning noise. In particular, we have shown that the larger sensibility of the GPS constellation to the lunisolar gravitational resonance has a negative impact and exacerbate the long-term temporal correlation of the GPS-derived positions. The effect is in particularly strong for equatorial stations. On the contrary, the other three GNSS constellations (Galileo, GLONASS and BeiDou) are not susceptible to introduce correlated positioning noise owing to the better stability of their orbits and constellation geometry over time.

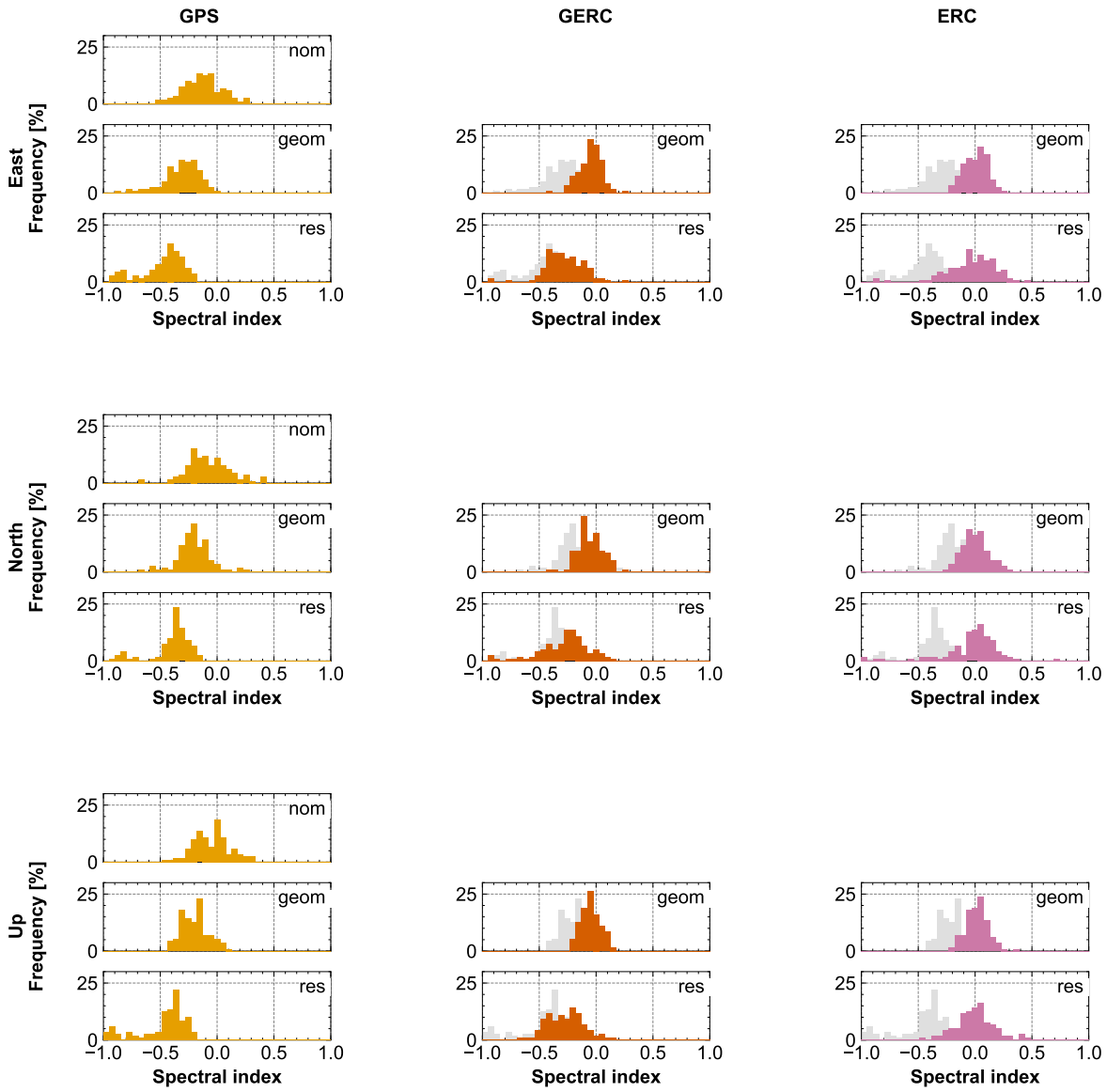

Figure 5.16: Distribution of the spectral indices estimated from multi-GNSS coordinates obtained with the simulated orbits and PPP. GERC refers to the combination of GPS, Galileo, GLONASS and BeiDou. ERC refers to the combination without GPS. The histograms for GPS-only solutions are in light gray in the background for comparison.

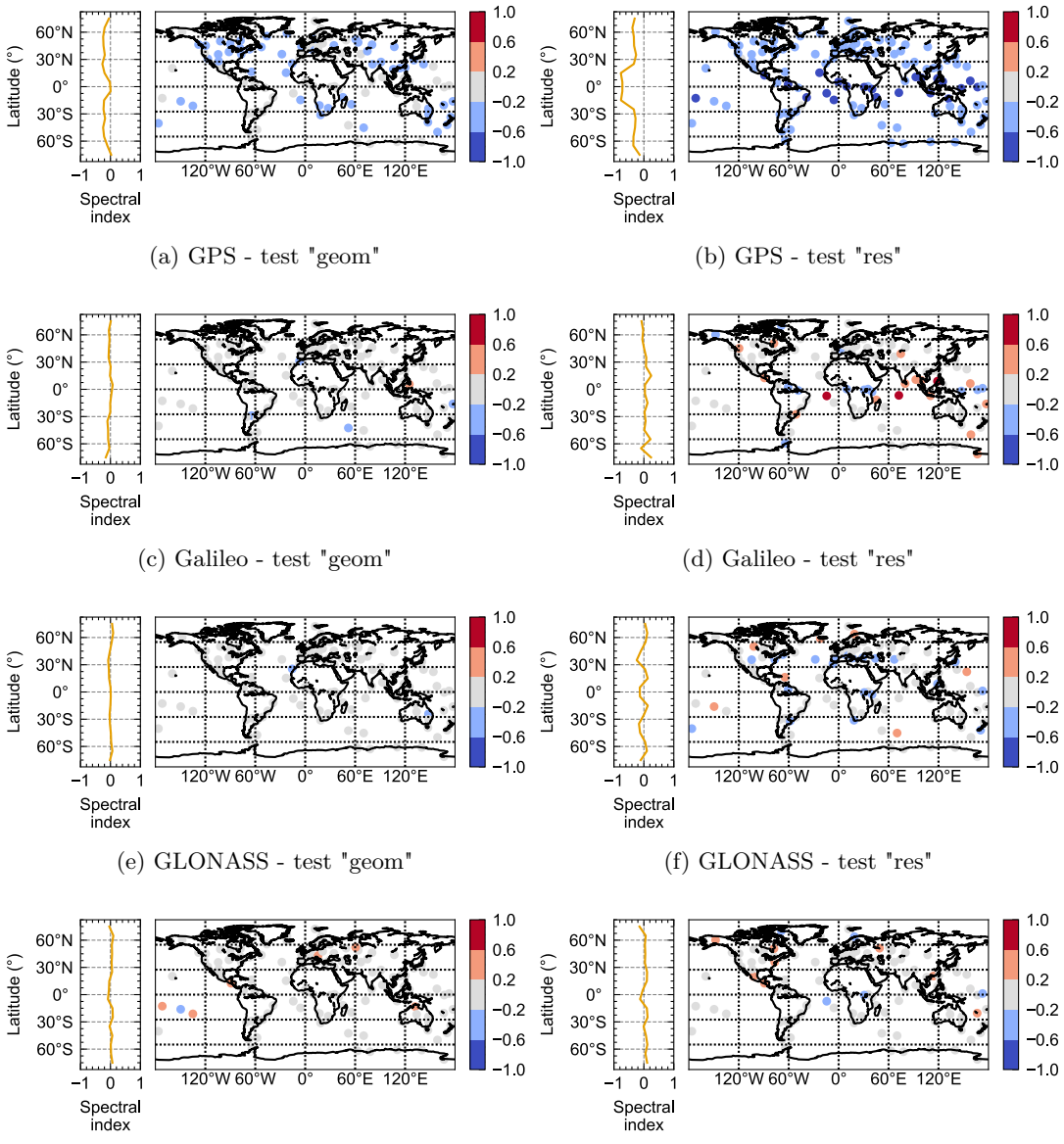

(a) GPS - test "geom"

(b) GPS - test "res"

(c) Galileo - test "geom"

(d) Galileo - test "res"

(e) GLONASS - test "geom"

(f) GLONASS - test "res"

(g) BeiDou - test "geom"

(h) BeiDou - test "res"

Figure 5.17: Global distribution (map) and mean over 10° bins in latitude (left plot) of the spectral index estimated from PPP vertical positions obtained from simulated observations and orbits. The left-handed subfigures (a, c, e, g) are with the Keplerian dynamics initialized with the IGS orbits. The right-handed subfigures (b, d, f, h) are with the resonant dynamics initialized with the IGS orbits.

5.4.3 Confirmation with PPP position time series and real GNSS data

Daily PPP solutions were computed using GRGS orbit and clock products (Katsigianni et al., 2019c) and the GINS software provided by CNES. We processed GNSS data provided from January 2019 to November 2021 for the same network of 118 IGS stations (Figure 5.8). We compare GPS-only and Galileo-only PPP solutions with fixed ambiguity to integers, and GLONASS-only PPP solutions with ambiguity-floating solutions. From these time series, we estimated using pytrf software (courtesy of P. Rebischung) a deterministic kinematic coordinate model with bias, linear rates and offsets as well as constellation-specific periodic signals. For GPS, we include 4 harmonics of the draconitic year (351.2 days). For Galileo and GLONASS, we also estimate 4 harmonics of their respective draconitic year (355.6 days for Galileo and 353.2 days for GLONASS), as well as additional high-frequency signals corresponding to 5 harmonics of the repeat period of the constellation (10 sidereal days for Galileo, 8 sidereal days for GLONASS).

In addition, we fit to the kinematic model using two alternative noise models with and without flicker noise. These two noise models will help us to compare the detection of colored noise in the series from each constellation. We assess the goodness-of-fit of each noise is model to the data with the Bayesian Information Criteria (BIC). This statistical criterion is based on the optimized value of the log-likelihood cost corrected by a term that accounts for the model complexity. The model complexity is determined through the number of estimated parameters in the model, and the number of observations used for the fit. The BIC is computed with the following expression:

$$\mathrm{BIC} = -2\ln(L^*) + k_p \ln(N_{obs})$$

with L^* the optimal value of the likelihood cost, k_p the number of estimated parameters in the model and N_{obs} the number of observations points.

Figure 5.18 shows the difference in the BIC between the two noise models fitted to each series. We use the estimated BIC to attribute the most likely noise model to each series. In this figure, the model with colored noise (flicker noise) is the best model to describe the data if the BIC difference is positive. The absolute value of this difference indicates how distinctly the Maximum Likelihood Estimation (MLE) can identify the difference between the two models.

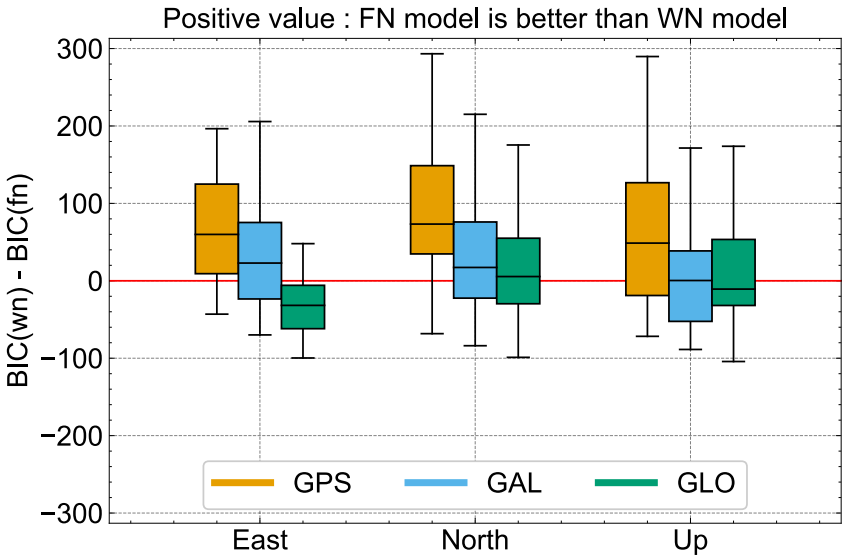

Figure 5.18: Difference in BIC statistics between flicker and white noise model in the real GPS-only, Galileo-only and GLONASS-only PPP positions.

According to this BIC statistics, the correlated noise (flicker noise) is particularly detected in the GPS-only positions. The result is less obvious for Galileo and GLONASS for which the MLE does not separate so clearly between flicker and white noise. One possible explanation is that white

noise predominates in the series making it more difficult to detect flicker noise. This is the case of the GLONASS-derived East positions that have a larger noise level because of the estimated float ambiguities that strongly correlate with the east positions. Nonetheless for Galileo and the two other coordinates (north and up), the BIC differences show that white noise is more predominant in the estimated positions, compared to GPS.

Even if the time span used for this noise analysis is too short to obtain accurate noise model estimations, the PPP solutions obtained with real GNSS data and the observed orbit products support the conclusions drawn from the simulated PPP solutions on the orbital contribution to correlated noise, which is more visible in GPS positions.

5.5 Spatial correlations of colored noise

This section provides a brief analysis of the spatial patterns of the GNSS error correlations, which are not only correlated temporally but also spatially. This analysis is first performed with GPS-only and Galileo-only PPP positions obtained with the real GNSS data. GLONASS positions are not considered because they have much more noise than Galileo and GPS positions. We computed the Pearson correlation between pairs of position time series and compare the correlation ρ with respect to the distance between the two stations d. From these pairwise correlations, we estimate a Gaussian correlation model given by Equation 5.7.

$$\rho(d) = \rho_\infty + \rho_0 * \exp(-(d^2/r^2)) \tag{5.7}$$

with

- d the inter-station distance,
- ρ_∞ the asymptotic correlation (for $d \to \infty$)
- ρ_0 the nugget term
- r the range which gives the distance at which the correlation is reduced by 95 % of the difference $\rho_0 - \rho_\infty$.

The displacements, expressed in the topocentric frame ENU, are converted into a local frame UVH. The UVH frame has been used in recent publications (Benoist et al., 2020; Niu et al., 2023) to analyze the spatial correlation of GNSS positions. The advantage of this frame is that these defined directions are the same regardless of the location of the pair of stations, contrary to the ENU frame. Mathematically, it is defined for 2 points on a sphere, by:

- U in the direction of the great circle between the 2 points, in the orientation A toward B
- V in the direction normal to the great circle, to complete the right-handed frame
- H in the radial (up) direction from the center of the sphere

We then compute two UVH frames for each station of the pair, as illustrated in Figure 5.19.

Figure 5.20a (first two columns) gives the resulting correlations for each pair of stations (dots) and the associated Gaussian correlation models estimated from them (red curves). The dash black curves representing the GPS position correlations model are plotted on the Galileo plots as a reference for the comparison. GPS-only and Galileo-only positions exhibit slightly different spatial correlations. Galileo positioning errors have a moderately reduced spatial correlation on short baselines compared to GPS positions. The common correlation could be attributed to the common loading displacement, but the differences must be specific to one of the constellations.

To remove all common displacements coming from loading or errors common to both constellations (e.g. troposphere), we analyze the series of differences of the GPS-derived and Galileo-derived

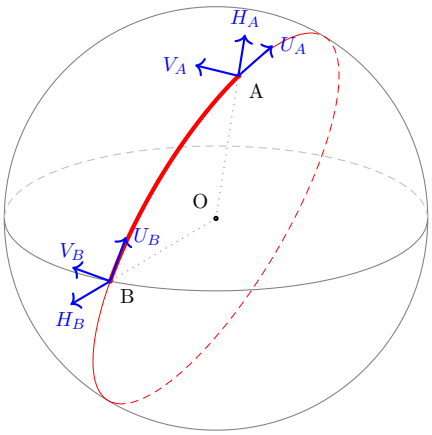

Figure 5.19: Definition of the UVH frame for a pair of stations (A, B) (adapted from Niu et al. (2023))

station displacements. These series are thus reflecting only the effects of the orbit errors or the propagation of a common error, like the troposphere or multipath, through a different orbital geometry evolution (GPS vs Galileo). We compute, similarly to the previous test, the inter-station correlation between the series of differentiated displacements. The differences of displacements observed by GPS and Galileo are also spatially correlated reaching a value of 0.16 to 0.21 at short distances, depending on the directions UVH. In addition, the correlations decrease faster for the displacement differences in the directions U and R, for which the estimated ranges of the Gaussian model are approximately half of the range estimated from the spatial correlation of the displacements themselves. We assumed that these spatial correlations reflect constellation-specific signals.

The same analysis performed with the positions estimated from the "geom" simulated orbits (Figure 5.20b) are not able to replicate the same results. We do not observe any spatial correlation with each of the constellations we simulated (GPS, Galileo or GLONASS). It is therefore likely that these spatial correlations cannot be explained by the type of site-specific errors we considered in the simulations. These spatial correlations can be explained only by constellation-specific errors. Further work would be needed to investigate their potential causes. For instance, possible candidates can be orbit errors that would be simultaneously observed by the stations in the area covered by the pass of the satellite, such as orbit errors from the mismodeling og the solar radiation pressure. Other possible causes might be common spatially correlated errors (such as from atmospheric propagation). Through different observation geometry provided by the constellations, they might propagate differently and thus introduce constellation-specific spatial correlated noise in the estimated station positions.

5.6 Discussion of the results and their implications

To accurately determine geophysical displacements, it is essential to account for colored, mostly flicker, noise in GPS station positions. Currently, the standard approach is to model the noise as a sum of white and colored noise processes. However, this approach does not improve the detection of subtle long-period non-linear Earth deformation hindered in the noise. To be able to observe these displacements, we need to reduce the colored noise in GNSS position time series. To reach that objective, it is first required to understand the mechanisms behind colored noise, including its origins and the extent to which it is generated by GNSS precise positioning. The emergence of new GNSS constellations providing accurate positioning has enabled us to determine the impact of the varying geometry of GNSS orbits on colored noise for the first time.

We demonstrate that the geometry change of GNSS orbits contributes to colored noise. The GPS constellation is particularly susceptible to resonances caused by lunisolar gravitational

accelerations, resulting in significant variations in its geometry that contribute to colored noise in PPP solutions. The Galileo, GLONASS, and BeiDou constellations appear less sensitive to this resonance and thus have more stable satellite geometry over time.

Three factors have been identified as necessary for generating colored noise in station positions: systematic station-dependent errors, an inadequate weighting function for these errors, and a gradually changing constellation geometry. If any of these factors is absent, the level of colored noise will be significantly reduced. As a result, our work opens perspectives for improving the weighting strategy to reduce colored noise in position series derived from the historical GPS dataset.

However, these three factors alone are not sufficient to fully explain the colored noise content in long GPS series. Longer Galileo series and comparisons with BeiDou positioning are needed to separate and quantify the contributions of orbit geometry and other sources of noise. This research complements previous studies examining unmodeled site displacements as sources of noise in GNSS positions, including include random ground or monument motion (Beavan, 2005; King and Williams, 2009; Williams, 2004) and non-tidal surface loading (Gobron et al., 2021; Memin et al., 2020; Rebischung et al., 2017). Our findings suggest that constellation geometry may also play a significant role.

In addition, gravitational accelerations are not the only source of resonance. Solar radiation pressure (SRP) may also contribute to interannual variations of the orbits through resonance currently only modeled with a simple "cannonball" toy model (Lemaître, 2019; McMahon, 2011; Valk, 2008), or through interannual variation of the solar forcing. Furthermore, past research has indicated that GNSS orbit errors may contribute to draconitic signals in GNSS position series (Allahverdi-zadeh et al., 2016; Amiri-Simkooei, 2013; Ray et al., 2008). Since we use a model that filters the periodic dynamics from the orbital period to the annual period, we could not analyze the impact of lunisolar resonance on the monthly, annual or draconitic signals.

The integration of new GNSS systems, such as Galileo and BeiDou, to determine station positions raises questions about how colored noise will change over time. As these systems are included in the data processing, the colored noise content may evolve over a decade or more. This will require more complex noise modeling for multi-GNSS position time series.

As for the spatial correlation of the positioning noise, the difference in GPS and Galileo positions indicates that the orbits or the constellation geometry may contribute to a certain level of the spatial correlation of the noise observed. However, our simulations failed to replicate the same pattern, possibly due to missing factors in our simulation model. One possible explanation for this discrepancy is the contribution of spatially correlated orbital errors that impact similarly all stations that have the same satellites in visibility. Our simulations include only station-dependent errors, and therefore, we may address only the fraction of colored noise that is not spatially correlated. Further analysis of the geographically correlated errors in the orbits is necessary to confirm or infirm this assumption. Another possible explanation would include the effect of the observation geometry associated with additional sources of spatially correlated errors troposphere errors or atmospheric turbulence (Böhm and Schuh, 2013; Nilsson and Haas, 2010; Romero-Wolf et al., 2012). Different constellations like BeiDou and GLONASS could explain the difference between GPS and Galileo as a different geometry of observations would propagate these errors differently to the position.

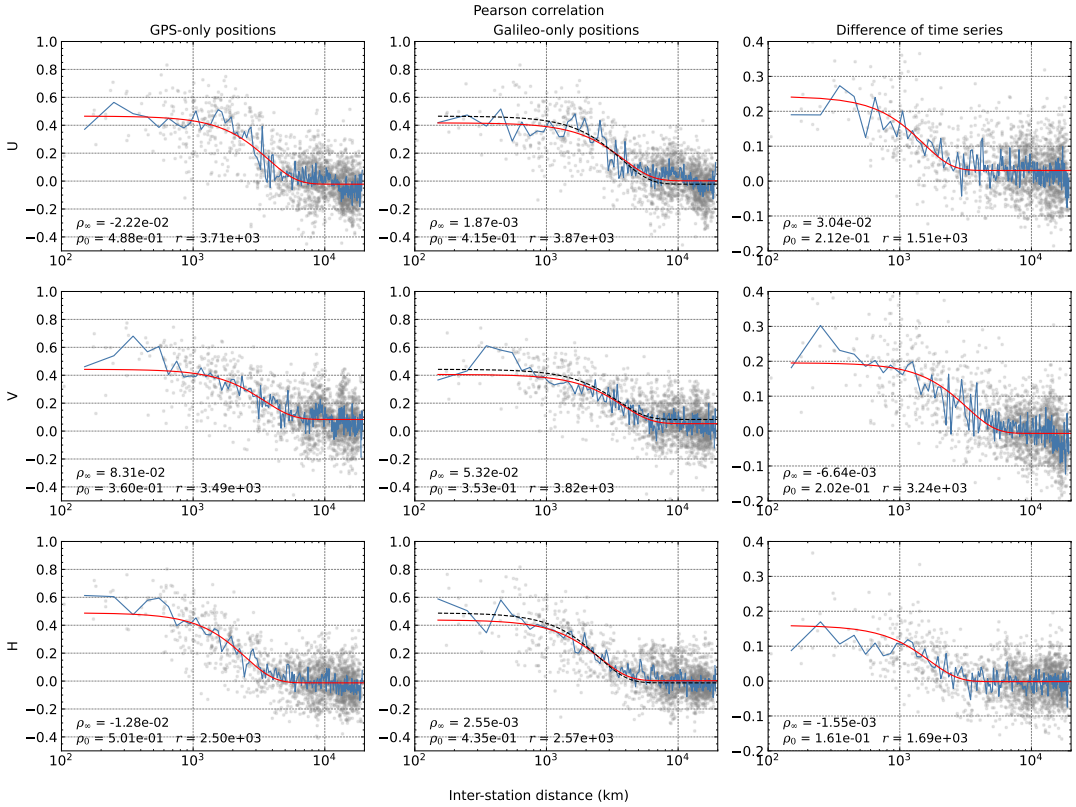

(a) Real PPP solutions: GPS (left), Galileo (middle) and the difference of GPS and Galileo positions (right)

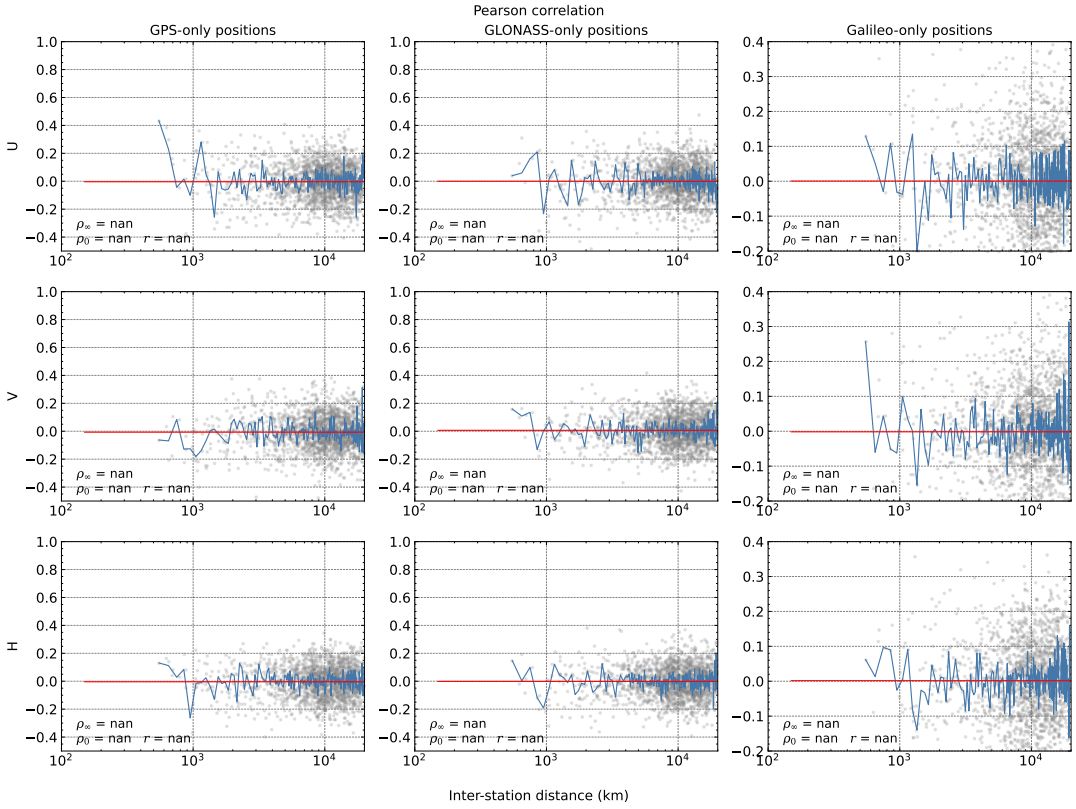

(b) Simulated PPP solutions: GPS (left), GLONASS (middle) and Galileo (right)

Figure 5.20: Pearson correlation of inter-station UVH coordinate time series. Inter-station correlations are represented by the dots, and correlations averaged over bins of 100 km are represented by the blue curves. The red curves represent the estimated Gaussian correlation model.

CHAPTER

6 Flicker noise as a result of stochastic dynamical systems: the case of the midnight orbit discontinuities

6.1 Introduction

The IGS orbit products are disseminated through SP3 files, that include the satellite positions (and optionally velocities) and satellite clock corrections. These products are provided on a 24-hour basis. Between two successive products, we observe discontinuities in the satellite positions, called "midnight orbit discontinuities". They are also referred to as "SP3 positional discontinuities" or "orbit misclosures".

The midnight orbit discontinuities can impact the precision of GNSS positioning. The SP3 precise orbit products are sampled at the integration step used by the IGS analysis centers, typically 5 or 15 minutes. To process GNSS observations, the users of these products need to interpolate the orbit products to determine the positions (and the clock corrections) of the satellites at each observation epoch. Different interpolation approaches are proposed by Schenewerk (2003), and have been examined with the IGS GPS orbits (Yousif and El-Rabbany, 2007). However, the presence of orbit discontinuities can still degrade the interpolated satellite positions, particularly near the day boundaries, leading to a significant reduction in positioning accuracy. Recent publications suggested improvement in the interpolation strategies to mitigate the effects of these orbit and clock discontinuities (Song et al., 2021). This has important implications for PPP applications, such as time transfer (Defraigne and Bruyninx, 2007) and high-frequency precise positioning (seismology, volcanism, etc), which rely on the continuity of estimated receiver/satellite positions and of receiver/satellite clocks that are simultaneously determined.

In addition, these discontinuities are a metric used to assess the repeatability of geocentric satellite positions and the accuracy of the orbit products. They are more rigorous than the historical IGS "orbit accuracy codes" that were provided in the early 2000s by the IGS analysis centers to inform the users about the accuracy of the orbits (Griffiths and Ray, 2009). Furthermore, analyzing the midnight orbit discontinuities helps identifying the error sources in the models used by the IGS analysis centers to determine these orbits. SLR observations between ground telescopes and Laser Reflector Arrays (LRA) embedded on the GNSS satellites can also be used to assess the quality of the estimated satellite orbits (Urschl et al., 2005). In the last three years, the presence of LRAs on GNSS satellites makes SLR ranges the most used metric to uncover modeling modeling errors in the Precise Orbit Determination (POD) and in the combination of the analysis centers products (Masoumi and Moore, 2021; Sakic et al., 2022; Sośnica et al., 2020; Tao et al., 2021; Zajdel et al., 2023). However, their relevance is limited to validating the orbits of satellites equipped with Laser Reflector Arrays (LRAs), such as Galileo satellites, as well as a restricted number of GPS, GLONASS, and BeiDou satellites. For the remaining satellites, orbit validation still relies on GNSS-based internal orbit criterion like midnight orbit discontinuities.

The spectra of orbit discontinuities have provided valuable insights into the POD errors. In their analysis of GPS orbit discontinuities from the 2nd IGS reprocessing products, Griffiths and Ray (2013) observed draconitic signals as well as spectral peaks with periods near 29, 14, 9, and 7

days. These signatures have been attributed to the orbital response to sub-daily tidal errors in Earth Orientation Parameters (EOP) models. Additionally, other factors such as satellite phase center offsets (Steigenberger et al., 2016) or tropospheric modeling (Navarro Trastoy et al., 2022) can also influence orbit discontinuities. In addition, for GPS satellite orbit discontinuities resulting from the 1st IGS reprocessing (Griffiths, 2009) or from the 2nd IGS reprocessing (Choi, 2015), a background noise characterized by a combination of white noise at high frequencies and flicker or power-law noise at low frequencies has been observed. However, the origin of the power-law noise in orbit discontinuities remains unexplained and it is still unclear whether there is a causal relationship between the noise in orbits and the similar background noise observed in station positions.

This chapter aims to achieve two objectives. First, we will investigate the impact of employing alternative procedures for computing midnight orbit discontinuities. Specifically, we will explore whether using the midnight positions directly provided in some SP3 files yields better results. We will also analyze the effects of orbit modeling on the computed daily orbit discontinuities when utilizing the orbit fitting approach. Second, we will conduct an analysis of orbit discontinuities based on the latest 3rd reprocessing orbit products, which includes, for the first time, GPS, Galileo, and GLONASS satellites. We will compare the noise characteristics across these satellite constellations and present a preliminary analysis and results aimed at explaining the source of power-law noise observed in orbit discontinuities.

6.2 Improving the computation of the midnight orbit discontinuities

The principle is to compare the positions of each satellite at the same epoch (near midnight), calculated independently from successive SP3 files. However, the majority of IGS analysis centers deliver SP3 products starting at 00:00:00 UTC and ending at 23:45:00 UTC in the case of 15-min sampled products, and 23:55:00 UTC in the case of 5-minute sampled products. In order to bridge the gap between two consecutive days and obtain satellite positions at the intermediary epoch of 23:52:30, orbit fitting and extrapolation need to be performed. An orbit model is estimated to minimize the satellite's position residuals, which are the differences between the positions derived from the SP3 files and the propagated positions obtained from the estimated orbit model (Griffiths and Ray, 2009). The orbit models from the two consecutive days are then extrapolated both backward and forward to compute the satellite positions. In the following, we will refer to this method as the "orbit fitting" approach. The top row in Figure 6.1 illustrates the steps followed for this analysis.

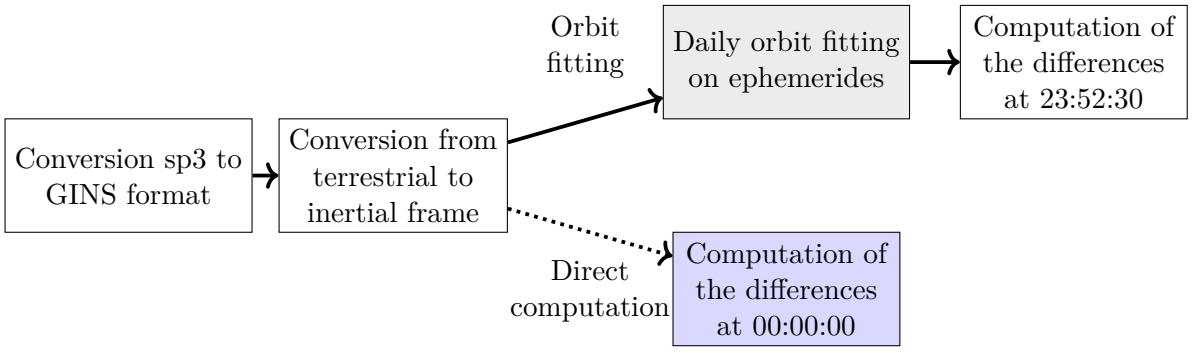

Figure 6.1: Flowchart of the computation of daily orbit discontinuities from SP3 files

Satellite coordinates can be expressed and compared in two different coordinate systems: an Earth-fixed system and an inertial system. An inertial system refers to a non-rotating coordinate system that remains fixed relative to distant stars, while an Earth-fixed system represents a rotating coordinate system that remains fixed relative to the Earth's surface. When comparing satellite positions in an Earth-fixed system, both the positions computed in each daily batch and

the earth orientation parameters (EOPs) determined simultaneously with satellite positions are actually compared (Lutz et al., 2016). Therefore, to isolate and accurately assess orbit consistency, we have computed the orbit differences in an inertial frame.

While estimated orbit discontinuities serve as accurate indicators of satellite position precision, it is important to note that errors arising during their computation can impact the accuracy of this metric. On one hand, a potential issue is the underestimation of orbit discontinuities if the successive SP3 orbit solutions are not independent. This is the case, for instance, of the CODE and GRGS analysis centers that generate their orbit products by applying different methods at midnight. Between two successive days, CODE uses continuity constraints and GRGS uses overlapping arcs. On the other hand, Griffiths and Ray (2009) highlighted that the "orbit fitting" approach can lead to an overestimation of orbit errors by approximately 8 mm RMS. This discrepancy can occur when the orbit model used to propagate the satellite position is not fully consistent with the model used by the analysis center for orbit determination. Alternatively to the "orbit fitting" approach, it is possible to directly compute orbit discontinuities when the SP3 files contain satellite positions from midnight to midnight of the next day. This approach will be referred to as "direct computation" in the following. Certain analysis centers, such as CODE or TUG, are indeed providing this information. In the upcoming section, this approach (in the blue box in Figure 6.1) will be tested to evaluate the precision of the orbit discontinuity computation strategy.

6.2.1 Impact of orbit modeling on daily orbit discontinuities using orbit fitting approach

To extrapolate the SP3 orbits, we fit over an entire day a dynamical model including the gravitational accelerations due to the Earth's static field and the tides (solid earth tide, ocean tide, solid earth pole tide, ocean pole tide). Among the various orbital perturbations affecting GNSS satellites, non-conservative accelerations arising from direct solar pressure radiation (SRP) are the second most significant factor, yet the least precisely modeled. Accurately modeling this contribution is challenging, particularly for satellites with limited information available (e.g., GLONASS or GPS) or when satellites pass through the Earth's shadow. To address these modeling uncertainties, empirical models like ECOM (Empirical CODE orbit model) have been developed. Recent studies have demonstrated that the latest version of ECOM yields improved performance specifically for Galileo and GLONASS satellites (Arnold et al., 2015; Sidorov et al., 2020; Tseng, 2021). Moreover, whenever available, these empirical models are combined with a semi-analytical macro-model of the spacecraft. This macro-model commonly takes the form of a box and wings model, and it incorporates a priori or estimated values of the spacecraft's surface properties. The integration of this macro-model contributes to even better performance in terms of orbit accuracy. Therefore, to evaluate the performance of these new models, our analysis initially focuses on testing and comparing the ECOM1 and ECOM2 models. Additionally, we test the contribution of an a priori SRP model during the process of fitting and extrapolating the SP3 satellite positions. This procedure is illustrated in the gray box within Figure 6.1.

6.2.1.1 ECOM and box-wing models

The most used model for mitigating the impact of SRP modeling errors on GNSS satellite orbits are the ECOM models which are expressed in the DYB coordinate system (Beutler et al., 1994). This coordinate system uses the satellite's center of mass as the origin. The D-axis points toward the direction of the vector satellite-sun and the Y-axis points along the solar panel direction. The B-axis is perpendicular to the D-Y plane to complete a right-handed system.

The ECOM models represent the SRP acceleration in the given coordinate system as a harmonic decomposition, which accounts for constant biases and periodic accelerations at the orbital frequencies and their harmonics with the argument of latitude u of the satellite with respect to the Sun's position (Figure 6.2). This decomposition allows us to accurately analyze the behavior

of the SRP acceleration and its variations over time. The first model ECOM1 introduced in (Beutler et al., 1994) has 9 parameters (Equations 6.1). This is the model used in Griffiths and Ray (2009) to analyze the orbit discontinuities of the IGS REPRO1 orbit products. Arnold et al. (2015) introduced extended ECOM (or ECOM2) models that account for higher harmonics ($2u$) to better retrieve the SRP model discrepancies during POD. The ECOM2 models with 7 parameters are given in Equations 6.2.

$$\begin{cases} D(u) = D_0 + D_C \cos(\Delta u) + D_S \sin(\Delta u) \\ Y(u) = Y_0 + Y_C \cos(\Delta u) + Y_S \sin(\Delta u) \\ B(u) = B_0 + B_C \cos(\Delta u) + B_S \sin(\Delta u) \end{cases} \tag{6.1}$$

$$\begin{cases} D(u) = D_0 + D_{2C} \cos(2\Delta u) + D_{2S} \sin(2\Delta u) \\ Y(u) = Y_0 \\ B(u) = B_0 + B_C \cos(\Delta u) + B_S \sin(\Delta u) \end{cases} \tag{6.2}$$

with $\Delta u = u - u_s$ with the argument of latitude of the satellite u, and of the subsolar point (projection on the orbital plane of the position of the Sun) u_s as defined in Figure 6.2.

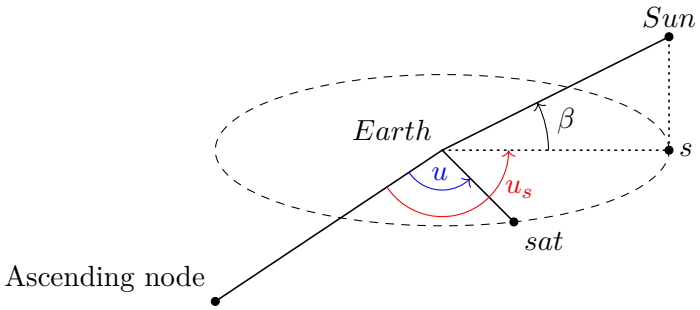

Figure 6.2: Angles describing the satellite-Sun geometry in ECOM models

Box-wing macro-models decompose the SRP acceleration applied to spacecraft by a sum of acceleration applied on various plates. The box represents the platform, while the wing represents the solar panel. The parameters for this model include the surface and optical properties of each plate, which can be derived during POD processing by minimizing the estimated ECOM parameters and their systematic signatures (e.g. bias, dependence on the β angle) (Duan and Hugentobler, 2022; Duan et al., 2019). For Galileo, prior knowledge of these parameters is available from the Galileo Satellite Metadata (European GNSS Service Centre). The SRP model is limited during eclipses, even with box-wing macro-models. This is because we do not know the satellites' attitude perfectly during the eclipse when the absolute value of β is less than or equal to 13.8° for GPS, 14.4° for GLONASS, and 12.4° for Galileo.

6.2.1.2 Results of the comparison of SRP models

In this analysis, we aim to compare different configurations for modeling the SRP accelerations while fitting the daily orbit models. We test the inclusion of a macro-model, specifically the GRGS2021 macro-model that is applied for the generation of the alternative REPRO3 products by the GRGS analysis center. Additionally, we vary the parameters estimated in the empirical ECOM model. We then compute the midnight orbit discontinuities for each of the configurations and evaluate the impact of these changes on the discontinuities. The orbit discontinuities are expressed in the satellite local frame RTN defined by the radial (center of the Earth – center of the satellite's mass), the along-track and cross-track directions (cf Appendix A) to interpret them in terms of model errors. We will present the following results for the REPRO3 products provided by the IGS analysis center TUG from 2018 to 2021. We use these products because they give us two independent estimates of the satellites' positions at midnight (one for each adjacent day). Table 6.1 gives for each constellation (GPS, Galileo and GLONASS) and each direction (RTN) the reduction in the variance of the orbit discontinuities series between a reference setting and the three other orbit models tested. As the TUG orbits have been generated using macro-models

combined with ECOM2 models, the setting GRGS2021+ECOM2 is taken as a reference that should give the more consistent results, and therefore be the most accurate.

Table 6.1: Variance reduction (in mm^2) in the TUG REPRO3 orbit discontinuities due to dynamic modeling strategies. The reduction is given with respect to GRG2021 + ECOM2, which is the setting used for GRGS REPRO3 products. Negative values mean that the test model is better than the reference.

SRP model		GPS			Galileo			GLONASS		
Macro-model	Empirical	R	T	N	R	T	N	R	T	N
None	ECOM2	119.84	177.92	4.94	253.96	239.95	8.64	278.77	337.69	9.86
None	ECOM	-8.30	-1.63	2.79	-8.30	-1.63	2.79	4.03	21.90	-2.61
GRGS2021	ECOM	-0.51	-9.49	4.60	-14.87	-3.75	-0.83	7.52	11.68	-2.28

In Figures 6.4b, 6.4c and 6.4a, we see samples of time series of the orbit discontinuities for each constellation. The color of the point is dependent on the value of the β angle, that is the angle between the direction of the sun and the orbital plane. The darker the color, the lower the β angle is, meaning that the fraction of the satellite orbit crossing the Earth's shadow is larger.

In the second columns of 6.4a, Figures 6.4b and6.4c, we observe that in the absence of any apriori macro-model (the SRP accelerations are only modeled with the ECOM model), the new ECOM2 model introduces artificial signatures during eclipse seasons, and results in degraded orbit discontinuities. The variances of the series are increased by up to 330 mm^2 in the radial and along-track directions (first row in Table 6.1). On the contrary, the macromodel+ECOM and macromodel+ECOM2 combinations have similar performance and are both able to mitigate the signatures during the eclipse visible in the radial and along-track direction. But, it has moderate differences in the cross-track direction.

Overall, in the absence of exact knowledge about the macro-model used by the IGS analysis centers for POD, the ECOM model as applied in Griffiths and Ray (2009) still give the best trade-off. This is particularly the case for the GPS (or GLONASS) satellites for which each analysis center may develop its own macro-model.

6.2.2 Validation with the direct use of midnight position discontinuities from SP3 files

Some IGS analysis centers provide SP3 files with positions from midnight to midnight included. This gives direct orbit discontinuities independent of any orbit fitting discrepancies. Although direct computation is currently available for a limited number of analysis centers, a comparison is performed to assess the accuracy of the "orbit fitting" method.

However, errors may still remain due to inconsistencies with frame transformation from terrestrial to inertial. Indeed, the SP3 files give the satellite positions in a terrestrial frame, but and the computation of the orbit discontinuities requires the orbits to be in an inertial frame. This can be achieved by either using the EOPs estimated, simultaneously with the orbits, by each analysis center or by using the same EOPs for all products and comparing them in the same inertial frame, not necessary the one used for the orbit determination. In the first case, both the satellite positions and the estimated EOPs are compared while in the second case, only the satellite orbits are compared. In this analysis, the second approach was used to compute and compare the orbit discontinuities. The following tests were always performed with TUG products. We compare them with the orbit discontinuities computed with the configuration GRGS2021+ECOM2 by the "orbit fitting" approach. We chose this configuration because it is the most similar to what the TUG analysis center has used for the generation of the orbits (Strasser, 2022). Figure 6.3 gives

the RMS of the 3D orbit discontinuity differences computed with the "orbit fitting" approach and the direct computation.

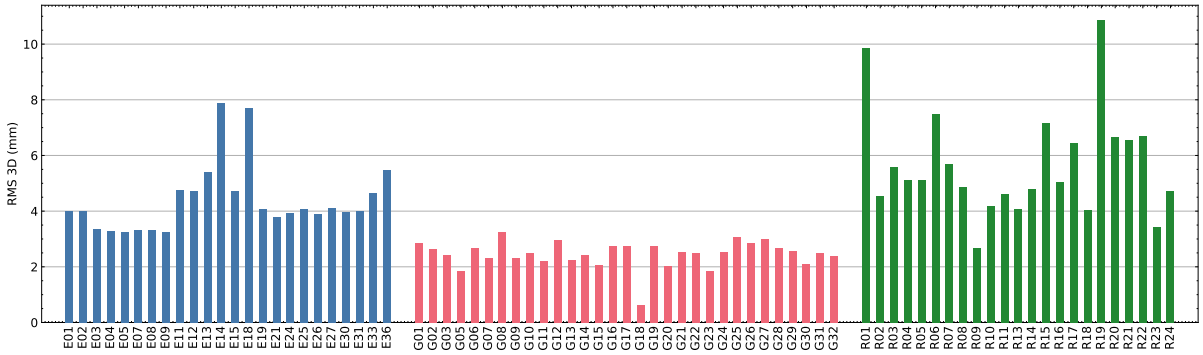

Figure 6.3: Differences of the orbit discontinuities computed from the "orbit fitting" and "direct" approaches for Galileo (E), GPS (G) and GLONASS (R) satellites.

The "orbit fitting" approach has not the same precision for all constellations. The estimated orbit discontinuities are twice worse for Galileo than for GPS. The differences between the two computation methods were found to be 2 mm RMS for GPS and 4 mm RMS for Galileo, with up to 8 mm RMS for Galileo eccentric satellites. This is a significant improvement over the estimated 8 mm of noise introduced by orbit fitting in (Griffiths and Ray, 2009). For GLONASS, differences range from 2 mm to 10 mm RMS. These results can be compared the noise of 8 mm added by orbit fitting as estimated for the GPS constellation in the REPRO1 results in Griffiths and Ray (2009). We retrieve here the differences of the orbit modeling between the constellations, as already observed in Table 6.1.

The "orbit fitting" approach overestimates orbit discontinuities due to the inconsistencies between the orbit modeling used for the generation of the products and the orbit fitting. The errors on the estimated orbit discontinuities differ between constellations, with the method being more accurate for the GPS satellites than for the Galileo or GLONASS satellites. This makes it important for the analysis centers to provide SP3 products that include the satellite positions from midnight to midnight of the next day

6.3 Analysis of the midnight orbit discontinuities of the multi-GNSS REPRO3 orbit products

6.3.1 Overall statistics

Based on the results of the preliminary analyses presented in the previous section, we compute the midnight orbit discontinuities using the "orbit fitting" approach. We test the orbit products between January 2018 and December 2020 for six IGS analysis centers that provided multi-GNSS solutions for REPRO3. Because we do not necessarily have the information about the macro-model used by each analysis center, we use the ECOM model without applying any a priori macro-model. Figure 6.5 presents the root mean square (RMS) of the orbit discontinuities in the satellite local frame, which is defined by the radial (Earth to satellite), along-track, and cross-track directions (see Figure A.1).

We observed variations among the different constellations as well as among analysis centers for the same constellation. Part of them can come from the estimation errors of the orbit discontinuities, but the variations that are above the precision of the estimation still enable to assess the quality of the orbits. In terms of the magnitudes of the discontinuities, both GPS and Galileo orbits exhibit similar performance, with values ranging from 1 cm up to 3 cm RMS, and outperform GLONASS orbits, where the orbit discontinuities range from 2 cm in the radial direction to 10

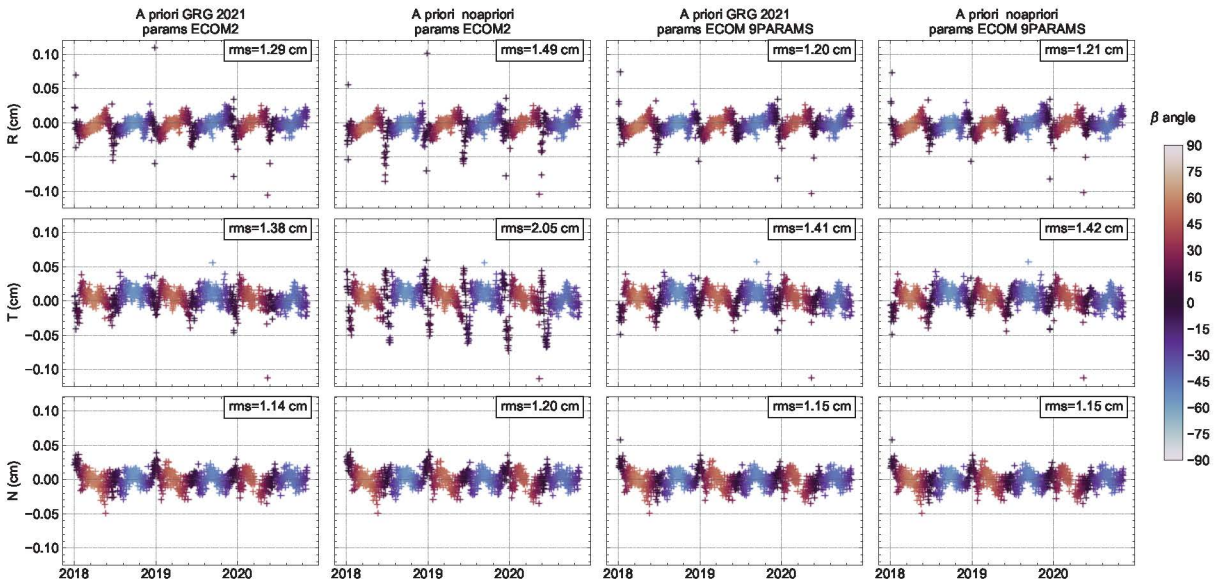

(a) TUG - Satellite G01

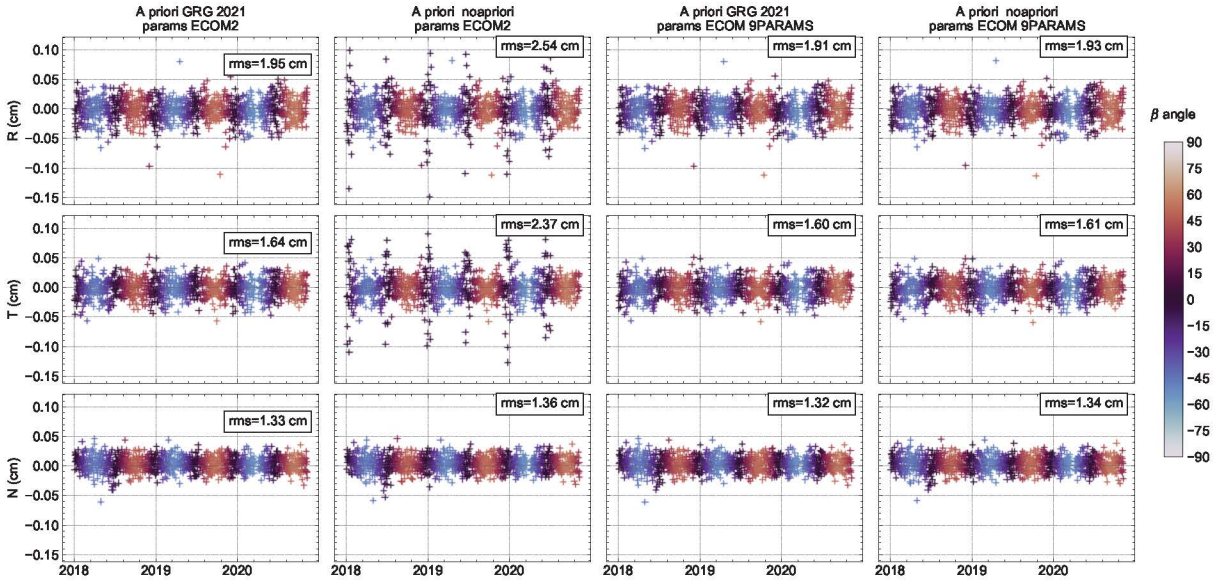

(b) TUG - Satellite E01

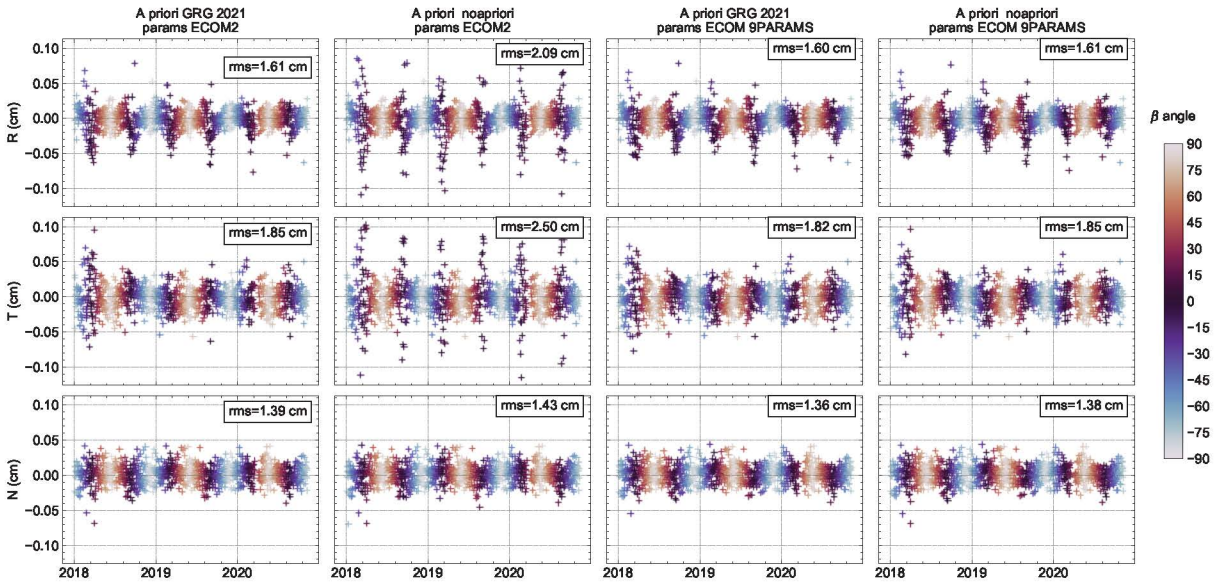

(c) TUG - Satellite R02

Figure 6.4: Time series of orbits discontinuities based on REPRO3 TUG orbits products - effects of different orbit dynamics strategies

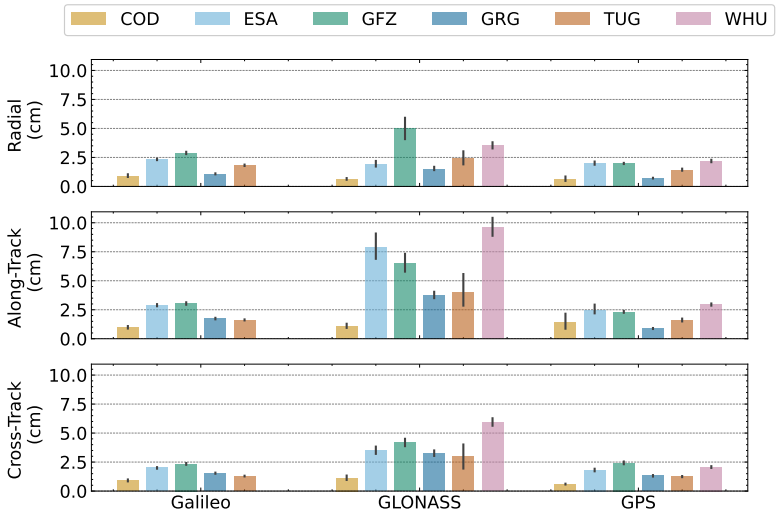

Figure 6.5: RMS of orbit discontinuities

cm RMS in the along-track direction. The accuracy of GLONASS orbits can be influenced by various factors, such as the quality of spacecraft dynamical modeling. The current accuracy of GLONASS box-and-wing models, if utilized by an analysis center, is inferior to that of GPS and Galileo due to the lack of detailed information regarding spacecraft materials, even with re-estimated optical coefficients (Duan et al., 2020). Additionally, the ECOM empirical models do not yield the same performance for GLONASS satellites than for GPS or Galileo satellites (Prange et al., 2017).

We also observed significant differences among the analysis centers, with the most notable being the smaller orbit discontinuities in CODE products, followed by the GRGS that applies orbit overlaps. In fact, these discontinuities are 2 to 3 times smaller compared to the other centers. This discrepancy arises from the fact that CODE utilizes a larger processing window of 72 hours, which is constructed by stacking normal equations, instead of the usual 24-hour window. In particular, the estimation of stochastic pulses at midnight is equivalent to constraining the position and velocity to be continuous at that epoch (Beutler et al., 1996). Consequently, two pairs of positions around midnight become strongly correlated, resulting in smoothed and reduced orbit discontinuities. This is of interest for the PPP applications mentioned above, but at the same time, it artificially hides the true orbital error, which is what we are focused on in this chapter.

6.3.2 Periodic signatures

For each analysis center, we additionally calculated the normalized power spectra of the orbit discontinuities for each individual satellite and stacked them according to the respective constellations. The averaged spectra can be found in Figure 6.6a, while Figures 6.6b to 6.6d provide closer views of the higher frequencies.

Draconitic signals

In Figure 6.6a, strong peaks can be observed at the harmonics of the constellation draconitic year, which represents the repeat period for the geometry of the satellite-Sun-Earth system. These peaks are particularly strong for GPS in all three directions. When we look at the time series of the orbit discontinuities for a GPS satellite (Figure 6.4a), we observe the pattern that evolve with the value of the β-angle. In particular, we see that the orbit discontinuities are larger when the satellite passes through the eclipse season (β|-angle between $\pm 13.9°$). Thus, this pattern has a period equal to the draconitic frequencies, and may be the cause of the larger draconitic signals.

Aliased tidal signals

In the spectra of the orbit discontinuities, long-period signals may appear in the fortnightly frequency band. These signals result from the beat between errors in the high-frequency tidal model for Earth Orientation Parameters (EOPs) and the 24-hour processing windows used in the product analysis (Griffiths and Ray, 2013; Kouba, 2003). A new EOP tides model based on the ocean tides atlas TPX08 has been applied in the REPRO3 processing (Desai and Sibois, 2016; Egbert and Erofeeva, 2002). However, the effects of this model on orbit quality, specifically on the midnight discontinuities, have not been assessed yet.

In Figures 6.6b to 6.6d (bottom plots), most of the aliasing signals in GPS orbit discontinuities discussed in Kouba (2003) and Griffiths and Ray (2013) (represented by red lines in the figures) have disappeared. The errors in model for the subdiurnal tidal variations of the EOPs were found to be the cause of these signals. The "Desai & Sibois" model, which is used to generate the REPRO3 products, is an improved model that includes additional subdiurnal tides. However, a 13.15-day signal (Griffiths and Ray, 2013), remains in the orbit discontinuities of the REPRO3 products. This signal that closely agrees with the theoretical frequency of 13.17 days can be attributed to the aliasing of errors in the OO1 tide (period of 22.31 hours) within the EOP tide model. In the case of GRGS and GFZ orbits, there are also aliased signals at approximately 14.70 days. This signal can correspond to the aliasing of errors in the M2 tide or in the 255,545 tide, which has a period of 12.42 hours. Indeed the theoretical period is of 14.77 days for the M2 aliasing and of 14.73 days for the 255,545 tide (Griffiths and Ray, 2013). This indicates mismodeling errors in these tidal components, but due to the limited spectral resolution from only 3 years of data, it is not possible to determine the exact sources of these signals.

Finally, we observe additional aliasing signals in the orbit discontinuities that do not correspond to any tide reported in Table 1 in Griffiths and Ray (2013). This table only lists the largest tides included in the IERS EOP tidal correction model. With the same propagation model described by the authors, I expanded the list of the possible aliasing tidal signal in the orbit discontinuities to all tides included in the Desai & Sibois' model. In Figure 6.7, we plot the period of the aliasing signals for the 12-hour tides (left panel) and the 24-hour tides (right panel). The black dots in this figure illustrate all the possible aliasing signals that may occur from errors in the Desai & Sibois' model.

For GPS, all orbit products exhibit a strong signal at 15.38 days in the cross-track direction. This signal could correspond to the aliased periods of either the tides τ_1 (147.555, 25.67 hours) or 256.554 (12.40 hours), as both generate an aliased signal at approximately 15.387 days. However, this signal is not visible in the Galileo or GLONASS orbits. Rather, in the cross-track direction of the Galileo orbit, there is a distinct peak at 2.73 days, which is consistently present regardless of the orbit products. Similarly, a signal at approximately 4.96 days is observed in the GLONASS orbit.

Because these signals are common to all products, we can reasonably think that these are aliasing signal from errors in the EOP model. If the signals in the Galileo and GLONASS orbits are from the same errors than the signals in the GPS orbits, then this suggests that there is a constellation-specific propagation of the errors. In the propagation model that we use, the aliasing

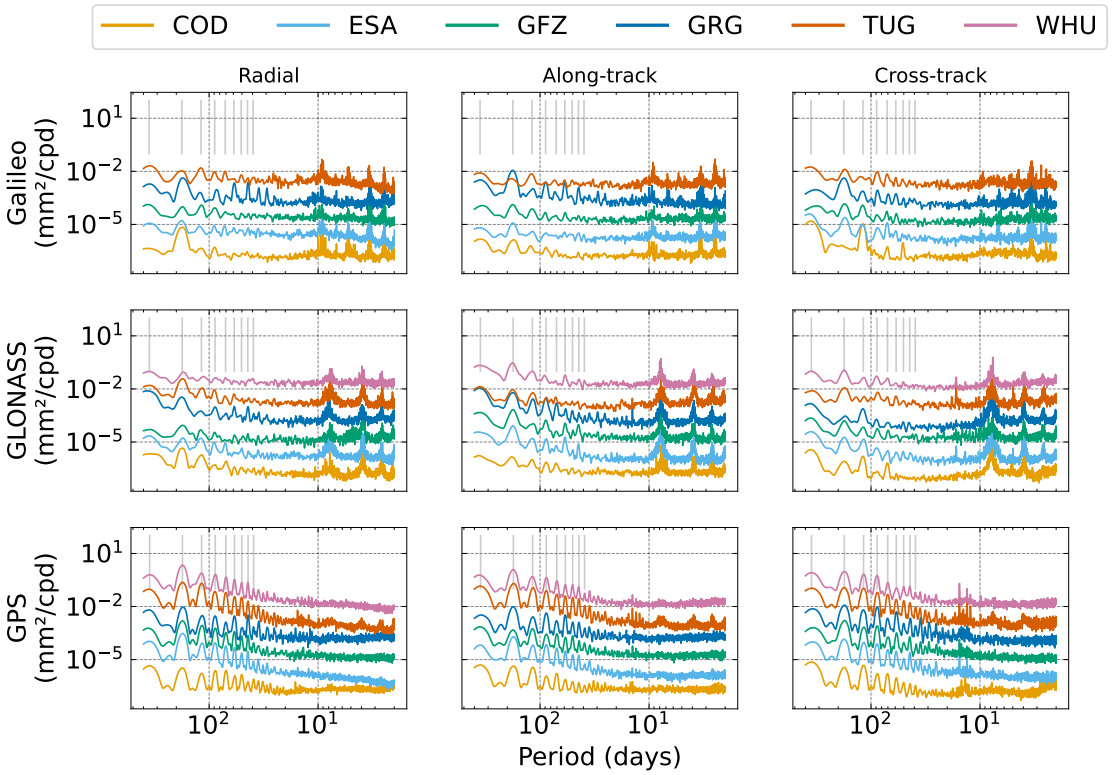

(a) Full spectra

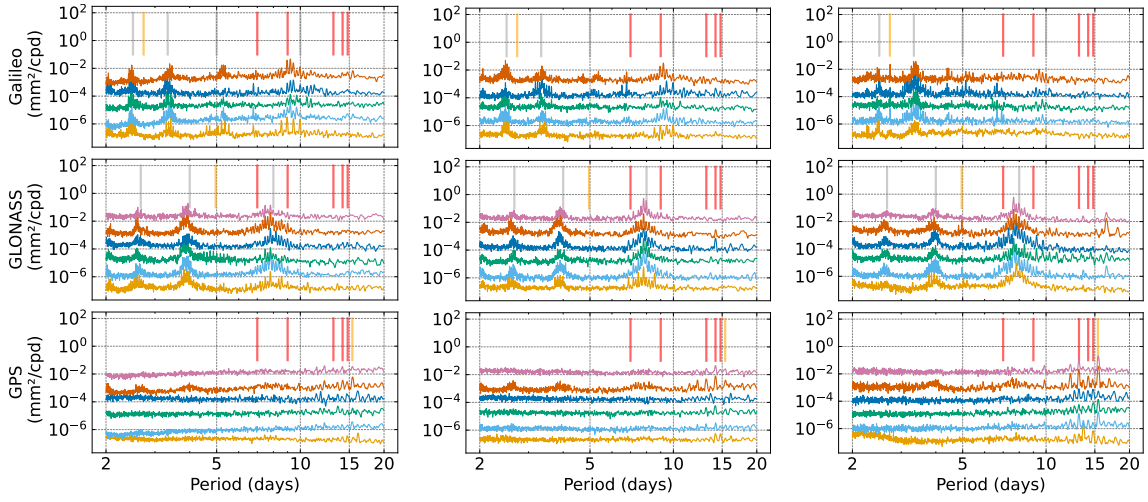

(b) Zoom - Radial (c) Zoom - Along-track (d) Zoom - Cross-track

Figure 6.6: Normalized power spectra of the orbit discontinuities for different analysis centers. The curves have been shifted by a factor 10^i for visualization purposes. The gray lines represent constellation-specific signals (top: draconitic, bottom: constellation repeat for Galileo and GLONASS), red lines the aliased tide signals already observed, orange lines are observed signals that remain unexplained.

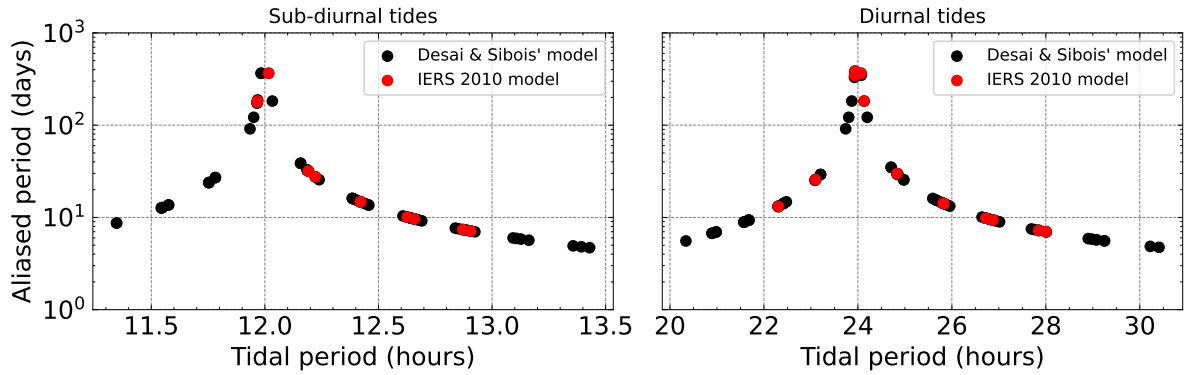

Figure 6.7: Alias periods (vertical coordinates) for the tidal frequencies (horizontal axis) included in the Desai & Sibois' model assuming 24-hour sampling. The black dots correspond to the tides that are only included in the Desai & Sibois' model, the red dots are the tides included in the IERS and the Desai & Sibois' models.

only depends on the tide period and whether it affects the retrograde or prograde part of the polar motion, and the sampling frequency, that is 24 hours corresponding to the arc length for the generation of the orbits.

In summary, the REPRO3 orbits have reduced aliasing signals due to errors in the subdiurnal tide EOP model thanks to the improved Desai & Sibois' model. However, additional aliasing signals, corresponding to newly added tides are visible at periods depending on the constellation. These signals cannot be explained by the available propagation model introduced in Griffiths and Ray (2013), which neglects the orbital characteristics of the constellation.

Orbital signals

In the GLONASS orbits, we observe wide combs centered around 8 days, as well as the harmonics of this frequency, in all three RTN directions. Similarly, for Galileo orbits, signals at the period of 10 days and their harmonics are visible across all analysis centers' products. These signals, which directly refer to the constellation repeat period can be attributed to errors in orbit dynamics modeling, just like the draconitic signals. Comparable signatures have also been observed in station positions spectra determined by PPP and discussed in Chapter 3 (refer to Section 3.3.2.1).

In TUG products, the GLONASS-related signals at the harmonics of 8 days appear to propagate to the orbit discontinuities of GPS satellites. This can be observed in the three directions RTN in the brown curves in the bottom panels of Figures 6.6b, 6.6c, and 6.6d. Since we test orbit products that are determined with multi-GNSS solutions, it is assumed that this effect may be due to differences in TUG's weighting strategy for attributing the weights to observations from each constellation (GPS, Galileo and GLONASS) when generating their solutions.

6.3.3 Background noise

We can also compare the background noise of the orbit discontinuity spectra in Figure 6.6a. The background noise in the orbit discontinuities is similar to the background noise observed in the station positions. At high frequencies, the orbit discontinuities follow a white noise. However, at low frequencies, the nature of the noise seems to be dependent on the constellation. We use Maximum Likelihood Estimation (MLE) to infer noise models for each satellite and orbit product. We estimate the parameters of a noise model, as well as sinusoidal signals at 10 first harmonics of the draconitic frequencies for all three constellations. For Galileo and GLONASS, we also estimate the harmonics of the constellation repeat period. As for the noise model, for Galileo and GLONASS, we only estimate a power-law model whereas for GPS orbits, which evidences two

different regimes in the low and high frequencies according to the spectra shape (Figure 6.6a), we also include white noise. The solid bars in Figures 6.8a to 6.8c give for each direction (RTN) the variance σ_{PL} and the spectral index of the power-law model, and for GPS we additionally compare the variance σ_{Wh} of the white noise.

The analysis of the values of the spectral index gives information about the presence of colored noise in the orbit discontinuities. As for the Galileo and GLONASS orbit discontinuities, the spectral indices of the power-law model is closer to 0, which means that noise is predominantly white. For the GPS satellites, they are close to -1 for all directions RTN, and all analysis centers except for CODE. Indeed, for these products, we observe a noise closer to random walk (spectral index of -2). Nevertheless, the values of the variances σ_{PL} for CODE are 2 to 10 times smaller than for the other products, indicating that the noise present in the CODE orbit discontinuities is much smaller. In consequence, the separation of the noise model parameters is more difficult because of the lower noise. Indeed, MLE is based on the computation of the gradient of the likelihood function, and with smaller change in the noise type the variations of the gradients are not large enough to be able to discriminate the optimal values of the model parameters. This is also the case for GRG products for which the variance σ_{PL} of the PL noise. For these two analysis centers' products, the results cannot be interpreted with the other products as the orbit discontinuities are artificially small.

Then, we examine the variance of the white noise in the high frequencies. For that, we compare the values of σ_{Wh} for GPS, and σ_{PL} for Galileo and GLONASS (which is possible because the spectral index is approximately 0). The level of the white noise for the Galileo and GPS satellites are equivalent for the three directions, while the variance of the white noise for GLONASS satellite is between 40 and 100 mm in the along-track direction (Figure 6.8b), and between 20 and 50 mm inthe cross-track direction (Figure 6.8c), that is 2 to 5 times larger than for Galileo and GPS satellites. One analysis center (TUG, in dark orange) provides significantly better GLONASS orbits.

Finally, we tested the sensitivity of the flicker noise to the presence of the signals during the eclipses, that we have previously observed in the GPS orbit discontinuities time series (Figure 6.4a). Indeed, these signals are characterized by temporal variations of the mean of the discontinuities during the eclipses, and thus could contribute to the observed flicker noise. So, we also performed the same noise analysis with the series in which we removed the days when there was one orbital plane in the eclipse season. The results are given in Figures 6.8a to 6.8c with the hatched boxplots. This test shows that there is not significant influence of the eclipses on the estimated type of noise.

In conclusion, flicker noise is mainly observed in all GPS orbit discontinuities, while Galileo orbit discontinuities seem better described by only white noise. For GLONASS, no clear conclusion can be drawn, possibly due to the poorer quality of GLONASS orbits compared to GPS and Galileo. The white noise dominates over the flicker noise, if any for GLONASS. The difference in the nature of the noise in orbit discontinuities raises questions regarding the origin of the GPS-specific flicker noise, which will be investigated, but also questions about whether this can impact the noise observed in station positions.

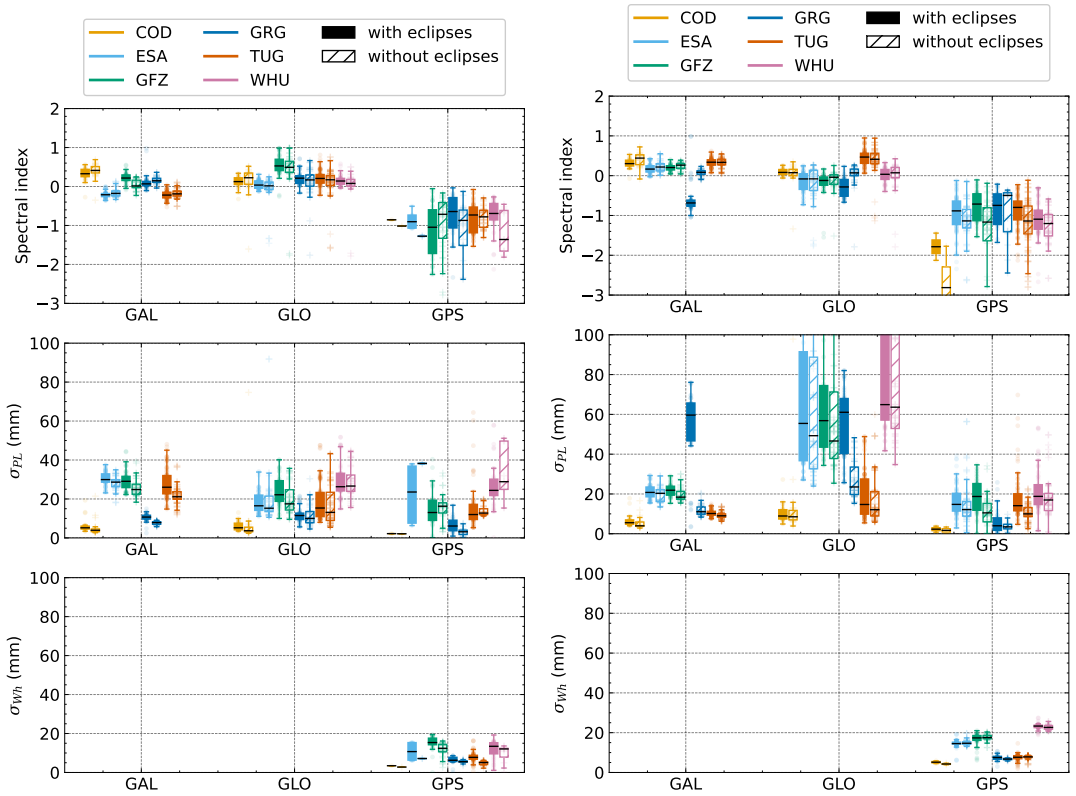

(a) Radial

(b) Along-track

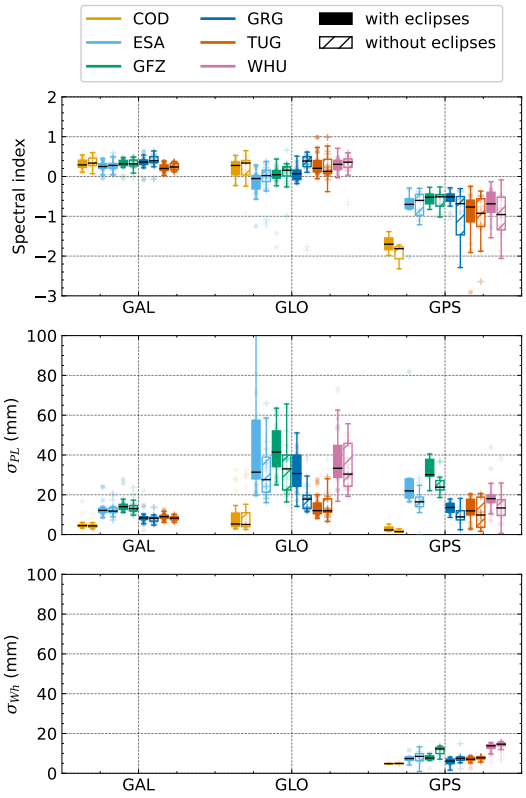

(c) Cross-track

Figure 6.8: Noise model parameters estimated from the midnight orbit discontinuities in the RTN directions.

6.4 Investigation of the origin of the flicker noise in midnight orbit discontinuities

In the previous section, we analyzed the midnight orbit discontinuities of REPRO3 precise orbit products provided by six IGS analysis centers. We demonstrated that the background noise differ between the constellations, in particular flicker noise appears specific to the GPS satellites. We investigate in this section one possible explanation for the emergence of flicker noise only in the GPS orbit discontinuities, which is the effect of stochastic perturbations of the spacecraft's dynamics induced by either fluctuations of the spacecraft's response (e.g. attitude), or by the environment (eg. solar flux). In reason of the complexity of identifying and modeling the dynamical response which is dependent on accurate knowledge not only of each component of the satellite (control law, materials) but also of the environment, our analysis is limited to oversimplified toy models. Despite their simplicity, the preliminary results of such analysis could give insight into potential sources of noise in the orbits.

6.4.1 Noise in the orbital elements and orbit discontinuities: Santamaria & Ray's toy model

In this section, we have re-implemented in Python a simple toy model that was developed to identify the type of noise needed in satellite positions to result in flicker noise in the orbit discontinuities. The principle is to generate a continuous sinusoidal signal $s(t)$ of period T_0, over 1000 days, into which a power-law (PL) noise $n(t)$ is introduced. Five types of PL noise are tested: white noise (WN), flicker noise (FN), random-walk noise (RW), integrated flicker noise (iFN) and integrated random-walk noise (iRW). For each noise type, we generate 10 realizations of noisy sinusoidal signals $s_n(t) = s(t) + n(t)$. For each realization, daily fitting is then performed on $s_n(t)$ of a sinusoidal signal of fixed period T_0. We obtain then a fitted sinusoidal signal $\tilde{s}(t)$, that represents the daily orbit fit and from which the midnight discontinuities are computed. This test will be referred to as "sine" model. In Figure 6.9, we plot for each type of introduced noise the spectra of the midnight discontinuities averaged over the 10 realizations. Table 6.2 summarizes the nature of the noise present in the discontinuities for each type of added noise in $s(t)$.

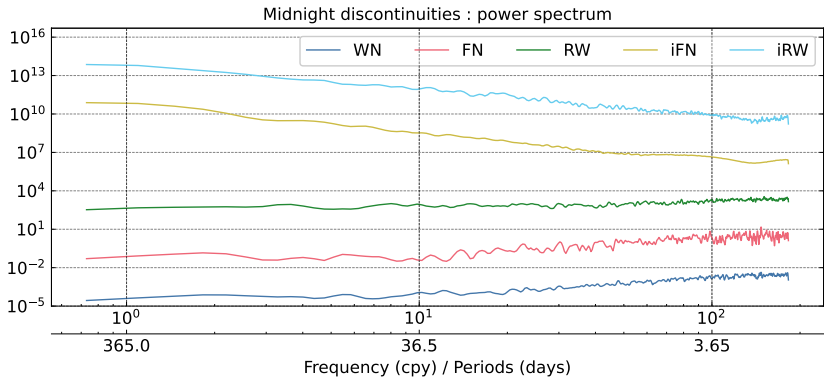

Figure 6.9: Stacked spectra of the simulated discontinuities with the "sine" model

The result of this test shows that the noise found in the orbit discontinuities is equivalent to the differentiation of the noise in the coordinates themselves. Indeed, the spectral index of the noise in the discontinuities is exactly the spectral index of the input noise minus two, which corresponds to the differentiation in the spectral domain. Among the noise tested, this is hence the integrated flicker noise that is able to explain flicker noise in the GPS orbit discontinuities.

Table 6.2: Spectral index of the noise in the discontinuities in function of the type of noise introduced in the sinusoidal signal with the "sine" model

Input noise		Noise in the discontinuities	
Type	Spectral index	Type	Spectral index
White noise	0	Violet noise	2
Flicker noise	-1	Blue noise	1
Random-walk noise	-2	White noise	0
Integrated flicker noise	-3	Flicker noise	-1
Integrated random-walk noise	-4	Random-walk noise	-2

As a consequence, the emergence of the flicker noise in the orbit discontinuities necessitates the presence of integrated flicker noise in the coordinates of the satellites. Yet, this type of noise is never encountered in the GNSS-derived parameters. In addition, there are not many known physical processes that would generate such noise type.

6.4.2 Extension of the toy model to the orbital elements: noise generated by stochastic accelerations

According to the previous test, an integrated flicker noise must be present in the Cartesian positions of satellites to produce flicker noise in orbit discontinuities. However, Cartesian coordinate, even in the satellite's local RTN frame, are not the natural coordinates for expressing a satellite's state and therefore for characterizing and interpreting the origin of noise in orbits. Furthermore, the positions of the satellite do not account for all information about the dynamics of the satellites, which required at least 6 parameters. We then propose an extension of the previous test using the 6 Keplerian parameters, which will be called "extended" model in the following.

As in the toy model, we generate a continuous ephemerides for a GPS satellite by propagating the Gauss' variational equations for the Keplerian parameters (Appendix A) from an initial bulletin. Our goal here is to identify or at least emulate a physical source of the noise observed in orbits. Indeed, correlated noise in a dynamical system's output could result from the presence of stochastic processes affecting its dynamical response. It is necessary to model the dynamics of a system that is no longer deterministic but stochastic. This can be addressed within the framework of stochastic differential equations, the basic principles of which are presented below.

Let be Z the state vector of the satellite defined by the Keplerian elements $[a, e, i, \omega, \Omega, M]$. We define the differential equations followed for the vector Z by

$$\dot{Z} = f(Z,t)dt + g(Z,t)dW \tag{6.3}$$

, where

- $f(Z,t)$ is the Gauss equations (see Appendix A)
- $g(Z,t)$ is the noise matrix representing any stochastic accelerations resulting either from stochastic forcing, or stochastic dynamical response of the spacecraft
- dW is the derivative of a Brownian motion, white noise

The integration of the equations gives

$$Z(t) = Z_0 + \int_0^t f(Z(u), u)du + \int_0^t g(Z(u), u)dW(u) \tag{6.4}$$

The first integral in the given equation represents the standard solution to the differential equations. The second integral is derived from the integration of a stochastic process, commonly referred to as Ito's integral. Similar to how numerical methods are used to approximate integrals, Ito's integral can also be approximated using an extension of Euler's algorithm, known as the Euler-Murayama algorithm (Øksendal, 2003). We use the Python implementation of this algorithm available in the library *sdeint* that can be retrieved online via pypi [1].

For this analysis, choosing the shape of the matrix $g(Z, t)$ was the most challenging part. We tested a simple model with an additive noise independent of Z, with no dependency between the noise in the 6 Keplerian parameters. The matrix $g(Z, t)$ is then a diagonal matrix with constant values

$$[\sigma_a^2, \sigma_e^2, \sigma_i^2, \sigma_\omega^2, \sigma_\Omega^2, \sigma_M^2] = [10^{-4}, 10^{-10}, 10^{-10}, 10^{-10}, 10^{-10}, 10^{-10}]$$

This is equivalent to the toy model mentioned earlier but with random walk noise introduced in each Keplerian parameter.

As for the toy model, the second step is daily orbit fitting performed based on the continuous ephemerides previously generated. We implemented a simplified version of orbit fitting that iterates only over the initial bulletin of the satellite and uses a fixed orbit model (Keplerian motion) to propagate the orbit. The optimal solution is found by minimizing the satellite positions residuals (observed positions - propagated positions). The fitted orbits are then converted into Cartesian coordinates to compute the midnight orbit discontinuities. In Figure 6.10a, we plot the time series of the midnight orbit discontinuities, and in Figure 6.10b associated the power spectra.

When white noise is introduced in the dynamics of the satellite, we can observe orbit discontinuities of several centimeters that are comparable in terms of magnitude with the one that we can observe in the IGS orbits. In addition, the slopes of the spectra of the discontinuities, which represent the spectral indices κ of the power-law noise model, range between -1.08 and -1.27. The noise is then close to flicker noise. These results indicates that flicker noise in the orbit discontinuities can be caused by sources as "simple" as white noise, compared to the complex integrated flicker noise identified with the toy model. This would hence be interesting to investigate the possible relationship between white noise in the dynamics, or equivalently random-walk noise in the Keplerian parameters, and an integrated flicker noise in the satellite Cartesian coordinates. A possible method could be to investigate the propagation of noise through the matrix relation used to convert the Keplerian parameters into Cartesian coordinates.

This analysis suggests that the flicker noise present in orbit discontinuities can stem from simple stochastic processes in the satellite dynamics. We identify that the addition of white noise acceleration, or equivalently random walk noise in orbital parameters, can be a possible cause of flicker noise in the orbit discontinuities. While the exact sources of this noise are still unknown, examining the noise content in the orbital parameter series from the IGS products is needed to confirm this hypothesis.

[1] https://pypi.org/project/sdeint

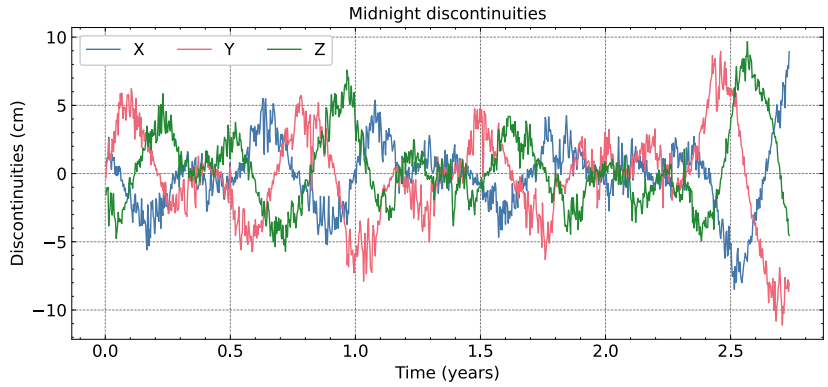

(a) Time series of the midnight orbit discontinuities

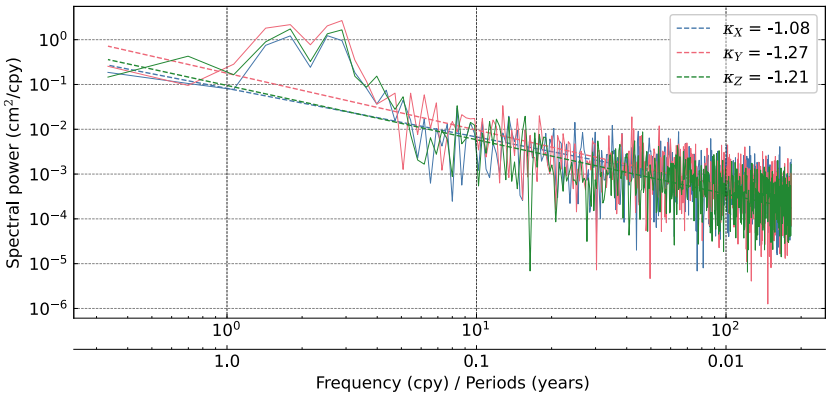

(b) Power spectra of the midnight orbit discontinuities

Figure 6.10: Midnight orbit discontinuities obtained with the "extended" model

6.5 Discussion and conclusions

The recent publications focus on using SLR observations to evaluate the quality of GNSS orbit products. Analyzing the daily orbit discontinuities can provide additional insights into model errors and help to better understand the spectral characteristic of geodetic series derived from GNSS. Our analysis of orbit discontinuities of the REPRO3 products shows a reduction in aliasing signals caused by errors in the model of subdiurnal variations of EOPs due to ocean tides used in the REPRO3 products. This is consistent with the better agreement between Desai & Sibois' model and the EOP estimates from GNSS as reported in Zajdel et al. (2020). However, we found that the model for the OO1 tides does not agree with GNSS data, resulting in aliased signals at 13.17 days. This is confirmed by the aliasing signals corresponding to the same tide that have also been observed in the station position spectra in Rebischung et al. (2021).

In addition to these aliasing signals, we have also observe constellation-specific signals in Galileo and GLONASS orbits that are common to all products. These cannot be directly explained by the aliasing signals of the EOP model as predicted in Griffiths and Ray (2013), although a logical cause might still be this model. One possible explanation could be that the propagation of the tidal errors in EOPs model, described in this paper, is not working for Galileo or GLONASS orbits. For instance, it does account for the 24-hour sampling of the orbit generation, but the orbital characteristics of the constellation are absent. As for the draconitic signals that were already observed in the GPS series, similar signals are present in the Galileo and GLONASS orbits but are less predominant compared to the GPS draconitic signals. If the better orbital modeling can explain the results for Galileo, for GLONASS, another explanation is needed. Indeed, the variance of the white noise in the GLONASS orbits is much larger than for GPS or Galileo, and thus may hide part of the draconitic peaks. For Galileo and GLONASS, we do observe significant signals at the harmonics of each constellation repeat period up to 10 days. The

same signals were also found in the station positions determined by Galileo- or GLONASS-only observations (see Section 3.3.2.1), indicating a common origin or a propagation of orbital errors to the observations between the station and the satellites.

The second focus of this chapter is analyzing the noise content in the orbit discontinuities. They exhibit different types of noise depending on the constellation, with colored or flicker noise being predominantly visible in the GPS orbits. This suggests that some amount of the noise is specific to each constellation's or satellites' design. We investigated one possible explanation through the simulation of the computation of the orbit discontinuities. We included stochastic accelerations in the dynamics of a GPS satellite. This simple model demonstrates that additive noise in the dynamics of the satellites can introduce temporal correlation in the noise in the orbit discontinuities. Multiple physical origins may cause stochastic fluctuations of the accelerations applied to the satellites or of the dynamical response of the satellite, that may differ between GPS and the other constellations. For instance, the satellite attitude may fluctuate over time. Previous studies about GPS' attitude have focused on modeling the yaw of the satellite (Bar-Sever, 1996; Kouba, 2009; Montenbruck et al., 2015), no published analyses of the remaining attitude variations, in particular stochastic variations. The published analyses of the deviations to the nominal satellite's attitude with other missions such as GRACE give a glimpse about the noise in the attitude law (Goswami et al., 2018; Yang et al., 2022). Another potential factor could be a different sensitivity of the satellite's response to stochastic environmental forcing such as the variation of the solar irradiance (Montillet et al., 2022) on the magnitude of the SRP accelerations. To investigate this, stochastic differential equations with multiplicative noise instead of additive noise, as we did in this work, can also be constructed based on Gauss variational equations. Contrary to additive noise, multiplicative noise is depend on the satellite state (i.e. Keplerian parameters) over time, and may be used to test the effects of white noise introduced in the RTN directions or directly in the forces' model (Cresson et al., 2013; Pierret, 2015). The model that I developed to extend the toy model in this study could be used in future research to analyze the sensitivity of the GNSS orbits to specific stochastic perturbations or errors introduced in the satellite dynamics.

The flicker noise is found in the GPS orbit discontinuities and in the GPS-only station position series. However, the causal relationship between the orbit noise and positioning noise is not self-evident. For instance, we detect the same amount of flicker noise in the position series regardless of the orbit products we used, including the CODE products where the orbit discontinuities are very low. However, this does not exclude the possibility of having a common source of noise impacting both the orbit discontinuities and the station positions.

CHAPTER

7 Conclusion and perspectives

The Global Navigation Satellite Systems (GNSS) currently provide millimeter-to-centimeter precise positioning of points on the surface of the Earth. The interpretation of the GNSS-derived displacements as geophysical processes requires the thorough identification and understanding of the systematic errors present in the GNSS position time series. This thesis aims to improve our understanding of the systematic errors that affect precise GNSS position time series. It focuses on two sources of these errors: the subdiurnal ocean tide loading (OTL) model errors and the temporal and spatial correlations of the positioning noise. To investigate these errors, we compare different GNSS constellations, in particular the Galileo constellation which provides the opportunity to study the impact of the constellation design. By using multiple GNSS constellations, we can conduct a more comprehensive analysis of systematic positioning errors.

7.1 Main contributions of this thesis

7.1.1 Assessment of OTL modeling errors and impact on GNSS precise positioning

Part 1 of this thesis assesses subdiurnal ocean tidal loading displacement model errors and their propagation at longer periods observed in the GNSS position time series.

In Chapter 3, we developed a new static estimation strategy, based on the addition and estimation of OTL displacement parameters in the PPP processing and the stacking of normal equations over a long period, typically one year. Compared to the usual kinematic strategy, that relies on the extraction of the residual OTL displacements from sub-daily PPP positions, the estimates from the static strategy have reduced formal estimation errors. Indeed, stacking the normal equations enables to reduce the correlations between the estimated parameters, and thus the propagation of errors to the OTL parameters' estimates from troposphere parameters, which is not accessible, and thus unknown, from the kinematic approach, for instance. Second, we sought to identify the systematic errors of each constellation (GPS, Galileo and GLONASS), that contaminate the estimation of the OTL model errors. The GPS-specific orbital signals, perturbing the observation of the K1 and K2 tide frequencies, can be avoided by using Galileo (or GLONASS) observations, improving by up to 50 % the assessment of the K1 and K2 tidal displacement modeling errors. Besides, the eastward tidal displacements have been accurately estimated using Galileo observations for the first time, thanks to the capability to process them with integer carrier-phase ambiguities. In this context of multi-GNSS observations, we applied an optimal weighting strategy, specific to each constellation and each tide frequency to reduce the sensitivity of the estimated OTL modeling errors to the limitations of each constellation.

Chapter 4 examines the impact of OTL model errors on the systematic signals in the GNSS position time series, particularly the propagation of sub-diurnal tidal errors to long periodic signals. From the analysis of the currently available propagation model and the analysis of the

PPP position time series, we identified different propagated signals at fortnightly and seasonal frequencies for the three constellations involved in the REPRO3 products: GPS, GLONASS, and Galileo. In particular, we isolated without ambiguity for the first time the aliased signal at 13.6 days, which is generated by the GPS constellation only. This indicates that the Mf tidal displacement modeling errors cannot be observed with the GPS constellation. The separation of Mf tide modeling errors and aliased signals of subdiurnal tide modeling errors can be achieved by using the Galileo constellation. Similarly, the seasonal displacements estimated from GPS observations are impacted by the aliasing of the errors in the K1 and K2 tide model, which can explain the discrepancies between GNSS and the other geodetic techniques. We showed that these aliased signals does not occur with the Galileo constellation. In addition, we found that using the static estimation, as presented in Chapter 3, can reduce these aliasing signals by including the empirical OTL parameters recovering the subdiurnal OTL modeling discrepancies in PPP processing.

7.1.2 Linking GNSS satellite orbit errors to the colored noise in the GNSS position time series

Part 2 of this thesis discusses the contribution of orbital dynamics to the flicker noise observed in the GNSS position series. While previous research on the origin of noise in GNSS position series has primarily focused on environmental factors such as geological processes and surface loading, we address three points in this part:

Colored (or flicker) noise in multi-GNSS series

While different periodic signals between the constellations were observed in the position time series, this work is the first to observe differences in the correlation of the noise in both the position time series and the GNSS orbits. The analyses of the GNSS PPP positions time series in Chapter 5 and the analyses of the GNSS orbit midnight discontinuities in Chapter 6 indicate that the colored (or flicker) noise is significantly stronger in GPS-only products, which suggests that part of this noise is constellation-specific. In the scope of this thesis, we investigated the potential orbital origins of this GPS-specific flicker noise.

Orbital contributions to the colored noise in the PPP positions

In Chapter 5, we examined the interannual stability of the GNSS constellation geometry. We showed that the GPS satellites are more prone to a drifting behavior than the other GNSS constellations (Galileo, GLONASS, and BeiDou) owing to a larger sensitivity to the resonance caused by the lunisolar gravitation. We then demonstrated that the resulting deformation of the GPS constellation geometry is a contributing factor to the colored noise in the position series.

The difference in the noise contained in the orbit discontinuities gives insight into the other GPS-specific orbit errors, such as the presence of stochastic accelerations applying to the satellite. In Chapter 6, we introduced a simple model, based on stochastic differential equations, to test this hypothesis. We found that the colored noise in the orbit discontinuities may result from a "simple" white noise perturbation present in the dynamics of the satellite. Several physical processes, that remain to be investigated, can cause these stochastic accelerations. Further research is needed to better link these stochastic accelerations to the physical behavior of the satellites.

Mechanism underlying the propagation of orbit errors to correlated errors in GNSS positioning

In Chapter 5, we identified three factors that contribute to the emergence of flicker noise in the station positions:

1. The time-varying observation geometry caused by long-term instability in satellite orbits
2. The presence of observation errors that do not average to zero over satellite elevations
3. The limitations of observation weighting in mitigating these errors

All the three factors are present only in GPS-derived positioning, and explain a fraction of the observed flicker noise that is not spatially correlated.

Furthermore, further research is needed to determine if there is an actual relationship between the flicker noise in orbit discontinuities, analyzed in Chapter 6, and the noise in station positions. It is worth noting that not all GPS orbit products contain flicker noise in the orbit discontinuities, whereas the station position series do, whatever the origin of the orbit products. Investigating mechanisms that involve all the parameters estimated in the network solutions (orbits, EOPs, and station positions) may help reveal a more complex propagation mechanism.

7.2 Perspectives and suggestions for future work

Identification and mitigation of other sources of systematic signals in GNSS-derived time series

While the methods developed in Part 1 focus on analyzing OTL model errors, they could be extended to investigate other sources of periodic errors in PPP positioning resulting from orbital or environmental factors. For example, the atmospheric "tides" at S1 and S2 frequencies are not commonly included in all GNSS data processing strategies, despite being a recommended correction in the IERS conventions (Petit and Luzum, 2010). The currently available model has not shown significant advantages when used with GPS-only positions. For example, the S2 tide modeling using a pressure field with a 6-hour resolution does not provide accurate enough displacement predictions for positioning. Additionally, we demonstrated the possibility of adding empirical parameters to account for periodic subdiurnal displacement errors. This is particularly useful when accurate knowledge or models are difficult to obtain, such as with periodic displacements of monumentation or bedrock due to thermal expansion. It may be possible to derive GNSS models for these errors.

Identifying contributing factors of correlated noise in position series opens up opportunities for future research to improve the quality of the series by reducing correlated noise levels, particularly with the increasing use of multi-GNSS observations. This makes the deployment and maintenance of stations tracking multi-GNSS observations, including Galileo and BeiDou, even more important. In this thesis, for example, we found only a limited global dataset with Galileo observations available in multi-GNSS RINEX3 format. Denser regional networks providing multi-GNSS data could be used to perform detailed geophysical studies, such as observing and analyzing the geographical propagation of the tidal loading displacements in certain regions of interest.

For historical datasets containing only GPS observations, which are important for obtaining long series, future research is needed to improve our understanding of systematic observation noise from environmental factors (e.g., multipath, troposphere) or antenna calibration (phase center location).

For example, because individual antenna calibration does not necessarily exist for all stations, one can use a common calibration to one type of antenna, neglecting the properties variability between all produced antennas. In addition, most GNSS processing strategies assumes an observation weighting function that are estimated from a sub-network of stations, and averaged over several

days. Reducing the observation noise or developing better weighting strategies to mitigate its effects on positioning (e.g., improving observation weighting, accounting for variation in observation geometry) would not only improve the precision of the positions but also help to reduce the time-correlation of the errors in the longest series.

As for the orbital contribution to the correlated noise, we have only started to explore the topic. Our work opens questions about how the orbits could contribute to the spatial correlation of positioning errors. For example, variations in orbital errors or observation geometry could influence how orbital or observation errors (e.g., spatio-temporal troposphere variations) would propagate to station positions.

Modeling of GNSS-derived time series

Identifying different types of systematic periodic signals and noise with different constellations raises issues for processing and modeling future multi-GNSS position series. Currently, most strategies are based on GPS-only series. In the future, handling the diversity of remaining systematic errors (periodic signals or stochastic content) will become increasingly important for improving the accuracy and reliability of GNSS positions for geophysical and geodetic applications. Most current coordinate models assume that time series characteristics remain constant over time (same noise, same periodic signals). However, with the progressive integration of multi-GNSS constellations in GNSS processing, these characteristics are more likely to vary with the weights of each constellation's observations in position solutions. Few publications currently address how statistical models or strategies could handle this type of time series.

7.3 Conclusions en français

Les systèmes de positionnement par satellite (Global Navigation Satellite Systems, GNSS) permettent actuellement de positionner des points à la surface de la Terre avec une précision de l'ordre de quelques millimètres à quelques centimètres. L'interprétation des déplacements estimés par GNSS en tant que processus géophysiques nécessite une identification et une compréhension approfondies des erreurs systématiques présentes dans les séries temporelles de positions GNSS. L'objectif de cette thèse est d'améliorer notre compréhension des erreurs systématiques présentes dans les séries temporelles de positions GNSS. Elle met l'accent sur deux aspects de ces erreurs : les erreurs sous-journalières des modèles de surcharge des marées océaniques (OTL) et les corrélations temporelles des erreurs de positionnement. Pour étudier ces erreurs, nous comparons les différentes constellations GNSS actuellement disponibles, en particulier la constellation européenne Galileo. En utilisant plusieurs constellations, nous pouvons en effet analyser plus spécifiquement l'impact de la constellation elle-même (type d'orbites, erreurs d'orbites).

Principales contributions de cette thèse

Évaluation des erreurs de modèles OTL et leur impact sur le positionnement précis par GNSS

La première partie de cette thèse traite des erreurs du modèle de déplacement subdiurnes dus aux surcharges de marées océaniques et de leur propagation à des périodes plus longues.

Dans le chapitre 3, nous avons développé une nouvelle stratégie d'estimation, dite statique, basée sur l'ajout de paramètres d'un modèle de déplacement OTL estimés lors du traitement PPP, ainsi que sur le cumul des équations normales sur une longue période, typiquement un an. Par rapport à la stratégie dite cinématique, qui repose sur l'extraction des déplacements OTL résiduels à partir des séries de positions PPP sous-journalières, les erreurs estimées avec la stratégie statiques sont plus précises, avec des erreurs formelles réduites. En effet, le cumul des équations normales permet de réduire les corrélations entre les paramètres estimés, et ainsi la propagation des erreurs d'autres modèles, par example de la troposphère, aux estimations des paramètres OTL. Ensuite, nous avons cherché à identifier les erreurs systématiques à chaque constellation (GPS, Galileo et GLONASS) susceptibles de contaminer l'estimation des erreurs du modèle OTL. Les signaux orbitaux spécifiques à la constellation GPS, perturbant l'observation des fréquences de marée K1 et K2, peuvent être évités en utilisant les observations Galileo (ou GLONASS). Ce qui améliore jusqu'à 50 % la précision de l'estimation des erreurs de modélisation du déplacement des marées K1 et K2. En outre, les déplacements de marée dans la direction Est sont estimés avec une plus grande précision avec les observations de Galileo, grâce à la capacité de les traiter avec des ambiguïtés de phase entières. Dans ce contexte d'utilisation d'observations multi-GNSS, nous avons appliqué une stratégie de pondération optimale, qui est spécifique à chaque constellation et à chaque fréquence de marée, afin de réduire la sensibilité de l'estimation des erreurs aux limitations de chaque constellation.

Le chapitre 4 examine l'impact des erreurs OTL sur le positionnement GNSS, en particulier la propagation des erreurs de marée sub-diurnes à des périodes plus longues. A partir de l'analyse du modèle de propagation actuellement disponible et de l'analyse des séries de positions PPP, nous avons identifié différents signaux propagés autour de 14 jours et aux périodes annuelles et semi-annuelles pour les trois constellations actuellement impliquées dans les produits REPRO3 (GPS, GLONASS et Galileo). En particulier, les signaux propagés à 13,6 jours ne se produisent que pour la constellation GPS; ce qui indique que les erreurs du modèle du déplacement dû à la marée Mf ne peuvent pas être observées avec la constellation GPS.

La séparation des erreurs Mf et des signaux propagés des erreurs des marées subdiurne ne peut être réalisée qu'en utilisant une autre constellation, comme Galileo. De plus, nous avons constaté que l'utilisation de la stratégie d'estimation statique, telle que décrite dans le chapitre 3, permet

de réduire ces signaux propagés grâce à l'estimation de paramètres empiriques récupérant les erreurs de modélisations de déplacement subdiurne dans le traitement PPP.

Lien entre les erreurs d'orbites des satellites GNSS et le bruit coloré dans les séries de positions PPP

La partie 2 de cette thèse traite de la contribution de la dynamique orbitale au bruit de scintillation observé dans les séries de positions GNSS. Alors que les résultats précédents sur l'origine de ce bruit se sont principalement concentrés sur les facteurs environnementaux tels que les processus géologiques et les déplacements dus aux surcharges non-maréales, nous avons abordé trois points dans cette partie :

Bruit coloré (ou bruit de scintillation) dans les séries multi-GNSS

Alors que des signaux périodiques différents entre les constellations ont été observés dans les séries temporelles de positions, ce travail effectué dans le cadre de cette thèse est le premier à montrer la différences de corrélation du bruit dans les orbites des satellites GNSS, ainsi que dans les positions des stations. D'après les analyse des positions PPP (Chapitre 5) et des discontinuités des orbites à minuit (Chapitre 6), le bruit coloré (ou bruit de scintillation, bruit flicker) apparaît avec l'utilisation des produits GPS ; ce qui suggère qu'une partie de ce bruit proviendrait de la constellation ou des orbites des satellites. Dans le cadre de cette thèse, nous avons étudié les potentielles origines orbitales de ce bruit de scintillation spécifique de la constellation GPS.

Contributions orbitales au bruit coloré dans les positions PPP

Au chapitre 5, nous avons examiné la stabilité interannuelle de la géométrie de la constellation GNSS. Nous avons montré que les satellites GPS sont plus enclins à dériver que les autres constellations GNSS (Galileo, GLONASS et BeiDou) en raison d'une plus grande sensibilité à la résonance due à la gravitation luni-solaire. Nous avons ensuite démontré que la déformation de la géométrie de la constellation GPS qui en résulte est un facteur contribuant au bruit coloré dans les séries de positions PPP.

La différence du bruit contenu dans les discontinuités des orbites à minuit donne un aperçu d'autres possibles erreurs d'orbite spécifiques aux satellites GPS, telles que la présence d'accélérations stochastiques s'appliquant au satellite. Dans le chapitre 6, nous avons présenté un modèle simple, basé sur des équations différentielles stochastiques, pour tester cette hypothèse. Nous avons constaté que le bruit coloré dans les discontinuités des orbite peut résulter d'une "simple" perturbation sous forme de bruit blanc présente dans la dynamique du satellite. Plusieurs processus physiques, qui restent à étudier, peuvent être à l'origine de ces accélérations stochastiques. Des études supplémentaires sont nécessaires pour mieux relier ces accélérations stochastiques à un comportement physique des satellites.

Mécanisme de la propagation des erreurs d'orbite aux erreurs corrélées de positionnement GNSS

Dans le chapitre 5, nous avons identifié trois facteurs qui contribuent à l'émergence du bruit de scintillation dans les positions des stations:

1. Une géométrie d'observation variable dans le temps causée par la variation à long terme des orbites des satellites
2. La présence d'erreurs d'observation dont les effets ne s'annulent pas en fonction de l'angle d'élévation du satellite
3. Les limites des fonctions de pondération des observations pour atténuer l'impact de ces erreurs

Ces trois facteurs sont présents dans le positionnement effectué avec la constellation GPS, et expliquent une fraction du bruit de scintillation qui n'est pas spatialement corrélée.

En outre, quant à l'influence du bruit des orbites, des études supplémentaires sont nécessaires pour déterminer s'il existe une relation réelle entre le bruit de scintillation dans les discontinuités d'orbite, analysé au chapitre 6, et le bruit dans les positions des stations. Il est à noter que tous les produits d'orbite GPS ne contiennent pas de bruit de scintillation dans les discontinuités, alors que les séries de positions PPP des stations en contiennent quel que soit l'origine des produits d'orbites. L'étude de mécanismes faisant intervenir tous les paramètres estimés dans les solutions réseau (orbites, EOP et positions des stations) peut aider à mettre en évidence un mécanisme de propagation plus complexe.

Perspectives et suggestions pour de futures études

Identification et atténuation d'autres sources de signaux systématiques dans les séries temporelles GNSS

Bien que les méthodes développées dans la partie 1 se concentrent sur l'analyse des erreurs OTL, elles pourraient être étendues pour étudier d'autres sources d'erreurs périodiques dans le positionnement PPP. Par exemple, les marées atmosphériques aux fréquences S1 et S2 ne sont pas systématiquement incluses dans les traitement des données GNSS, bien que leur correction soit recommandée dans la convention IERS. Ceci est principalement dû au fait que il n'a pas été possible de démontrer une amélioration significative à utiliser les modèles actuellement disponibles sur le positionnement obtenu avec GPS uniquement. L'utilisation d'observations multi-GNSS pourrait permettre de mieux évaluer l'apport de ces modèles. En outre, nous avons démontré la possibilité d'ajouter des paramètres empiriques pour tenir compte d'erreurs de modélisation de déplacements subdiurnes. Ceci est particulièrement utile lorsqu'il est difficile d'obtenir une connaissance ou des modèles précis, comme dans le cas de déformations périodiques des monuments ou de la croûte terrestre en raison de la dilatation thermique. Il peut être possible de dériver des observations GNSS des modèles pour ces erreurs.

De plus, l'identification des facteurs contribuant au bruit corrélé dans les séries de positions ouvre la voie à de futurs travaux visant à améliorer la qualité des séries, en particulier avec l'utilisation croissante d'observations multi-GNSS pour le positionnement précis pour la géodésie. Le déploiement et la maintenance d'un réseau de stations capables de suivre plusieurs constellations, y compris Galileo et BeiDou, sont donc des tâches d'autant plus importantes. Par exemple, durant cette thèse, nous avons eu des difficultés pour trouver des données Galileo disponibles au format RINEX version 3 (version adaptée à la diffusion de données multi-GNSS) pour pouvoir réaliser des études géophysiques, telles que l'observation et l'analyse de la propagation géographique des déplacements dus à la surcharge de marée dans certaines régions d'intérêt.

En ce qui concerne le traitement des données les plus anciennes, contenant uniquement des observations GPS et qui sont essentielles pour obtenir de longues séries de positions, il est nécessaire d'améliorer notre compréhension du bruit systématique d'observations qui peut provenir de facteurs environnementaux (par exemple, le multi-trajet ou la troposphère) ou du calibrage des antennes (position du centre de phase). Par exemple, la plupart des stratégies de traitement GNSS utilisent un calibrage d'antenne commun à un type d'antenne, négligeant la variabilité des propriétés entre plusieurs antennes d'un même modèle. La plupart des traitements GNSS supposent une fonction de pondération moyenne des observations, estimée soit sur un sous-réseau de stations, soit sur une journée. La réduction du bruit d'observation ou le développement de meilleures stratégies de pondération pour atténuer ses effets sur le positionnement (par exemple, l'amélioration de la pondération de l'observation, la prise en compte de la variation de la géométrie de l'observation) permettrait non seulement d'améliorer la précision des positions, mais aussi de réduire la corrélation temporelle du bruit dans les séries les plus longues.

Quant à la contribution de l'orbite au bruit corrélé, nous n'en avons qu'effleuré le sujet. Notre travail soulève des questions sur la manière dont les orbites pourraient contribuer à la corrélation spatiale des erreurs de positionnement. Par exemple, les variations des erreurs orbitales ou de la géométrie d'observation pourraient influencer la façon dont les erreurs orbitales ou d'observation (par exemple, les variations spatio-temporelles de la troposphère) se propagent aux positions des stations.

Modélisation des séries temporelles de positions GNSS

L'identification de différents types de signaux périodiques et de bruit différents entre les constellations GNSS pose la question du traitement et de la modélisation des futures séries de positions qui seront obtenues par des observations multi-GNSS. Actuellement, la plupart des stratégies ont été développées uniquement à partir de séries GPS. À l'avenir, la gestion de la diversité des erreurs systématiques dans les positions des stations (signaux périodiques et processus stochastiques) deviendra un point clé pour améliorer la précision et la fiabilité de l'application des positions GNSS en géophysique et géodésie. La plupart des modèles actuels de coordonnées supposent des caractéristiques qui restent constantes dans le temps (même type de bruit, mêmes signaux périodiques). Cependant, avec l'intégration progressive de nouvelles constellations dans les traitements GNSS, ces caractéristiques seront plus susceptibles de varier en fonction du poids de chacune des constellations dans les solutions de position. Peu de publications traitent actuellement de la manière dont les modèles statistiques ou les stratégies pourraient être adaptés pour traiter de telles séries temporelles.

CHAPTER

A Orbits: description and equations of motion

This appendix introduces fundamental concepts of orbital mechanics used throughout this thesis. Unless otherwise specified, the explanations of these concepts and the associated notations are based on Vallado and McClain (2013).

A.1 Two-body problem and Keplerian motion

The trajectories of celestial bodies within a two-body system, influenced by gravitational forces, are described by the fundamental concept of Keplerian motion. Under the assumption that the central body is punctual and there are no perturbing accelerations, the motion of the orbiting body is elliptical and described by six Keplerian parameters. These parameters include three angles that define the plane of the orbit: the inclination i, the longitude of the ascending node Ω, and the argument of periapsis ω. The shape of the orbit is defined by two parameters: the semi-major axis a and the eccentricity e. Finally, the position of the orbiting body along its orbit is described by the true anomaly ν. These parameters are illustrated in Figure A.1.

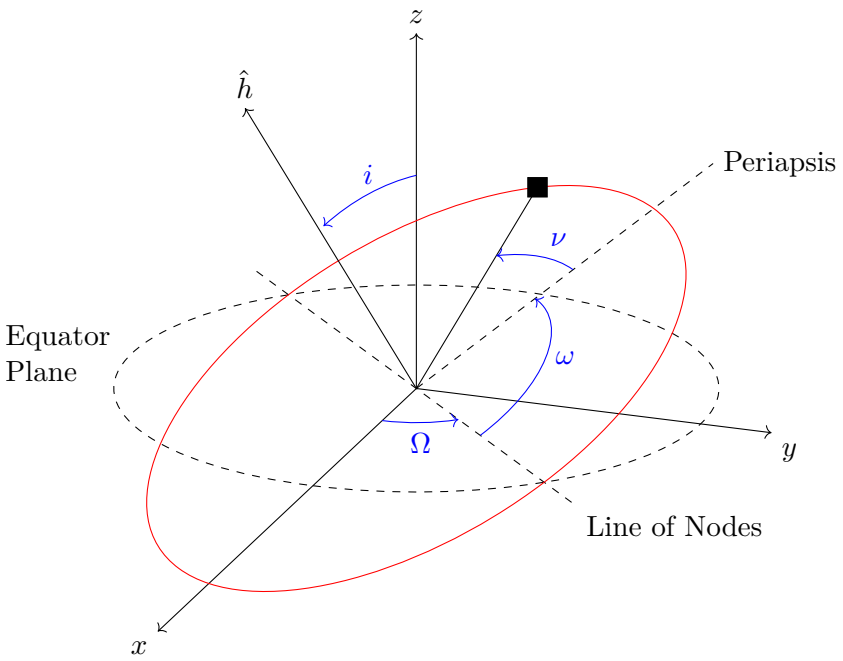

Figure A.1: Description of the Keplerian elements

A.2 Orbital reference frame

Earth-centered inertial (ECI) frame

An inertial terrestrial frame is more convenient for propagating the dynamical equations of motion of a satellite and thus determining its orbit. This is a non-rotating Earth-fixed frame whose origin is set to the center of mass of the Earth. The axes, represented in Figure A.2, are given by the axis x_{ECI} is defined by the direction of the vernal equinox at a conventional initial epoch t_0 and the axis of rotation of the Earth z_{ECI}. The y_{ECI} completes the right-handed frame.

The Cartesian coordinates of the position and velocity vectors are related to the 6 Keplerian parameters. For this thesis, we computed the Keplerian parameters from the position and the velocity of the satellites using the algorithm given in Vallado and McClain (2013, Algorithm 9).

Local orbital frame RTN

A local orbital frame is more suitable when it comes to the description of the forces acting on the satellite. For instance, we can define one by

- the direction R of the position vector in the inertial frame: $R = \frac{\mathbf{r_{ECI}}}{||\mathbf{r_{ECI}}||}$
- the direction N perpendicular to the orbital plane: $N = \frac{\mathbf{r_{ECI}} \times \mathbf{v_{ECI}}}{||\mathbf{r_{ECI}} \times \mathbf{v_{ECI}}||}$
- the direction T along the track of the satellite, that completes the right-handed frame

Earth-centered Earth-fixed (ECEF) frame

The motion of the GNSS satellites are disseminated through the SP3 files in a format which is suitable for the applications in navigation and positioning on the Earth's surface. For that, the motion of a satellite is described by the Cartesian coordinates of its position and velocity vectors, expressed in a geocentric frame co-rotating with the Earth. This frame is represented by the vectors $\{x_{ECEF}, y_{ECEF}, z_{ECEF}\}$ in Figure A.2. The direction z_{ECEF} and z_{ECI} are the same, while the direction x_{ECEF} is rotated by an angle $\theta(t)$, the longitude of the Greenwich meridian with respect to the vernal equinox direction x_{ECI}.

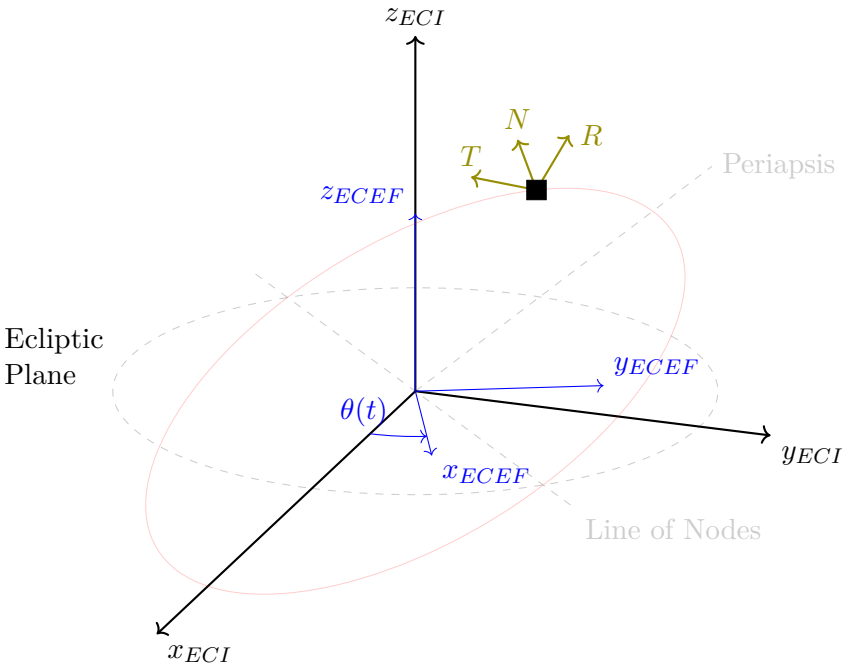

ECI: Earth-Centered Inertial (frame) ECEF: Earth-centered Earth-fixed (frame)

Figure A.2: Reference frames for describing orbits

A.3 Perturbed motion

For the satellite is subject to small perturbations, its motion can be approximated by the solution of the Keplerian motion (unperturbed system), called the osculating orbit, for which the orbital parameters are changing over time.The variations of the Keplerian parameters are given by the Gauss equations. Considering a perturbing force expressed in the local orbital frame RTN as

$$\mathbf{F} = F_R\mathbf{R} + F_T\mathbf{T} + F_N\mathbf{N}$$

the equations write:

$$\frac{da}{dt} = \frac{2}{n\sqrt{1-e^2}}(F_R\ e\sin\nu + F_T\ (1+e\cos\nu)) \tag{A.1}$$

$$\frac{de}{dt} = \frac{\sqrt{1-e^2}}{na}(F_R\ \sin\nu + F_T\ (\cos E + \cos\nu)) \tag{A.2}$$

$$\frac{di}{dt} = \frac{1}{na\sqrt{1-e^2}}\frac{r}{a}\cos\omega + \nu\ F_N \tag{A.3}$$

$$\frac{d\Omega}{dt} = \frac{1}{na\sqrt{1-e^2}}\frac{r}{a}\frac{\sin\omega+\nu}{\sin i}\ F_N \tag{A.4}$$

$$\frac{d\omega}{dt} = \frac{\sqrt{1-e^2}}{nae}\left[-\cos\nu\ F_R + \frac{2+e\cos\nu}{1+e\cos\nu}\sin\nu\ F_T - \frac{e\cos i}{1-e^2}\frac{r}{a}\frac{\sin\omega+\nu}{\sin i}\ F_N\right] \tag{A.5}$$

$$\frac{dM}{dt} = n + \frac{1-e^2}{nae}\left[(\cos\nu - \frac{2e}{1+e\cos\nu})\ F_R - \frac{2+e\cos\nu}{1+e\cos\nu}\sin\nu\ F_T\right] \tag{A.6}$$

with

- n is the mean motion expressed by $n = \sqrt{\frac{\mu}{a^3}}$, where μ is the Earth's gravitational constant ($\mu = G\ M_{Earth}$)
- M is the mean anomaly, E is the eccentric anomaly related by the relationship

$$M = E - e\sin E$$

- r is the distance between the Earth's and satellite's centers of mass expressed by

$$r = a(1 - e\cos E)$$

In a first approximation, the integration of these equations can be used to express the satellite's trajectory as a function of time given the initial position and velocity of the satellite, and the disturbing accelerations affecting the orbit.

GNSS draconitic periods

Due to the gravitational effects of the Earth's oblateness, the orbital planes of the GNSS satellites are rotating given by the precession rate of the orbital plane is given by:

$$\frac{d\Omega}{dt} = \frac{3}{2}J_2\frac{R_{Earth}}{a}n\cos(i) \tag{A.7}$$

with

- $J_2 = 1.08262668\ 10^{-3}$ the geopotential term representing the oblateness of Earth
- R_{Earth} the mean radius of the Earth

From the precession rate, we first compute the delay (in angle) Δ_Ω between the direction of the ascending node and its position after one year :

$$\Delta_\Omega \text{ [rad]} = \frac{d\Omega}{dt} \cdot 365.25 \text{ [d]} \cdot 86400 \text{ [s]} \tag{A.8}$$

We then can convert it into the mean delay $\Delta\tau_\Omega$ between the orbital plane with respect to the solar year by:

$$\Delta\tau_\Omega \text{ [day]} = \Delta_\Omega \cdot \frac{365.25}{2\pi} \tag{A.9}$$

Finally, the mean draconitic period is given by $T_{drac} = 365.25 - \Delta\tau_\Omega$ and the corresponding draconitic frequency by $f_{drac} = \frac{365.25}{T_{drac}}$. The numerical applications for the current GNSS constellations is given in Table A.1.

Table A.1: Draconitic periods and frequencies of the GNSS constellations

Constellation	**Semi-major axis [m]**	**Eccentricity**	**Inclination [deg]**	T_{drac} **[solar days]**	f_{drac} **[cpy]**
GPS	26559.8 10^3	0.0	55.0	350.6	1.040932
GAL	29600.318 10^3	0.0	56.0	355.4	1.026940
GLO	25510.0 10^3	0.0	64.8	352.7	1.034784
BEI	27840.0 10^3	0.0	55.0	352.8	1.034500

β-angle and eclipses

As a result of the J2 perturbation, the position of the Sun relative to the orbital planes of a GNSS constellation varies over time, with the draconitic period. The angle between the direction of the Sun and the orbital plane of the satellite is the $\beta - angle$, as illustrated in Figure A.3.

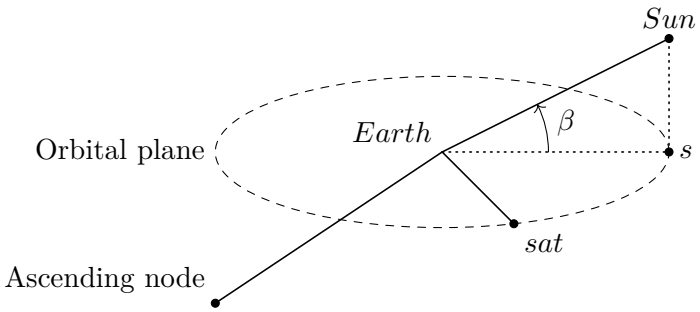

Figure A.3: Description of the β-angle

This angle can be computed from the position of the Sun r_{Sun} and the position r_{ECI} and velocity v_{ECI} of the satellite by:

$$\beta(t) = \pi - \cos^{-1}\left(\frac{r_{ECI} \times v_{ECI}}{||r_{ECI} \times v_{ECI}||} \cdot \frac{r_{Sun}}{||r_{Sun}||}\right) \tag{A.10}$$

The vector r_{Sun} is computed from the model described in Montenbruck and Gill (2000, Section 3.3.2).

Table A.2: Critical β-angle defining the eclipse seasons

Constellation	**GPS**	**GAL**	**GLO**	**BEI**
β_c [deg]	13.894647	12.443141	14.478672	13.243786

The eclipse season is the period when the satellite has a fraction of its orbits going through the shadow of the Earth. One can characterize it when the β-angle is lower, in absolute value, than a critical value β_c given by $\beta_c = \sin^{-1} \frac{R_{earth}}{a}$. The values for each constellation are given in Table A.2

CHAPTER

B List of publications resulting from this thesis

B.1 Peer-reviewed publications

- Ait-Lakbir, H., Santamaría-Gómez, A., & Perosanz, F. (2023). Assessment of sub-daily ocean tide loading errors and mitigation of their propagation in multi-GNSS position time series. GPS Solutions, 27(3), 129. https://doi.org/10.1007/s10291-023-01467-9
- Ait-Lakbir, H., Santamaría-Gómez, A., & Perosanz, F. (2023). Impact of the GPS orbital dynamics on spurious interannual Earth deformation. Geophysical Journal International, 235(1), 796–802. https://doi.org/10.1093/gji/ggad268

B.2 Presentations in international conferences

- Ait-Lakbir H., Santamaria A., & Perosanz F. (2021). Assessing daily and sub-daily ocean tidal loading displacements using GPS, Galileo, and GLONASS observations. Scientific Assembly of the International Association of Geodesy (IAG), Virtual conference
- Ait-Lakbir H., Santamaria A., & Perosanz F. (2021). Validation of Ocean Tidal Loading Corrections with GPS and Galileo Precise Point Positioning. American Geosciences Union (AGU), New Orleans, USA
- Ait-Lakbir H., Santamaria A., Perosanz F., & Ray J. (2022). Investigation of the flicker nature of the day-boundary differences of GNSS orbits. European Geosciences Union (EGU), Vienna, Austria
- Ait-Lakbir H., Santamaria A., Perosanz F., & Ray J. (2022). Linking the dynamic instability of GPS orbits to long-memory processes in station position time series. American Geosciences Union (AGU), Chicago, USA
- Ait-Lakbir H., Santamaria A., Perosanz F., & Ray J. (2023). Comparison and analysis of the long-term dynamics of GNSS orbits. European Geosciences Union (EGU), Vienna, Austria.

GPS Solutions _####################_
https://doi.org/10.1007/s10291-023-01467-9

ORIGINAL ARTICLE

Assessment of sub-daily ocean tide loading errors and mitigation of their propagation in multi-GNSS position time series

H. Ait-Lakbir[1] · A. Santamaría-Gómez[1] · F. Perosanz[2]

Received: 23 September 2022 / Accepted: 29 April 2023

Abstract

The Global Navigation Satellite Systems (GNSS) can monitor earth deformation at different frequencies, including sub-diurnal, fortnightly and seasonal bands. In standard 24-h GNSS data processing, we correct ocean tide loading (OTL) displacements by conventional models. Errors in the OTL modeling may lead to incorrect geophysical interpretation of observed displacements due to residual sub-daily OTL signals propagated to longer periods. OTL models and propagated signals have been studied mainly using GPS data, which introduce systematic errors at K1 and K2 tidal periods. We analyze the OTL residual displacements of eight major diurnal and semidiurnal tides derived from the FES2014b ocean tide atlas, using GPS, Galileo and GLONASS observations, and comparing both kinematic and static estimation approaches. The static method appears to be the most reliable way to retrieve the OTL residuals from other error sources with lower formal uncertainty. For the K1, K2 and S2 tides, the agreement improves by up to 55% when using Galileo and/or GLONASS, compared to GPS. We implemented an optimal weighting strategy with downweighted GPS contribution to the observation of K1/K2 for improving the estimation of the residual OTL errors. Several spurious signals appear for GPS, Galileo and GLONASS at the fortnightly band resulting from the propagation of mismodeled OTL. Estimating residual tidal coefficients alongside the 24-h static station positions mitigates the spectral power of these signals. Additional spurious signals appear at harmonics of the Galileo and GLONASS constellation repeat periods of 10 and 8 sidereal days, respectively. These signals cannot be attributed to mismodeled OTL.

Keywords Precise point positioning · GPS · GLONASS · Galileo · Geodesy · Ocean tide loading

Introduction

The Global Navigation Satellite Systems (GNSS) provide station position time series to analyze surface displacements ranging from seismic deformation, at sub-daily temporal scales, to environmental surface loading and glacial isostatic adjustment, at inter-annual temporal scales. On top of these genuine displacements, several systematic GNSS errors may affect the interpretation of geophysical signals extracted from GNSS position time series. Spurious oscillations were identified by Collilieux et al. (2007) and Ray et al. (2008) at the GPS draconitic period of 351.2 days and its harmonics, and around the fortnightly band.

To achieve the most accurate positioning in standard 24-h processing, the International Earth Rotation Service (IERS) Conventions (Petit and Luzum 2010) recommend the correction of well-known displacements derived from geophysical models of solid earth, ocean and atmosphere tide loading. Predictions of crustal deformations at a given location are calculated by the convolution of an earth model and a load deformation model, for instance, an ocean tide atlas. The ocean tide loading (OTL) induces surface deformation that can reach the level of a few centimeters near the coast, about one order of magnitude smaller (bigger) than the solid earth tides (atmospheric tides) (Petit and Luzum 2010). However, OTL is also less well predicted by models due to the complexity of the land/sea interface, the bathymetry near the coast and knowledge of the ocean tides themselves (Martens et al. 2016; Lyard et al. 2021). The current

F. Perosanz: Formerly at GET, Université Paul Sabatier, CNES, CNRS, IRD, UPS, Toulouse, France.

✉ H. Ait-Lakbir
hanane.ait-lakbir@get.omp.eu

[1] CNES, CNRS, IRD, UPS, GET, Université Paul Sabatier, Toulouse, France

[2] CNES, Toulouse, France

convention is that the displacements due to the eight major semidiurnal and diurnal (M2, S2, N2, K2, K1, O1, P1, Q1) and three long-period (Mf, Mm and Ssa) tides are corrected while processing 24-h GNSS measurements. The eleven-tide spectrum is complemented with 342 minor tidal constituents obtained by interpolating tidal admittance functions (Petit and Luzum 2010).

The propagation of sub-daily OTL modeling errors has been identified as a source of spurious longer period signals in GPS coordinate time series from analytical and simulation studies (Penna and Stewart 2003; Stewart et al. 2005). Several analyses such as Penna et al. (2007) confirmed these findings with real GPS data. Table 1 shows the frequencies predicted by the model developed in Stewart et al. (2005) for GPS, Galileo and GLONASS. Certain propagated signals depend only on the frequency of the errors, namely the unmodeled tidal displacement and the processing window length, while others also depend on the orbital period. Stewart et al. (2005) derived analytical expressions for the periods of the propagated signals showing that the 14.77- and 14.19-day signals are produced theoretically by the respective aliasing of the M2 and O1 displacements with a 24-h processing window and are thus common to the GPS and GLONASS constellations. As for the 13.6-day signal specifically results from functional model deficiencies arising from the combination of the GPS orbital repeat period and a coordinate estimation window which assumes no M2 or O1 ground motion. The 13.6-day signal also coincides with the Mf tide; hence, whether the origin of the 13.6-day signal is true mismodeled earth deformation or systematic GPS error remains unclear using only GPS data. Abraha et al. (2018) used GPS and GLONASS data and distinguished GPS-specific signals at 13.6 days from propagation common to both constellations. Similarly, part of the observed annual signal is affected by GNSS systematic errors, as shown by Dong et al. (2002).

At the sub-daily band, the inconsistencies between the predicted OTL and GNSS-observed displacements can be determined by precise point positioning (PPP). Unlike other large-scale displacements such as the solid earth tide, the magnitude of OTL varies significantly along the coast and also decreases with distance from it. As a result, the GNSS orbit/clock products are less likely to be contaminated by mismodeled OTL because the orbit determination is more prone to be perturbed by common errors impacting stations in a large region like solid earth tides. We assume that the PPP positions recover locally the errors of the OTL models provided that the other models and processing settings (software, measurements preprocessing) are consistent with the orbit/clock products, which is the case in this analysis. Orbital modeling errors are also likely to appear in the PPP solution and affect the positioning, and they are the issue this contribution aims to investigate by comparing three of the available GNSS constellations. The PPP analyses using GPS are subject to constellation-related errors occurring at the harmonics of the sidereal day, in particular for the K2, S2 and K1 constituents as compared, for example, to VLBI estimates (Thomas et al. 2007). Indeed, these tidal periods are close to the nominal GPS orbital period of 11.9672 h (11 h 58 min 2 s) or ground track repeat period of 23.9344 h (23 h 56 min 4 s) and thus are impacted by resonant errors coming from the orbit determination or the geometry of the measurement (e.g., antenna or multipath errors) (Choi et al. 2004; Ragheb et al. 2007). Studies using GLONASS with float-valued phase carrier ambiguities have shown that the observation of the K2, S2 and K1 constituents could be improved because the GLONASS orbital period does not contribute systematic errors at these periods (Abbaszadeh et al. 2020; Matviichuk et al. 2020). Indeed, the GLONASS satellites have different orbits than GPS, in particular with an orbital period of 11.2622 h (11 h 15 min 44 s) and an orbital repeat period of 8 sidereal days (7.98 solar days).

Since the end of 2018, the Galileo constellation provides an "initial service" with 24 in-flight satellites. The Galileo satellites have a nominal orbital period of 14.0783 h (14 h 4 min 42 s) and a ground track repeat period of 10 sidereal days (9.97 solar days). It is therefore expected to prevent propagation at the fortnightly band and provide better observation of the K2, S2 and K1 constituents. Furthermore, the quality of the Galileo signals makes it possible to fix integer phase carrier ambiguities and therefore obtain a more precise positioning by combining GPS and Galileo (Katsigianni et al. 2019a). Wei et al. (2021) used Galileo in combination with GPS, GLONASS and BeiDou to assess OTL displacements in the Hong Kong bay focusing only on observing OTL model errors at the sub-daily band. Yet, in their work,

Table 1 Period (in days) and admittance in amplitude (percent) of the first largest aliased peaks for GPS, Galileo and GLONASS computed from the expressions developed in Stewart et al. (2005)

GPS		Galileo		GLONASS	
O1	M2	O1	M2	O1	M2
13.662/42.1	13.678/44.6	3.690/15.0	3.729/6.3	3.114/17.6	3.142/7.1
14.193/7.5	14.786/3.5	5.857/7.7	14.786/3.5	5.107/10.2	5.182/4.5
13.169/3.1	14.210/3.2	14.193/7.5	5.956/3.4	14.193/7.5	5.463/3.5
14.766/1.5	15.409/0.9	7.687/5.1	7.524/2.8	5.549/6.4	14.786/3.5
15.389/1.0	16.088/0.7	33.541/1.1	30.636/0.6	18.221/2.3	17.328/1.2

the contribution of Galileo and BeiDou may also be underestimated because both constellations were incomplete at the beginning of the time span used in their analysis.

We investigate the contribution of the Galileo constellation for assessing sub-daily OTL modeling errors and their propagation into longer periods and compare it to the use of the GLONASS constellation. We seek to differentiate between sub-daily and daily OTL propagation and other signals in the fortnightly and annual bands. Besides, we develop a strategy to mitigate the propagation of OTL errors and investigate the impacts of a weighted multi-GNSS combination.

GNSS data processing

The GNSS strategies to estimate the residual OTL displacements relative to model predictions are based on PPP (Zumberge et al. 1997). We processed the GNSS data with the GINS software (Marty et al. 2011) to process 24-h batches where positions per 24 h (static approach) or per 3 h (kinematic approach). We used the GRGS GNSS orbit and clock products issued for the 3rd International GNSS Service (IGS) reprocessing campaign (REPRO3) which includes GPS, GLONASS and Galileo (Katsigianni et al. 2019b). Alongside these products, we used consistent satellite bias products allowing the resolution of GPS and Galileo phase carrier integer ambiguities based on the undifferentiated approach described in Loyer et al. (2012). Table 2 lists the models and processing parameters applied in the analysis, which are consistent with the REPRO3 GRGS products.

We aimed for Galileo-only, GLONASS-only and GPS-only PPP solutions of similar quality. We therefore considered the period from January 2019 to November 2021 because, since late 2018, the GRGS integer products are available for Galileo.

We processed data from IGS stations located less than 200 km from the coast, where the effects of mismodeled OTL displacements are more likely to be detectable. We selected the stations based on the observation availability and the quality of the PPP such as data completeness above 80% for all constellations, and integer ambiguity resolution success rate above 80% for 30 randomly chosen days. Additionally, a threshold of 3 cm on the average repeatability of the 3-h vertical series is applied. Prior to the analysis of the position time series, outlier positions above 5-sigma were also removed. These outliers correspond mostly to data gaps due to missing or edited observations during the RINEX preprocessing. The global network of 64 stations finally selected for the analysis is shown in Fig. 1.

Table 2 Description of modeling and parameter estimation strategies in the PPP processing

Tests	Kinematic approach	Static approach
Satellite products		
Satellite orbits and clocks	GRGS products from IGS REPRO3	
Satellite biases	GRGS wide-lane biases	
Measurements models		
Ambiguity strategy	Zero-difference ambiguity resolution (Loyer et al. 2012)	
Elevation cutoff	8°	
Antenna phase center correction	igsR3_2077 Antex	
Troposphere model	GPT2 meteorological and mapping function	
Loading		
Solid earth pole tidal loading	2010 IERS Conventions with updated linear mean pole model	
Ocean pole tidal loading	2010 IERS Conventions with updated linear mean pole model	
Ocean tidal loading (tides atlas)	FES2014b ocean tides atlas (Lyard et al. 2021)	
Ocean tidal loading (load deformation)	Load deformation function from PREM model	
Atmospheric loading	2010 IERS S1/S2 model	
Non-tidal surface loading model	None	
Parameters estimation		
Processing batch length	24 h	24 h for NEQ generation
Station coordinates	1 set per 3 h	1 set per 24 h
Observation sampling	30 s	300 s
Clock corrections	1 per observation	
Troposphere: ZTD	1 piecewise linear model every 2 h	
Troposphere: horizontal gradients	1 constant parameter per 24 h	

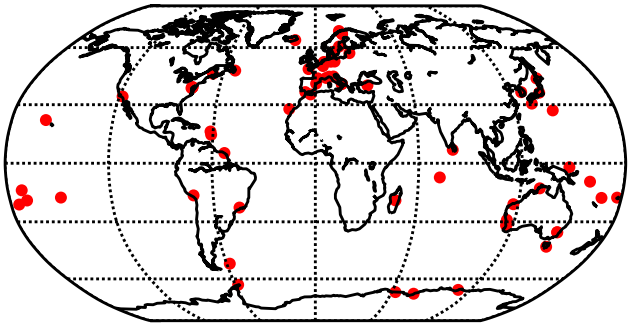

Fig. 1 Map of the network of stations

Modeling and estimating of OTL coefficients residual errors

The applied displacement models for solid earth pole tides and ocean pole tides are those of the last updates of the 2010 IERS Conventions released in 2018, which are used by the GRGS IGS Analysis Center. We computed the OTL displacement corrections with the FES2014b ocean tide atlas (Lyard et al. 2021) assuming the load deformation Green's functions derived from the Preliminary Reference Earth Model. By convention, the origin of the terrestrial frame realized by the GRGS precise orbit and clock products is corrected for the center of mass motion induced by OTL and aligned to the ITRF. OTL corrections in PPP need to be applied consistently with the orbit and clock products (Fu et al. 2012). Therefore, the computed OTL corrections for our PPP solution were expressed in the geocentric crust-fixed frame centered on the center of earth's figure as recommended in Dong et al. (2002) and Blewitt (2003).

King (2006) used two approaches to investigate OTL displacements with GPS observations. The so-called kinematic approach consists of a spectral analysis of sub-daily station positions to extract the residual error of the tidal constituents with respect to the reference model. Averaged spectra of sub-daily coordinates are given in the supplementary material (Figures S1 to S3). Rather than using 5- or 30-min positions like Penna et al (2015) or Wei et al (2021), we computed 3-h positions which allows us to use shorter time span to assess the OTL errors. In Penna et al. (2015), the authors show that a timespan of 4 years is required to significantly reduce the uncertainty on OTL estimation. With our longer observation window of 3 h, the estimated positions are less noisy and still short enough to observe the main tidal lines above 6 h (Nyquist frequency). The timespan of the series defines the frequency resolution available for the separation of the tidal lines. In this paper, we aim to assess the 8 major tides; thus, the time span required for the spectral separation of the two closest tide lines (S2 and K2) is only of 186 days, much shorter than the available 3 years. After fitting a linear trend and offsets in the 3-h positions time series, a harmonic function including the 8 major tides frequencies is fitted on the position residuals using the least squares method. This post-processing of the time series is a descriptive approach for assessing OTL errors without correcting them. In our analysis, we implemented the kinematic approach to validate and compare our new implementation of a static approach. Also referred to as harmonic parameter estimation, the static approach is based on the simultaneous estimation of the residual OTL coefficients with the other adjusted PPP parameters, namely the site coordinates, receiver clock and tropospheric parameters.

For the static approach, it is necessary to define the OTL parameters to be estimated in the PPP solution. We derived, from the ones used in King et al. (2005) and Yuan et al. (2013), a simplified harmonic expansion model consisting of 48 additional parameters to model the 8 major sub-daily tide constituents. Because we only used 3 years of data, the long-term modulation at 18.6 years is not separable from the short-term variations and it is not included in our modeling. As a means of improving the estimation of the residual coefficients of OTL, we assume that the OTL residual displacements are harmonic (constant amplitude). They are then estimated over a given period of time: mean of one-year periods for the static approach, and three years for the kinematic approach.

With 24-h processing batches, the estimation of the OTL parameters is weak. It is then necessary to combine the daily OTL estimates and their covariances over a longer time span. The aforementioned studies used a Kalman or a covariance matrix filter to improve the estimation of the OTL parameters. We generated the PPP daily normal equations (NEQs), including the station positions and the OTL parameters, separately for each station and constellation. The NEQs were then stacked for each year and inverted to solve for the daily station coordinates and the OTL coefficients of the eight major diurnal and semidiurnal tides (see Figure S4 in the supplementary material). We evaluated the impact of using the mean of three one-year periods or the full three-year time span and found differences well below the formal uncertainties of the estimates. The stacking of one-year periods was chosen for simplicity in the processing of the NEQs. Daily optimal weights were calculated for each constellation using the Helmert estimator of variance components (Sahin et al. 1992). The inversion was done by applying loose constraints of 5 mm on the OTL coefficients. For the K1 and K2 constituents, the influence of GPS orbital errors increases the amplitude of the potential residual errors, so the constraints were set to 10 mm.

Journal : Large 10291 | Article No : 1467 | Pages : 16 | MS Code : 1467 | Dispatch : 7-5-2023

GNSS-derived OTL residual displacements and implications on long-period propagated signals

Because the kinematic approach is commonly used in the literature to validate the OTL models with GPS observations, we first compare the outcome of the kinematic and static strategies to evaluate the impact of the chosen estimation strategy. We then compare the influence of a multi-GNSS estimation of the OTL errors, with particular attention given to the reduction in constellation-specific systematic signals which may affect the results. Finally, we analyze the propagated signatures of the sub-daily OTL and the constellation-specific errors on the spectra of the coordinates.

Sensitivity to estimation strategy using GPS only

Figure 2 summarizes the estimation of the OTL residual amplitude errors from GPS observations for the eight main sub-daily tides in the eastward, northward and upward directions for both the kinematic and the static methods. The values between the two methods for the Moon-driven tidal constituents agree within intervals of 0.02 mm for N2 and O1, 0.07 mm for Q1 and 0.28 mm for M2. By contrast, the estimations for the Sun-driven tidal constituents (S2, K2, K1 and P1) significantly differ. In the vertical direction, GPS-derived estimates differ by up to 0.5 mm in magnitude for all tide lines except S2 and K2, which corresponds from 10 to 25% of the estimated residual errors. For the S2 and K2 constituents, the difference reaches 65% of the estimated error (up to 0.8 mm). For the horizontal directions, we observe a difference of 0.06 mm in magnitude between the two strategies, representing up to 30% of the estimated residual error with respect to the a priori model.

We further compare the amplitude and phase of the M2 residual errors in the eastward, northward and upward directions in Figs. 3 and 4. The amplitude estimated by the two methods agrees within 0.5 mm, except for some stations such as Brest (BRST, station index 3 in Figs. 3 and 4) where the difference reaches 2 mm. This station is located near the English Channel, where there are large uncertainties in the modeled M2 tide (Melachroinos et al. 2008; Vergnolle et al. 2008; Penna et al. 2015; Bos et al. 2015). The phases of the residual displacements fluctuate noticeably because, with a small amplitude of the residual signal, the phase is almost indeterminate. However, the static estimation clearly reduces the uncertainties of both amplitude and phase estimates. The formal uncertainties of the estimated amplitudes and phases are reduced by a factor of 10 compared to the kinematic estimation. Indeed, the sub-daily position time series used in the kinematic approach has high variances, which makes it more complicated to fit an accurate sinusoidal signal.

We also analyze the correlation between the OTL errors and the other parameters adjusted during the PPP processing. For the static approach, the OTL parameters are estimated as annual constant values and are completely uncorrelated with the other PPP parameters: daily station

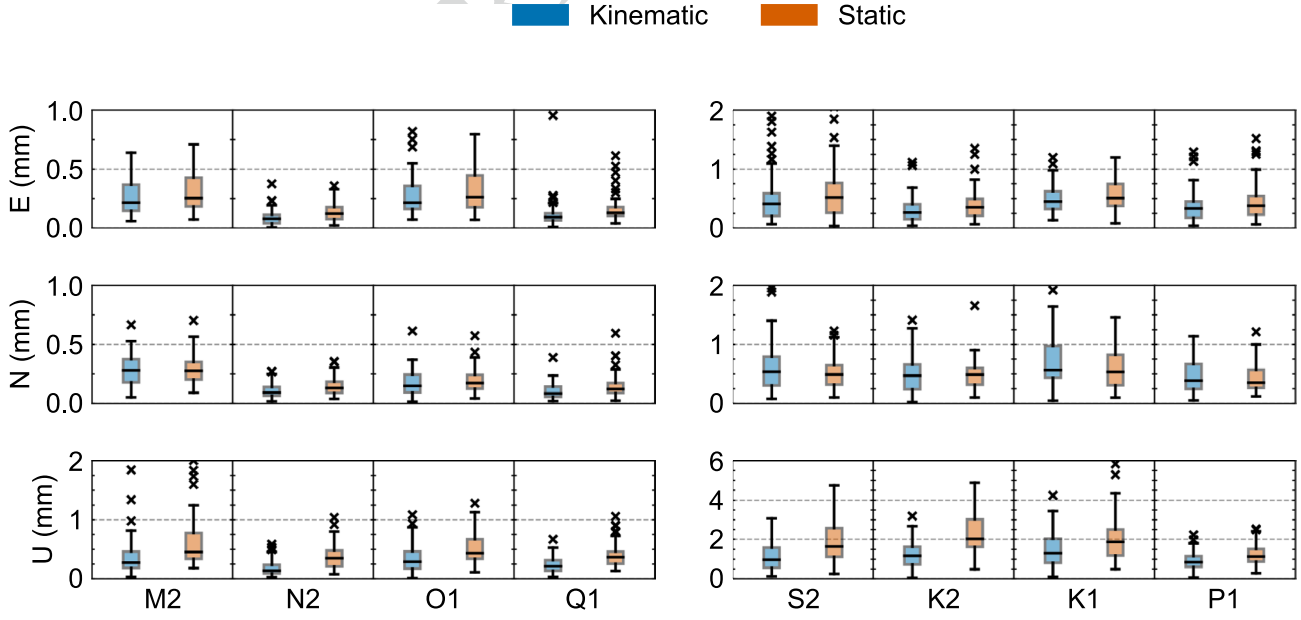

Fig. 2 Amplitude of GPS-only residual displacements with respect to the FES2014b-derived OTL displacements. Left: Moon-driven tides. Right: Sun-driven tides. Note the scale change between the left and right plots. The cross represents the points located outside the interval [Q1–1.5*IQR; Q3 + 1.5*IQR], with Q1 and Q3 the first/third quartile and IQR the interquartile range (Q3–Q1)

Journal : Large 10291 | Article No : 1467 | Pages : 16 | MS Code : 1467 | Dispatch : 7-5-2023

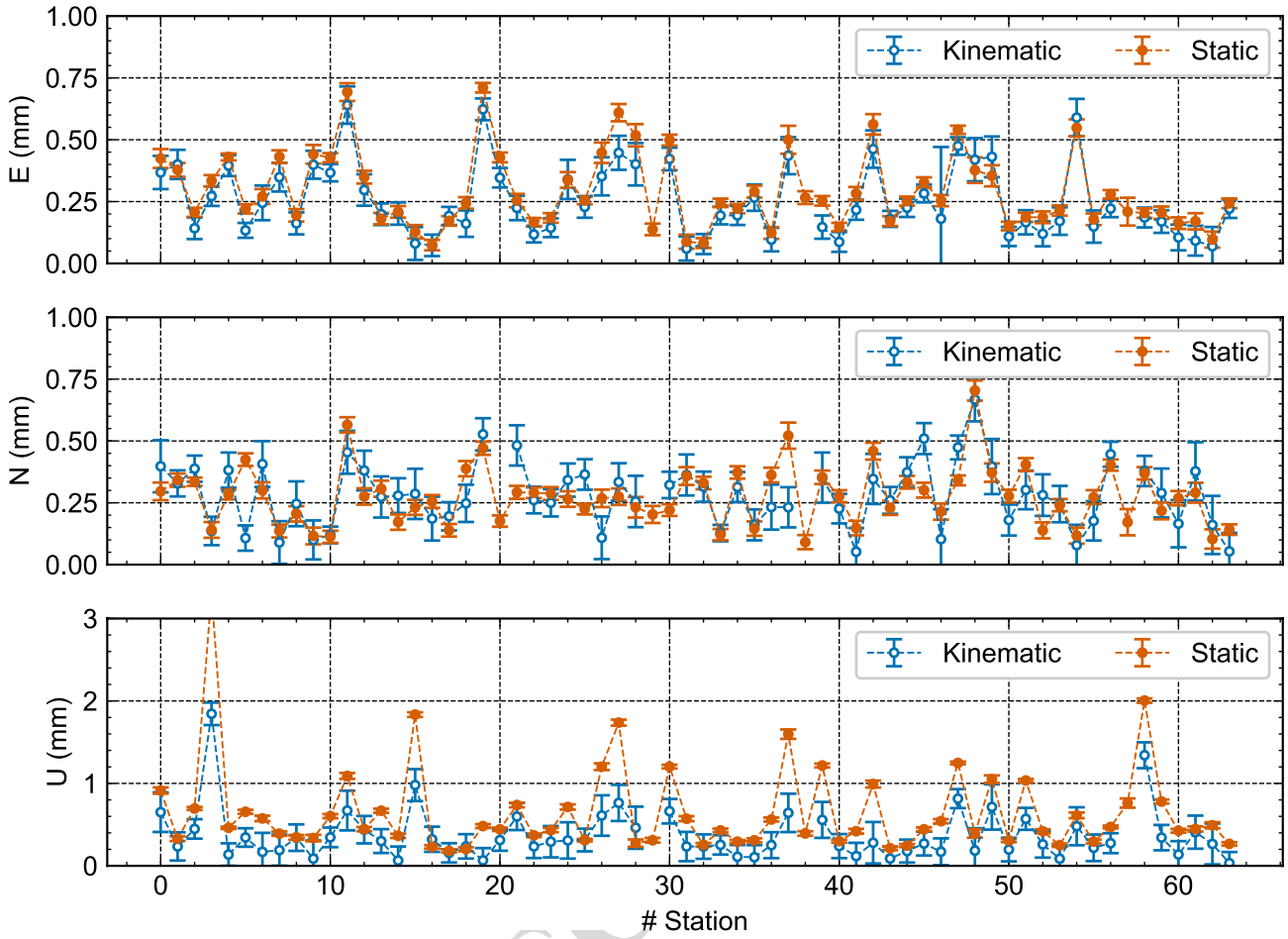

Fig. 3 Station-dependent estimates (curves) and formal uncertainties (error bars) of residual M2 amplitudes derived from GPS only with respect to the OTL displacements predicted by the FES2014b model. The abscissa axis corresponds to the index of the station

coordinates, troposphere bias estimated every 2 h and daily horizontal gradient coefficients. Hence, the static approach is mathematically more robust than the kinematic approach as the correlations between these parameters are obtained from consistent daily PPP processing and rigorously reduced during the NEQ stacking. Conversely, for the kinematic approach, we observe a correlation reaching 40% between the 3-h positions, used to derive the OTL error estimates, and the troposphere parameters, as illustrated in Fig. 5. Whether the coefficients estimated with the kinematic approach reflect only OTL errors or a combination of OTL errors and daily variability of the troposphere cannot be fully determined.

These results suggest that the estimation strategy significantly impacts the evaluation of the OTL residual errors. Although it is not possible to assess which approach is more accurately retrieving the OTL model errors, the static method appears better in terms of formal uncertainty and more rigorous, allowing better separation of the OTL residuals from other error sources, such as the troposphere model. In the following, the results will be based on the static approach.

Toward a multi-GNSS estimation

The characteristics of the observed OTL residuals for each constellation are compared in Fig. 6. Both Galileo and GLONASS agree better with the OTL model for the Sun-driven tides, especially the S2, K2 and K1 constituents. Compared to the GPS-based estimates, Galileo- or GLONASS-derived amplitudes of the residual OTL signals decrease by 36 to 60% in height, and by 9 to 47% in horizontal. Indeed, the Galileo and GLONASS constellations have repeat and orbital periods different from the diurnal or semidiurnal frequencies as occurs for GPS. With an orbital period of 14.0783 h, i.e.,14 h 04 min 42 s (resp. 11.2622 h, i.e., 11 h 15 min 44 s), the orbital errors of Galileo (resp. GLONASS) resonate at different frequencies, preventing perturbed observation of the Sun-driven tidal frequencies. However, no

Journal : Large 10291 | Article No : 1467 | Pages : 16 | MS Code : 1467 | Dispatch : 7-5-2023

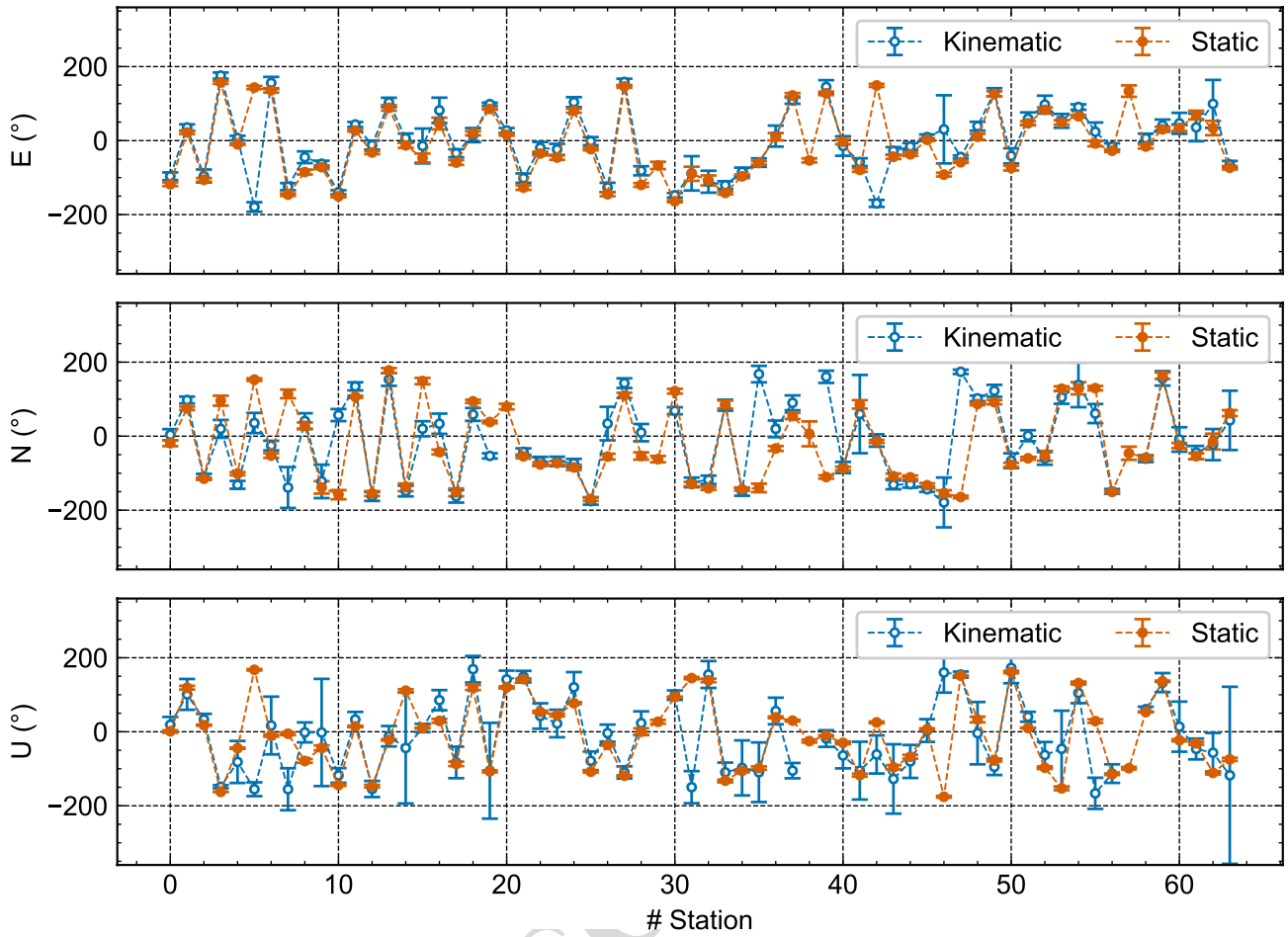

Fig. 4 Station-dependent estimates (curves) and formal uncertainties (error bars) of residual M2 phases derived from GPS only with respect to the OTL displacements predicted by the FES2014b model. The abscissa axis corresponds to the index of the station (see the station indices in supplementary information)

significant differences in the residual signals are visible for the Moon-driven tides.

The OTL residual errors in the East component with GLONASS are significantly larger in amplitude and in uncertainty, which we explain by the floating carrier phase ambiguities strategy. GPS and Galileo measurements are processed with integer-valued ambiguities, improving the positioning accuracy, especially in the East component. GLONASS floating ambiguities lead to less accurate positioning, which consequently affects the estimation accuracy of the OTL amplitudes for this component.

We further assess whether a combination of constellations could be used to improve the observed residual OTL displacements while minimizing systematic errors from each constellation. We estimated daily optimal weights for each station and constellation from the residuals of the NEQ combination.

The OTL residual errors obtained from the optimal multi-GNSS combination show that the solar tides K1, K2 and S2 are still contaminated by GPS systematic errors, as illustrated by the solid bars in Fig. 7. This is particularly the case in the vertical direction when comparing the ER solution to GE, GR or GRE solutions. We observe that adding Galileo reduces the sensitivity of the multi-GNSS estimation to GPS systematic errors when comparing GE to GR solutions. The highest consistency with the FES2014 OTL model (up to 0.5 mm horizontally and 1.1 mm vertically) is achieved when combining Galileo and GLONASS observations. As for the lunar tides (Fig. 8), the optimal multi-GNSS combination has no significant effect on their estimates.

To further improve the GNSS combination without excluding GPS, another solution is investigated to decrease the influence of the GPS effects on the Solar-driven tides. The NEQs are stacked again while downweighting the equations of the frequencies corresponding exactly to the GPS orbital and constellation repeat, K1 and K2, frequencies. In Figs. 7 and 8, the OTL residuals derived from this tide-specific weighting strategy are illustrated by the hatched bars.

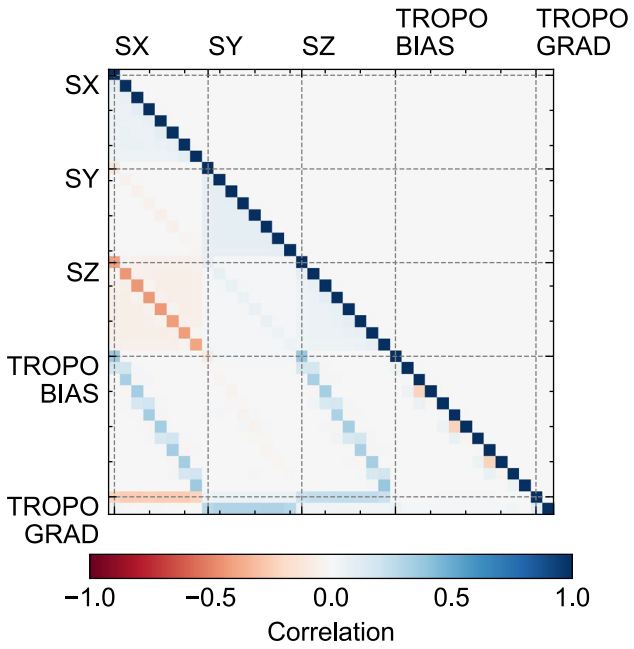

Fig. 5 Correlation between the 3-h Cartesian coordinates (SX, SY and SZ) and troposphere parameters in daily PPP solutions at BRST (latitude: 48.380°, longitude: −4.497°)

In the vertical direction, a clear improvement is perceptible for the K1 and K2 tides. Estimates of the S2 tide are also improved even if GPS observations are not downweighted for this constituent. Table 3 gives the numerical values for the medians and first/third quartiles for GPS-only and GRE combination with downweighting GPS. This shows the effects of the GPS system on the neighboring frequencies of K1 and K2. In addition, the weakness of GLONASS to observe K1 and K2 in the East component impacts the estimates and the formal uncertainties of these tides in the GR combination. East K1 and K2 coefficient estimates in the GR combination (Fig. 7) are larger with GPS-specific downweighting (dashed box) than with optimal weighting alone (solid box), or with a combination including Galileo (GE, ER, or GRE). This finding shows the advantages of using Galileo in the combination compared to GLONASS.

These findings demonstrate that an optimal weighting dependent on the constellation and on the tidal constituents is required to obtain the most accurate and consistent estimation of the residual OTL errors for the solar tides. On the other hand, the lunar tide constituents (M2, N2, O1, and Q1) are barely sensitive to which constellation is used (Fig. 8).

Analysis of long-period propagated signals

Another outcome of the static estimation approach is the generation of position time series corrected for the residual errors in the a priori OTL model as observed by GNSS. We individually compared the obtained coordinates to those computed with the nominal FES2014b model for each constellation. After removing a linear trend, position offsets and outliers, the Lomb–Scargle power periodogram of the coordinates themselves (see Figures S11 to S16 in

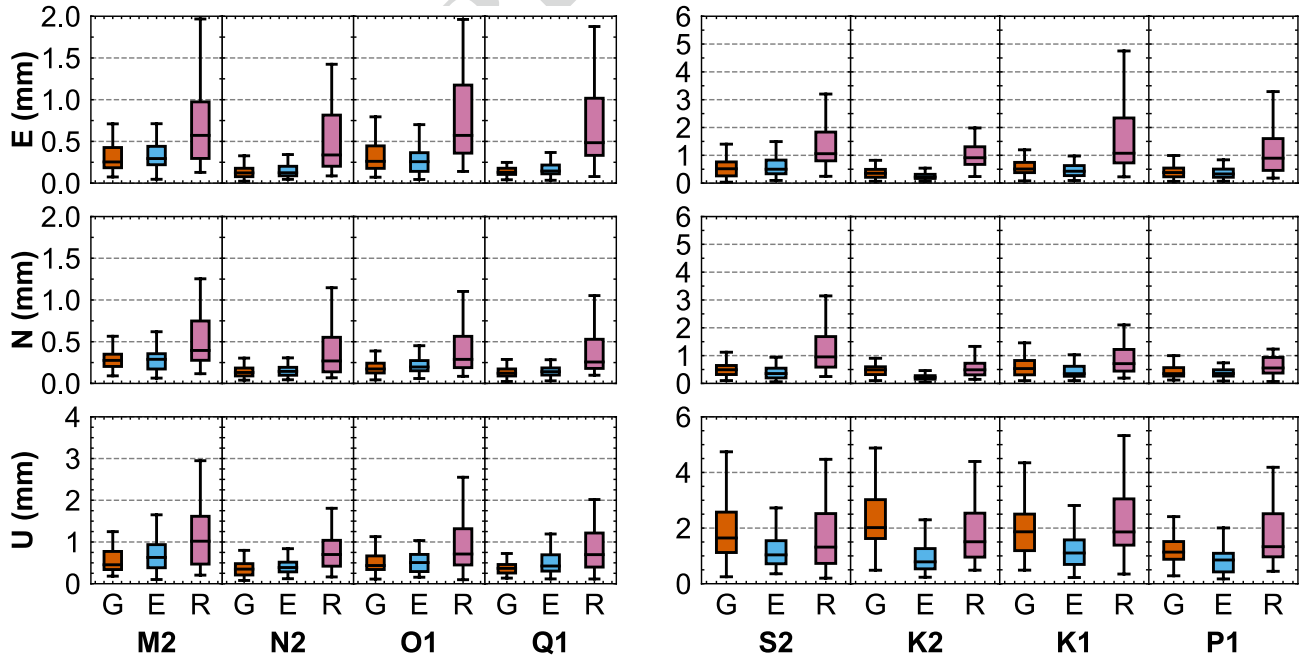

Fig. 6 Amplitudes of residual tidal displacements estimated for the 67 stations and for each constellation. Left: Moon-driven tides. Right: Sun-driven tides

Journal : Large 10291 | Article No : 1467 | Pages : 16 | MS Code : 1467 | Dispatch : 7-5-2023

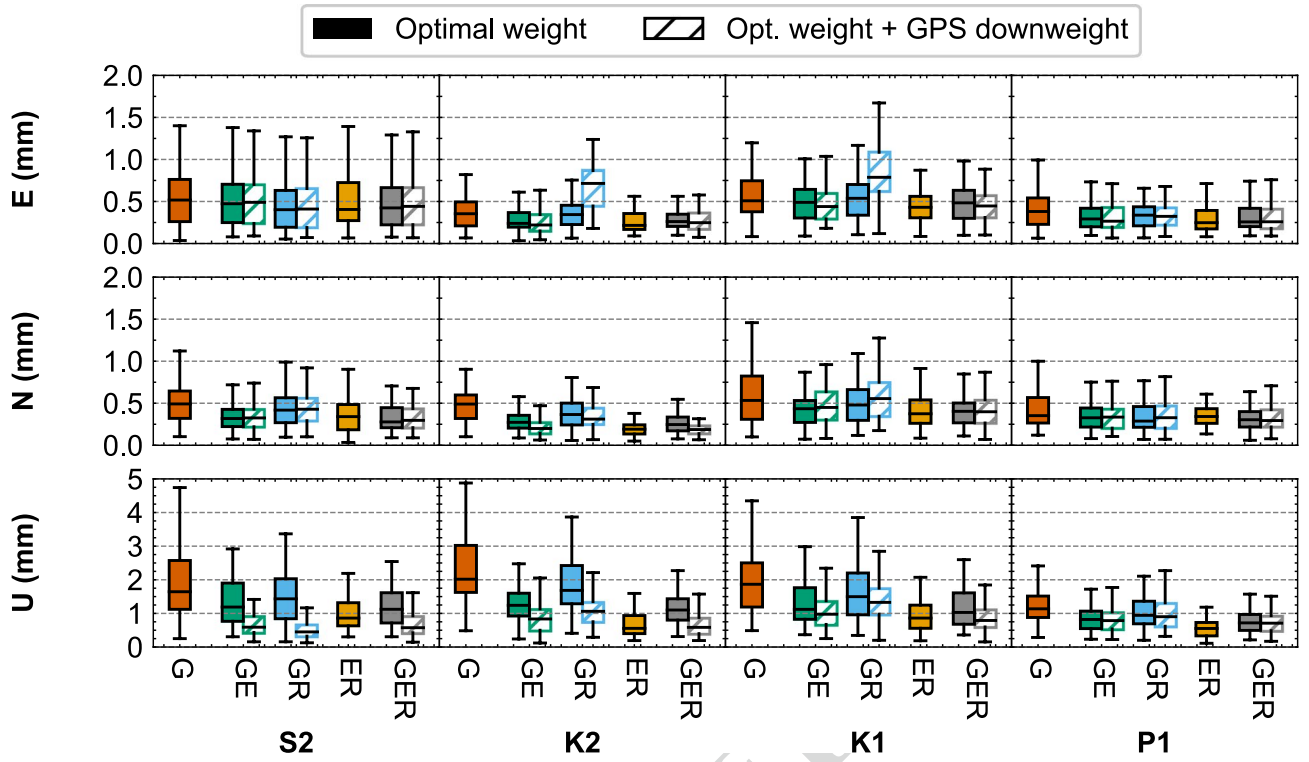

Fig. 7 Amplitudes of residual displacements from solar tides estimated from the combination of different GNSS constellations. The combination is performed using the optimal weighting (solid) or with additional downweighting of GPS for the K1 and K2 tides (hatch)

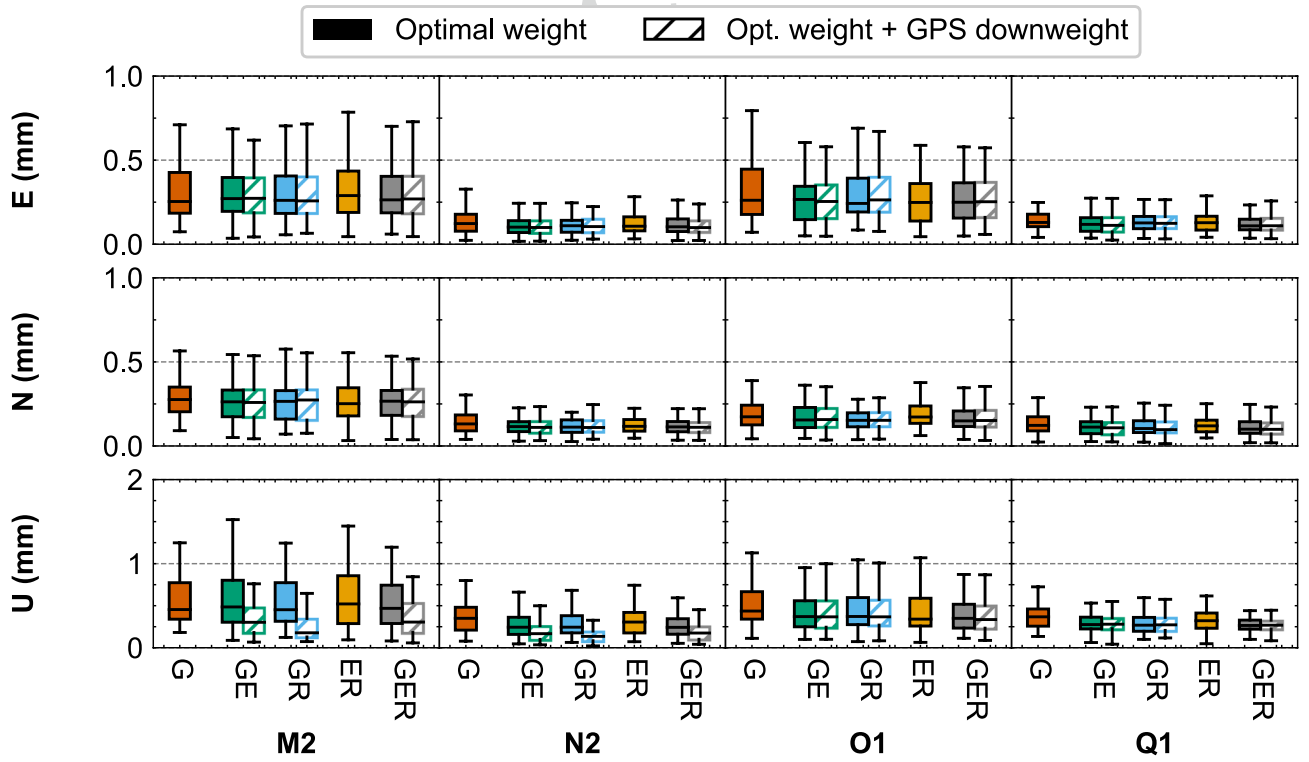

Fig. 8 Amplitudes of residual displacements from lunar tides estimated from the combination of different GNSS constellations. The combination is performed using the optimal weighting (solid) or with additional downweighting of GPS for the K1 and K2 tides (hatch)

Table 3 Median and first/third quartiles (in mm) of the estimated OTL residual errors for the major tides for GPS-only and the GER combination with optimal weighting and additional downweighting of GPS for the K1 and K2 tides

Tide	East		North		Up	
	G	GER	G	GER	G	GER
M2	0.25 [0.18–0.43]	0.27 [0.18–0.40]	0.28 [0.20–0.35]	0.26 [0.18–0.34]	0.45 [0.34–0.77]	0.31 [0.18–0.54]
N2	0.12 [0.08–0.18]	0.10 [0.07–0.14]	0.13 [0.09–0.18]	0.11 [0.08–0.14]	0.35 [0.21–0.48]	0.17 [0.10–0.26]
O1	0.26 [0.18–0.45]	0.25 [0.16–0.37]	0.17 [0.13–0.24]	0.15 [0.11–0.21]	0.44 [0.34–0.67]	0.34 [0.23–0.50]
Q1	0.13 [0.10–0.18]	0.11 [0.08–0.15]	0.12 [0.09–0.17]	0.10 [0.07–0.14]	0.37 [0.26–0.46]	0.27 [0.22–0.33]
S2	0.52 [0.26–0.76]	0.44 [0.22–0.67]	0.49 [0.32–0.65]	0.30 [0.21–0.44]	1.64 [1.12–2.57]	0.58 [0.43–0.93]
K2	0.35 [0.21–0.49]	0.25 [0.17–0.36]	0.49 [0.32–0.60]	0.19 [0.14–0.23]	2.02 [1.62–3.02]	0.59 [0.40–0.88]
K1	0.51 [0.38–0.75]	**0.45 [0.31–0.57]**	0.53 [0.31–0.82]	**0.40 [0.26–0.54]**	1.87 [1.19–2.50]	**0.79 [0.60–1.13]**
P1	0.38 [0.23–0.54]	0.26 [0.18–0.41]	0.35 [0.26–0.57]	0.29 [0.22–0.42]	1.14 [0.88–1.52]	0.71 [0.49–0.93]

The values in bold indicate the larger errors observed in each direction.

the supplementary material) is computed and normalized by the variance, owing to the series with the nominal and adjusted OTL models being unlikely to have similar variances. We also analyzed the normalized spectral power of the differences in the coordinates to better distinguish the effects of the adjusted OTL coefficients on propagated signals. Figures 9, 10 and 11 show the results for the vertical coordinates, but the observations and conclusions are still valid for the horizontal components (see Figures S5 to S10 in the supplementary material).

Figure 9 shows the errors in the harmonics of the Galileo ground track repeat period at 2.5, 3.33, and to a lesser extent at 5, and 10 days. Harmonics appear similarly for GLONASS at 2, 2.67, 4, and 8 days. The harmonics at 10 and 8 days appear as wide spectral combs for both constellations. For GLONASS, the maximum spectral power is reached at the first harmonic, while it is reached at the third harmonic for Galileo. A possible explanation for these signals may be orbital errors incorrectly separated by the low spectral resolution limited by the annual NEQ stacking. For instance, the Q1 (1.1195 cpd) and N2 (0.5274 cpd) tides cannot be spectrally distinct from the 9th (1.1111 cpd) and 19th (0.5263 cpd) harmonics of Galileo's ground track repeat period. The reduction of the 3.33- and 8-day peaks is clearly visible in the spectra of the coordinates with adjusted OTL coefficients.

Figure 9 also shows fortnightly aliased signals agreeing with the frequencies predicted by the model developed in Stewart et al. (2005) for GPS, whose largest modes are given in Table 1 for GPS, Galileo, and GLONASS. The Mf constituent was not adjusted in the static approach, so errors at this tidal line cancel out with the difference of coordinates. Therefore, the observed GPS-specific line at 13.6 days can only be caused by the propagation of errors at the M2 and O1 tidal frequencies. The peaks at 14.19 days correspond to the aliasing of the O1 tide and are consistently detected for the three constellations. A small peak at about 14.77 days appears only for the GLONASS coordinate differences corresponding to the aliasing of the M2 tide. For the three constellations, the admittance in amplitude between the sub-daily M2 error and the propagated wave is only 3.5% (Table 1), resulting in this signal likely being hidden below the noise level.

When we compare the power spectra of the coordinates with and without the estimation of OTL coefficients, we observe a reduction for these signals, especially in the East component, when the OTL coefficients are included (see Figure S5 in the supplementary material). Spectral peaks at 13.6 days are still present in both North and Up components, which may indicate residual errors caused by the Mf mismodeling. The power reduction in the Up component is smaller than the horizontal components as the height is the least well-determined component in GNSS positioning and is strongly correlated to other estimated parameters (troposphere delays and clock biases) in PPP processing (Table 4).

The harmonics of the draconitic frequencies for each constellation are also affected. Nevertheless, the impact is larger for GPS, indicating that GPS draconitic signals may be partly explained by orbit mismodeling and by the propagated signals of K1 and K2 tides. Galileo and GLONASS low frequencies appear less sensitive to the a priori OTL errors. The amplitudes themselves are moderately affected by the estimation of the OTL coefficients, which suggests that the propagation of the OTL mismodeling contributes to these frequencies to a small extent.

As for the multi-GNSS solutions, we analyze the coordinates from the combination with optimal weights and GPS-specific downweighting on K1 and K2 coefficients. Figures 10 and 11 show the superposition of the aforementioned constellation-specific signals. For periods between 2 days and the fortnight band, GPS helps mitigate the Galileo- and GLONASS-specific errors, except for the Galileo third (3.33 days) and fourth (2.5 days) harmonics. These peaks only decrease when all three constellations are

Journal : Large 10291 | Article No : 1467 | Pages : 16 | MS Code : 1467 | Dispatch : 7-5-2023

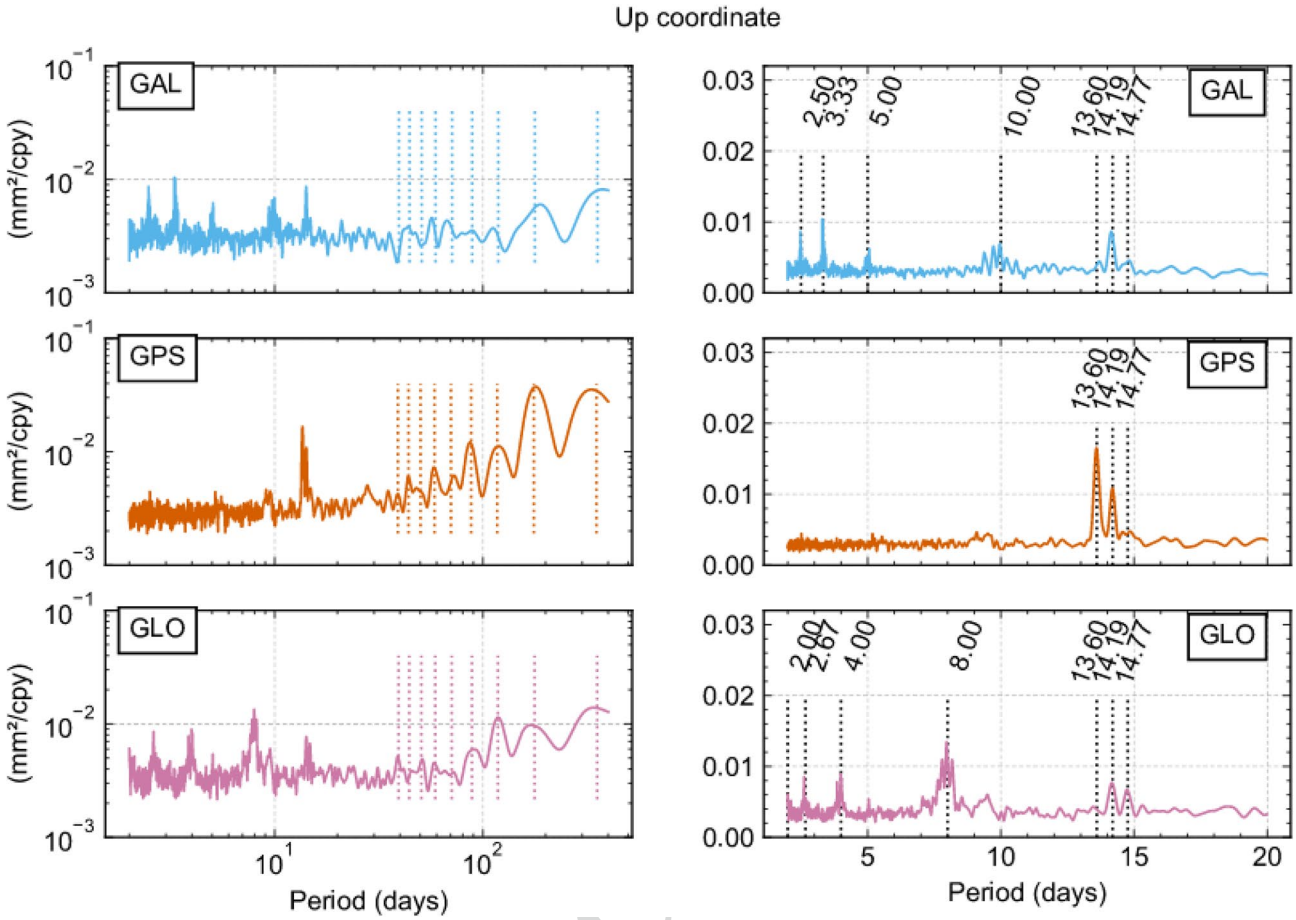

Fig. 9 Stacked normalized power spectra of the differences of Up coordinates computed with the nominal and the adjusted OTL coefficients for Galileo (top), GPS (center) and GLONASS (bottom). The left panel represents the full spectral domain with vertical dashed lines for the constellation draconitic frequencies and their harmonics. The right panel represents a zoom-in of short period band with the propagated periods (about 13.6, 14.19 and 14.77 solar days) and the harmonics of the ground track repeat periods (in sidereal days) represented by the vertical dashed lines

combined. Using GPS clearly introduces spurious signals at 13.6, 14.19 and 14.77 days, which are not visible in the Galileo + GLONASS combination. This suggests that these signals primarily originated from the geometry of the GPS observations rather than GNSS processing itself. The adjustment of the OTL coefficients does not significantly change the fortnightly band when the Galileo + GLONASS combination is used. The O1 and M2 coefficients computed in the FES2014b loading model are thus consistent with GLONASS and Galileo observations, at least at the noise level obtained with the stacked power spectrum.

Discussion and conclusions

Propagated signals appear in daily GNSS position time series due to mismodeling or unmodeled phenomena at the sub-daily band. We aim, on the one hand, to assess errors in the FES2014b OTL model by using the recently available ambiguity-fixed Galileo observations and also weighted multi-GNSS observations; and on the other hand, to mitigate the OTL aliasing into long-term signals from the simultaneous estimation of OTL errors and station positions.

We estimated the OTL residual errors together with the standard PPP parameters (station positions, tropospheric parameters) by NEQ stacking and compared them to the kinematic approach. Using these two approaches, we found significant differences in the estimated errors of OTL displacements. In addition, with the kinematic approach, the sub-daily positions remain significantly correlated with the troposphere bias. Conversely, the OTL parameters estimated by NEQ stacking are well separated from the troposphere parameters. King (2006) also shows a noticeable correlation between the estimated OTL parameters themselves. Such correlation vanishes with our approach because instead of combining the daily estimates and eventually the systematic

Journal : Large 10291 | Article No : 1467 | Pages : 16 | MS Code : 1467 | Dispatch : 7-5-2023

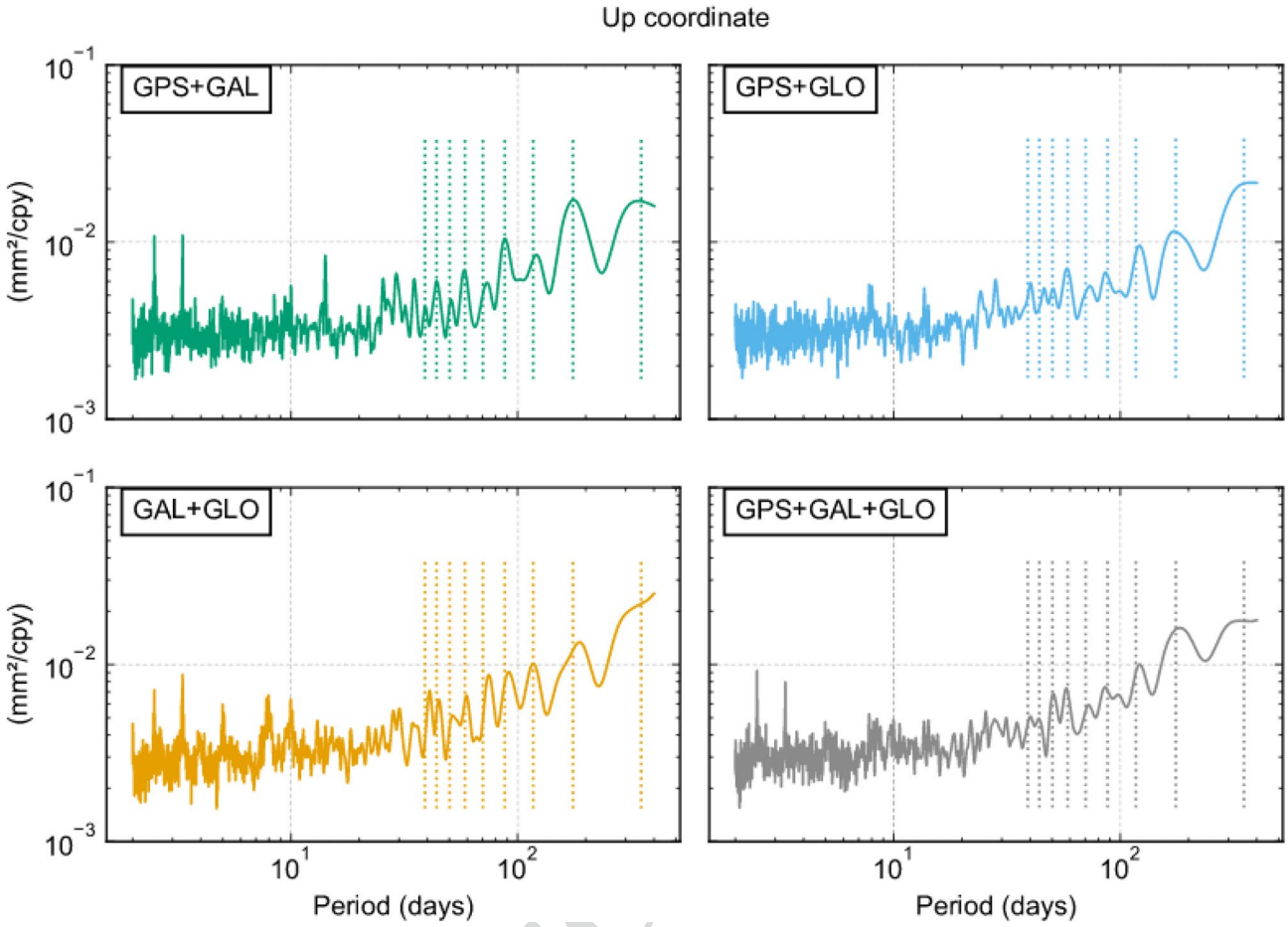

Fig. 10 Same as Fig. 9 for multi-GNSS solutions on the full spectral domain. The vertical dashed lines represent the GPS draconitic frequencies and their harmonics

errors, we accumulate the observations for a longer time span to better estimate the parameters. Hence, the tidal lines are less likely to absorb each other, which facilitates the identification of their origins. As in previous studies, our analysis addresses the major sub-daily ocean tides, which account for approximately 80% of the total OTL power spectrum. Due to the limited spectral resolution, the OTL displacements resulting from the remaining minor and neighboring tidal constituents were not explicitly considered, but their impact has been incorporated into the main tide results. The assumptions of constant OTL coefficients can also be questioned as the tidal height may have intra-annual variations (Haigh et al. 2020).

Our approach using three different GNSS constellations provides a more detailed assessment of an OTL model due to the ability to separate systematic constellation errors from OTL mismodeling. Globally, the differences between the GNSS observations and the FES2014 tide model are for most stations at the level of 0.60 mm (achieved in the Up direction for K1). By including either Galileo and/or GLONASS, the agreement is improved by 33 to 55% compared to GPS-only estimates, in particular for the sun-driven tides (K1, K2, S2, P1). These findings agree with previous studies exhibiting similar reductions in the K1, K2, and S2 residual amplitudes with GLONASS (Abbaszadeh et al. 2020; Matviichuk et al. 2020), with GLONASS/Galileo (Zajdel et al. 2022) and GLONASS/Galileo/Beidou (Wei et al. 2021) compared to GPS.

We computed the OTL errors from optimally weighted multi-GNSS PPP daily solutions. Including GPS degrades the estimation of the K1, K2 and S2 tides, suggesting that a specific weighting strategy is required when GPS observations are included in the GNSS combination. We suggest a solution with a downweighted GPS contribution to the observation of K1 and K2. Adding GLONASS to GPS has limited influence in our analysis, particularly in the East direction, compared to adding Galileo. Indeed, Galileo has a larger influence, despite the constellation not being complete yet. This indicates the benefit of better measurement modeling achieved with integer-valued carrier phase ambiguities over the number of observations. Future ambiguity-fixed results with BeiDou and GLONASS will certainly improve

Journal : Large 10291 | Article No : 1467 | Pages : 16 | MS Code : 1467 | Dispatch : 7-5-2023

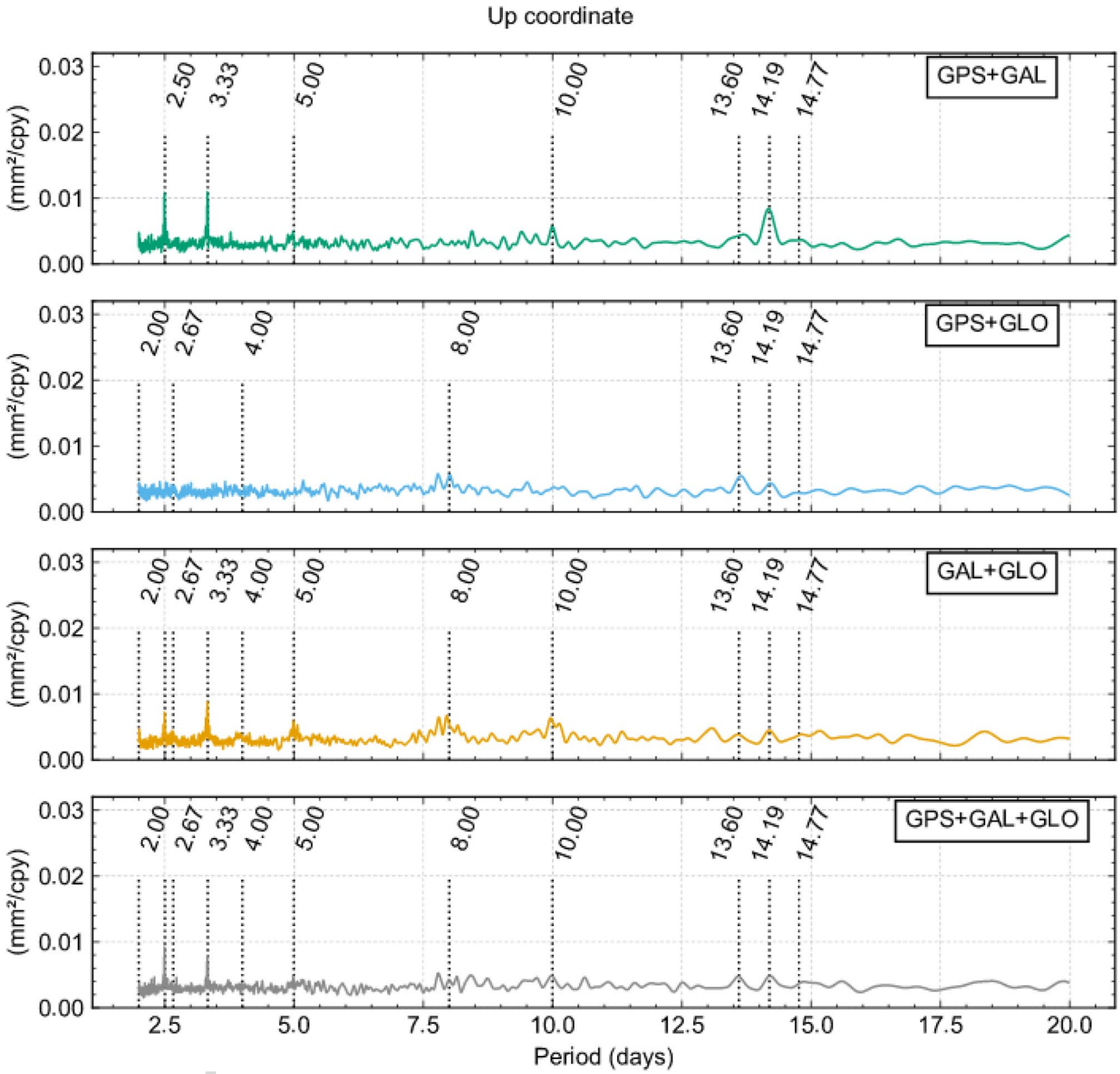

Fig. 11 Same as Fig. 9 for multi-GNSS solutions on the 14-day and higher frequencies domain. The propagated frequencies (~ 13.6, 14.19 and 14.77 days) and the harmonics of the ground track repeat periods (in sidereal days) are represented by the vertical dashed lines

Table 4 Period (in days) and admittance in amplitude (percent) of the first largest aliased peaks for GPS, Galileo and GLONASS computed from the expressions developed in Stewart et al. (2005)

GPS		Galileo		GLONASS	
O1	M2	O1	M2	O1	M2
13.662/42.1	13.678/44.6	3.690/15.0	3.729/6.3	3.114/17.6	3.142/7.1
14.193/7.5	14.786/3.5	5.857/7.7	14.786/3.5	5.107/10.2	5.182/4.5
13.169/3.1	14.210/3.2	14.193/7.5	5.956/3.4	14.193/7.5	5.463/3.5
14.766/1.5	15.409/0.9	7.687/5.1	7.524/2.8	5.549/6.4	14.786/3.5
15.389/1.0	16.088/0.7	33.541/1.1	30.636/0.6	18.221/2.3	17.328/1.2

Journal : Large 10291 | Article No : 1467 | Pages : 16 | MS Code : 1467 | Dispatch : 7-5-2023

the assessment of OTL errors. However, it is important to observe that the PPP technique only provides information on local-scale processes or mismodeling that are not absorbed into the preceding estimation of precise orbit and clock products. OTL has a multi-scale structure depending on the areas (coastline, water depth), the tides, or global processes such as the atmospheric dynamics (Pineau-Guillou et al. 2021), and the question of the assessment of the large-scale error of the OTL model is still open.

Furthermore, this study suggests a means to reduce the propagation of signals in GNSS position time series with the simultaneous estimation of the positions and OTL harmonic parameters, known as the harmonic or static approach. The fortnightly propagation errors occur at different frequencies depending on the constellation. The approximately 13.6-day peak is specific to GPS, while the 14.19- and 14.79-day peaks are common to the three constellations, as predicted by the model of Stewart et al. (2005), and as evidenced with GPS and GLONASS in Abraha et al. (2018). Our results using Galileo and the static approach confirm that the approximately 13.6-day peak is a GPS-propagated signal of the M2 tidal error. These findings only confirm an approximated version of the model, where a term in the denominator of equation 30 in Stewart et al. (2005) is neglected. This holds for the GPS constellation, as this term is close to 1, but for GLONASS and Galileo, this assumption is not valid. For Galileo and GLONASS observations, the model predicts several signals with smaller amplitudes in addition to the main propagated signals. Further work with longer Galileo observations is needed to assess the validity of this propagation model.

A similar reduction can be slightly observed for the draconitic oscillations. Nevertheless, the effects of propagated sub-daily OTL errors are minimal compared to the remaining constellation-specific long-period signals. Further analysis with a longer period is necessary to better assess the impact on the long-period aliased signals. In addition, Galileo- and GLONASS-specific signals appear at the harmonics of 8 days for GLONASS, also reported by Rebischung et al. (2021), and 10 days for Galileo as already reported by Zajdel et al. (2022). Even though they are partially reduced with the additional OTL parameters, none of the propagated OTL frequencies may explain these signals. A limitation of our study is that the spectral resolution reached in our work prevents us from separating constellation-specific frequencies (harmonics of ground track repeat periods) from OTL frequencies. A longer time span and further investigation into orbital modeling would help to properly infer the exact origin of these constellation-specific signatures.

Despite the continuous improvements in the sub-daily loading models recommended by the IERS Conventions, propagated OTL signals are still visible in the GNSS coordinates time series which may lead to improper interpretations of geophysical signals. This paper shows that the estimation of additional sub-daily OTL parameters improves the power spectrum of GNSS position time series at the fortnightly and annual bands. Other tidal loading models, such as solid earth, atmosphere and ocean pole tides, have been reported to generate seasonal signals (Watson et al. 2006; Li et al. 2018; Tregoning and Watson 2009; Niu et al. 2021). In addition, previous research documented periodic effects originating from antenna multipath (King and Watson 2010), phase center position variations (Sidorov and Teferle 2015), snow intrusion (Koulali and Clarke 2020), and the thermal expansion of the monument or bedrock (Yan et al. 2009; Wang et al. 2018). Accounting for these error sources is not yet standard practice in GNSS processing due to the absence of accurate knowledge and prediction models. The possibility of adding new parameters to the PPP processing to account for mismodeled sub-daily geophysical or apparent displacements opens new general perspectives to improve GNSS positioning and geophysical modeling, for instance, to constrain and infer more complex models, including the earth's response properties, or to study the seasonal variations of tides currently predicted by oceanographers (Haigh et al. 2020; Zhou et al. 2021).

Supplementary Information The online version contains supplementary material available at https://doi.org/10.1007/s10291-023-01467-9.

Acknowledgements We thank comments by Dr. Nigel Penna, an anonymous reviewer, and the handling editor Dr. Alfred Leick that increased the quality and clarity of this manuscript. We are grateful to Prof. Jean-Paul Boy from Ecole et Observatoire des Sciences de la Terre (EOST), France, for providing the program to compute the ocean tide loading corrections. We also thank Jim Ray for helpful comments on an early version of the manuscript. This work was supported by Region Occitanie and the Centre National d'Etudes Spatiales (CNES).

Author's contribution HA-L, AS-G and FP contributed to the design of the study. HA undertook software modifications, GNSS data processing, and drafted the preliminary manuscript. HA-L, AS-G and FP participated in the analysis of the results and reviewed the manuscript. All authors have read and approved the manuscript.

Data availability RINEX were obtained through the online archives of the Crustal Dynamics Data Information System (CDDIS) https://cddis.nasa.gov/archive/gnss/data/daily/. The orbit and clock products were provided by the GRGS Analysis Center.

Declarations

Conflict of interest The authors declare no competing interests.

References

Abbaszadeh M, Clarke PJ, Penna NT (2020) Benefits of combining GPS and GLONASS for measuring ocean tide loading displacement. J Geodesy 94(7):63. https://doi.org/10.1007/s00190-020-01393-5

Abraha KE, Teferle FN, Hunegnaw A, Dach R (2018) Effects of unmodelled tidal displacements in GPS and GLONASS coordinate time-series. Geophy J Int 214(3):2195–2206. https://doi.org/10.1093/gji/ggy254

Blewitt G (2003) Self-consistency in reference frames, geocenter definition, and surface loading of the solid Earth. J Geophys Res Solid Earth. https://doi.org/10.1029/2002JB002082

Bos MS, Penna NT, Baker TF, Clarke PJ (2015) Ocean tide loading displacements in western Europe: 2. GPS-observed anelastic dispersion in the asthenosphere. J Geophys Res Solid Earth 120(9):6540–6557. https://doi.org/10.1002/2015JB011884

Choi K, Bilich A, Larson KM, Axelrad P (2004) Modified sidereal filtering: implications for high-rate GPS positioning. Geophys Res Lett. https://doi.org/10.1029/2004GL021621

Collilieux X, Altamimi Z, Coulot D, Ray J, Sillard P (2007) Comparison of very long baseline interferometry, GPS, and satellite laser ranging height residuals from ITRF2005 using spectral and correlation methods. J Geophys Res Solid Earth. https://doi.org/10.1029/2007JB004933

Dong D, Fang P, Bock Y, Cheng MK, Miyazaki S (2002) Anatomy of apparent seasonal variations from GPS-derived site position time series. J Geophys Res Solid Earth 107(B4):ETG9-1-ETG9-16. https://doi.org/10.1029/2001JB000573

Fu Y, Freymueller JT, van Dam T (2012) The effect of using inconsistent ocean tidal loading models on GPS coordinate solutions. J Geodesy 86(6):409–421. https://doi.org/10.1007/s00190-011-0528-1

Haigh ID et al (2020) The tides they are A-Changin': a comprehensive review of past and future nonastronomical changes in tides, their driving mechanisms, and future implications. Rev Geophys 58(1):e2018RG000636. https://doi.org/10.1029/2018RG000636

Katsigianni G, Loyer S, Perosanz F (2019a) PPP and PPP-AR kinematic post-processed performance of GPS-only, Galileo-only and multi-GNSS. Remote Sens 11(21):2477. https://doi.org/10.3390/rs11212477

Katsigianni G, Loyer S, Perosanz F, Mercier F, Zajdel R, Sośnica K (2019b) Improving Galileo orbit determination using zero-difference ambiguity fixing in a Multi-GNSS processing. Adv Space Res 63(9):2952–2963. https://doi.org/10.1016/j.asr.2018.08.035

King M (2006) Kinematic and static GPS techniques for estimating tidal displacements with application to Antarctica. J Geodyn 41(1):77–86. https://doi.org/10.1016/j.jog.2005.08.019

King MA, Penna NT, Clarke PJ, King EC (2005) Validation of ocean tide models around Antarctica using onshore GPS and gravity data. J Geophys Res Solid Earth. https://doi.org/10.1029/2004JB003390

King MA, Watson C (2010) Long GPS coordinate time series: multipath and geometry effects. J Geophys Res Solid Earth. https://doi.org/10.1029/2009jb006543

Koulali A, Clarke PJ (2020) Effect of antenna snow intrusion on vertical GPS position time series in Antarctica. J Geodesy 94(10):101. https://doi.org/10.1007/s00190-020-01403-6

Li F, Lei J, Zhang S, Ma C, Hao W, E D, Zhang Q (2018) The impact of solid Earth-tide model error on tropospheric zenith delay estimates and GPS coordinate time series. Surv Rev 50(361): 355–363. https://doi.org/10.1080/00396265.2016.1277657

Loyer S, Perosanz F, Mercier F, Capdeville H, Marty J-C (2012) Zero-difference GPS ambiguity resolution at CNES–CLS IGS analysis center. J Geodesy 86(11):991–1003. https://doi.org/10.1007/s00190-012-0559-2

Lyard FH, Allain DJ, Cancet M, Carrère L, Picot N (2021) FES2014 global ocean tides atlas: design and performances. Ocean Sci. https://doi.org/10.5194/os-17-615-2021

Martens HR, Simons M, Owen S, Rivera L (2016) Observations of ocean tidal load response in South America from subdaily GPS positions. Geophy J Int 205(3):1637–1664. https://doi.org/10.1093/gji/ggw087

Marty JC et al (2011) GINS: the CNES/GRGS GNSS scientific software. In: 3rd international colloquium scientific and fundamental aspects of the galileo programme, ESA proceedings WPP326, vol. 31, pp 8–10

Matviichuk B, King M, Watson C (2020) Estimating ocean tide loading displacements with GPS and GLONASS. Solid Earth 11(5):1849–1863. https://doi.org/10.5194/se-11-1849-2020

Melachroinos SA et al (2008) Ocean tide loading (OTL) displacements from global and local grids: comparisons to GPS estimates over the shelf of Brittany, France. J Geodesy 82(6):357–371. https://doi.org/10.1007/s00190-007-0185-6

Niu Y, Li M, Wei N, Shi C, Chen G, Wang L (2021) The ocean pole tide loading and its effect on GPS position time-series. Geophy J Int 227(1):368–382. https://doi.org/10.1093/gji/ggab231

Penna NT, Clarke PJ, Bos MS, Baker TF (2015) Ocean tide loading displacements in western Europe: 1. Validation of kinematic GPS estimates. J Geophys Res Solid Earth 120(9):6523–6539. https://doi.org/10.1002/2015JB011882

Penna NT, King MA, Stewart MP (2007) GPS height time series: short-period origins of spurious long-period signals. J Geophys Res Solid Earth. https://doi.org/10.1029/2005JB004047

Penna NT, Stewart MP (2003) Aliased tidal signatures in continuous GPS height time series. Geophys Res Lett. https://doi.org/10.1029/2003GL018828

Petit G, Luzum B (2010) IERS conventions. IERS Technical Note 36, Verlag des Bundesamts für Kartographie und Geodäsie, Germany

Pineau-Guillou L, Lazure P, Wöppelmann G (2021) Large-scale changes of the semidiurnal tide along North Atlantic coasts from 1846 to 2018. Ocean Sci 17(1):17–34. https://doi.org/10.5194/os-17-17-2021

Ragheb AE, Clarke PJ, Edwards SJ (2007) GPS sidereal filtering: coordinate- and carrier-phase-level strategies. J Geodesy 81(5):325–335. https://doi.org/10.1007/s00190-006-0113-1

Ray J, Altamimi Z, Collilieux X, van Dam T (2008) Anomalous harmonics in the spectra of GPS position estimates. GPS Solut 12(1):55–64. https://doi.org/10.1007/s10291-007-0067-7

Rebischung P, Collilieux X, Metivier L, Altamimi Z, Chanard K (2021) Analysis of IGS REPRO3 station position time series. In: AGU 2021 Fall Meeting https://doi.org/10.1002/essoar.10509008.1

Sahin M, Cross PA, Sellers PC (1992) Variance component estimation applied to satellite laser ranging. Bull Géodésique 66(3):284–295. https://doi.org/10.1007/BF02033189

Sidorov D, Teferle FN (2015) Impact of antenna phase centre calibrations on position time series: preliminary results. In: international association of geodesy symposia, Springer International Publishing. pp 117–123 https://doi.org/10.1007/1345_2015_216

Stewart MP, Penna NT, Lichti DD (2005) Investigating the propagation mechanism of unmodelled systematic errors on coordinate time series estimated using least squares. J Geodesy 79(8):479–489. https://doi.org/10.1007/s00190-005-0478-6

Thomas ID, King MA, Clarke PJ (2007) A comparison of GPS, VLBI and model estimates of ocean tide loading displacements. J Geodesy 81(5):359–368. https://doi.org/10.1007/s00190-006-0118-9

Tregoning P, Watson C (2009) Atmospheric effects and spurious signals in GPS analyses. J Geophys Res Solid Earth. https://doi.org/10.1029/2009JB006344

Vergnolle M, Bouin M-N, Morel L, Masson F, Durand S, Nicolas J, Melachroinos SA (2008) GPS estimates of ocean tide loading in NW-France: determination of ocean tide loading constituents and comparison with a recent ocean tide model. Geophy J Int 173(2):444–458. https://doi.org/10.1111/j.1365-246X.2008.03734.x

Wang K, Chen H, Jiang W, Li Z, Ma Y, Deng L (2018) Improved vertical displacements induced by a refined thermal expansion model

and its quantitative analysis in GPS height time series. J Geophys Eng 15(2):554–567. https://doi.org/10.1088/1742-2140/aa93ae

Watson C, Tregoning P, Coleman R (2006) Impact of solid Earth tide models on GPS coordinate and tropospheric time series. Geophys Res Lett. https://doi.org/10.1029/2005GL025538

Wei G, Chen K, Ji R (2021) Improving estimates of ocean tide loading displacements with multi-GNSS: a case study of Hong Kong. GPS Solut 26(1):25. https://doi.org/10.1007/s10291-021-01212-0

Yan H, Chen W, Zhu Y, Zhang W, Zhong M (2009) Contributions of thermal expansion of monuments and nearby bedrock to observed GPS height changes. Geophys Res Lett. https://doi.org/10.1029/2009GL038152

Yuan L, Chao BF, Ding X, Zhong P (2013) The tidal displacement field at Earth's surface determined using global GPS observations. J Geophys Res Solid Earth 118(5):2618–2632. https://doi.org/10.1002/jgrb.50159

Zajdel R, Kazmierski K, Sośnica K (2022) Orbital artifacts in multi-GNSS precise point positioning time series. J Geophys Res Solid Earth 127(2):e2021JB022994. https://doi.org/10.1029/2021JB022994

Zhou M, Liu X, Yuan J, Jin X, Niu Y, Guo J, Gao H (2021) Seasonal variation of GPS-derived the principal ocean tidal constituents' loading displacement parameters based on moving harmonic analysis in Hong Kong. Remote Sens 13(2):279. https://doi.org/10.3390/rs13020279

Zumberge JF, Heflin MB, Jefferson DC, Watkins MM, Webb FH (1997) Precise point positioning for the efficient and robust analysis of GPS data from large networks. J Geophys Res Solid Earth 102(B3):5005–5017. https://doi.org/10.1029/96JB03860

Hanane Ait-Lakbir is a Ph.D. candidate in geophysics and space geodesy at the Observatoire Midi-Pyrénées (GET). She received a degree in Aerospace Engineering from ISAE (Institut Supérieur de l'Aéronautique et de l'Espace), Toulouse, France. Her current research is on the use of multi-GNSS precise positioning.

Alvaro Santamaría-Gómez received his Ph.D. in geodesy from the Astronomy and Astrophysics Doctoral School of Paris, France, in 2010. He is an Associate Professor at the Paul Sabatier University and the Observatoire Midi-Pyrénées, overseeing the Pyrenees GNSS RENAG network. His research focuses on earth surface deformation using GNSS observations.

Felix Perosanz was the head of the IGS GRGS Analysis Center at the GET/OMP laboratory in Toulouse (France) from 2010 to 2022 and the chairman of the IGS Governing Board from 2020 to 2023. He received his PhD from the University of Toulouse in 1995 and his Habilitation to direct research in 2016. He is currently in charge of the Solid Earth program at the Strategy Directorate of the French Space Agency.

Supplementary information

Assessment of sub-daily ocean tide loading errors and mitigation of their aliasing in multi-GNSS positions time series

Hanane Ait-Lakbir[1], Alvaro Santamaría-Gómez[1], and Félix Perosanz[1]

[1]GET, Université Paul Sabatier, CNES, CNRS, IRD, UPS, Toulouse, France

Corresponding author: Hanane Ait-Lakbir - hanane.ait-lakbir@get.omp.eu

The document is divided into four sections.

1. The first section introduces the spectra of subdaily positions used in the kinematic approach to infer the OTL-induced positioning errors.
2. The second section presents the steps involved in the static estimation of OTL errors based on normal equation stacking and optimal weighting.
3. The third and fourth sections contain spectra for the horizontal components of the positions to supplement the analysis on the vertical component presented in the main manuscript.

Table S1 Longitude, latitude and distance to ocean of the stations

Index	Site	Longitude (°)	Latitude (°)	Distance to ocean (km)	Index	Site	Longitude (°)	Latitude (°)	Distance to ocean (km)
0	ABMF00GLP	-61.53	16.26	2.27	32	MATE00ITA	16.70	40.65	28.67
1	ABPO00MDG	47.23	-19.02	186.41	33	MAW100ATA	62.87	-67.60	5.99
2	AREG00PER	-71.49	-16.47	83.22	34	MEDI00ITA	11.65	44.52	50.22
3	BRST00FRA	-4.50	48.38	2.23	35	MELI00ESP	-2.95	35.28	2.79
4	BRUX00BEL	4.36	50.80	52.38	36	MRC100USA	-77.37	38.50	5.69
5	CAS100ATA	110.52	-66.28	1.37	37	NIUM00NIU	-169.93	-19.08	2.04
6	CCJ200JPN	142.20	27.07	1.66	38	NNOR00AUS	116.19	-31.05	74.62
7	CHPI00BRA	-44.99	-22.69	52.06	39	OHI300ATA	-57.90	-63.32	1.27
8	DAEJ00KOR	127.37	36.40	58.74	40	ONSA00SWE	11.93	57.40	0.89
9	DARW00AUS	131.13	-12.84	29.98	41	PERT00AUS	115.89	-31.80	15.81
10	DAV100ATA	77.97	-68.58	21.29	42	PNGM00PNG	147.37	-2.04	1.93
11	DGAR00GBR	72.37	-7.27	0.10	43	POTS00DEU	13.07	52.38	166.19
12	EBRE00ESP	0.49	40.82	17.48	44	PTBB00DEU	10.46	52.30	144.86
13	FALK00FLK	-57.87	-51.69	2.25	45	REDU00BEL	5.14	50.00	152.96
14	GENO00ITA	8.92	44.42	0.89	46	RIGA00LVA	24.06	56.95	9.63
15	GMSD00JPN	131.02	30.56	0.64	47	ROAG00ESP	-6.21	36.46	1.72
16	GODE00USA	-76.83	39.02	22.16	48	SGOC00LKA	79.87	6.89	2.88
17	GRAC00FRA	6.92	43.75	21.44	49	SOLO00SLB	159.95	-9.43	0.72
18	HOB200AUS	147.44	-42.80	7.66	50	SPT000SWE	12.89	57.71	57.19
19	HOFN00ISL	-15.20	64.27	0.18	51	STJ300CAN	-52.68	47.60	1.39
20	JPLM00USA	-118.17	34.20	36.54	52	STK200JPN	141.84	43.53	35.30
21	KARR00AUS	117.10	-20.98	34.71	53	STR100AUS	149.01	-35.32	116.17
22	KIR000SWE	21.06	67.88	143.92	54	THTG00PYF	-149.61	-17.58	3.84
23	KIR800SWE	21.06	67.88	143.92	55	TID100AUS	148.98	-35.40	115.43
24	KOKB00USA	-159.66	22.13	4.82	56	TLSG00FRA	1.49	43.55	140.68
25	KOS100NLD	5.82	52.17	90.17	57	TONG00TON	-175.18	-21.14	1.72
26	KOUR00GUF	-52.81	5.25	6.11	58	TRO100NOR	18.94	69.66	4.07
27	LAUT00FJI	177.45	-17.61	1.78	59	UNB300CAN	-66.64	45.95	72.98
28	LMMF00MTQ	-61.00	14.59	1.85	60	USN700USA	-77.07	38.92	2.08
29	MAR700SWE	17.26	60.60	5.17	61	USN900USA	-77.07	38.92	2.08
30	MAS100ESP	-15.63	27.76	2.07	62	USUD00JPN	138.36	36.13	110.87
31	MAT100ITA	16.70	40.65	28.66	63	YAR300AUS	115.35	-29.05	48.48

1. Kinematic estimation of OTL errors

The kinematic strategy involves analyzing sub-daily station positions, whose spectra are depicted in Figures S1 to S3 for GPS, Galileo, and GLONASS. The stacked spectra illustrate the residual displacements induced by OTL mismodeling for the Q1, O1, P1, K1, N2, M2, S2, and K2 tides for all three constellations. An additional signal close to the J1 tide appears on the spectra, especially with GPS. It is noteworthy that this tide is not part of the conventional site displacements model recommended by the IERS 2010 Conventions.

Furthermore, we observe signals that are specific to each constellation. For GPS, three peaks at approximately 1, 0.5, and 0.33 days coincide with the constellation repeat periods. The spectral power of these peaks is considerably higher than that of Galileo and GLONASS, suggesting that they are not only due to common factors such as the OTL model but also orbital errors. For Galileo and GLONASS, orbital signals are present at the subdiurnal harmonics of the orbital repeat period (10 for Galileo and 8 sidereal days for GLONASS).

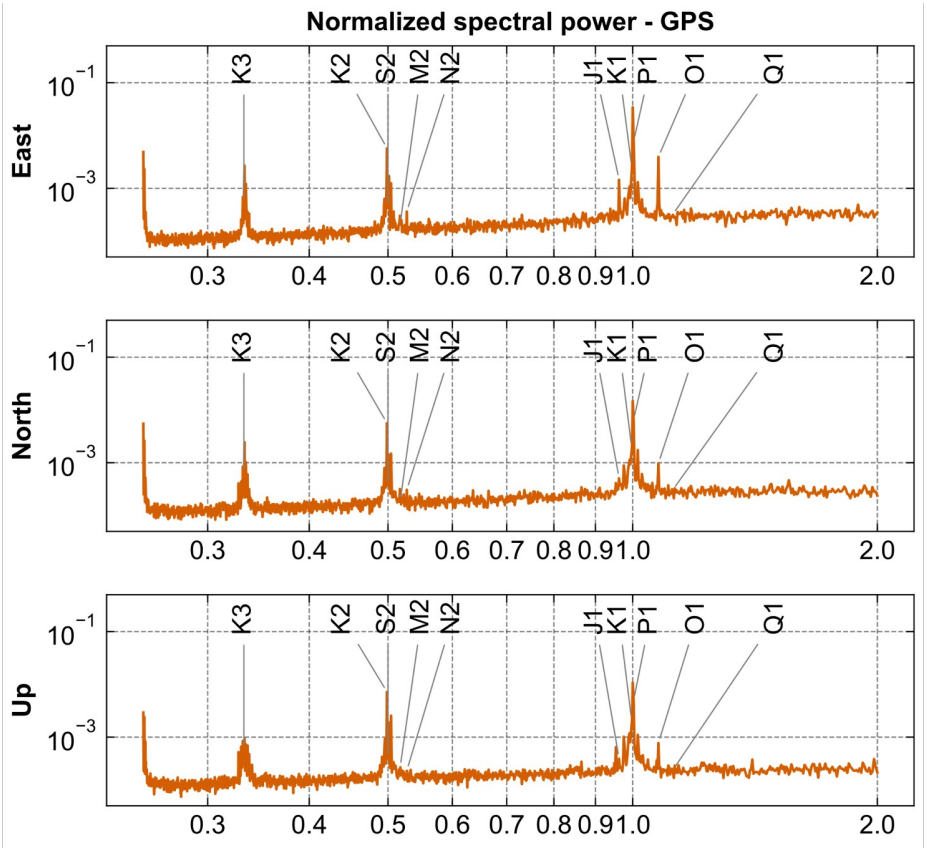

Fig. S1 Stacked normalized power spectra of 3-hour positions - GPS

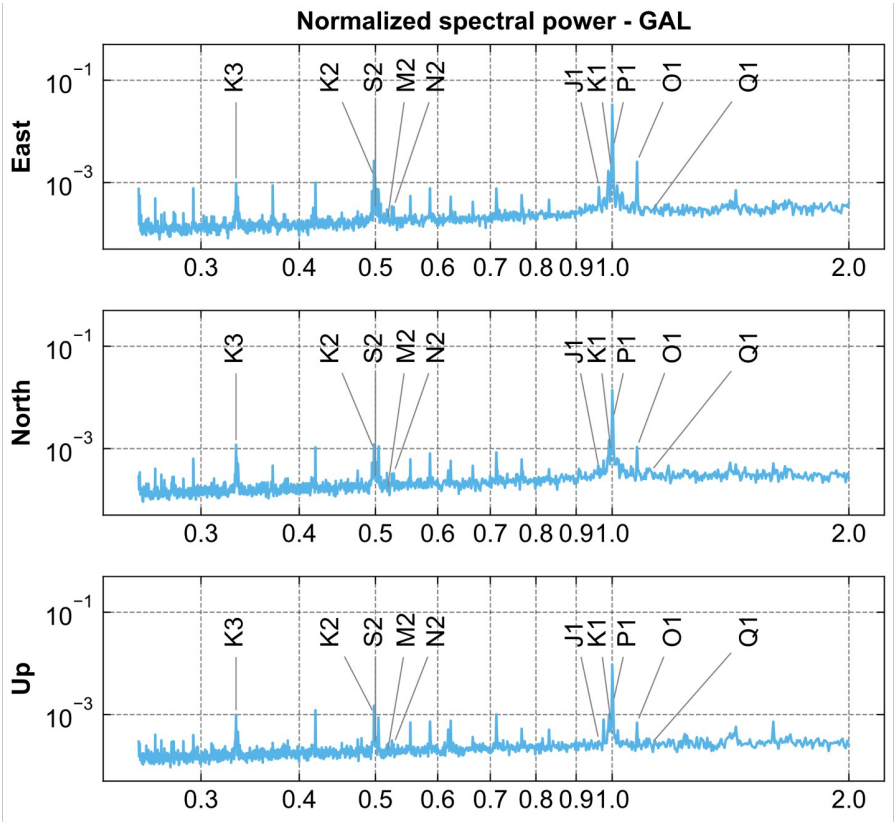

Fig. S2 Stacked normalized power spectra of 3-hour positions – Galileo

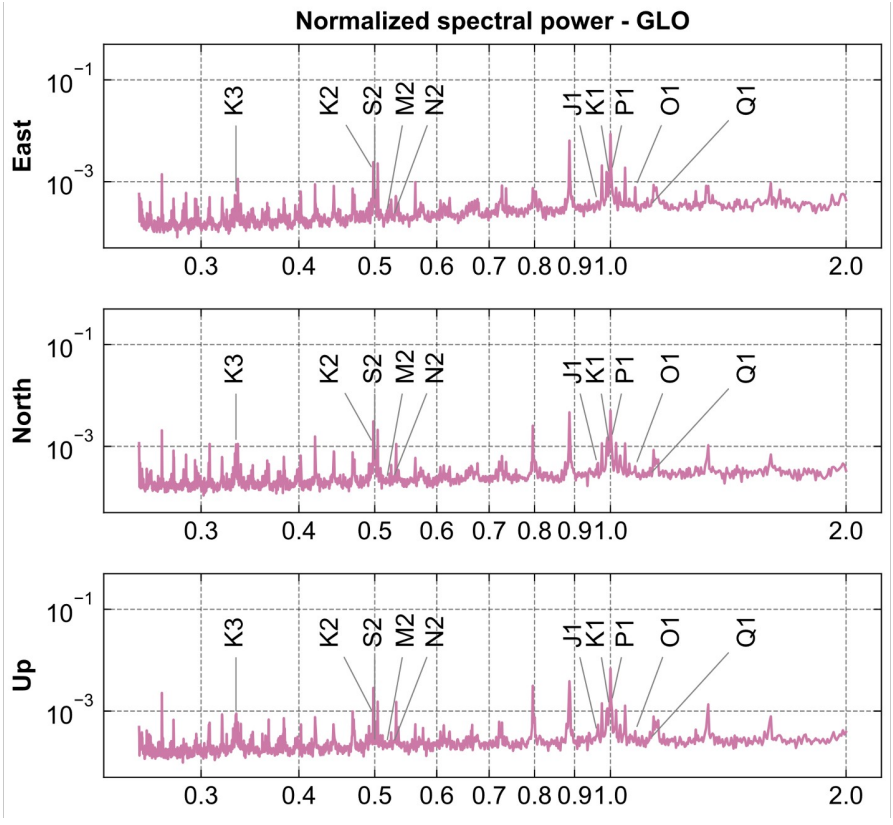

Fig. S3 Stacked normalized power spectra of 3-hour positions - GLONASS

2. Static estimation of OTL errors

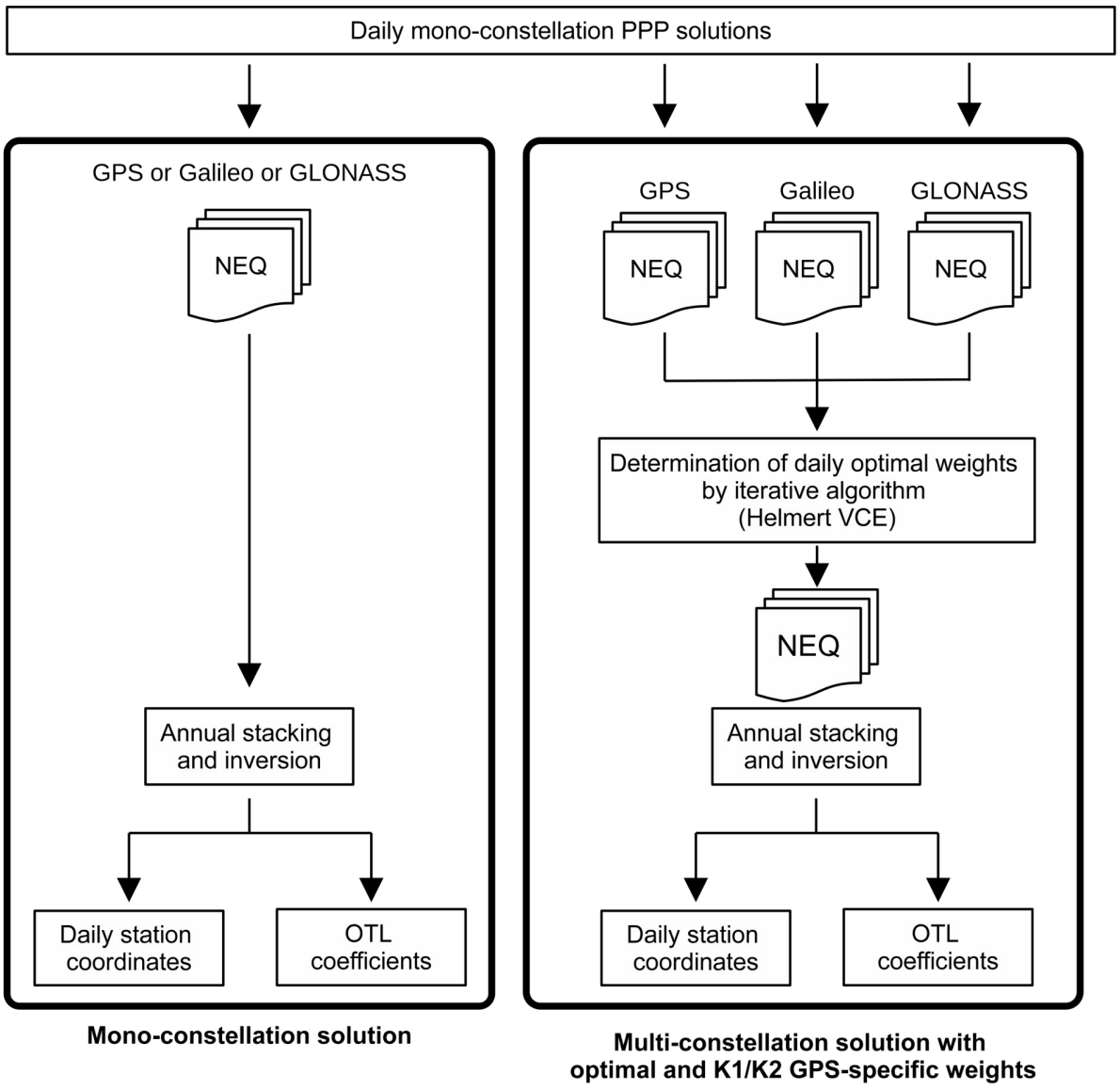

Fig. S4 Schematic of the static estimation of the OTL errors with mono-constellation (left) and multi-constellation PPP solutions. The normal equations (NEQ) contain the partial derivatives with respect to the daily XYZ stations coordinates, the ocean tide loading (OTL) coordinates and the troposphere biases and horizontal gradients.

3. Analysis of the aliased signals with the differences of coordinates

Spectra of the differences between the coordinates computed with and without estimated OTL errors using the static strategy are shown in Figures S5 to S10. These figures allow us to identify the effects of OTL error corrections, particularly in terms of propagated signals in the annual and fortnightly bands. The figures show results for the horizontal directions, while results for the vertical direction are presented in the main manuscript. However, the observations and conclusions are consistent with those described and discussed in the article for the vertical component.

Figures S5 and S6, which correspond to single constellation solutions, enable us to identify common (14.19 days, 14.77 days) and constellation-specific propagated periods (orbital repeat period for Galileo and GLONASS, and 13.6 days for GPS). Significant signatures at the GLONASS and GPS draconitic periods are also visible in the East and North components. Figures S7 to S10 provide the spectra for multi-GNSS solutions, and show the superposition of the aforementioned signatures.

3.1. GPS-, Galileo- and GLONASS-only solutions

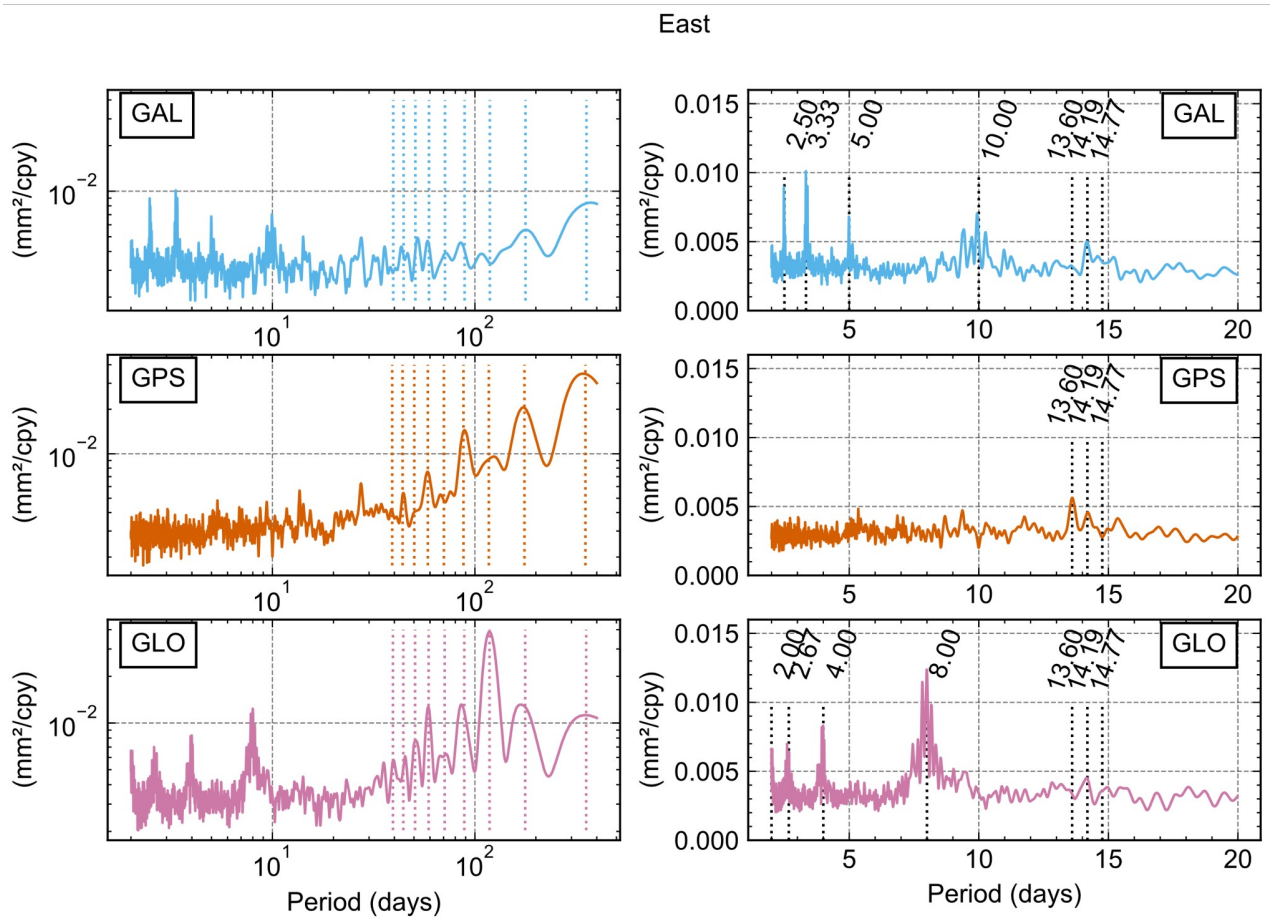

Fig. S5 Stacked normalized power spectra of the differences of East coordinates computed with the nominal and the OTL coefficients adjustment for Galileo (top), GPS (center) and GLONASS (bottom). On the right panels, the aliased frequencies (~ 13.6, 14.19 and 14.77 days) and the harmonics of the ground track repeat periods are represented by the vertical dashed lines.

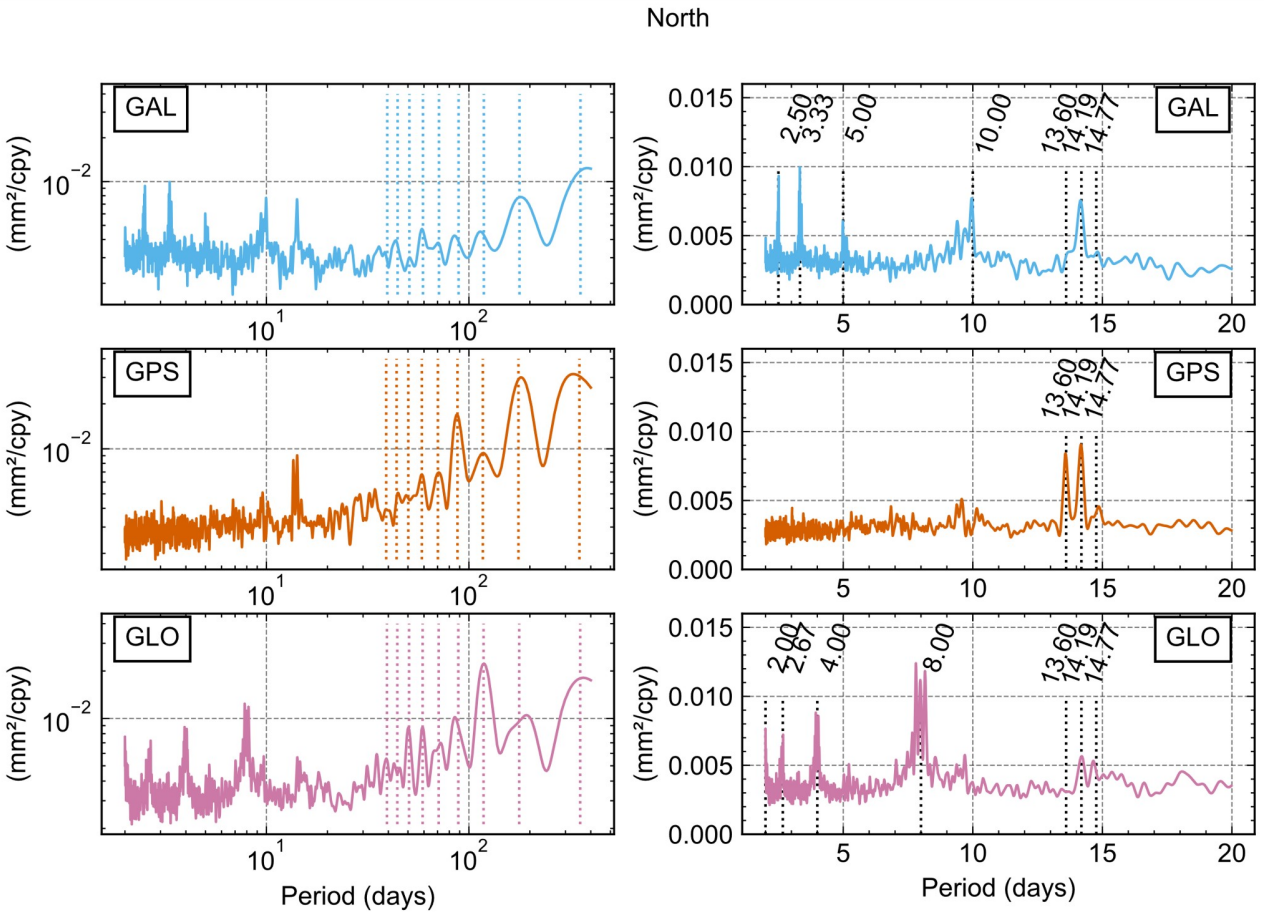

Fig. S6 Same as Figure S5 for North coordinates

77 3.2. Multi-constellation solutions

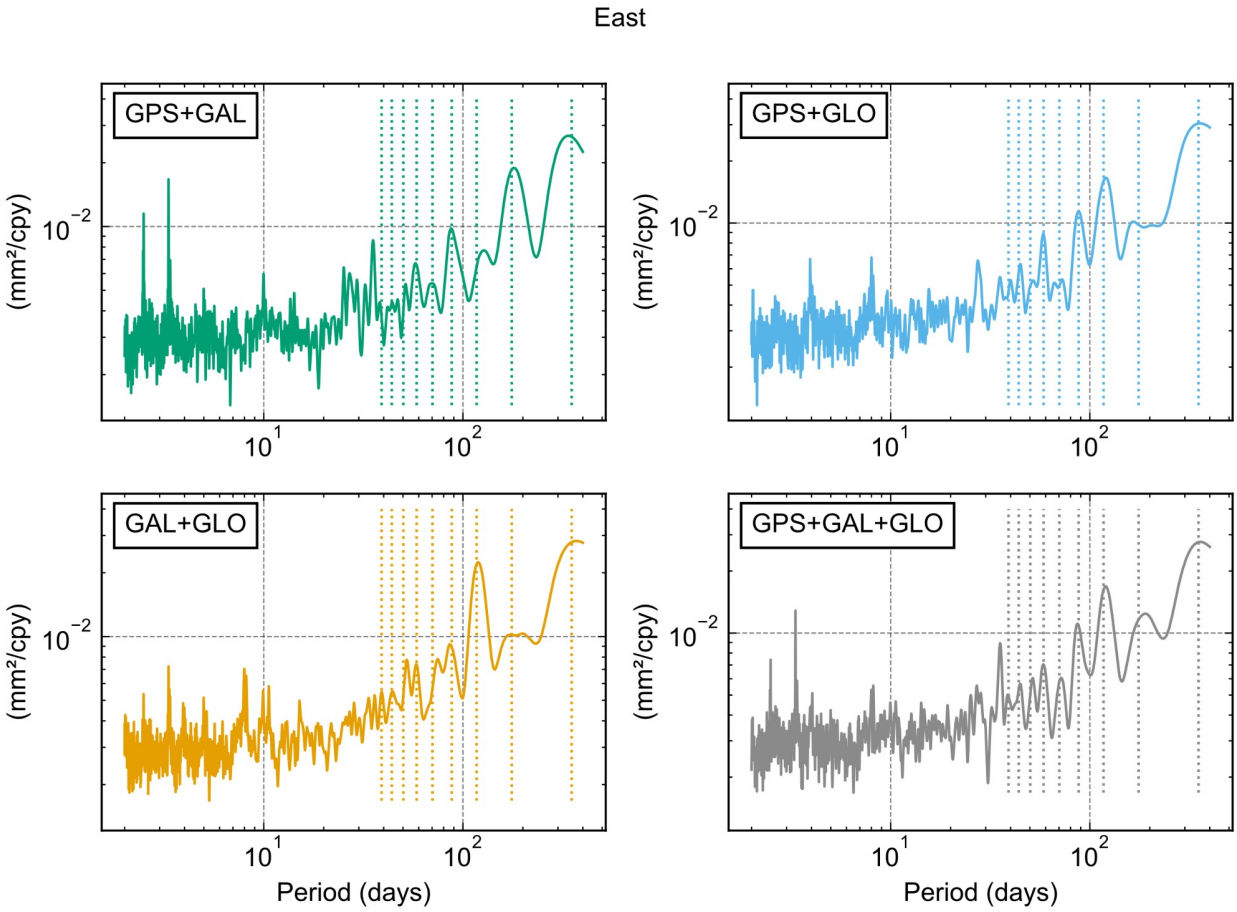

78

79 **Fig. S7** Same as Figure S5 for multi-GNSS solutions and the East coordinates on the full spectral

80 domain. The vertical dashed lines represent the GPS draconitic frequencies and their harmonics.

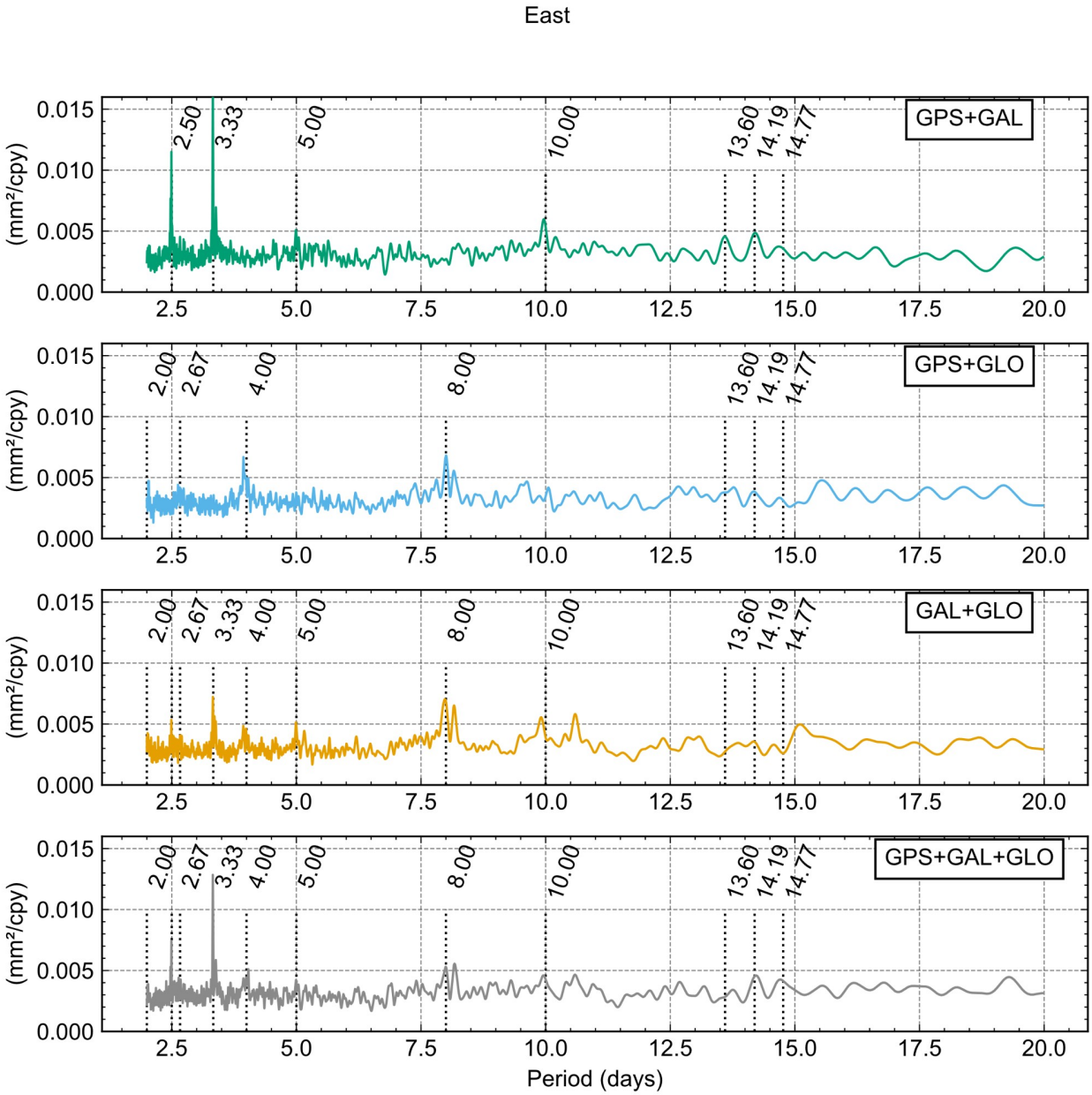

Fig. S8 Same as Figure S5 for multi-GNSS solutions and the East coordinates on the 14-day and higher frequencies domain. The aliased frequencies (~ 13.6, 14.19 and 14.77 days) and the harmonics of the ground track repeat periods are represented by the vertical dashed lines.

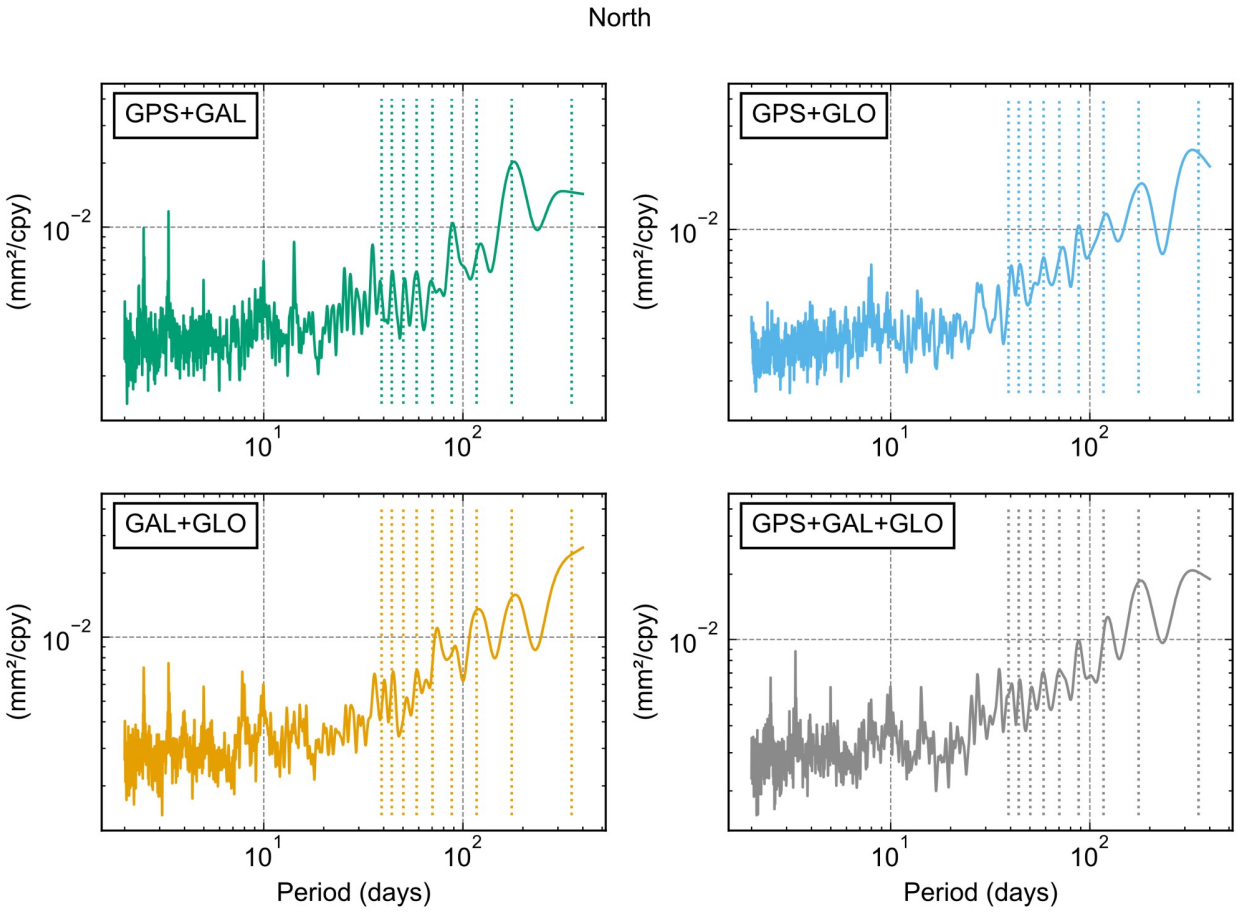

Fig. S9 Same as Figure S5 the North coordinates on the full spectral domain. The vertical dashed lines represent the GPS draconitic frequencies and their harmonics.

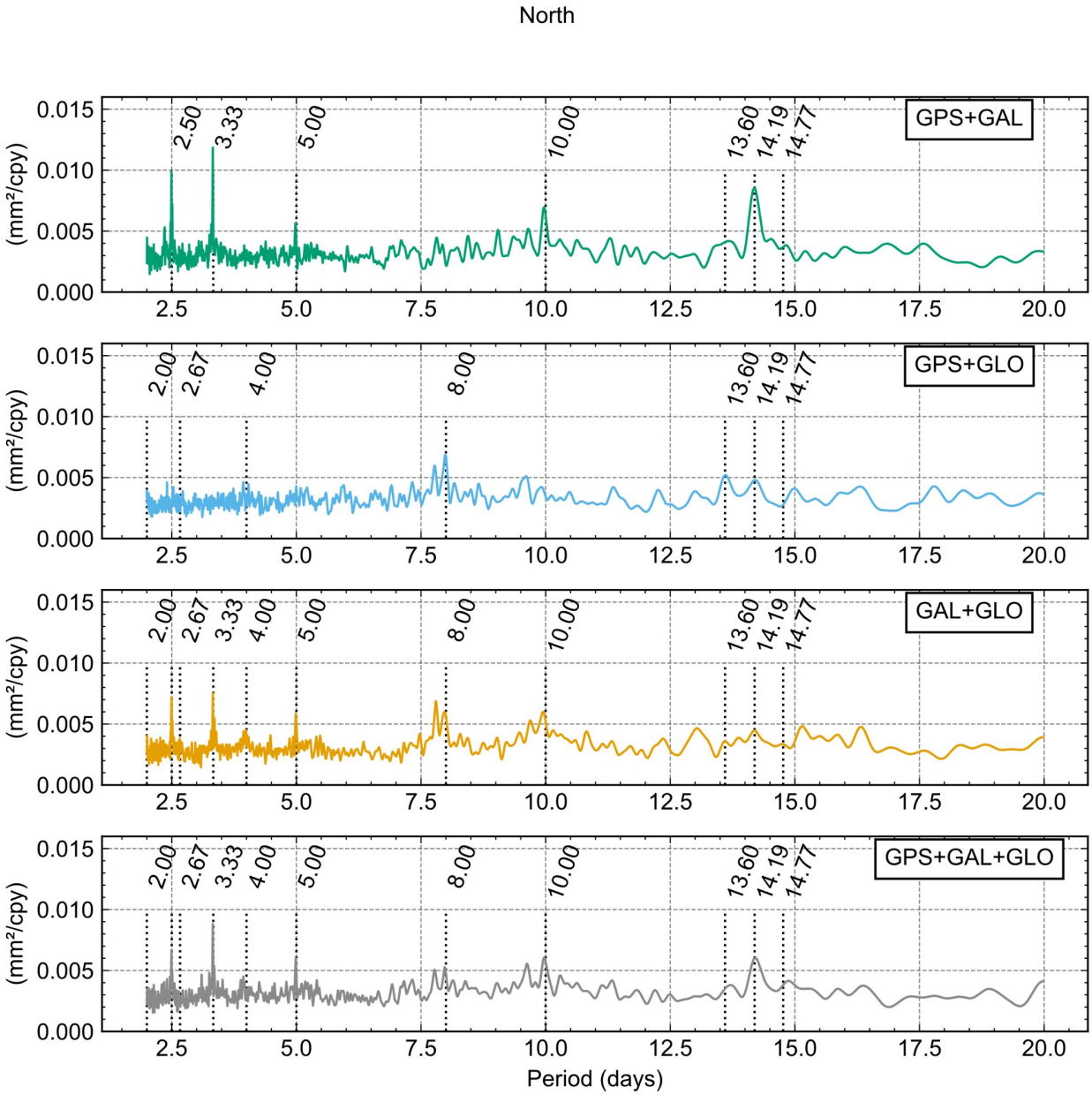

Fig. S10 Same as Figure S5 for the North coordinates on the full spectral domain. The aliased frequencies (~ 13.6, 14.19 and 14.77 days) and the harmonics of the ground track repeat periods are represented by the vertical dashed lines.

4. Analysis of the aliased signals with the spectra of coordinates

Figures S11 to S16 display the stacked normalized spectra of the multi-GNSS position solutions. The influence of the estimated OTL coefficients on the draconitic oscillations is found to be moderate, indicating that OTL mismodeling propagation only marginally contributes to these frequencies. Regarding the fortnightly signals, there is evidence of a reduction especially in the eastward direction. Despite the reduction, peaks at 13.6 days are still evident in both the North and Up components, suggesting errors induced by Mf mismodeling. The vertical component exhibits a more modest reduction compared to the horizontal components.

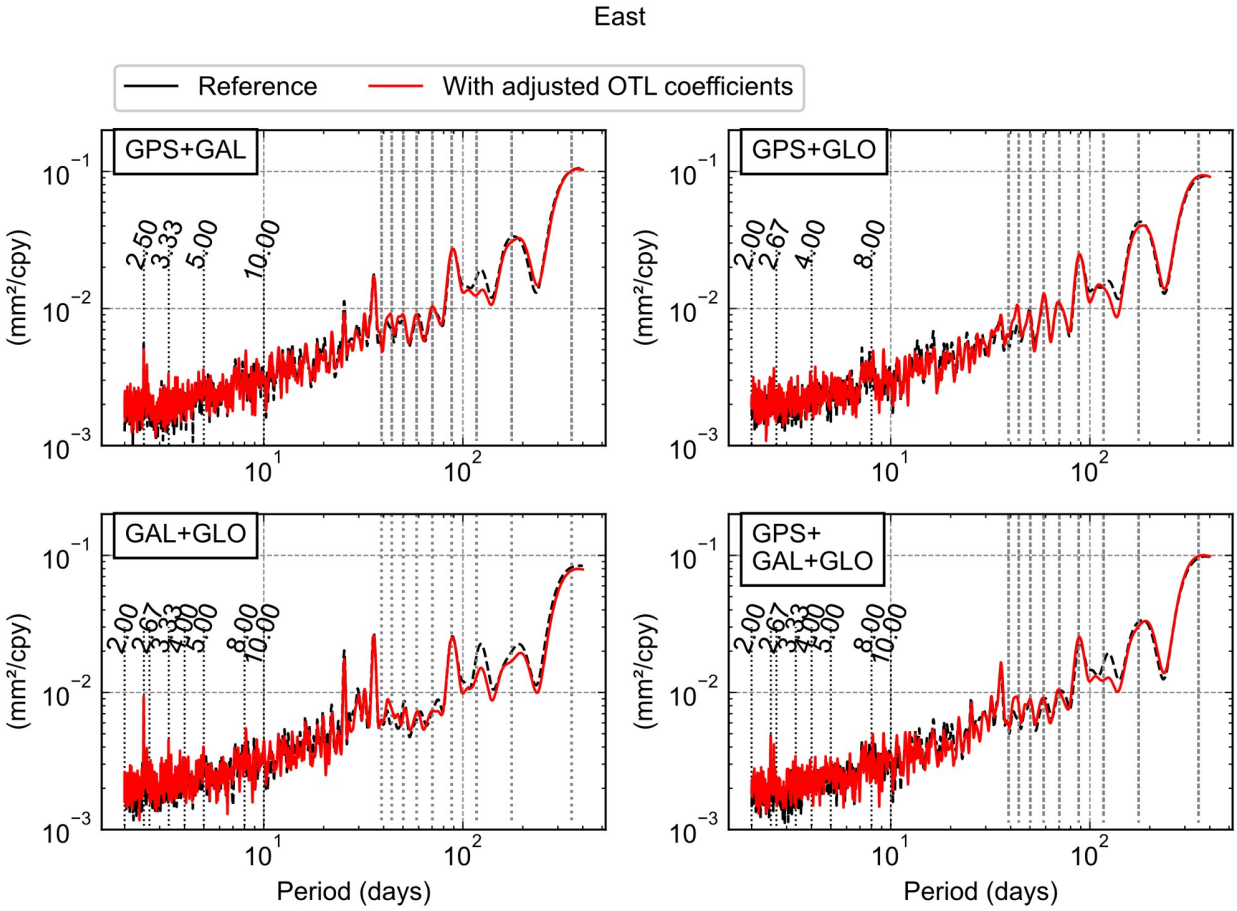

Fig. S11 Stacked normalized power spectra of the East coordinates computed with the nominal (black line) and the OTL coefficients adjustment (red line). The vertical lines are showing the draconitic harmonics (top panel) and the 3 main fortnightly frequencies (bottom panel).

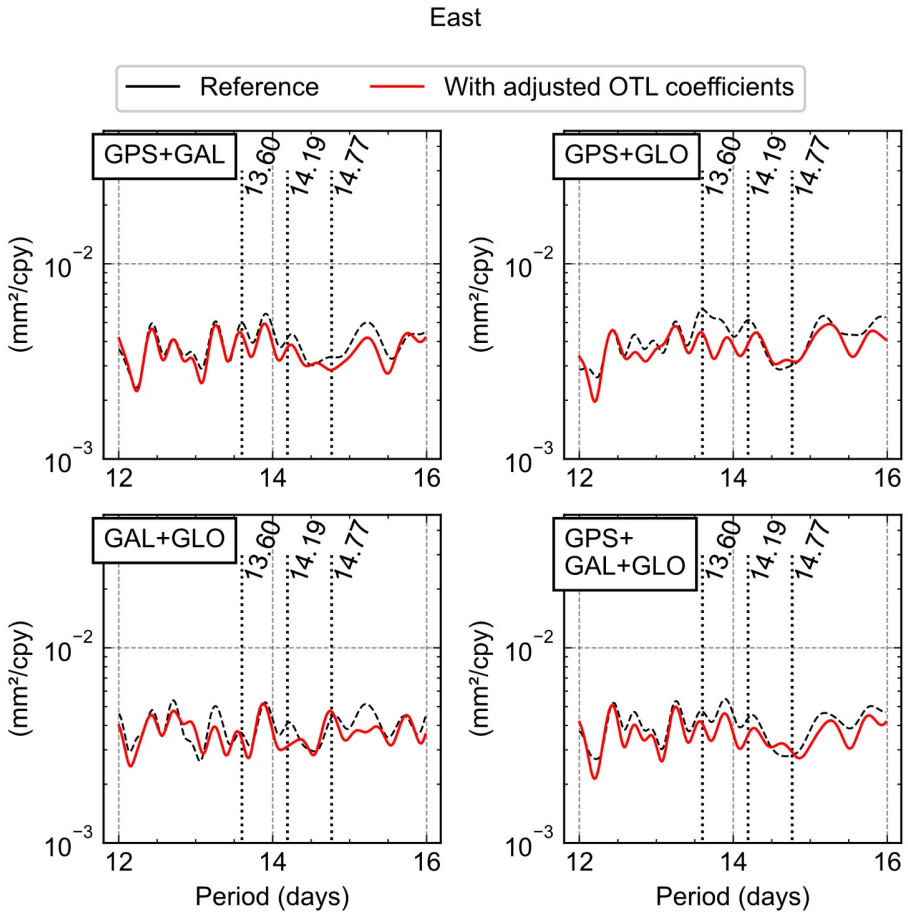

Fig. S12 Zoom of Figure S11 on 14-day band. The vertical lines are the 3 main fortnightly frequencies.

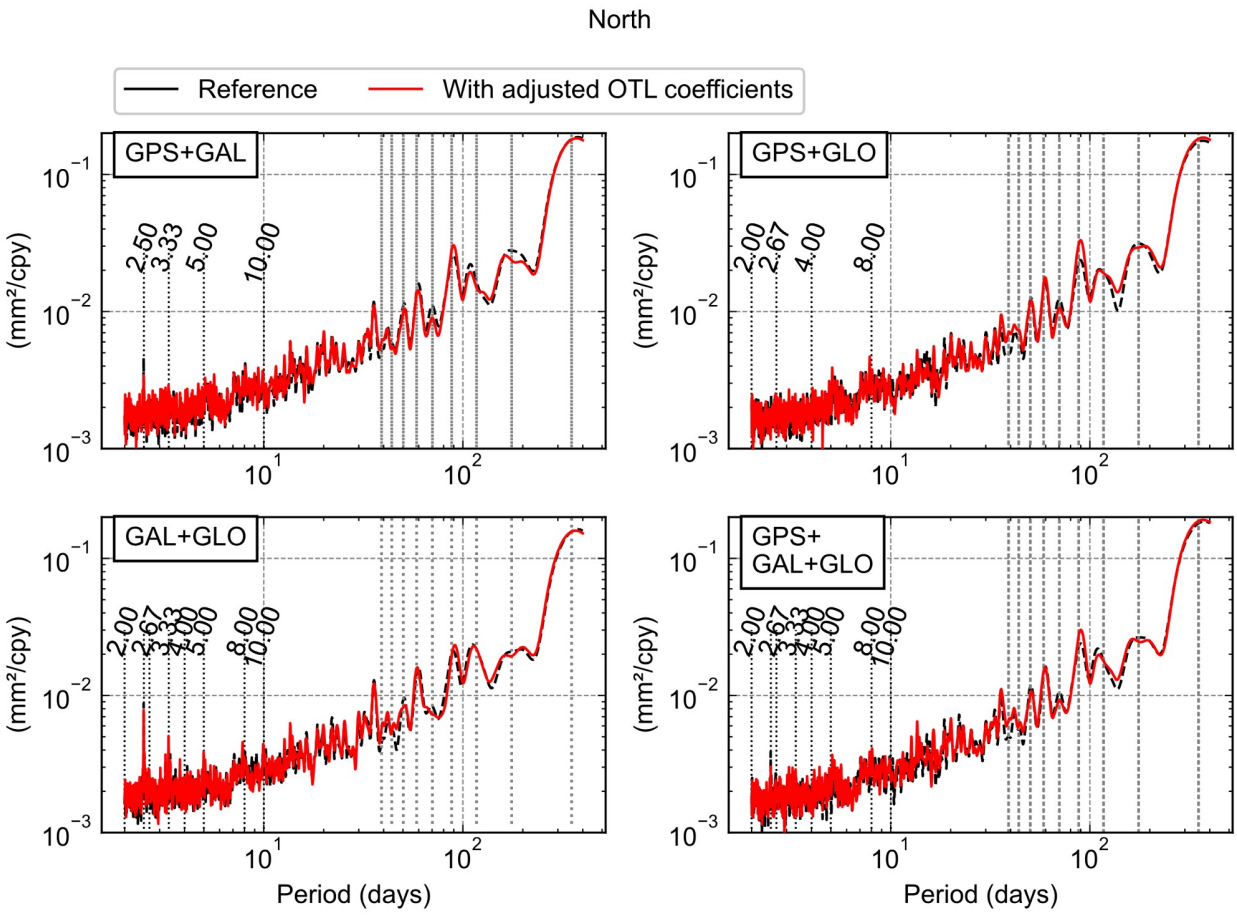

Fig. S13 Same as Figure S11 for the North coordinates.

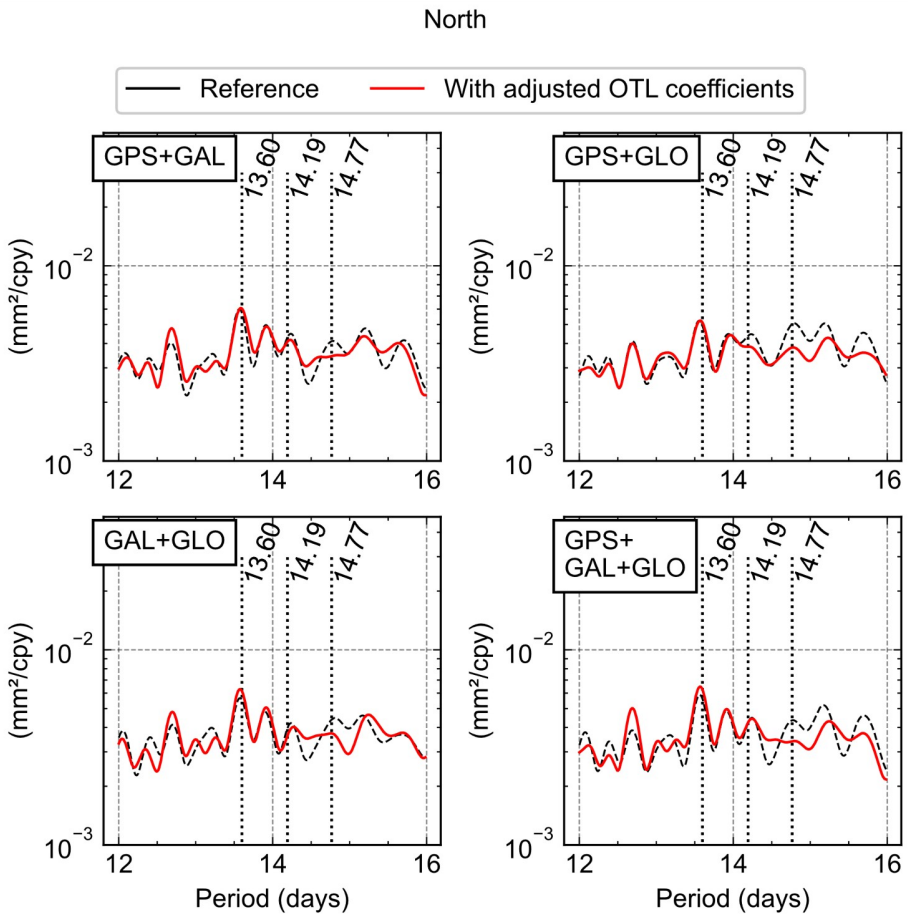

Fig. S14 Zoom of Figure S13 on 14-day band. The vertical lines are the 3 main fortnightly frequencies.

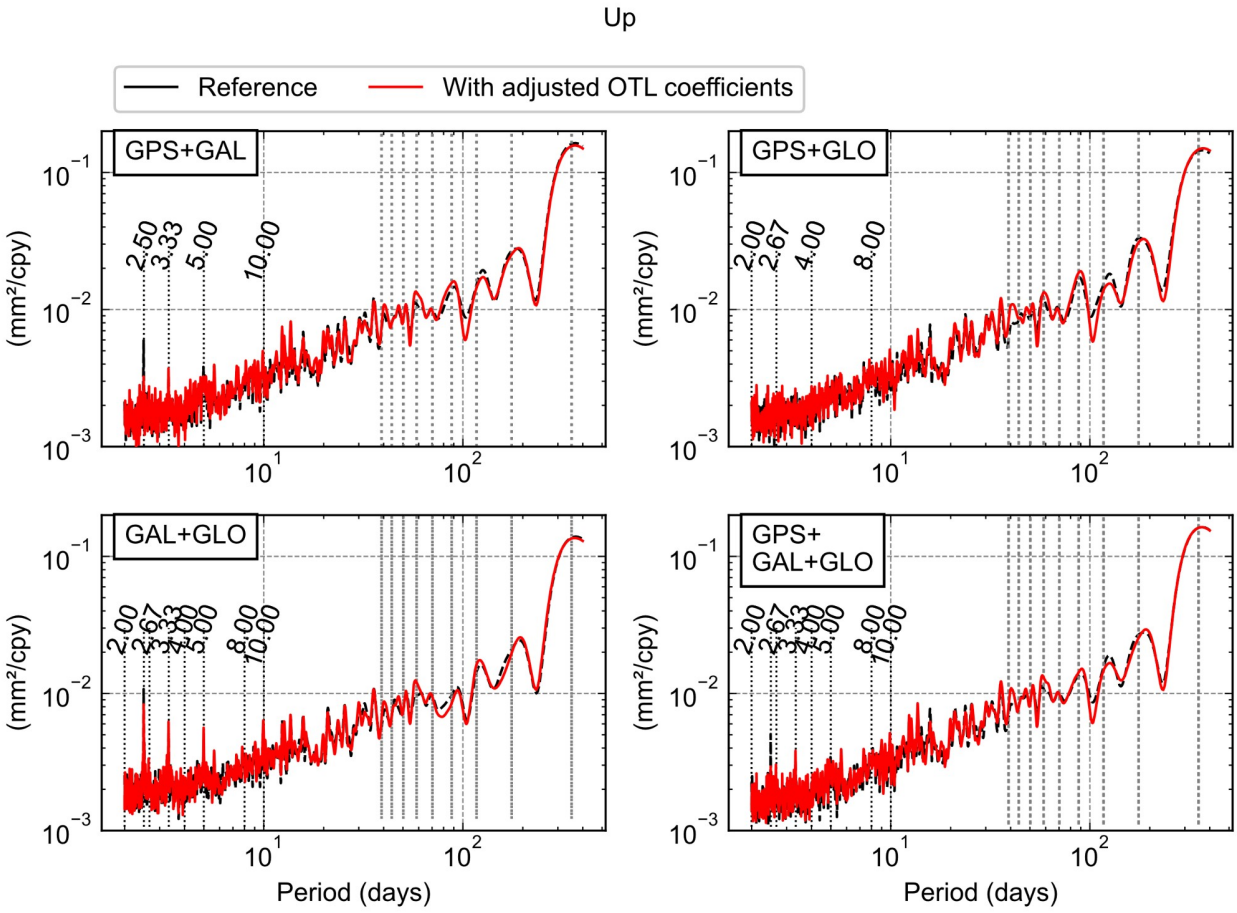

Fig. S15 Same as Figure S11 for the Up coordinates.

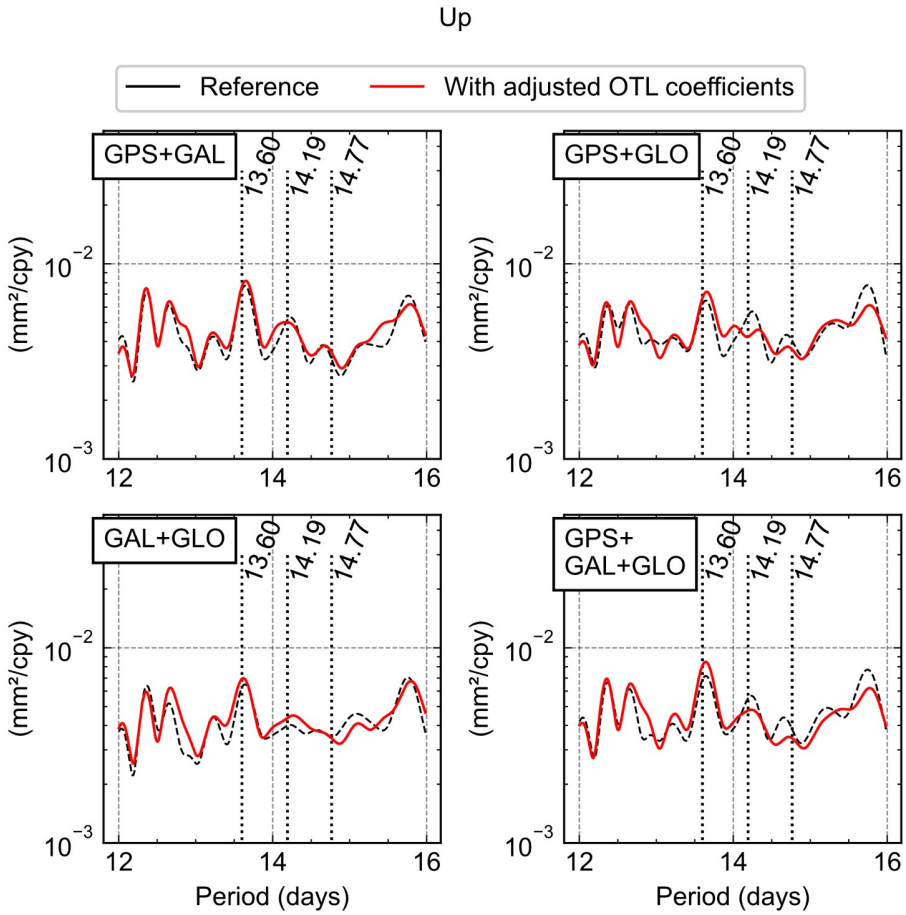

Fig. S16 Zoom of Figure S15 on 14-day band. The vertical lines are the 3 main fortnightly frequencies.

Geophys. J. Int. (xxx) **xxx**, 1–6

Impact of the GPS orbital dynamics on spurious interannual Earth deformation

H. Ait-Lakbir[1], A. Santamaría-Gómez[1], F. Perosanz[2]
[1] *GET, Université Paul Sabatier, CNES, CNRS, IRD, Toulouse, France*
[2] *CNES, Toulouse, France*

Received xxx

SUMMARY
Global Positioning System (GPS) daily position time series have a standard precision of a few millimeters. However, GPS position series contain large temporal correlations that impede the observation of subtle interannual Earth deformation. We show that the specific configuration of the GPS constellation, compared to other Global Navigation Satellite Systems (GNSS), contributes to the temporal correlation. Based on the analysis of observed and simulated GPS, Galileo, GLONASS and BeiDou orbits, we determine that the GPS orbital dynamics are more prone to interannual drifts caused by their higher sensitivity to the lunisolar gravitational resonance. This leads to substantial changes in the observation geometry over time, which, combined with mismodeled station-dependent systematic errors, results in a larger temporal correlation for GPS position time series. Improving the weighting of the GPS observations may mitigate the effect of geometry, which is absent in other GNSS constellations.

Key words: Satellite geodesy; Time-series analysis.

1 INTRODUCTION

In the past three decades, Global Navigation Satellite Systems (GNSS), mostly Global Positioning System (GPS), have significantly contributed to geosciences by providing long series of precise station coordinates that are used to observe and model crustal deformations. The station coordinates are modeled with a deterministic function that typically accounts for both trend and seasonal signals, which reflect underlying geophysical and measurement processes. However, it has been demonstrated that GPS positions exhibit temporally correlated errors that need to be considered to obtain meaningful uncertainties of the deterministic parameters. For instance, assuming uncorrelated noise instead of correlated noise can lead to underestimated uncertainties in GNSS velocities by a factor of 5 (Mao et al. 1999; Williams 2003; Santamaría-Gómez et al. 2011; Langbein 2012; Klos et al. 2017).

Mao et al. (1999) and Williams (2004) determined that the noise in GPS positions for global and regional networks of stations is a combination of white noise, flicker noise, and possibly some amount of random walk noise. White noise predominates at high frequencies, while power-law noise with a spectral index close to flicker noise, with a value of -1, predominates at low frequencies. These noise models are still in use nowadays, despite technique-specific errors that also influence the spectra of the GPS positions. Williams (2003), Santamaría-Gómez et al. (2011) and Gobron et al. (2022) highlighted the importance of considering position discontinuities when assessing the noise in GPS time series, as they obscure the colored noise at long periods.

The noise in GPS position time series has also been related to long-term and unaccounted-for displacements, such as site-specific random motion due to ground (Wyatt 1982, 1989) or monument instability (Williams 2004; Beavan 2005; King & Williams 2009). Non-tidal surface loading can potentially contribute to GPS positioning noise, although the current models primarily explain noise at intra-seasonal periods rather than long periods, where the variance of the state-of-the-art load models is still far from the observed GPS variance (Rebischung et al. 2017; Memin et al. 2020; Gobron et al. 2021; Michel et al. 2021).

Despite being equally impacted by the same geophysical processes, the station positions determined from the other space geodetic techniques, such as Doppler Orbitography by Radiopositioning Integrated on Satellite (DORIS), Satellite Laser Ranging (SLR) and Very Long Baseline Interferometry (VLBI) have demonstrated that a power-law process with a spectral index closer to white noise is a better stochastic model (Le Bail 2006; Ray et al. 2008; Feissel-Vernier et al. 2007; Klos et al. 2018). The reason why colored noise seems specific to GPS observations remains a subject of ongoing research. Although the positioning noise variance is lower for GPS, it is worth noting that DORIS and SLR use different types of satellite orbits, which are absent in VLBI. This could potentially explain the type of positioning noise. Indeed, King & Watson (2010) used simulated GPS data and showed that a time-varying satellite geometry, associated with multipath errors may contribute to colored noise in GPS positions. Yet, their work did not elaborate on the mechanisms behind the variations of the satellite geometry, and how they propagate positioning errors into long-period correlation.

Previous studies characterizing the color noise in GNSS position series have focused on GPS data. In this study, we use the four

available GNSS constellations and demonstrate that part of the colored noise is due to the specific design of the GPS constellation geometry. The geometry of the other GNSS constellations is significantly less prone to introduce colored noise.

2 IMPACT OF THE GNSS CONSTELLATION GEOMETRY

To assess the sensitivity of colored noise to the geometries of the different GNSS constellations, we run precise point positioning (PPP) simulations using precise GPS, Galileo and GLONASS orbits provided by the analysis centers of the International GNSS Service (IGS) from January 2018 through January 2021. Simulated GNSS observations above a cut-off elevation of 10° are computed every 900 s from the geometric distance between the real orbits and a network of 118 globally distributed stations. The PPP processing applies the usual linearization of the observation equations, and is based on the solution of the corresponding normal equations by weighted least squares. A set of station coordinates is estimated every 24 hours between 2018 and 2021, while we determine receiver clock biases per observation epoch.

In order to isolate the impact of the GNSS constellation geometry, the observations are simulated by neglecting satellite clocks and phase ambiguities. We add a zero-mean random noise and a systematic error following a non-zero elevation-dependent mean that may reflect antenna phase center, atmospheric delay, and multipath errors. This systematic error was simulated using the multipath model from King & Watson (2010) under the assumption that all stations are identical in terms of antenna characteristics (height and antenna gain) and environment (ground roughness, refractive indices).

Figure 1 shows the stacked power spectra of the estimated position series for the up coordinates (see Figures S1 and S2 for the horizontal coordinates). The power spectra are not normalized, making them comparable in terms of variance. The spectral power of GPS-derived coordinates increases at long periods, following a power law with a steep slope. Conversely, with Galileo and GLONASS orbits, the position spectra are flatter and closer to white noise at long periods. The same test performed with zero-mean elevation-dependent random measurement noise (Figure S3) does not result in colored noise. These findings suggest that at least some amount of the colored noise observed in GPS position series could be related to the GPS orbits themselves, in the presence of systematic errors, and could not be present in position series from the other GNSS constellations.

Elevation-dependent weighting functions are commonly used to mitigate unmodeled measurement errors in GNSS data processing. We assess the impact of three weighting functions on the colored noise: an elevation-independent function, an inverse sine function estimated from post-fit observation residuals, and an optimal elevation-dependent function derived from a priori knowledge of the systematic errors. Figure 1 shows that a post-fit estimated weighting function reduces the noise variance in positions by a factor of 10. Yet, the estimated weighting function does not significantly impact the power-law noise type. Long-period colored noise is only mitigated by optimal observation weights that correspond to the known statistical characteristics of the systematic errors. Therefore, reducing the colored noise content in GPS positions may be achieved by either limiting site-specific systematic errors, such as multipath, antenna phase centers or tropospheric propagation, or by using an optimized empirical weighting function not based only on

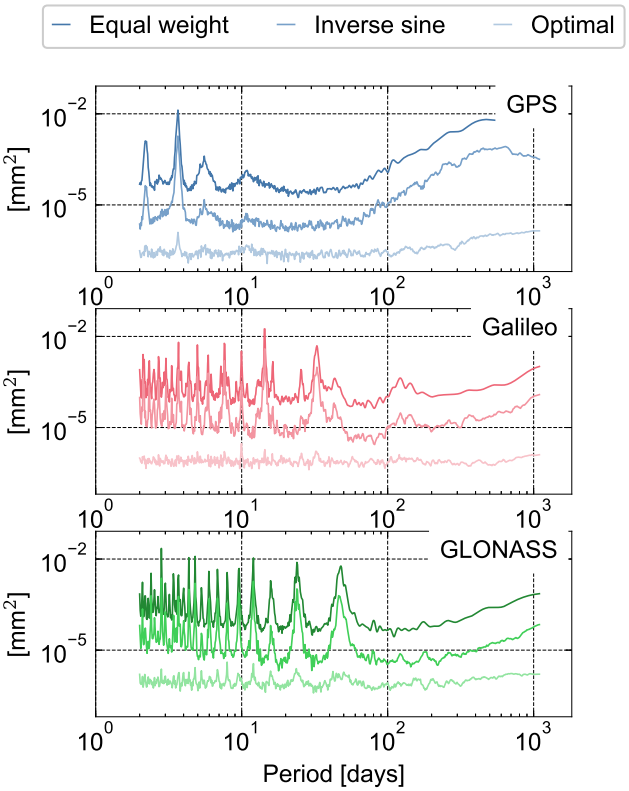

Figure 1. Stacked power spectra of simulated station heights obtained from real GPS (top), Galileo (middle) and GLONASS (bottom) precise orbits. Spectra are given for different weighting strategies: equal, inverse sine and optimal.

post-fit residuals. After several decades of improvements in GNSS data processing, both objectives have proven difficult to achieve in practice.

Galileo- or GLONASS-derived positions are impacted by systematic periodic signals up to 47 days caused by the repeat period of the constellation and the presence of the systematic error. Their magnitudes are not reduced by the post-fit weighting function, but only with optimal weighting. Additional GPS peaks occur at approximately 10, 5, 3.5, and 2.3 days, which vary among the orbits produced by different analysis centers, and do not directly relate to GPS orbital characteristics. The orbits calculated by the ESA analysis center for the third IGS reprocessing campaign, including GPS, Galileo and GLONASS, were used to obtain the spectra in Figure 1, however, these signals are also observed when using the IGS combined GPS orbits (Figure S4). Multiple factors affecting the orbits could explain these signals, such as the alignment to the terrestrial frame, which is mostly counterbalanced by the satellite clock and earth orientation parameters products, or error transfers from the other constellations. While these signals deserve further investigation, this does not affect the conclusions regarding the colored noise over long periods.

Real positioning confirms the stronger GPS-specific colored noise. For the same network of 118 stations, daily PPP solutions were computed between January 2019 and November 2021 using GRGS orbit and clock products (Katsigianni et al. 2019-09-05) and the GINS software provided by CNES. We are limited to almost 3 years of data because of the availability of homogeneously reprocessed orbit and clock products for the different

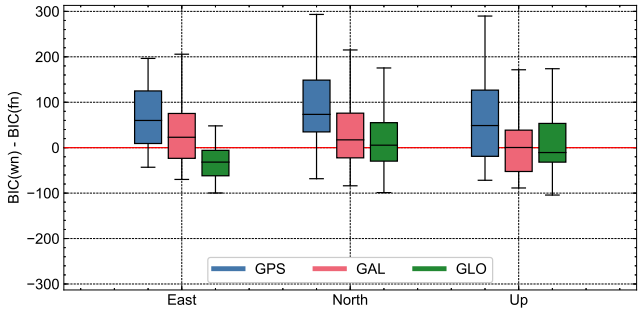

Figure 2. Distribution of the BIC differences between flicker noise and white noise models for GPS-only (blue), Galileo-only (red) and GLONASS-only (green) for the East (left), North (middle) and Up (right) coordinate components. A positive value means flicker noise is statistically preferred over white noise.

GNSS constellations, especially Galileo. Position series were generated for GPS-only and Galileo-only integer-ambiguity solutions, and GLONASS-only ambiguity-floating solutions. For each PPP series we analyze the noise content while fitting a kinematic model that includes a linear trend, positions jumps and constellation-specific periodic signals: 4 draconitic harmonics with periods of 351.2 days for GPS, 355.6 days for Galileo, and 353.2 days for GLONASS, and 5 harmonics of the constellation repeat periods, with periods of approximately 10 days for Galileo and 8 days for GLONASS.

Concerning the choice of the noise model, we analyze the goodness-of-fit of the flicker noise and white noise models by using a Bayesian Information Criterion (BIC), which gives the maximum log-likelihood corrected by the degrees of freedom of the noise model and the number of observations used for the fitting. Figure 2 show the difference between the BIC for the flicker noise and the white noise models. The value of the BIC difference is used to attribute a flicker noise model or a white noise model to each series. A positive value indicates that the flicker noise model better describes the position residuals, which implies the presence of colored noise.

According to this test, most of the GPS-only series contain flicker noise, while it is more difficult to distinguish it from white noise for Galileo-only and GLONASS-only series. As the series have similar variance for GPS and Galileo, the BIC differences presented in Figure 2 indicate that the background noise in GPS coordinates is indeed closer to flicker noise than to white noise. Ambiguity-fixed Galileo series contain less variance than GLONASS, especially for the east component, facilitating the separation between the white and the flicker noise, observed mostly for GPS. Despite the short period of simultaneous orbit and clock products available for the three constellations, both real and simulated GNSS observations confirm that GPS-only series are likely to contain more colored noise than Galileo-only or GLONASS-only series.

3 TIME-VARIABLE GPS CONSTELLATION GEOMETRY CAUSED BY RESONANT DYNAMICS

The distinct contribution of the geometry of different GNSS constellations on the colored noise raises questions about which orbital factors are responsible for these results. We focus on the long-term orbital dynamics of the four available constellations, including Bei-

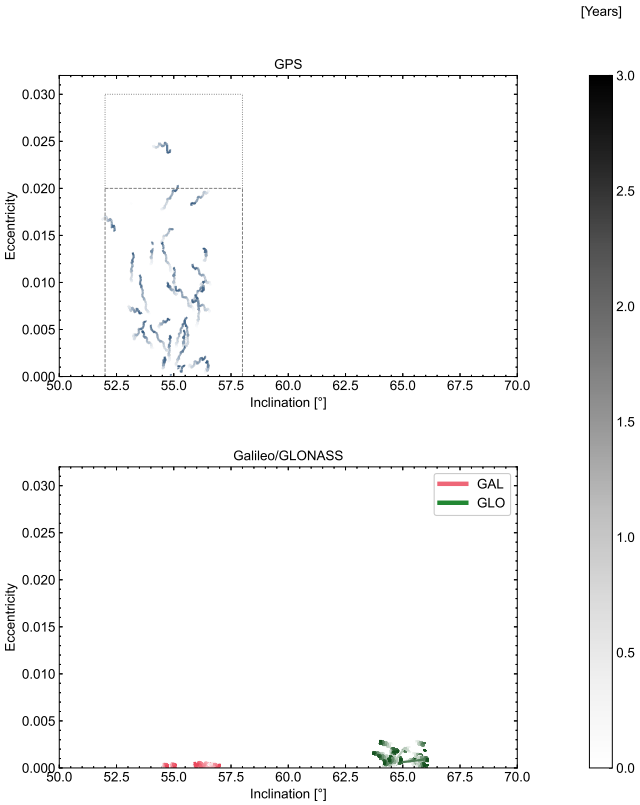

Figure 3. Estimated inclination (horizontal axis) and eccentricity (vertical axis) from precise orbits of the GPS, GLONASS, and Galileo constellations. The color gradient represents the time that has passed from January 1, 2018 to December 31, 2020. Darker shades are the latest epochs. The operational (dashed line) and tolerance (dotted line) ranges for GPS eccentricities and inclinations are also indicated.

Dou, and evaluate their impact on the colored noise of position series. Figure 3 shows the evolution of the eccentricity and inclination of the GPS, Galileo and GLONASS orbits over three years (2018 – 2020). These values are extracted from the IGS REPRO3 precise orbits.

GPS satellites show a wide dispersion with eccentricities rising up to 0.025, and inclinations ranging within a $\pm$ 2° interval around the nominal value of 55°. The GPS satellites are initially launched in their nominal orbits, but they drift in eccentricity and inclination within the operational interval (dashed area) published in the GPS Standard Positioning Service (SPS) Performance Standard (2020), except for the GPS satellite SVN45, which falls in the tolerance zone (dotted area). For the same period, the Galileo and GLONASS orbits show less variability within the constellation and remain closer to the published nominal values (Teunissen & Montenbruck 2017). No public information about the operational ranges of these two constellations could be found.

Resonances due to the gravitation of the moon and the sun are the primary cause responsible of the long-term orbital behavior in inclination and eccentricity. Characterized by a commensurability between the orbital elements of the satellites, the moon and the sun (Hughes 1981), lunisolar resonances cause the eccentricity to drift over time for the Medium Earth Orbits (Deleflie et al. 2005, 2011; Rosengren et al. 2015). By conservation of energy, this drift perturbs the other satellite's orbital elements such as the inclination (Deleflie et al. 2011; Hughes 1981). GPS maneuvers do not correct for the satellites' drifts in eccentricity and inclination, but only

for their semi-major axis. Therefore, we assume that the lunisolar resonance may account for most of the observed long-term orbital behavior for GPS shown in Figure 3.

To assess the impact of the lunisolar resonance on the colored noise, we compare three simulation scenarios with the GPS, Galileo, GLONASS, and BeiDou constellations. In the first scenario "nom", we set the eccentricities and inclinations of the orbits at their nominal values. We keep them constant by propagating the Kepler equations of motion, but consider the precession of the orbital planes due to the Earth's oblateness (J2) which gives the draconitic periodicity of the GNSS constellations. In the second scenario "geom", the eccentricities and inclinations remain constant, but are replaced by the actual values for each satellite at the epoch January 1, 2018 for GPS and GLONASS, January 1, 2019 for Galileo and January 1, 2021 for BeiDou. This configuration reflects a realistic constellation geometry, at a specific epoch, affected by the gravitational and other non-gravitational accelerations since each satellite was launched. The choice of the products does not matter for this analysis as the orbit differences between analysis centers do not significantly affect these parameters. The orbits are also propagated with the Kepler and J2 dynamics, i.e. the "nom" and "geom" scenarios differ only in their constant constellation geometry because both are propagated without resonant dynamics. In the third scenario "res", we use the same initial satellite positions as the "geom" scenario. However, the orbit propagation uses a semi-analytical model for the secular time-derivative orbital elements considering the lunisolar gravitation (Chao & Gick 2004; Chao 2005).

We use the same setting as stated in the previous section to simulate the GNSS observations, but in this case using the orbits simulated in the three different scenarios. To lessen the computational burden and because we focus on the long-term behavior, the observations and daily positions are computed only every 7 days. We fit a power-law noise model to the simulated series where the spectral index and variance are estimated.

Figure 4 shows the distribution of spectral indices estimated from the positions determined with the nominal, reference, and resonant orbits. While we focus on the vertical coordinate component, the conclusions drawn also apply to the horizontal coordinates (see Figure S5). To investigate deviations of the constellation geometry from the nominal values, we compare the spectral indices of the estimated noise models using the nominal GPS satellite positions ("nom") and the real, but constant, GPS satellite positions ("geom"). The spectral indices with "nom" orbits, centered at 0, indicate white or uncorrelated noise. In contrast, the mean of the spectral indices slightly shifts towards flicker when using a more realistic constellation geometry, as given by the "geom" scenario. These results suggest that even non-evolving, deformed constellation geometries play a role in the emergence of colored noise in station positions.

Lunisolar resonant dynamics deform the geometry of the constellation with respect to the nominal values and, more importantly, makes the geometry to gradually change with time, as shown in Figure 2. Because, the variations of the orbital elements due to lunisolar resonances depend on the satellite's eccentricity and inclination (Hughes 1980, 1981), an even more irregular evolution of the geometry of the GPS constellation occurs due to the dispersion of the eccentricity and inclination among the GPS satellites. In Figure 4, GPS-only position time series show that a resonant dynamic in the "res" scenario has a net negative impact on colored noise. Conversely, the noise in Galileo, GLONASS or BeiDou positions remains uncorrelated with power-law spectral indices always centered at 0 for any scenario. The impact of the lunisolar resonance on the GPS constellation is still noticeable when combining multi-GNSS observations (Figure S6).

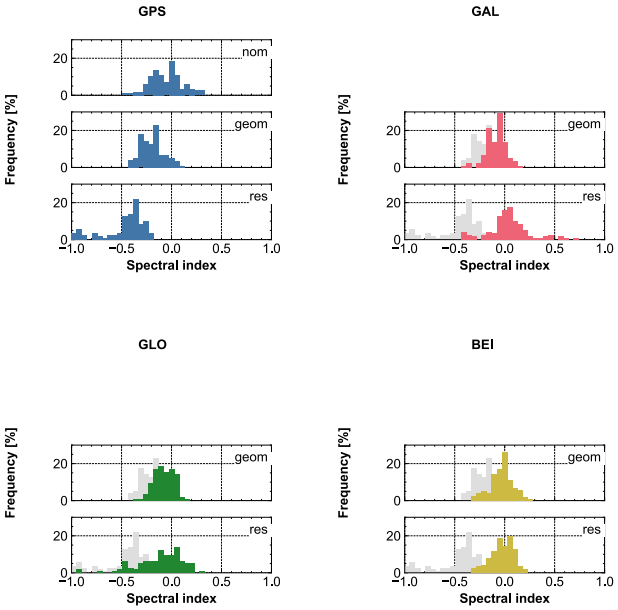

Figure 4. Distribution of the estimated power-law spectral indices in PPP time series of vertical coordinates obtained from simulated observations and orbits under three scenarios: "nom" (top), "geom" (middle) and "res" (bottom). The "nom" case is ignored for Galileo, GLONASS, and BeiDou since their actual orbits are close to nominal. The GPS histograms are displayed in light gray in the background for comparison with the other constellations.

4 DISCUSSIONS AND CONCLUSIONS

To infer geophysical parameters accurately such as the tectonic rate, it is critical to consider the colored noise observed in GPS station positions. Currently, the standard practice is to describe the noise in decade-long GPS position series by a combination of white noise and colored noise processes. However, proper noise modeling does not allow us to better observe subtle long-period Earth deformation hidden by the noise. The only way forward is to understand the mechanism behind the colored noise, including its origin and what fraction of it is generated by the complexity of the GNSS precise positioning, which remains unclear. The recent availability of precise positioning from new GNSS constellations allowed us to identify, for the first time, the contribution of the different GNSS orbits. We analyzed the impact of the geometry of the different GNSS constellations on the colored noise of position series. Despite the importance of long-term positioning stability and accuracy, no research has been conducted on the contribution of GNSS orbit stability.

Using real and simulated GPS, Galileo, GLONASS and BeiDou orbits, we found that GPS clearly differs from the other constellations. We utilized simulated orbits that account for secular dynamics to investigate the different long-term variations in satellite orbits between GPS and the other constellations. We show that the GPS constellation is particularly sensitive to resonances caused by lunisolar gravitational accelerations. In comparison, the geometry of the Galileo, GLONASS and BeiDou constellations appears

more stable over time, and stays closer to their nominal configurations. The observed orbital variations for GPS introduce a significant amount of colored noise in GPS positions compared to Galileo and GLONASS. This suggests that at least part of the colored noise seen in GPS position time series is generated by the specific design of the GPS constellation. We confirmed this conclusion by simulating GNSS observations between a network of ground stations and real GNSS orbits. Simulating GNSS observations, that considered only the geometry of the satellites' positions, allowed us to identify three necessary, but not sufficient, factors that combined will generate a significant level of colored noise in the station positions. First, the presence of systematic station-dependent errors whose non-zero mean depends on the satellite elevation, such as antenna phase center, multipath or tropospheric delays; second, an inadequate observation weighting function with respect to the actual measurement errors, such as those derived from post-fit residuals; and third, a constellation geometry that changes gradually, such as the GPS constellation, which is consistent with the findings by (King & Watson 2010). Our results demonstrate that if any of these three factors is missing, the fraction of colored noise will significantly reduce. For instance, different observation weighting strategies may explain the reduced colored noise observed for GPS positions determined by JPL (Rebischung et al. 2016).

It is very likely that the contribution of the geometry of the GNSS orbits alone is not enough to fully explain the colored noise content in long GPS series. Longer Galileo series are needed to separate and quantify the level of noise generated by the orbits from the noise generated by additional processes common to all GNSS observations. This analysis will also benefit from the comparison with BeiDou positioning. Our results complete previous work that has focused on describing the stochastic nature of GPS positions by examining unmodeled site displacements during data processing. These include random ground or monumentation motion (Beavan 2005; King & Williams 2009; Williams 2004) or non-tidal surface loading (Gobron et al. 2021; Memin et al. 2020; Rebischung et al. 2017). Our findings are a step toward demonstrating that the constellation geometry may also play a significant role.

Previous work has suggested a contribution of the GNSS orbits to the draconitic signals observed in the positions (Ray et al. 2008; Amiri-Simkooei 2013; Allahverdi-zadeh et al. 2016). In our study, we do not observe these draconitic signals. We only accessed the long-term orbital contribution to positioning errors with a semi-analytical model that neglects the orbital, lunar and solar periods. Furthermore, non-conservative accelerations such as solar radiation pressure also affect the satellite orbital evolution (Valk et al. 2009; McMahon 2011; Lemaître 2019). Addressing the orbital contribution to these short-period signals observed in position series would require deriving analytical dynamic equations that do not average out over these periods; which is out of the scope of this paper.

The differences in noise types among the constellations raise the question of how the colored noise would evolve over time as new GNSS systems are integrated to determine the station positions, especially for the estimation of velocities. In particular, the amount of undetectable random walk noise, which is typically not included in the standard noise models, limits the assessment of the uncertainty of tectonic rates estimated from GPS series. Long Galileo series with reduced flicker noise may provide constraints for the random walk noise hidden in the longer GPS series and therefore improve the estimated uncertainty of the tectonic rate at the same stations. Additionally, the standard noise model involves a flicker or power law noise constant throughout the entire period. The integration of Galileo and BeiDou could result in a progressive evolution of the colored noise content over at least a decade. Consequently, more complex noise models will be required to model multi-GNSS position time series.

A reduced flicker noise in GNSS positions will facilitate the detection of interannual non-linear geophysical processes, such as years-long slow slip events (Peng & Gomberg 2010; Kobayashi 2017; Ducellier et al. 2022), or inter-annual deformations resulting from changes in groundwater storage (White et al. 2022). While Galileo looks promising for better observing interannual Earth deformation, GPS series still contain reduced systematic signals at higher frequencies and remain privileged observations of geophysical processes occurring at periods of a few days. Regarding the linear rates, GPS observations will still provide better estimates due to the longer time series already available. This will probably be the case for many years to come and only longer Galileo series will allow us to answer this question. Nevertheless, it is worth mentioning that the uncertainty of the linear rate is strongly impacted by the estimation of position discontinuities Griffiths & Ray (2016); Santamaría-Gómez & Ray (2021) and these are common to all GNSS constellations.

ACKNOWLEDGMENTS

We thank Florent Deleflie from the Observatoire de Paris for his explanation about orbital resonance, Paul Rebischung from IGN for providing the pytrf software that we used for the noise analysis, and Jim Ray for his constructive comments on an earlier version of the manuscript. This work was supported by Region Occitanie and the Centre National d'Etudes Spatiales (CNES).

DATA AVAILABILITY

The GNSS RINEX observation files, the REPRO3 precise orbit and clock products for GPS, Galileo and GLONASS and the broadcast files for BeiDou were obtained through the online archives of the International GNSS Services (IGS) hosted by the Crustal Dynamics Data Information System (CDDIS).

REFERENCES

Allahverdi-zadeh, A., Asgari, J., & Amiri-Simkooei, A., 2016. Investigation of gps draconitic year effect on gps time series of eliminated eclipsing gps satellite data, *Journal of Geodetic Science*, **6**(1).

Amiri-Simkooei, A., 2013. On the nature of gps draconitic year periodic pattern in multivariate position time series, *Journal of Geophysical Research: Solid Earth*, **118**(5), 2500–2511.

Beavan, J., 2005. Noise properties of continuous gps data from concrete pillar geodetic monuments in new zealand and comparison with data from u.s. deep drilled braced monuments, *Journal of Geophysical Research: Solid Earth*, **110**(B8).

Chao, C.-C., 2005. *Applied Orbit Perturbation and Maintenance*, American Institute of Aeronautics and Astronautics, Inc.

Chao, C.-C. & Gick, R., 2004. Long-term evolution of navigation satellite orbits: Gps/glonass/galileo, *Advances in Space Research*, **34**(5), 1221–1226.

Deleflie, F., Legendre, P., Exertier, P., & Barlier, F., 2005. Long term evolution of the galileo constellation due to gravitational forces, *Advances in Space Research*, **36**(3), 402–411.

Deleflie, F., Rossi, A., Portmann, C., Métris, G., & Barlier, F., 2011. Semi-analytical investigations of the long term evolution of the eccentricity of galileo and gps-like orbits, *Advances in Space Research*, **47**(5), 811–821.

Ducellier, A., Creager, K., & Schmidt, D., 2022. Detection of slow slip events using wavelet analysis of gnss recordings, *Bulletin of the Seismological Society of America*, **112**(5), 2408–2424.

Feissel-Vernier, M., Viron, O., & Le Bail, K., 2007. Stability of vlbi, slr, doris, and gps positioning, *Earth, Planets and Space*, **59**(6), 475–497.

Gobron, K., Rebischung, P., Camp, M., Demoulin, A., & Viron, O., 2021. Influence of aperiodic non-tidal atmospheric and oceanic loading deformations on the stochastic properties of global gnss vertical land motion time series, *Journal of Geophysical Research: Solid Earth*, **126**(9), 2021 022370.

Gobron, K., Rebischung, P., Viron, O., Demoulin, A., & Camp, M., 2022. Impact of offsets on assessing the low-frequency stochastic properties of geodetic time series, *Journal of Geodesy*, **96**(7), 46.

Griffiths, J. & Ray, J., 2016. Impacts of gnss position offsets on global frame stability, *Geophysical Journal International*, **204**(1), 480–487.

Hughes, S., 1980. Earth satellite orbits with resonant lunisolar perturbations i. resonances dependent only on inclination. proceedings of the royal society of london, *A. Mathematical and Physical Sciences*, **372**(1749), 243–264.

Hughes, S., 1981. Earth satellite orbits with resonant lunisolar perturbations—ii. some resonances dependent on the semi-major axis, eccentricity and inclination, *Proceedings of the Royal Society of London. A. Mathematical and Physical Sciences*, **375**(1762), 379–396.

Katsigianni, G., Loyer, S., Perosanz, F., Mercier, F., & Santamaría-Gómez, A., 2019-09-05. Galileo precise positioning with ambiguity resolution and its contribution to earth rotation solutions.

King, M. & Watson, C., 2010. Long gps coordinate time series: Multipath and geometry effects, *Journal of Geophysical Research*.

King, M. & Williams, S., 2009. Apparent stability of gps monumentation from short-baseline time series, *Journal of Geophysical Research: Solid Earth*, **114**(B10).

Klos, A., Olivares, G., Teferle, F., Hunegnaw, A., & Bogusz, J., 2017. On the combined effect of periodic signals and colored noise on velocity uncertainties, *GPS Solutions*, **22**(1), 1.

Klos, A., Bogusz, J., & Moreaux, G., 2018. Stochastic models in the doris position time series: estimates for ids contribution to itrf2014, *Journal of Geodesy*, **92**, 743–763.

Kobayashi, A., 2017. Objective detection of long-term slow slip events along the nankai trough using gnss data (1996–2016, *Earth, Planets and Space*, **69**(1), 171.

Langbein, J., 2012. Estimating rate uncertainty with maximum likelihood: Differences between power-law and flicker–random-walk models, *Journal of Geodesy*, **86**(9), 775–783.

Le Bail, K., 2006. Estimating the noise in space-geodetic positioning: The case of doris, *Journal of Geodesy*, **80**(8), 541–565.

Lemaître, A., 2019. Space debris: From leo to geo, in *Satellite Dynamics and Space Missions*, vol. 34, p. 115–157, eds Baù, G., Celletti, A., Galeș, C., & Gronchi, G., Springer International Publishing.

Mao, A., Harrison, C., & Dixon, T., 1999. Noise in gps coordinate time series, *Journal of Geophysical Research: Solid Earth*, **104**(B2), 2797–2816.

McMahon, J., 2011. An analytical theory for the perturbative effect of solar radiation pressure on natural and artificial satellites [university of colorado.

Memin, A., Boy, J.-P., & Santamaría-Gómez, A., 2020. Correcting gps measurements for non-tidal loading, *GPS Solutions*, **24**.

Michel, A., Santamaría-Gómez, A., Boy, J.-P., Perosanz, F., & Loyer, S., 2021. Analysis of gnss displacements in europe and their comparison with hydrological loading models, *Remote Sensing*, **13**(22), 22.

Peng, Z. & Gomberg, J., 2010. An integrated perspective of the continuum between earthquakes and slow-slip phenomena, *Nature Geoscience*, **3**(9), 9.

Ray, J., Altamimi, Z., Collilieux, X., & Dam, T., 2008. Anomalous harmonics in the spectra of gps position estimates, *GPS Solutions*, **12**(1), 55–64.

Rebischung, P., Altamimi, Z., Ray, J., & Garayt, B., 2016. The igs contribution to itrf2014, *Journal of Geodesy*, **90**(7), 611–630.

Rebischung, P., Chanard, K., Metivier, L., & Altamimi, Z., 2017. Flicker noise in gnss station position time series: How much is due to crustal loading deformations?

Rosengren, A., Alessi, E., Rossi, A., & Valsecchi, G., 2015. Chaos in navigation satellite orbits caused by the perturbed motion of the moon, *Monthly Notices of the Royal Astronomical Society*, **449**(4), 3522–3526.

Santamaría-Gómez, A. & Ray, J., 2021. Chameleonic noise in gps position time series, *Journal of Geophysical Research: Solid Earth*, **126**(3), 2020 019541.

Santamaría-Gómez, A., Bouin, M.-N., Collilieux, X., & Wöppelmann, G., 2011. Correlated errors in gps position time series: Implications for velocity estimates, *Journal of Geophysical Research: Solid Earth*, **116**(B1).

eds Teunissen, P. & Montenbruck, O., 2017. *Springer Handbook of Global Navigation Satellite Systems*, Springer International Publishing.

Valk, S., Delsate, N., Lemaître, A., & Carletti, T., 2009. Global dynamics of high area-to-mass ratios geo space debris by means of the megno indicator, *Advances in Space Research*, **43**(10), 1509–1526.

White, A., Gardner, W., Borsa, A., Argus, D., & Martens, H., 2022. A review of gnss/gps in hydrogeodesy: Hydrologic loading applications and their implications for water resource research, *Water Resources Research*, **58**(7), 2022 032078.

Williams, S., 2003. The effect of coloured noise on the uncertainties of rates estimated from geodetic time series, *Journal of Geodesy*, **76**(9–10), 483–494.

Williams, S., 2004. Error analysis of continuous gps position time series, *Journal of Geophysical Research*, **109**(B3), 03412.

Wyatt, F., 1982. Displacement of surface monuments: Horizontal motion, *Journal of Geophysical Research: Solid Earth*, **87**(B2), 979–989.

Wyatt, F., 1989. Displacement of surface monuments: Vertical motion, *Journal of Geophysical Research: Solid Earth*, **94**(B2), 1655–1664.

Geophysical Journal International

Supplementary information for

Impact of the GPS orbital dynamics on spurious interannual Earth deformation

H. Ait-Lakbir[1], A. Santamaría-Gómez[1], and F. Perosanz[2]

[1]GET, Université Paul Sabatier, CNES, CNRS, IRD, Toulouse, France
[2]CNES, Toulouse, France

Introduction

The supporting information provides additional figures to complete the analysis with the horizontal directions and multi-GNSS positioning.

The average spectra of the station positions determined from the simulated observations to the IGS precise orbits in the east (Figure S1) and north (Figure S2) directions confirm the conclusion about the required factors for the occurrence of time-correlated noise.

Additional tests have been carried out to compare the impact of different types of observation noise in the simulations. Figure S3 compares the spectra between positions determined by simulated observations including random noise or elevation-dependent noise. We see that colored noise appears only with a systematic error such as elevation-dependent noise whose effects repeat itself with the same geometry of observations.

Spurious signals with periods of approximately 10, 5, 3.5, and 2.3 days have been found in the spectra of positions obtained from simulated observations using precise orbits. We assumed that these signals are originated from the generation of multi-GNSS precise orbits, as these periods do not correspond to any GPS-related characteristic frequencies, but could be related to Galileo constellation repeat period of 10 days. The exact mechanism is however not clearly understood. We tested another set of GPS precise orbits issued from the IGS combination, which is thought to be less sensitive to the strategies for the orbit determination or the orbit alignment to the ITRF from individual analysis centers. Figure S4 shows that these spurious signals are reduced, and even the 10-day peaks do not appear in the spectra of the positions. Unfortunately, the IGS combined orbits are available for GPS and GLONASS only.

Positioning was also performed using simulated observations to simulated orbits under different scenarios. Figure S5 shows the distribution of the spectral indices of the noise power-law model estimated in the east and north directions. We remind the nomenclature and description of the simulated orbital dynamics scenarios:

- “nom”: the nominal constellation geometry, propagated with Kepler and J2 dynamics
- “geom”: a real constellation geometry at a given epoch, propagated with Kepler and J2 dynamics
- “res”: a real constellation geometry at a given epoch, propagated with Kepler, J2 and lunisolar resonant dynamics

As an additional test, we also performed simulated multi-GNSS positioning which was analyzed following the same methodology. The results for the vertical coordinates (Figure S6) show that time-correlated noise appears when the combination of constellations includes GPS.

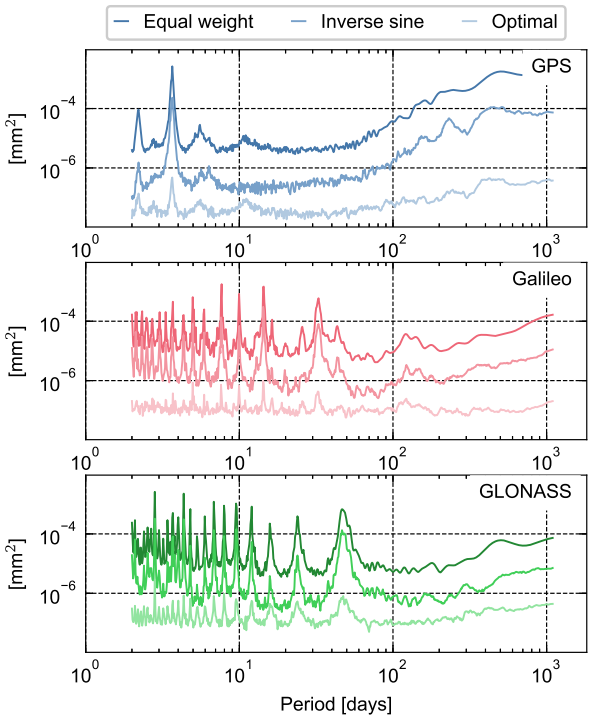

Figure S1: Temporal correlation of **East** positions observed in the power spectra of simulated PPP positions based on GPS, Galileo, and GLONASS constellations.

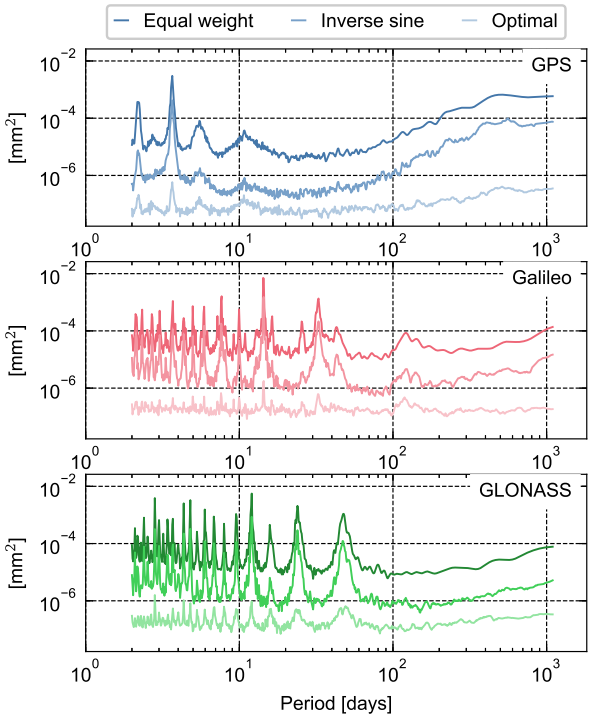

Figure S2: Temporal correlation of **North** positions observed in the power spectra of simulated PPP positions based on GPS, Galileo, and GLONASS constellations.

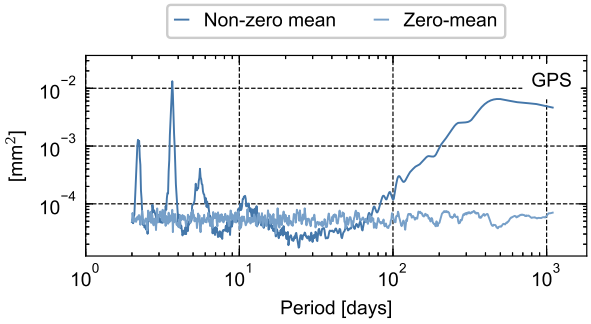

Figure S3: Temporal correlation of vertical positions observed in the power spectra of simulated PPP positions with two types for elevation-dependent noise: **with zero and non-zero mean**

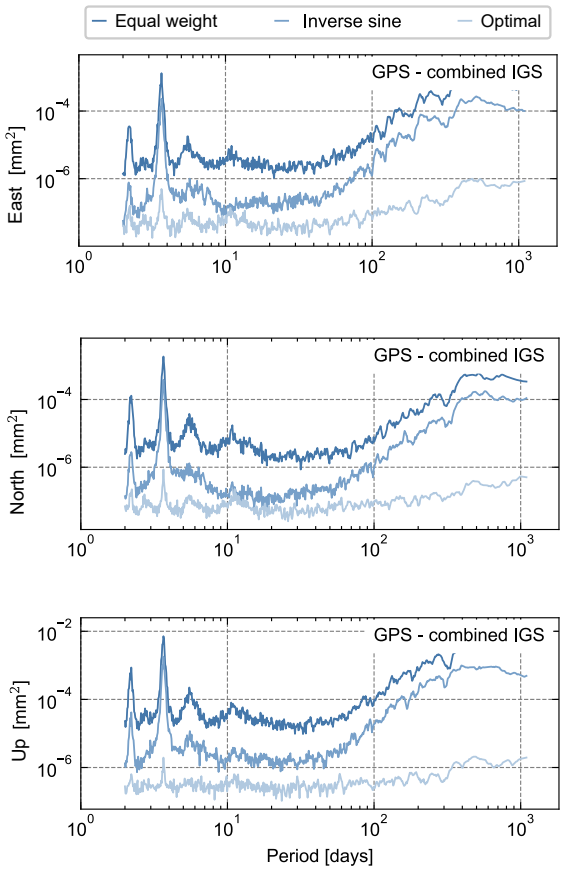

Figure S4: Temporal correlation of positions observed in the power spectra of simulated PPP positions based on the **IGS combined precise orbits**.

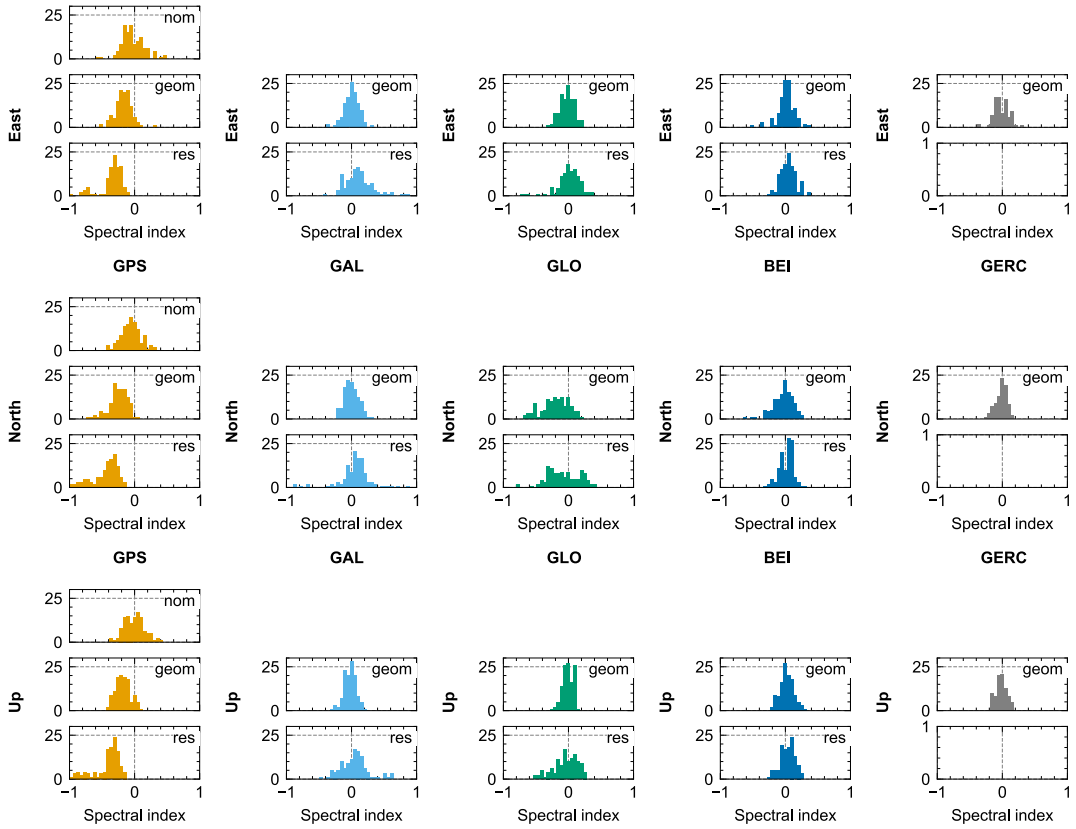

Figure S5: Distribution of the spectral indices estimated from the east (top panel), north (middle panel) and up (bottom panel) coordinates obtained with the simulated orbits and PPP. The nominal ("nom") case is ignored for Galileo, GLONASS, and BeiDou since their orbits are close to nominal, and the GPS histograms are displayed in light gray in the background for comparison.

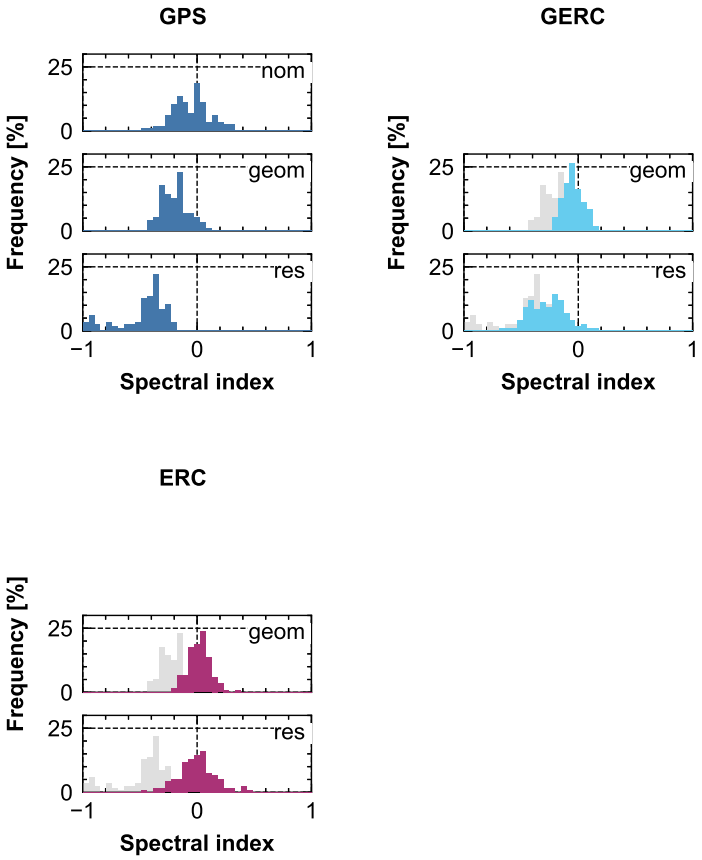

Figure S6: Distribution of the spectral indices estimated from multi-GNSS vertical coordinates obtained with the simulated orbits and PPP. GERC refers to the combination of GPS, Galileo, GLONASS and BeiDou. ERC refers to the combination without GPS.

List of Figures

List of Tables

Bibliography

M. Abbaszadeh, P. J. Clarke, and N. T. Penna. Benefits of combining GPS and GLONASS for measuring ocean tide loading displacement. *Journal of Geodesy*, 94(7):63, July 2020. ISSN 0949-7714, 1432-1394. doi: 10.1007/s00190-020-01393-5.

C. Abbondanza, T. M. Chin, R. S. Gross, M. B. Heflin, J. W. Parker, B. S. Soja, T. van Dam, and X. Wu. JTRF2014, the JPL Kalman filter and smoother realization of the International Terrestrial Reference System: JTRF2014. *Journal of Geophysical Research: Solid Earth*, 122(10):8474–8510, Oct. 2017. ISSN 21699313. doi: 10.1002/2017JB014360.

K. E. Abraha, F. N. Teferle, A. Hunegnaw, and R. Dach. Effects of unmodelled tidal displacements in GPS and GLONASS coordinate time-series. *Geophysical Journal International*, 214(3):2195–2206, Sept. 2018. ISSN 0956-540X. doi: 10.1093/gji/ggy254.

H. Ait-Lakbir, A. Santamaría-Gómez, and F. Perosanz. Assessment of sub-daily ocean tide loading errors and mitigation of their propagation in multi-GNSS position time series. *GPS Solutions*, 27(3):129, May 2023a. ISSN 1521-1886. doi: 10.1007/s10291-023-01467-9.

H. Ait-Lakbir, A. Santamaría-Gómez, and F. Perosanz. Impact of the GPS orbital dynamics on spurious interannual Earth deformation. *Geophysical Journal International*, 235(1):796–802, July 2023b. ISSN 0956-540X, 1365-246X. doi: 10.1093/gji/ggad268.

A. Allahverdi-zadeh, J. Asgari, and A. Amiri-Simkooei. Investigation of GPS draconitic year effect on GPS time series of eliminated eclipsing GPS satellite data. *Journal of Geodetic Science*, 6(1), Jan. 2016. ISSN 2081-9943. doi: 10.1515/jogs-2016-0007.

Z. Altamimi, L. Métivier, P. Rebischung, H. Rouby, and X. Collilieux. ITRF2014 plate motion model. *Geophysical Journal International*, 209(3):1906–1912, June 2017. ISSN 0956-540X, 1365-246X. doi: 10.1093/gji/ggx136.

Z. Altamimi, P. Rebischung, X. Collilieux, L. Métivier, and K. Chanard. ITRF2020: An augmented reference frame refining the modeling of nonlinear station motions. *Journal of Geodesy*, 97(5):47, May 2023. ISSN 0949-7714, 1432-1394. doi: 10.1007/s00190-023-01738-w.

A. R. Amiri-Simkooei. Noise in multivariate GPS position time-series. *Journal of Geodesy*, 83(2):175–187, Feb. 2009. ISSN 1432-1394. doi: 10.1007/s00190-008-0251-8.

A. R. Amiri-Simkooei. On the nature of GPS draconitic year periodic pattern in multivariate position time series. *Journal of Geophysical Research: Solid Earth*, 118(5):2500–2511, 2013. ISSN 2169-9356. doi: 10.1002/jgrb.50199.

A. R. Amiri-Simkooei, T. H. Mohammadloo, and D. F. Argus. Multivariate analysis of GPS position time series of JPL second reprocessing campaign. *Journal of Geodesy*, 91(6):685–704, June 2017. ISSN 1432-1394. doi: 10.1007/s00190-016-0991-9.

D. F. Argus, Y. Fu, and F. W. Landerer. Seasonal variation in total water storage in California inferred from GPS observations of vertical land motion. *Geophysical Research Letters*, 41(6):1971–1980, 2014a. ISSN 1944-8007. doi: 10.1002/2014GL059570.

D. F. Argus, W. R. Peltier, R. Drummond, and A. W. Moore. The Antarctica component of postglacial rebound model ICE-6G_C (VM5a) based on GPS positioning, exposure age dating of ice thicknesses, and relative sea level histories. *Geophysical Journal International*, 198(1):537–563, July 2014b. ISSN 0956-540X. doi: 10.1093/gji/ggu140.

D. F. Argus, F. W. Landerer, D. N. Wiese, H. R. Martens, Y. Fu, J. S. Famiglietti, B. F. Thomas, T. G. Farr, A. W. Moore, and M. M. Watkins. Sustained Water Loss in California's Mountain Ranges During Severe Drought From 2012 to 2015 Inferred From GPS. *Journal of Geophysical Research: Solid Earth*, 122(12):10,559–10,585, 2017. ISSN 2169-9356. doi: 10.1002/2017JB014424.

D. Arnold, M. Meindl, G. Beutler, R. Dach, S. Schaer, S. Lutz, L. Prange, K. Sośnica, L. Mervart, and A. Jäggi. CODE's new solar radiation pressure model for GNSS orbit determination. *Journal of Geodesy*, 89(8):775–791, Aug. 2015. ISSN 0949-7714, 1432-1394. doi: 10.1007/s00190-015-0814-4.

J. Arnoso, M. S. Bos, M. Benavent, N. T. Penna, and S. Sainz-Maza. Anelastic response of the Earth's crust underneath the Canary Islands revealed from ocean tide loading observations. *Geophysical Journal International*, 235(1):273–286, Oct. 2023. ISSN 0956-540X. doi: 10.1093/gji/ggad205.

Y. E. Bar-Sever. A new model for GPS yaw attitude. *Journal of Geodesy*, 70(11):714–723, Nov. 1996. ISSN 1432-1394. doi: 10.1007/BF00867149.

J. Beavan. Noise properties of continuous GPS data from concrete pillar geodetic monuments in New Zealand and comparison with data from U.S. deep drilled braced monuments. *Journal of Geophysical Research: Solid Earth*, 110(B8), 2005. ISSN 2156-2202. doi: 10.1029/2005JB003642.

C. Benoist, X. Collilieux, P. Rebischung, Z. Altamimi, O. Jamet, L. Métivier, K. Chanard, and L. Bel. Accounting for spatiotemporal correlations of GNSS coordinate time series to estimate station velocities. *Journal of Geodynamics*, 135:101693, Apr. 2020. ISSN 02643707. doi: 10.1016/j.jog.2020.101693.

G. Beutler, E. Brockmann, W. Gurtner, U. Hugentobler, L. Mervart, M. Rothacher, and A. Verdun. Extended orbit modeling techniques at the CODE processing center of the international GPS service for geodynamics (IGS): Theory and initial results. *Manuscr. Geod.*, 19:367–386, Sept. 1994.

G. Beutler, E. Brockmann, U. Hugentobler, L. Mervart, M. Rothacher, and R. Weber. Combining consecutive short arcs into long arcs for precise and efficient GPS Orbit Determination. *Journal of Geodesy*, 70(5):287–299, May 1996. ISSN 1432-1394. doi: 10.1007/BF00867349.

M. Bevis, J. Wahr, S. A. Khan, F. B. Madsen, A. Brown, M. Willis, E. Kendrick, P. Knudsen, J. E. Box, T. van Dam, D. J. Caccamise, B. Johns, T. Nylen, R. Abbott, S. White, J. Miner, R. Forsberg, H. Zhou, J. Wang, T. Wilson, D. Bromwich, and O. Francis. Bedrock displacements in Greenland manifest ice mass variations, climate cycles and climate change. *Proceedings of the National Academy of Sciences*, 109(30):11944–11948, July 2012. doi: 10.1073/pnas.1204664109.

M. Bevis, C. Harig, S. A. Khan, A. Brown, F. J. Simons, M. Willis, X. Fettweis, M. R. van den Broeke, F. B. Madsen, E. Kendrick, D. J. Caccamise, T. van Dam, P. Knudsen, and T. Nylen. Accelerating changes in ice mass within Greenland, and the ice sheet's sensitivity to atmospheric forcing. *Proceedings of the National Academy of Sciences*, 116(6):1934–1939, Feb. 2019. doi: 10.1073/pnas.1806562116.

I. Bij de Vaate, A. N. Vasulkar, D. C. Slobbe, and M. Verlaan. The Influence of Arctic Landfast Ice on Seasonal Modulation of the M2 Tide. *Journal of Geophysical Research: Oceans*, 126(5):e2020JC016630, 2021. ISSN 2169-9291. doi: 10.1029/2020JC016630.

G. Blewitt, W. Hammond, and C. Kreemer. Harnessing the GPS Data Explosion for Interdisciplinary Science. *Eos*, 99, Sept. 2018. ISSN 2324-9250. doi: 10.1029/2018EO104623.

Y. Bock and D. Melgar. Physical applications of GPS geodesy: A review. *Reports on Progress in Physics*, 79(10):106801, Oct. 2016. ISSN 0034-4885, 1361-6633. doi: 10.1088/0034-4885/79/10/106801.

J. Boehm, R. Heinkelmann, and H. Schuh. Neutral Atmosphere Delays: Empirical Models Versus Discrete Time Series from Numerical Weather Models. In H. Drewes, editor, *Geodetic Reference Frames: IAG Symposium Munich, Germany, 9-14 October 2006*, International Association of Geodesy Symposia, pages 317–321. Springer, Berlin, Heidelberg, 2009. ISBN 978-3-642-00860-3. doi: 10.1007/978-3-642-00860-3_49.

J. Bogusz and M. Figurski. GPS-derived height changes in diurnal and sub-diurnal timescales. *Acta Geophysica*, 60(2):295–317, Apr. 2012. ISSN 1895-7455. doi: 10.2478/s11600-011-0074-5.

J. Bogusz, A. Klos, and G. Moreaux. Assessment of IDS contribution to ITRF2020, 2022.

J. Böhm and H. Schuh, editors. *Atmospheric Effects in Space Geodesy*. Springer Atmospheric Sciences. Springer Berlin Heidelberg, Berlin, Heidelberg, 2013. ISBN 978-3-642-36931-5 978-3-642-36932-2. doi: 10.1007/978-3-642-36932-2.

D. Booker, P. J. Clarke, and D. A. Lavallée. Secular changes in Earth's shape and surface mass loading derived from combinations of reprocessed global GPS networks. *Journal of Geodesy*, 88(9):839–855, Sept. 2014. ISSN 1432-1394. doi: 10.1007/s00190-014-0725-9.

G. H. Born, M. E. Parke, P. Axelrad, K. L. Gold, J. Johnson, K. W. Key, D. G. Kubitschek, and E. J. Christensen. Calibration of the TOPEX altimeter using a GPS buoy. *Journal of Geophysical Research: Oceans*, 99(C12):24517–24526, 1994. ISSN 2156-2202. doi: 10.1029/94JC00920.

M. S. Bos, R. M. S. Fernandes, S. D. P. Williams, and L. Bastos. Fast error analysis of continuous GNSS observations with missing data. *Journal of Geodesy*, 87(4):351–360, Apr. 2013. ISSN 1432-1394. doi: 10.1007/s00190-012-0605-0.

M. S. Bos, N. T. Penna, T. F. Baker, and P. J. Clarke. Ocean tide loading displacements in western Europe: 2. GPS-observed anelastic dispersion in the asthenosphere. *Journal of Geophysical Research: Solid Earth*, 120(9):6540–6557, 2015. ISSN 2169-9356. doi: 10.1002/2015JB011884.

J.-P. Boy. Comparison of ITRF2020 residual displacements with environmental loading models, Dec. 2022.

C.-C. G. Chao. An analytical integration of the averaged equations of variation due to sun-moon perturbations and its application. Technical report, Space Division - Air Force Systems Command, 1979.

C.-C. G. Chao. *Applied Orbit Perturbation and Maintenance*. American Institute of Aeronautics and Astronautics, Inc., Washington, DC, Nov. 2005. ISBN 978-1-884989-17-9. doi: 10.2514/4.989179.

C.-C. G. Chao and R. Gick. Long-term evolution of navigation satellite orbits: GPS/GLONASS/GALILEO. *Advances in Space Research*, 34(5):1221–1226, Jan. 2004. ISSN 02731177. doi: 10.1016/j.asr.2003.01.021.

China Satellite Navigation Office. Constellation Status. http://www.csno-tarc.cn/en/system/constellation, 2023.

K. Choi. Preliminary GPS orbit combination results of the IGS 2nd reprocessing campaign. *EGU General Assembly 2015*, page 14204, Apr. 2015.

K. Choi, A. Bilich, K. M. Larson, and P. Axelrad. Modified sidereal filtering: Implications for high-rate GPS positioning. *Geophysical Research Letters*, 31(22), 2004. ISSN 1944-8007. doi: 10.1029/2004GL021621.

J. Cresson, F. Pierret, and B. Puig. Stochastic perturbation of the two-body problem. *Société Francaise d'Astronomie et d'Astrophysique (SF2A) 2013*, page 9, 2013.

J.-F. Crétaux, S. Calmant, V. Romanovski, A. Shabunin, F. Lyard, M. Bergé-Nguyen, A. Cazenave, F. Hernandez, and F. Perosanz. An absolute calibration site for radar altimeters in the continental domain: Lake Issykkul in Central Asia. *Journal of Geodesy*, 83(8):723–735, Aug. 2009. ISSN 1432-1394. doi: 10.1007/s00190-008-0289-7.

B. W. Crowell, Y. Bock, Z. Liu, Z. Liu, and Z. Liu. Single-station automated detection of transient deformation in GPS time series with the relative strength index: A case study of Cascadian slow slip. *Journal of Geophysical Research*, 2016. doi: 10.1002/2016jb013542.

R. Dach, J. Böhm, S. Lutz, P. Steigenberger, and G. Beutler. Evaluation of the impact of atmospheric pressure loading modeling on GNSS data analysis. *Journal of Geodesy*, 85(2):75–91, Feb. 2011. ISSN 1432-1394. doi: 10.1007/s00190-010-0417-z.

R. Dach, I. Selmke, A. Villiger, D. Arnold, L. Prange, S. Schaer, D. Sidorov, P. Stebler, A. Jäggi, and U. Hugentobler. Review of Recent GNSS Modelling Improvements Based on CODEs Repro3 Contribution. *Advances in Space Research*, May 2021. ISSN 0273-1177. doi: 10.1016/j.asr.2021.04.046.

P. Defraigne and C. Bruyninx. On the link between GPS pseudorange noise and day-boundary discontinuities in geodetic time transfer solutions. *GPS Solutions*, 11(4):239–249, Nov. 2007. ISSN 1521-1886. doi: 10.1007/s10291-007-0054-z.

F. Deleflie, A. Rossi, C. Portmann, G. Métris, and F. Barlier. Semi-analytical investigations of the long term evolution of the eccentricity of Galileo and GPS-like orbits. *Advances in Space Research*, 47(5): 811–821, Mar. 2011. ISSN 02731177. doi: 10.1016/j.asr.2010.11.038.

P. Delva, A. Hees, S. Bertone, E. Richard, and P. Wolf. Test of the gravitational redshift with stable clocks in eccentric orbits: Application to Galileo satellites 5 and 6. *Classical and Quantum Gravity*, 32 (23):232003, Nov. 2015. ISSN 0264-9381. doi: 10.1088/0264-9381/32/23/232003.

S. D. Desai and A. E. Sibois. Evaluating predicted diurnal and semidiurnal tidal variations in polar motion with GPS-based observations. *Journal of Geophysical Research: Solid Earth*, 121(7):5237–5256, 2016. ISSN 2169-9356. doi: 10.1002/2016JB013125.

P. M. R. DeVries and B. J. Meade. Earthquake cycle deformation in the Tibetan plateau with a weak mid-crustal layer: EARTHQUAKE CYCLE WITH A WEAK LAYER. *Journal of Geophysical Research: Solid Earth*, 118(6):3101–3111, June 2013. ISSN 21699313. doi: 10.1002/jgrb.50209.

Y. Dodge. Weighted Least-Squares Method. In *The Concise Encyclopedia of Statistics*, pages 566–569. Springer, New York, NY, 2008. doi: 10.1007/978-0-387-32833-1_422.

D. Dong, P. Fang, Y. Bock, M. K. Cheng, and S. Miyazaki. Anatomy of apparent seasonal variations from GPS-derived site position time series. *Journal of Geophysical Research: Solid Earth*, 107(B4):ETG 9–1–ETG 9–16, 2002. ISSN 2156-2202. doi: 10.1029/2001JB000573.

D. Dong, P. Fang, Y. Bock, F. H. Webb, L. Prawirodirdjo, S. Kedar, and P. Jamason. Spatiotemporal filtering using principal component analysis and Karhunen-Loeve expansion approaches for regional GPS network analysis. *Journal of Geophysical Research*, 2006. doi: 10.1029/2005jb003806.

A. Donnellan, R. Arrowsmith, and S. DeLong. Spatio-Temporal Mapping of Plate Boundary Faults in California Using Geodetic Imaging. *Geosciences*, 7(1):15, Mar. 2017. ISSN 2076-3263. doi: 10.3390/geosciences7010015.

B. Duan and U. Hugentobler. Estimating surface optical properties and thermal thrust for Galileo satellite body and solar panels. *GPS Solutions*, 26(4):135, Aug. 2022. ISSN 1521-1886. doi: 10.1007/s10291-022-01324-1.

B. Duan, U. Hugentobler, and I. Selmke. The adjusted optical properties for Galileo/BeiDou-2/QZS-1 satellites and initial results on BeiDou-3e and QZS-2 satellites. *Advances in Space Research*, 63(5):1803–1812, Mar. 2019. ISSN 02731177. doi: 10.1016/j.asr.2018.11.007.

B. Duan, U. Hugentobler, M. Hofacker, and I. Selmke. Improving solar radiation pressure modeling for GLONASS satellites. *Journal of Geodesy*, 94(8):72, July 2020. ISSN 1432-1394. doi: 10.1007/s00190-020-01400-9.

A. M. Dziewonski and D. L. Anderson. Preliminary reference Earth model. *Physics of the Earth and Planetary Interiors*, 25(4):297–356, June 1981. ISSN 00319201. doi: 10.1016/0031-9201(81)90046-7.

G. D. Egbert and S. Y. Erofeeva. Efficient Inverse Modeling of Barotropic Ocean Tides. *Journal of Atmospheric and Oceanic Technology*, 19(2):183–204, Feb. 2002. ISSN 0739-0572, 1520-0426. doi: 10.1175/1520-0426(2002)019<0183:EIMOBO>2.0.CO;2.

European GNSS Service Centre. Galileo Satellite Metadata. https://www.gsc-europa.eu/support-to-developers/galileo-satellite-metadata#6, 2019.

European GNSS Service Centre. Constellation Information. https://www.gsc-europa.eu/system-service-status/constellation-information, 2023.

W. E. Farrell. Deformation of the Earth by surface loads. *Reviews of Geophysics*, 10(3):761, 1972. ISSN 8755-1209. doi: 10.1029/RG010i003p00761.

M. Feissel-Vernier, O. de Viron, and K. Le Bail. Stability of VLBI, SLR, DORIS, and GPS positioning. *Earth, Planets and Space*, 59(6):475–497, June 2007. ISSN 1880-5981. doi: 10.1186/BF03352712.

Y. Fialko. Probing the mechanical properties of seismically active crust with space geodesy: Study of the coseismic deformation due to the 1992 Mw7.3 Landers (southern California) earthquake. *Journal of Geophysical Research*, 2004. doi: 10.1029/2003jb002756.

H. F. Fliegel, T. E. Gallini, and E. R. Swift. Global Positioning System Radiation Force Model for geodetic applications. *Journal of Geophysical Research: Solid Earth*, 97(B1):559–568, 1992. ISSN 2156-2202. doi: 10.1029/91JB02564.

J. T. Freymueller. GPS, Tectonic Geodesy. In H. K. Gupta, editor, *Encyclopedia of Solid Earth Geophysics*, pages 431–449. Springer Netherlands, Dordrecht, 2011. ISBN 978-90-481-8701-0 978-90-481-8702-7. doi: 10.1007/978-90-481-8702-7_77.

F. Fund, L. Morel, and A. Mocquet. A discussion of height reductions for Zenith Hydrostatic Delays derived from weather models. 5(2):71–80, Aug. 2011. ISSN 1862-9024. doi: 10.1515/jag.2011.006.

M. Ge, G. Gendt, M. Rothacher, C. Shi, and J. Liu. Resolution of GPS carrier-phase ambiguities in Precise Point Positioning (PPP) with daily observations. *Journal of Geodesy*, 82(7):389–399, July 2008. ISSN 1432-1394. doi: 10.1007/s00190-007-0187-4.

K. Gobron, P. Rebischung, M. Van Camp, A. Demoulin, and O. de Viron. Influence of Aperiodic Non-Tidal Atmospheric and Oceanic Loading Deformations on the Stochastic Properties of Global GNSS Vertical Land Motion Time Series. *Journal of Geophysical Research: Solid Earth*, 126(9):e2021JB022370, 2021. ISSN 2169-9356. doi: 10.1029/2021JB022370.

K. Gobron, P. Rebischung, O. de Viron, A. Demoulin, and M. Van Camp. Impact of offsets on assessing the low-frequency stochastic properties of geodetic time series. *Journal of Geodesy*, 96(7):46, June 2022. ISSN 1432-1394. doi: 10.1007/s00190-022-01634-9.

K. Gobron, P. Rebischung, J. Barnéoud, K. Chanard, and Z. Altamimi. Toward a realistic spatio-temporal description of GNSS station position time series, 2023.

A. Gonzalez-Ortega, Y. Fialko, D. T. Sandwell, F. A. Nava-Pichardo, J. M. Fletcher, J. J. Gonzalez-Garcia, J. J. Gonzalez-Garcia, J. Gonzalez-Garcia, B. Lipovsky, B. Lipovsky, M. Floyd, and G. J. Funning. El Mayor-Cucapah (Mw 7.2) earthquake: Early near-field postseismic deformation from InSAR and GPS observations. *Journal of Geophysical Research*, 2014. doi: 10.1002/2013jb010193.

S. Goswami, B. Klinger, M. Weigelt, and T. Mayer-Gurr. Analysis of Attitude Errors in GRACE Range-Rate Residuals—A Comparison Between SCA1B and the Fused Attitude Product (SCA1B + ACC1B). *IEEE Sensors Letters*, 2(2):1–4, June 2018. ISSN 2475-1472. doi: 10.1109/LSENS.2018.2825439.

GPS Navigation Center. GPS Standard Positioning Service (SPS) Performance Standard. Technical report, US Government, 2020.

GPS Navigation Center. GPS Constellation. https://www.navcen.uscg.gov/gps-constellation, 2023.

J. Griffiths. IGS Reprocessed GPS Satellite Orbits. http://acc.igs.org/orb-repro1_old.html, 2009.

J. Griffiths and J. Ray. Impacts of GNSS position offsets on global frame stability. *Geophysical Journal International*, 204(1):480–487, Jan. 2016. ISSN 0956-540X. doi: 10.1093/gji/ggv455.

J. Griffiths and J. R. Ray. On the precision and accuracy of IGS orbits. *Journal of Geodesy*, 83(3-4): 277–287, Mar. 2009. ISSN 0949-7714, 1432-1394. doi: 10.1007/s00190-008-0237-6.

J. Griffiths and J. R. Ray. Sub-daily alias and draconitic errors in the IGS orbits. *GPS Solutions*, 17(3): 413–422, July 2013. ISSN 1521-1886. doi: 10.1007/s10291-012-0289-1.

I. D. Haigh, M. D. Pickering, J. A. M. Green, B. K. Arbic, A. Arns, S. Dangendorf, D. F. Hill, K. Horsburgh, T. Howard, D. Idier, D. A. Jay, L. Jänicke, S. B. Lee, M. Müller, M. Schindelegger, S. A. Talke, S.-B. Wilmes, and P. L. Woodworth. The Tides They Are A-Changin': A Comprehensive Review of Past and Future Nonastronomical Changes in Tides, Their Driving Mechanisms, and Future Implications. *Reviews of Geophysics*, 58(1):e2018RG000636, 2020. ISSN 1944-9208. doi: 10.1029/2018RG000636.

X. He, M. S. Bos, J.-P. Montillet, R. Fernandes, T. Melbourne, W. Jiang, and W. Li. Spatial Variations of Stochastic Noise Properties in GPS Time Series. *Remote Sensing*, 13(22):4534, Jan. 2021. ISSN 2072-4292. doi: 10.3390/rs13224534.

P. Huang, R. L. Sulzbach, V. Klemann, Y. Tanaka, H. Dobslaw, Z. Martinec, and M. Thomas. The Influence of Sediments, Lithosphere and Upper Mantle (Anelastic) With Lateral Heterogeneity on Ocean Tide Loading and Ocean Tide Dynamics. *Journal of Geophysical Research: Solid Earth*, 127(11): e2022JB025200, 2022. ISSN 2169-9356. doi: 10.1029/2022JB025200.

U. Hugentobler, D. Ineichen, and G. Beutler. GPS satellites: Radiation pressure, attitude and resonance. *Advances in Space Research*, 31(8):1917–1926, Apr. 2003. ISSN 0273-1177. doi: 10.1016/S0273-1177(03)00174-1.

IGS. International GNSS Service website. https://igs.org/, 2020.

D. Ineichen, G. Beutler, and U. Hugentobler. Sensitivity of GPS and GLONASS orbits with respect to resonant geopotential parameters. *Journal of Geodesy*, 77(7-8):478–486, Oct. 2003. ISSN 0949-7714, 1432-1394. doi: 10.1007/s00190-003-0348-z.

K. H. Ji and T. A. Herring. A method for detecting transient signals in GPS position time-series: Smoothing and principal component analysis. *Geophysical Journal International*, 2013. doi: 10.1093/gji/ggt003.

G. Katsigianni, S. Loyer, and F. Perosanz. PPP and PPP-AR Kinematic Post-Processed Performance of GPS-Only, Galileo-Only and Multi-GNSS. *Remote Sensing*, 11(21):2477, Jan. 2019a. doi: 10.3390/rs11212477.

G. Katsigianni, S. Loyer, F. Perosanz, F. Mercier, and A. Santamaría-Gómez. Galileo Precise Positioning with Ambiguity Resolution and its contribution to Earth Rotation solutions, Sept. 2019b.

G. Katsigianni, S. Loyer, F. Perosanz, F. Mercier, R. Zajdel, and K. Sośnica. Improving Galileo orbit determination using zero-difference ambiguity fixing in a Multi-GNSS processing. *Advances in Space Research*, 63(9):2952–2963, May 2019c. ISSN 02731177. doi: 10.1016/j.asr.2018.08.035.

M. King. Kinematic and static GPS techniques for estimating tidal displacements with application to Antarctica. *Journal of Geodynamics*, 41(1):77–86, Jan. 2006. ISSN 0264-3707. doi: 10.1016/j.jog.2005.08.019.

M. A. King and C. Watson. Long GPS coordinate time series: Multipath and geometry effects. *Journal of Geophysical Research*, 2010. doi: 10.1029/2009jb006543.

M. A. King and S. D. P. Williams. Apparent stability of GPS monumentation from short-baseline time series. *Journal of Geophysical Research: Solid Earth*, 114(B10), 2009. ISSN 2156-2202. doi: 10.1029/2009JB006319.

M. A. King, N. T. Penna, P. J. Clarke, and E. C. King. Validation of ocean tide models around Antarctica using onshore GPS and gravity data. *Journal of Geophysical Research: Solid Earth*, 110(B8), 2005. ISSN 2156-2202. doi: 10.1029/2004JB003390.

M. A. King, Z. Altamimi, J. Boehm, M. Bos, R. Dach, P. Elosegui, F. Fund, M. Hernández-Pajares, D. Lavallee, P. J. Mendes Cerveira, N. Penna, R. E. M. Riva, P. Steigenberger, T. van Dam, L. Vittuari, S. Williams, and P. Willis. Improved Constraints on Models of Glacial Isostatic Adjustment: A Review of the Contribution of Ground-Based Geodetic Observations. *Surveys in Geophysics*, 31(5):465–507, Sept. 2010. ISSN 1573-0956. doi: 10.1007/s10712-010-9100-4.

A. Klos, M. S. Bos, and J. Bogusz. Detecting time-varying seasonal signal in GPS position time series with different noise levels. *GPS Solutions*, 22(1):21, Nov. 2017a. ISSN 1521-1886. doi: 10.1007/s10291-017-0686-6.

A. Klos, G. Olivares, F. N. Teferle, A. Hunegnaw, and J. Bogusz. On the combined effect of periodic signals and colored noise on velocity uncertainties. *GPS Solutions*, 22(1):1, Nov. 2017b. ISSN 1521-1886. doi: 10.1007/s10291-017-0674-x.

A. Klos, J. Bogusz, and G. Moreaux. Stochastic models in the DORIS position time series: Estimates for IDS contribution to ITRF2014. *Journal of Geodesy*, 92(7):743–763, July 2018. ISSN 1432-1394. doi: 10.1007/s00190-017-1092-0.

J. Kouba. Testing of the IERS2000 Sub-Daily Earth Rotation Parameter Model. *Studia Geophysica et Geodaetica*, 47:725–739, 2003. doi: 10.1023/A:1026338601516.

J. Kouba. A simplified yaw-attitude model for eclipsing GPS satellites. *GPS Solutions*, 13(1):1–12, Jan. 2009. ISSN 1521-1886. doi: 10.1007/s10291-008-0092-1.

J. Kouba. Testing of general relativity with two Galileo satellites in eccentric orbits. *GPS Solutions*, 25 (4):139, Aug. 2021. ISSN 1521-1886. doi: 10.1007/s10291-021-01174-3.

A. Koulali and P. J. Clarke. Effect of antenna snow intrusion on vertical GPS position time series in Antarctica. *Journal of Geodesy*, 94(10):101, Oct. 2020. ISSN 1432-1394. doi: 10.1007/s00190-020-01403-6.

D. Kuang, H. J. Rim, B. E. Schutz, and P. A. M. Abusali. Modeling GPS satellite attitude variation for precise orbit determination. *Journal of Geodesy*, 70(9):572–580, Sept. 1996. ISSN 1432-1394. doi: 10.1007/BF00867865.

D. Landskron and J. Böhm. VMF3/GPT3: Refined discrete and empirical troposphere mapping functions. *Journal of Geodesy*, 92(4):349–360, Apr. 2018. ISSN 1432-1394. doi: 10.1007/s00190-017-1066-2.

J. Langbein. Estimating rate uncertainty with maximum likelihood: Differences between power-law and flicker–random-walk models. *Journal of Geodesy*, 86(9):775–783, Sept. 2012. ISSN 1432-1394. doi: 10.1007/s00190-012-0556-5.

J. Langbein and H. Johnson. Correlated errors in geodetic time series: Implications for time-dependent deformation. *Journal of Geophysical Research: Solid Earth*, 102(B1):591–603, 1997. ISSN 2156-2202. doi: 10.1029/96JB02945.

J. Langbein and J. L. Svarc. Evaluation of Temporally Correlated Noise in Global Navigation Satellite System Time Series: Geodetic Monument Performance. *Journal of Geophysical Research: Solid Earth*, 124(1):925–942, 2019. ISSN 2169-9356. doi: 10.1029/2018JB016783.

D. Laurichesse, F. Mercier, J.-P. Berthias, P. Broca, and L. Cerri. Integer Ambiguity Resolution on Undifferenced GPS Phase Measurements and Its Application to PPP and Satellite Precise Orbit Determination. *NAVIGATION*, 56(2):135–149, 2009. ISSN 2161-4296. doi: 10.1002/j.2161-4296.2009.tb01750.x.

K. Le Bail. Estimating the noise in space-geodetic positioning: The case of DORIS. *Journal of Geodesy*, 80(8):541–565, Nov. 2006. ISSN 1432-1394. doi: 10.1007/s00190-006-0088-y.

C. Le Provost, F. Lyard, and J.-M. Molines. Improving ocean tide predictions by using additional semidiurnal constituents from spline interpolation in the frequency domain. *Geophysical Research Letters*, 18(5):845–848, 1991. ISSN 1944-8007. doi: 10.1029/91GL01065.

F. Lefevre. *Modelisation Des Marees Oceaniques a l'echelle Globale : Assimilation de Donnees in Situ et Altimetriques*. These de doctorat, Toulouse 3, Jan. 2000.

A. Lemaître. Space Debris: From LEO to GEO. In G. Baù, A. Celletti, C. B. Galeș, and G. F. Gronchi, editors, *Satellite Dynamics and Space Missions*, volume 34, pages 115–157. Springer International Publishing, Cham, 2019. ISBN 978-3-030-20632-1 978-3-030-20633-8. doi: 10.1007/978-3-030-20633-8_3.

F. Li, J. Lei, S. Zhang, C. Ma, W. Hao, D. E, and Q. Zhang. The impact of solid Earth-tide model error on tropospheric zenith delay estimates and GPS coordinate time series. *Survey Review*, 50(361):355–363, July 2018. ISSN 0039-6265. doi: 10.1080/00396265.2016.1277657.

W. Li, F. Li, C. K. Shum, C. Shu, F. Ming, S. Zhang, Q. Zhang, and W. Chen. Assessment of Contemporary Antarctic GIA Models Using High-Precision GPS Time Series. *Remote Sensing*, 14(5):1070, Jan. 2022. ISSN 2072-4292. doi: 10.3390/rs14051070.

Z. Li, T. van Dam, X. Collilieux, Z. Altamimi, P. Rebischung, and S. Nahmani. Quality Evaluation of the Weekly Vertical Loading Effects Induced from Continental Water Storage Models. In *IAG 150 Years*, pages 45–54. Springer, Cham, 2015. doi: 10.1007/1345_2015_174.

S. Loyer, F. Perosanz, F. Mercier, H. Capdeville, and J.-C. Marty. Zero-difference GPS ambiguity resolution at CNES–CLS IGS Analysis Center. *Journal of Geodesy*, 86(11):991–1003, Nov. 2012. ISSN 0949-7714, 1432-1394. doi: 10.1007/s00190-012-0559-2.

S. Lutz, M. Meindl, P. Steigenberger, G. Beutler, K. Sośnica, S. Schaer, R. Dach, D. Arnold, D. Thaller, and A. Jäggi. Impact of the arc length on GNSS analysis results. *Journal of Geodesy*, 90(4):365–378, Apr. 2016. ISSN 0949-7714, 1432-1394. doi: 10.1007/s00190-015-0878-1.

F. H. Lyard, D. J. Allain, M. Cancet, L. Carrère, and N. Picot. FES2014 global ocean tides atlas: Design and performances. *Ocean Science Discussions*, pages 1–40, Oct. 2020. ISSN 1812-0784. doi: 10.5194/os-2020-96.

F. H. Lyard, D. J. Allain, M. Cancet, L. Carrère, and N. Picot. FES2014 global ocean tide atlas: Design and performance. *Ocean Science*, 17(3):615–649, May 2021. ISSN 1812-0784. doi: 10.5194/os-17-615-2021.

A. Mao, C. G. A. Harrison, and T. H. Dixon. Noise in GPS coordinate time series. *Journal of Geophysical Research: Solid Earth*, 104(B2):2797–2816, 1999. ISSN 2156-2202. doi: 10.1029/1998JB900033.

H. R. Martens and M. Simons. A comparison of predicted and observed ocean tidal loading in Alaska. *Geophysical Journal International*, 223(1):454–470, Oct. 2020. ISSN 0956-540X, 1365-246X. doi: 10.1093/gji/ggaa323.

H. R. Martens, M. Simons, S. Owen, and L. Rivera. Observations of ocean tidal load response in South America from subdaily GPS positions. *Geophysical Journal International*, 205(3):1637–1664, June 2016. ISSN 0956-540X. doi: 10.1093/gji/ggw087.

A. Martín-Español, A. Zammit-Mangion, P. J. Clarke, T. Flament, V. Helm, M. A. King, S. B. Luthcke, E. Petrie, F. Rémy, N. Schön, B. Wouters, and J. L. Bamber. Spatial and temporal Antarctic Ice Sheet mass trends, glacio-isostatic adjustment, and surface processes from a joint inversion of satellite

altimeter, gravity, and GPS data. *Journal of Geophysical Research: Earth Surface*, 121(2):182–200, Feb. 2016. ISSN 2169-9003. doi: 10.1002/2015JF003550.

J. C. Marty, S. Loyer, F. Perosanz, F. Mercier, G. Bracher, B. Legresy, L. Portier, H. Capdeville, F. Fund, J. M. Lemoine, and R. Biancale. GINS: The CNES/GRGS GNSS Scientific Software. In *3rd International Colloquium Scientific and Fundamental Aspects of the Galileo Programme, ESA Proceedings WPP326*, volume 31, pages 8–10, 2011.

S. Masoumi and M. Moore. Multi-GNSS orbit solutions from the third IGS Reprocessing, 2021.

B. Matviichuk, M. King, and C. Watson. Estimating ocean tide loading displacements with GPS and GLONASS. *Solid Earth*, 11(5):1849–1863, Oct. 2020. ISSN 1869-9510. doi: 10.5194/se-11-1849-2020.

B. Matviichuk, M. A. King, C. S. Watson, and M. S. Bos. Limitations in One-Dimensional (an)Elastic Earth Models for Explaining GPS-Observed M2 Ocean Tide Loading Displacements in New Zealand. *Journal of Geophysical Research: Solid Earth*, 126(6):e2021JB021992, June 2021. ISSN 2169-9356. doi: 10.1029/2021JB021992.

J. W. McMahon. *An Analytical Theory for the Perturbative Effect of Solar Radiation Pressure on Natural and Artificial Satellites*. PhD thesis, University of Colorado, 2011.

S. A. Melachroinos, R. Biancale, M. Llubes, F. Perosanz, F. Lyard, M. Vergnolle, M. N. Bouin, F. Masson, J. Nicolas, L. Morel, and S. Durand. Ocean tide loading (OTL) displacements from global and local grids: Comparisons to GPS estimates over the shelf of Brittany, France. *Journal of Geodesy*, 82(6): 357–371, June 2008. ISSN 1432-1394. doi: 10.1007/s00190-007-0185-6.

A. Memin, J.-P. Boy, and A. Santamaría-Gómez. Correcting GPS measurements for non-tidal loading. *GPS Solutions*, 24, Apr. 2020. doi: 10.1007/s10291-020-0959-3.

A. Michel, A. Santamaría-Gómez, J.-P. Boy, F. Perosanz, and S. Loyer. Analysis of GNSS Displacements in Europe and Their Comparison with Hydrological Loading Models. *Remote Sensing*, 13(22):4523, Jan. 2021. ISSN 2072-4292. doi: 10.3390/rs13224523.

C. Milliner, K. Materna, R. Bürgmann, Y. Fu, A. W. Moore, D. Bekaert, S. Adhikari, and D. F. Argus. Tracking the weight of Hurricane Harvey's stormwater using GPS data. *Science Advances*, 4(9):eaau2477, Sept. 2018. doi: 10.1126/sciadv.aau2477.

O. Montenbruck and E. Gill. *Satellite Orbits*. Springer Berlin Heidelberg, Berlin, Heidelberg, 2000. ISBN 978-3-540-67280-7 978-3-642-58351-3. doi: 10.1007/978-3-642-58351-3.

O. Montenbruck, A. Hauschild, P. Steigenberger, U. Hugentobler, P. Teunissen, and S. Nakamura. Initial assessment of the COMPASS/BeiDou-2 regional navigation satellite system. *GPS Solutions*, 17(2): 211–222, Apr. 2013. ISSN 1521-1886. doi: 10.1007/s10291-012-0272-x.

O. Montenbruck, R. Schmid, F. Mercier, P. Steigenberger, C. Noll, R. Fatkulin, S. Kogure, and A. S. Ganeshan. GNSS satellite geometry and attitude models. *Advances in Space Research*, 56(6):1015–1029, Sept. 2015. ISSN 0273-1177. doi: 10.1016/j.asr.2015.06.019.

O. Montenbruck, P. Steigenberger, L. Prange, Z. Deng, Q. Zhao, F. Perosanz, I. Romero, C. Noll, A. Stürze, G. Weber, R. Schmid, K. MacLeod, and S. Schaer. The Multi-GNSS Experiment (MGEX) of the International GNSS Service (IGS) – Achievements, prospects and challenges. *Advances in Space Research*, 59(7):1671–1697, Apr. 2017. ISSN 02731177. doi: 10.1016/j.asr.2017.01.011.

J.-P. Montillet and M. S. Bos, editors. *Geodetic Time Series Analysis in Earth Sciences*. Springer Geophysics. Springer International Publishing, Cham, 2020. ISBN 978-3-030-21717-4 978-3-030-21718-1. doi: 10.1007/978-3-030-21718-1.

J.-P. Montillet, W. Finsterle, G. Kermarrec, R. Sikonja, M. Haberreiter, W. Schmutz, and T. Dudok de Wit. Data Fusion of Total Solar Irradiance Composite Time Series Using 41 Years of Satellite Measurements. *Journal of Geophysical Research: Atmospheres*, 127(13):e2021JD036146, 2022. ISSN 2169-8996. doi: 10.1029/2021JD036146.

A. Navarro Trastoy, S. Strasser, L. Tuppi, M. Vasiuta, M. Poutanen, T. Mayer-Gürr, and H. Järvinen. Coupling a weather model directly to GNSS orbit determination – case studies with OpenIFS. *Geoscientific Model Development*, 15(7):2763–2771, Apr. 2022. ISSN 1991-959X. doi: 10.5194/gmd-15-2763-2022.

T. Nilsson and R. Haas. Impact of atmospheric turbulence on geodetic very long baseline interferometry. *Journal of Geophysical Research: Solid Earth*, 115(B3), 2010. ISSN 2156-2202. doi: 10.1029/2009JB006579.

Y. Niu, M. Li, N. Wei, C. Shi, G. Chen, and L. Wang. The ocean pole tide loading and its effect on GPS position time-series. *Geophysical Journal International*, 227(1):368–382, Oct. 2021. ISSN 0956-540X. doi: 10.1093/gji/ggab231.

Y. Niu, P. Rebischung, M. Li, N. Wei, C. Shi, and Z. Altamimi. Temporal spectrum of spatial correlations between GNSS station position time series. *Journal of Geodesy*, 97(2):12, Feb. 2023. ISSN 1432-1394. doi: 10.1007/s00190-023-01703-7.

B. Øksendal. *Stochastic Differential Equations*. Universitext. Springer Berlin Heidelberg, Berlin, Heidelberg, 2003. ISBN 978-3-540-04758-2 978-3-642-14394-6. doi: 10.1007/978-3-642-14394-6.

N. T. Penna and M. P. Stewart. Aliased tidal signatures in continuous GPS height time series. *Geophysical Research Letters*, 30(23), 2003. ISSN 1944-8007. doi: 10.1029/2003GL018828.

N. T. Penna, M. A. King, and M. P. Stewart. GPS height time series: Short-period origins of spurious long-period signals. *Journal of Geophysical Research: Solid Earth*, 112(B2), 2007. ISSN 2156-2202. doi: 10.1029/2005JB004047.

N. T. Penna, P. J. Clarke, M. S. Bos, and T. F. Baker. Ocean tide loading displacements in western Europe: 1. Validation of kinematic GPS estimates. *Journal of Geophysical Research: Solid Earth*, 120 (9):6523–6539, 2015. ISSN 2169-9356. doi: 10.1002/2015JB011882.

P. B. Persson and C. D. Wagner. General principles of chaotic dynamics. *Cardiovascular Research*, 31(3): 332–341, Mar. 1996. ISSN 0008-6363.

G. Petit and B. Luzum. Displacement of reference points. In *IERS Conventions 2010*, number 36 in Technical Note, pages 99–122. IERS, iers edition, 2010. ISBN 1019-4568.

L. Petrov and J.-P. Boy. Study of the atmospheric pressure loading signal in very long baseline interferometry observations. *Journal of Geophysical Research: Solid Earth*, 109(B3), 2004. ISSN 2156-2202. doi: 10.1029/2003JB002500.

F. Pierret. *Modélisation de Systèmes Dynamiques Déterministes, Stochastiques Ou Discrets*. Theses, Observatoire de Paris, Oct. 2015.

L. Pineau-Guillou, P. Lazure, and G. Wöppelmann. Large-scale changes of the semidiurnal tide along North Atlantic coasts from 1846 to 2018. *Ocean Science*, 17(1):17–34, Jan. 2021. ISSN 1812-0784. doi: 10.5194/os-17-17-2021.

H.-P. Plag and M. Pearlman, editors. *Global Geodetic Observing System*. Springer Berlin Heidelberg, Berlin, Heidelberg, 2009. ISBN 978-3-642-02686-7 978-3-642-02687-4. doi: 10.1007/978-3-642-02687-4.

L. Prange, E. Orliac, R. Dach, D. Arnold, G. Beutler, S. Schaer, and A. Jäggi. CODE's five-system orbit and clock solution—the challenges of multi-GNSS data analysis. *Journal of Geodesy*, 91(4):345–360, Apr. 2017. ISSN 1432-1394. doi: 10.1007/s00190-016-0968-8.

J. Ray, Z. Altamimi, X. Collilieux, and T. van Dam. Anomalous harmonics in the spectra of GPS position estimates. *GPS Solutions*, 12(1):55–64, Jan. 2008. ISSN 1521-1886. doi: 10.1007/s10291-007-0067-7.

J. D. Ray, M. S. M. Vijayan, and A. Kumar. Noise characteristics of GPS time series and their influence on velocity uncertainties. *Journal of Earth System Science*, 128(6):1–14, Aug. 2019. ISSN 0973-774X. doi: 10.1007/s12040-019-1179-5.

P. Rebischung. Terrestrial frame solutions from the IGS third reprocessing. Technical Report EGU21-2144, Copernicus Meetings, Mar. 2021.

P. Rebischung, K. Chanard, L. Metivier, and Z. Altamimi. Flicker Noise in GNSS Station Position Time Series: How much is due to Crustal Loading Deformations? *American Geophysical Union, Fall Meeting*, 2017:G13A–04, Dec. 2017.

P. Rebischung, K. Chanard, L. Metivier, and Z. Altamimi. Aperiodic surface mass transport observed in GRACE and GNSS time series. In *IGS Workshop 2018*, Wuhan, 2018.

P. Rebischung, X. Collilieux, L. Metivier, Z. Altamimi, and K. Chanard. Analysis of IGS repro3 Station Position Time Series. Other, Geodesy, Dec. 2021.

J. M. Reusen, R. Steffen, H. Steffen, B. C. Root, and W. van der Wal. Simulating horizontal crustal motions of glacial isostatic adjustment using compressible Cartesian models. *Geophysical Journal International*, 235(1):542–553, Oct. 2023. ISSN 0956-540X. doi: 10.1093/gji/ggad232.

C. J. Rodriguez-Solano, U. Hugentobler, and P. Steigenberger. Adjustable box-wing model for solar radiation pressure impacting GPS satellites. *Advances in Space Research*, 49(7):1113–1128, Apr. 2012. ISSN 0273-1177. doi: 10.1016/j.asr.2012.01.016.

C. J. Rodriguez-Solano, U. Hugentobler, P. Steigenberger, M. Bloßfeld, and M. Fritsche. Reducing the draconitic errors in GNSS geodetic products. *Journal of Geodesy*, 88(6):559–574, June 2014. ISSN 0949-7714, 1432-1394. doi: 10.1007/s00190-014-0704-1.

A. Romero-Wolf, C. S. Jacobs, and J. T. Ratcliff. Effects of Tropospheric Spatio-temporal Correlated Noise on the Analysis of Space Geodetic Data. *IVS 2012 General Meeting Proceedings*, 2012.

A. J. Rosengren, E. M. Alessi, A. Rossi, and G. B. Valsecchi. Chaos in navigation satellite orbits caused by the perturbed motion of the Moon. *Monthly Notices of the Royal Astronomical Society*, 449(4): 3522–3526, June 2015. ISSN 0035-8711. doi: 10.1093/mnras/stv534.

M. T. Rosenstein, J. J. Collins, and C. J. De Luca. A practical method for calculating largest Lyapunov exponents from small data sets. *Physica D: Nonlinear Phenomena*, 65(1):117–134, May 1993. ISSN 0167-2789. doi: 10.1016/0167-2789(93)90009-P.

P. Sakic, G. Mansur, B. Männel, A. Brack, and H. Schuh. An Experimental Combination of IGS repro3 Campaign's Orbit Products Using a Variance Component Estimation Strategy. In *International Association of Geodesy Symposia*. Springer Berlin Heidelberg, Berlin, Heidelberg, 2022. doi: 10.1007/1345_2022_158.

A. Santamaría-Gómez. SARI: Interactive GNSS position time series analysis software. *GPS Solutions*, 23 (2):52, Mar. 2019. ISSN 1521-1886. doi: 10.1007/s10291-019-0846-y.

A. Santamaría-Gómez and A. Mémin. Geodetic secular velocity errors due to interannual surface loading deformation. *Geophysical Journal International*, 202(2):763–767, Aug. 2015. ISSN 1365-246X, 0956-540X. doi: 10.1093/gji/ggv190.

A. Santamaría-Gómez and J. Ray. Chameleonic Noise in GPS Position Time Series. *Journal of Geophysical Research: Solid Earth*, 126(3):e2020JB019541, 2021. ISSN 2169-9356. doi: 10.1029/2020JB019541.

A. Santamaría-Gómez, M.-N. Bouin, X. Collilieux, and G. Wöppelmann. Correlated errors in GPS position time series: Implications for velocity estimates. *Journal of Geophysical Research: Solid Earth*, 116(B1), 2011. ISSN 2156-2202. doi: 10.1029/2010JB007701.

M. Schenewerk. A brief review of basic GPS orbit interpolation strategies. *GPS Solutions*, 6(4):265–267, Mar. 2003. ISSN 1080-5370. doi: 10.1007/s10291-002-0036-0.

M. Seitz, M. Bloßfeld, D. Angermann, and F. Seitz. DTRF2014: DGFI-TUM's ITRS realization 2014. *Advances in Space Research*, 69(6):2391–2420, Mar. 2022. ISSN 02731177. doi: 10.1016/j.asr.2021.12.037.

E. Serpelloni, G. Vannucci, S. Pondrelli, A. Argnani, G. Casula, M. Anzidei, P. Baldi, and P. Gasperini. Kinematics of the Western Africa-Eurasia plate boundary from focal mechanisms and GPS data. *Geophysical Journal International*, 169(3):1180–1200, June 2007. ISSN 0956540X, 1365246X. doi: 10.1111/j.1365-246X.2007.03367.x.

A. E. Sibois, S. D. Desai, W. Bertiger, and B. J. Haines. Analysis of decade-long time series of GPS-based polar motion estimates at 15-min temporal resolution. *Journal of Geodesy*, 91(8):965–983, Aug. 2017. ISSN 1432-1394. doi: 10.1007/s00190-017-1001-6.

D. Sidorov and F. N. Teferle. Impact of Antenna Phase Centre Calibrations on Position Time Series: Preliminary Results. In C. Rizos and P. Willis, editors, *IAG 150 Years*, volume 143, pages 117–123. Springer International Publishing, Cham, 2015. ISBN 978-3-319-24603-1 978-3-319-30895-1. doi: 10.1007/1345_2015_216.

D. Sidorov, R. Dach, B. Polle, L. Prange, and A. Jäggi. Adopting the empirical CODE orbit model to Galileo satellites. *Advances in Space Research*, 66(12):2799–2811, Dec. 2020. ISSN 0273-1177. doi: 10.1016/j.asr.2020.05.028.

C. Song, H. Chen, W. Jiang, X. An, Q. Chen, and W. Li. An effective interpolation strategy for mitigating the day boundary discontinuities of precise GNSS orbit products. *GPS Solutions*, 25(3):99, May 2021. ISSN 1521-1886. doi: 10.1007/s10291-021-01130-1.

K. Sośnica, R. Zajdel, G. Bury, J. Bosy, M. Moore, and S. Masoumi. Quality assessment of experimental IGS multi-GNSS combined orbits. *GPS Solutions*, 24:54, Mar. 2020. doi: 10.1007/s10291-020-0965-5.

K. Sośnica, G. Bury, R. Zajdel, K. Kazmierski, J. Ventura-Traveset, R. Prieto-Cerdeira, and L. Mendes. General relativistic effects acting on the orbits of Galileo satellites. *Celestial Mechanics and Dynamical Astronomy*, 133(4):14, Mar. 2021. ISSN 1572-9478. doi: 10.1007/s10569-021-10014-y.

J. C. Sprott. *Chaos and Time-Series Analysis*. Oxford Univ. Press, Oxford, 2. repr edition, 2006. ISBN 978-0-19-850840-3 978-0-19-850839-7.

R. Steffen. AGU Geodesy Section Webinar: Models of Glacial Isostatic Adjustment and Their Use in Geodesy and Tectonics, 2023.

P. Steigenberger, M. Fritsche, R. Dach, R. Schmid, O. Montenbruck, M. Uhlemann, and L. Prange. Estimation of satellite antenna phase center offsets for Galileo. *Journal of Geodesy*, 90(8):773–785, Aug. 2016. ISSN 1432-1394. doi: 10.1007/s00190-016-0909-6.

M. P. Stewart, N. T. Penna, and D. D. Lichti. Investigating the propagation mechanism of unmodelled systematic errors on coordinate time series estimated using least squares. *Journal of Geodesy*, 79(8): 479–489, Nov. 2005. ISSN 1432-1394. doi: 10.1007/s00190-005-0478-6.

S. Strasser. *Reprocessing Multiple GNSS Constellations and a Global Station Network from 1994 to 2020 with the Raw Observation Approach*. PhD thesis, Technischen Universität Graz, 2022.

S. H. Strogatz. *Nonlinear Dynamics and Chaos: With Applications to Physics, Biology, Chemistry, and Engineering*. Westview Press, a member of the Perseus Books Group, Boulder, CO, second edition edition, 2015. ISBN 978-0-8133-4910-7.

A. Takahashi and M. Hashimoto. Cluster Analysis of Dense GNSS Velocity Field Reveals Characteristics Associated With Regional Tectonics in New Zealand. *Journal of Geophysical Research: Solid Earth*, 127 (11):e2022JB024793, Nov. 2022. ISSN 2169-9313, 2169-9356. doi: 10.1029/2022JB024793.

E. Tao, N. Guo, K. Xu, B. Wang, and X. Zhou. Validation of Multi-Year Galileo Orbits Using Satellite Laser Ranging. *Remote Sensing*, 13(22):4634, Jan. 2021. doi: 10.3390/rs13224634.

K. Teke. The principle diurnal and semidiurnal tides of the ocean loading displacements and their long-term variability as observed by VLBI. *Acta Geodaetica et Geophysica*, May 2021. ISSN 2213-5820. doi: 10.1007/s40328-021-00340-w.

P. J. Teunissen and O. Montenbruck, editors. *Springer Handbook of Global Navigation Satellite Systems*. Springer International Publishing, Cham, 2017. ISBN 978-3-319-42926-7 978-3-319-42928-1. doi: 10.1007/978-3-319-42928-1.

I. D. Thomas, M. A. King, and P. J. Clarke. A comparison of GPS, VLBI and model estimates of ocean tide loading displacements. *Journal of Geodesy*, 81(5):359–368, May 2007. ISSN 0949-7714, 1432-1394. doi: 10.1007/s00190-006-0118-9.

X. Tong, D. T. Sandwell, and B. R. Smith-Konter. High-resolution interseismic velocity data along the San Andreas Fault from GPS and InSAR. *Journal of Geophysical Research*, 2013. doi: 10.1029/2012jb009442.

P. Tregoning and C. Watson. Atmospheric effects and spurious signals in GPS analyses. *Journal of Geophysical Research: Solid Earth*, 114(B9), 2009. ISSN 2156-2202. doi: 10.1029/2009JB006344.

T.-P. Tseng. A Hybrid ECOM Model for Solar Radiation Pressure Effect on GPS Reference Orbit Derived by Orbit Fitting Technique. *Remote Sensing*, 13(22):4681, Jan. 2021. doi: 10.3390/rs13224681.

UN Commitee of experts on Global Geospatial Information Management (UN-GGIM). Position Paper on Sustaining the Global Geodetic Reference Frame. Position Paper Add. 2, UN-GGIM, 2021.

C. Urschl, R. Dach, U. Hugentobler, S. Schaer, and G. Beutler. Validating ocean tide loading models using GPS. *Journal of Geodesy*, 78(10):616–625, May 2005. ISSN 0949-7714, 1432-1394. doi: 10.1007/s00190-004-0427-9.

S. Valk. *Global Dynamics of Geosynchronous Space Debris with High Area-to-Mass Ratios*. Ph. D. Thesis in Mathematics, University of Namur, Belgium, 2008.

D. A. Vallado and W. D. McClain. *Fundamentals of Astrodynamics and Applications*. Number 21 in Space Technology Library. Microcosm Press, Hawthorne, Calif, 4. ed edition, 2013. ISBN 978-1-881883-18-0.

T. van Dam, J. Wahr, P. C. D. Milly, A. B. Shmakin, G. Blewitt, D. Lavallée, and K. M. Larson. Crustal displacements due to continental water loading. *Geophysical Research Letters*, 28(4):651–654, 2001. ISSN 1944-8007. doi: 10.1029/2000GL012120.

T. van Dam, X. Collilieux, J. Wuite, Z. Altamimi, and J. Ray. Nontidal ocean loading: Amplitudes and potential effects in GPS height time series. *Journal of Geodesy*, 86(11):1043–1057, Nov. 2012. ISSN 1432-1394. doi: 10.1007/s00190-012-0564-5.

M. Vergnolle, M.-N. Bouin, L. Morel, F. Masson, S. Durand, J. Nicolas, and S. A. Melachroinos. GPS estimates of ocean tide loading in NW-France: Determination of ocean tide loading constituents and comparison with a recent ocean tide model. *Geophysical Journal International*, 173(2):444–458, May 2008. ISSN 0956540X, 1365246X. doi: 10.1111/j.1365-246X.2008.03734.x.

D. Walwer, E. Calais, and M. Ghil. Data-adaptive detection of transient deformation in geodetic networks: DATA-ADAPTIVE GPS TIME SERIES ANALYSIS. *Journal of Geophysical Research: Solid Earth*, 121(3):2129–2152, Mar. 2016. ISSN 21699313. doi: 10.1002/2015JB012424.

D. Wang, H. Pan, G. Jin, and X. Lv. Seasonal variation of the principal tidal constituents in the Bohai Sea. *Ocean Science*, 16(1):1–14, Jan. 2020a. ISSN 1812-0784. doi: 10.5194/os-16-1-2020.

J. Wang, N. T. Penna, P. J. Clarke, and M. S. Bos. Asthenospheric anelasticity effects on ocean tide loading around the East China Sea observed with GPS. *Solid Earth*, 11(1):185–197, Feb. 2020b. ISSN 1869-9510. doi: 10.5194/se-11-185-2020.

K. Wang, H. Chen, W. Jiang, Z. Li, Y. Ma, and L. Deng. Improved vertical displacements induced by a refined thermal expansion model and its quantitative analysis in GPS height time series. *Journal of Geophysics and Engineering*, 15(2):554–567, Apr. 2018. ISSN 1742-2132, 1742-2140. doi: 10.1088/1742-2140/aa93ae.

C. Watson, P. Tregoning, and R. Coleman. Impact of solid Earth tide models on GPS coordinate and tropospheric time series. *Geophysical Research Letters*, 33(8), 2006. ISSN 1944-8007. doi: 10.1029/2005GL025538.

G. Wei, K. Chen, and R. Ji. Improving estimates of ocean tide loading displacements with multi-GNSS: A case study of Hong Kong. *GPS Solutions*, 26(1):25, Dec. 2021. ISSN 1521-1886. doi: 10.1007/s10291-021-01212-0.

A. M. White, W. P. Gardner, A. A. Borsa, D. F. Argus, and H. R. Martens. A Review of GNSS/GPS in Hydrogeodesy: Hydrologic Loading Applications and Their Implications for Water Resource Research. *Water Resources Research*, 58(7):e2022WR032078, 2022. ISSN 1944-7973. doi: 10.1029/2022WR032078.

P. L. Whitehouse, N. Gomez, M. A. King, and D. A. Wiens. Solid Earth change and the evolution of the Antarctic Ice Sheet. *Nature Communications*, 10(1):503, Jan. 2019. ISSN 2041-1723. doi: 10.1038/s41467-018-08068-y.

S. Wiggins. *Introduction to Applied Nonlinear Dynamical Systems and Chaos*. Number 2 in Texts in Applied Mathematics. Springer, New York, 2nd ed edition, 2003. ISBN 978-0-387-00177-7.

S. D. P. Williams. The effect of coloured noise on the uncertainties of rates estimated from geodetic time series. *Journal of Geodesy*, 76(9-10):483–494, Feb. 2003a. ISSN 0949-7714, 1432-1394. doi: 10.1007/s00190-002-0283-4.

S. D. P. Williams. Offsets in Global Positioning System time series. *Journal of Geophysical Research: Solid Earth*, 108(B6), 2003b. ISSN 2156-2202. doi: 10.1029/2002JB002156.

S. D. P. Williams. Error analysis of continuous GPS position time series. *Journal of Geophysical Research*, 109(B3):B03412, 2004. ISSN 0148-0227. doi: 10.1029/2003JB002741.

S. D. P. Williams. CATS: GPS coordinate time series analysis software. *GPS Solutions*, 12(2):147–153, Mar. 2008. ISSN 1080-5370, 1521-1886. doi: 10.1007/s10291-007-0086-4.

S. D. P. Williams and N. T. Penna. Non-tidal ocean loading effects on geodetic GPS heights. *Geophysical Research Letters*, 38(9), 2011. ISSN 1944-8007. doi: 10.1029/2011GL046940.

G. Wöppelmann and M. Marcos. Vertical land motion as a key to understanding sea level change and variability. *Reviews of Geophysics*, 54(1):64–92, 2016. ISSN 1944-9208. doi: 10.1002/2015RG000502.

F. Wyatt. Displacement of surface monuments: Horizontal motion. *Journal of Geophysical Research: Solid Earth*, 87(B2):979–989, 1982. ISSN 2156-2202. doi: 10.1029/JB087iB02p00979.

F. Wyatt. Displacement of surface monuments: Vertical motion. *Journal of Geophysical Research: Solid Earth*, 94(B2):1655–1664, 1989. ISSN 2156-2202. doi: 10.1029/JB094iB02p01655.

H. Yan, W. Chen, Y. Zhu, W. Zhang, and M. Zhong. Contributions of thermal expansion of monuments and nearby bedrock to observed GPS height changes. *Geophysical Research Letters*, 36(13), 2009. ISSN 1944-8007. doi: 10.1029/2009GL038152.

F. Yang, L. Liang, C. Wang, and Z. Luo. Attitude Determination for GRACE-FO: Reprocessing the Level-1A SC and IMU Data. *Remote Sensing*, 14(1):126, Jan. 2022. ISSN 2072-4292. doi: 10.3390/rs14010126.

H. Yousif and A. El-Rabbany. Assessment of Several Interpolation Methods for Precise GPS Orbit. *Journal of Navigation*, 60(3):443–455, Sept. 2007. ISSN 0373-4633, 1469-7785. doi: 10.1017/S0373463307004250.

L. Yuan, B. F. Chao, X. Ding, and P. Zhong. The tidal displacement field at Earth's surface determined using global GPS observations. *Journal of Geophysical Research: Solid Earth*, 118(5):2618–2632, 2013. ISSN 2169-9356. doi: 10.1002/jgrb.50159.

R. Zajdel, K. Sośnica, G. Bury, R. Dach, L. Prange, and K. Kazmierski. Sub-daily polar motion from GPS, GLONASS, and Galileo. *Journal of Geodesy*, 95(1):3, Dec. 2020. ISSN 1432-1394. doi: 10.1007/s00190-020-01453-w.

R. Zajdel, K. Kazmierski, and K. Sośnica. Orbital Artifacts in Multi-GNSS Precise Point Positioning Time Series. *Journal of Geophysical Research: Solid Earth*, 127(2), Feb. 2022. ISSN 2169-9313, 2169-9356. doi: 10.1029/2021JB022994.

R. Zajdel, K. Sośnica, S. Masoumi, G. Bury, and D. Strugarek. SLR validation of the IGS Repro3 orbits for ITRF2020. Technical Report EGU23-455, Copernicus Meetings, Feb. 2023.

J. Zhang, Y. Bock, H. Johnson, P. Fang, S. Williams, J. Genrich, S. Wdowinski, and J. Behr. Southern California permanent GPS geodetic array: Error analysis of daily position estimates and site velocities. *Journal of Geophysical Research: Solid Earth*, 102(B8):18035–18055, 1997. ISSN 2156-2202. doi: 10.1029/97JB01380.

H. Zhao, Z. Liu, G. Jiang, Z. Liu, Y. Sun, and D. He. Estimation of the ocean tide loading displacements by GPS and GLONASS kinematic Precise Point Positioning. *Survey Review*, 0(0):1–13, Dec. 2021. ISSN 0039-6265. doi: 10.1080/00396265.2021.1982178.

M. Zhou, X. Liu, J. Yuan, X. Jin, Y. Niu, J. Guo, and H. Gao. Seasonal Variation of GPS-Derived the Principal Ocean Tidal Constituents' Loading Displacement Parameters Based on Moving Harmonic Analysis in Hong Kong. *Remote Sensing*, 13(2):279, Jan. 2021. doi: 10.3390/rs13020279.

J. F. Zumberge, M. B. Heflin, D. C. Jefferson, M. M. Watkins, and F. H. Webb. Precise point positioning for the efficient and robust analysis of GPS data from large networks. *Journal of Geophysical Research: Solid Earth*, 102(B3):5005–5017, Mar. 1997. ISSN 01480227. doi: 10.1029/96JB03860.